Dissertation
submitted to the
Combined Faculties for the Natural Sciences and for Mathematics
of the Rupertus Carola University of
Heidelberg, Germany
for the degree of
Doctor of Natural Sciences

presented by

Diplom-Physicist: Zoltán Kovács
born in: Sopron, Hungary
Oral examination: 11th January 2006

Test of the Infrared Wide-Field Camera OMEGA2000 and its Application for an Extragalactic Survey

Referees: Prof. Dr. Klaus Meisenheimer

Prof. Dr. Immo Appenzeller

Zusammenfassung

OMEGA2000 ist eine Weitfeld-Nahinfrarot-Kamera, angebracht im Primaerfokus des 3.5m-Teleskopes auf Calar Alto. In der Fokalebene befindet sich ein 2k×2k HAWAII-2 CCD-Detektor, der in dem Wellenlängenbereich vom z- bis zum K-Band empfindlich ist. In dem ersten Teil der Dissertation beschreiben wir unsere Anstrengung, die Funktionsweise des HAWAII-2 Detektors zu optimieren. Dafür haben wir drei Exemplare aus der HAWAII-2-Familie getestet und miteinander verglichen. Um die Ergebnisse der Durchmusterung COMBO-17 mit Hilfe von OMEGA2000 zu höheren Rotverschiebungen zu erweitern, wurde eine tiefe Durchmusterung "MANOS", genannt auch COMBO-17+4, geplannt. Die gegenwärtig vorhandenen Daten beschränken das ursprüngliche Projekt auf die COMBO-17+2 Nahinfrarot-Durchmusterung. In dem zweiten Teil der Arbeit besprechen wir die ersten Ergebnisse von COMBO-17+2 NIR. Wir präsentieren hier die Rotverschiebungsverteilung der hellen Infrarotgalaxien im COMBO S11 Feld und analysieren die Anzahlentwicklung von vier Galaxientypen, die auf Grund von Ruhesystem-Farben definiert sind. Wir stellen einen Rückgang fest in der Zahl der alten elliptischen und der entwickelten Spiral-Galaxien bei der Rotverschiebung Dies steht in Ubereinstimmung mit früheren Ergebnissen. Für die "Extrem Roten Objekten" (EROs) im COMBO S11 Feld, die durch $R - H < 4$ ausgewählt wurden, beobachten wir ähnliche Rotverschiebungsverteilung und Häufungssignal, wie sie auch aus den anderen Durchmusterungen abgeleitet wurden. In unserer Auswahl von ERO's sind keine Galaxien mit heftiger Sternentstehung enthalten, was die Ergebnisse der frühere Beobachtungen bestaetigt. Die vollständige Abwesenheit der Sternentstehungssysteme kann auch eine Folge der ausgewählte Spektralschablonenbibliothek sein, die für die Multi-Farben Klassifikation in der COMBO-17+2 NIR eingesetzt wurde.

Abstract

OMEGA2000 is a prime-focus, near-infrared, wide-field camera, mounted on the 3.5m telescope at Calar Alto. The camera uses a 2k×2k HAWAII-2 Focal plane array with a sensitivity from z to K band. In the first part of the thesis, we discuss the work aimed at optimizing the operation of the HAWAII-2 detector installed in the camera. We tested the operation of three speciemen from the HAWAII-2 family and compared their performances with each other. The MANOS Deep Field Survey, called COMBO-17+4 NIR, is planned to to extend the results of the COMBO-17 project to higher redshifts by using this camera. The currently available data restricted the original project to the COMBO-17+2 NIR survey. In the second part of the thesis we discuss the results produced by COMBO-17+2 NIR. We present the redshift distribution of bright infrared galaxies observed in the COMBO S11 field and analyse the evolution of their number counts for four galaxy types defined by their restframe colors. We find a decline in the number of the old elliptical and evolved spiral galaxies at $z > 1.5$, whereas the actively star-forming galaxies become the dominating population at $z > 1$. This is in a broad agreement with earlier results. For Extremely Red Objects (EROs) in the COMBO S11 field selected with $R - H < 4$, we measure similar redshift distribution and clustering signal to those derived in other surveys. Our ERO sample does not contain starburst galaxies, confirming the results of earlier observations. The total absence of the star-forming systems may also be attributed to the spectral template library used in the COMBO-17+2 NIR multi-color classification.

Contents

Introduction

Infrared Astronomy is the study of the infrared radiation emitted from objects in the Universe. All of the celestial objects radiate some amount of energy in the infrared wavelength regime. Studying the infrared part of their emitted energy provides interesting information on their physical properties and helps us to understand the astrophysical processes associated with them. The infrared regime lies between wavelengths of about 1 and 300 μm. It is usually divided into 3 spectral regions: near (0.7-4 μm), mid-infrared (4-40 μm), and far-infrared (40-350 μm).

Many objects in the universe which are much too cool and distant to be detected with visible light, can be studied in the infrared wavelength range. These include cool stars, clouds of dust particles around stars, nebulae, interstellar molecules, brown dwarfs, planets, and evolved galaxies. In space, there also are many regions which are hidden from optical telescopes because they are embedded in dense regions of gas and dust. However, infrared radiation can pass through dusty regions of space without being significantly scattered. Infrared astronomy can observe optically hidden parts of our galaxy and regions of newly forming stars.

In the infrared regime we can gather information about the early Universe and study the evolution of galaxies as well. As a result of the Big Bang, the universe is expanding and most of the galaxies within it are accelerating away from each other. This recession of galaxies away from the Milky Way causes a redshift in the in the wavelength of the light emitted from these galaxies. At large redshifts, all of the ultraviolet and much of the visible light is shifted into the infrared part of the observed spectrum. So the study of infrared light from these distant sources is important. Telescopes observing in infrared regime can locate more galaxies, which are at a sufficiently large distance as to be indetectable with visible light. Therefore infrared astronomy will provide a great deal of information on how and when the universe was formed and what the early universe was like. In addition, it allows us to observe the old stellar component in evolved massive elliptical galaxies. Such discoveries may help to find new constraints on the theories about galactic evolution. It is believed that the bulk of most galaxies is composed of cool stars. Infrared telescopes can see these cool stars very clearly since they emit more infrared than visible frequencies of light. Thus infrared astronomy will play a role in determining the mass of the universe.

Infrared detectors are also well suited to looking at distant objects, such as quasars. These unusual objects with incredibly high red shifts may be the most distant (and therefore the oldest) objects in the universe. Observing them in visible light is very difficult since the quasars' red shifts have stretched their visible light into the infrared part of the spectrum, but this makes them ideal targets for an infrared telescope. Both the determination of the universe's mass and the observation of quasars assist cosmologists in refining the big bang theory - the currently

accepted description of the evolution of the universe.

Unfortunately the Earth's atmosphere causes a problem for ground based infrared observations. The atmosphere lets visible light, most radio waves, and small wavelength ranges of infrared light through whereas the rest is absorbed by water vapor and carbon dioxide. The atmosphere itself radiates strongly in the infrared as well, often producing a more intensive infrared background noise than the light of the objects in space being observed. This atmospheric infrared emission peaks at a wavelength of about 10 microns. The observers can use only a few windows in the infrared wavelength regime with both high sky transparency and low sky emission. These windows, called J, H and K bands, are mainly at Near Infrared (NIR) wavelengths below 4 microns. All the ground based NIR observations are adapted to these windows and obtain information from only these wavelength intervals.

Astronomers in the 1970s began making observations of the sky using infrared detectors, but in order to produce an image they needed long exposures. Because of the small size and therefore the small field of view of the infrared sensors, they produced small pieces of mosaics that had to be fit together to form a larger image with low resolution. The situation improved in the 1980s when large infrared detectors were developed for military use. Astronomers were able to adapt these new instruments for their own purposes. The new devices are tuned to specific near or far infrared wavelengths. Combined with satellite technology, these new imaging devices are extending to prospects of the observation of the Universe. Nowadays infrared detector technology has a rapid development. Astronomers use InSb and HgCdTe detectors for the 1 to 5 micron range, which are much more sensitive then the traditional infrared CCDs. The development of infrared array detectors from the 1980's to now has been increasing the sensitivity of infrared observations to a great extent. During this time detector arrays were introduced, as a combination of several single detectors. They, together with the sophisticated optical systems built in cameras, allow astronomers to produce high resolution images containing tens of millions of pixels.

Infrared instrumentation at Calar Alto is essential for German and Spanish astronomy in the northern hemisphere. In recent years, the MPIA and Calar Alto Observatory have made a great leap in the development of infrared instrumentation and astronomy. The principal instruments used until 2003 were Omega Cass and Omega Prime. These cameras have 1k×1k HAWAII-1 HgCdTe arrays manufactured by Rockwell Science Center in the USA. These were the largest available arrays of their type at the time, and the Omega Prime camera still has one of the largest field of view (6.8 arcmin) on a 4m class telescope for infrared astronomy. However, this is small compared to optical cameras (e.g. 33 arcmin for the Wide Field Imager on MPG/ESO 2.2m at La Silla), and only now are larger arrays being fabricated. As a continuation of these achievements, the MPIA started the OMEGA2000 project. In the framework of this project the OMEGA2000 instrument has been built and mounted on the 3.5m telescope in Calar Alto. The OMEGA2000 is a wide field NIR imaging camera, which uses a 2k×2k HAWAII-2 HgCdTe Focal Plane Array from Rockwell. The camera was successfully installed and is already in operation, producing valuable data in observations runing in the last two years.

The goal of this doctoral thesis is to present the work I made as a participant in the OMEGA2000 projects and as a scientific user of the instrument. As a project member, I had the technical task to implement and test the operation of the OMEGA2000 camera and as an

astronomer I carried out observations with the wide field imager, reduced, evaluated, and interpreted the observed data. According to this twofold task, the thesis consists of two parts. The first part is devoted to the technical side of the project - discussing how to impelement and optimize the operation of the HAWAII-2 Focal Plane Array (FPA) installed in the OMEGA2000 instrument and to test its performance. The first part of thesis starts with an overview on the HAWAII-2 detector, describing its architecture and operation. Then I give the detailed specifications of this work, where we discuss the solutions of the problems related to the operation of the camera. We also describe the methods and techniques applied to optimize the detector operation. MPIA had an opportunity to test three specimen of this type of FPA which were used in different scientific projects and compare their performance. In the end of the first part we also present the results of the performance tests of these detectors. The second part of the thesis presents a scientific application of the OMEGA2000 instrument. This application was the COMBO-17+2 NIR survey, a preliminary study of the MANOS Deep or COMBO-17+4 NIR project. MANOS Deep Field Survey was planned to extend the results of the COMBO-17 galaxy survey, which provided reliable photometric redshifts derived from an optical data set of 17 filters for about 25,000 galaxies in three fields. The aim of COMBO-17+4 NIR survey is to extend the statistics of various astrophysical properties in this galaxy sample to higher redshifts and to improve the measurement of these properties by supplementing the optical data set of the COMBO-17 survey with NIR band data of 4 filters. In the preliminary survey the OMEGA2000 camera produced NIR data in two bands for a COMBO-17 field which already have a full set of optical data. In the second part of the thesis we review the results of the COMBO-17 survey and discuss the technical and astrophysical results of the preliminary survey. We analyze the improvement in the measurement due to the NIR-band extention and the increase of the number of filters, comparing the measurement process based on only optical data with that based on the optical and the NIR-band data. Due to the still limited depth of the NIR observations, the original plan to extent the results of the COMBO-17 survey to higher redshifts was postponed. We restricted the aim of thesis to the study of objects which are especially bright in H band. Therefore we discuss the preliminary results produced by COMBO-17+2 NIR survey in astrophysical context. We present the redshift distribution of bright infrared galaxies selected from the COMBO-17 sample and analyse the redshift evolution of their number counts for four galaxy types defined by their restframe colors. As a special astrophysical application related to the bright infrared sources, we study the sample of the Extremely Red Object (EROs) detected in the COMBO-17+2 NIR survey and complete the thesis with some results on their properties and nature, which were derived from survey data.

Part I

Test of the wide-field Infrared Camera OMEGA2000

Chapter 1

OMEGA2000 Instrument

The OMEGA2000 instrument is a prime focus near infrared (NIR) wide-field camera mounted on the 3.5 m telescope at Calar Alto in Spain (Fig. 1.1). The camera uses a HAWAII-2 2kx2k HgCdTe Focal Plane Array (FPA), which is a new generation of the large format NIR image sensors developed by the Rockwell company. The instrument, designed particularly for survey observations, has an excellent optical quality and high sensitivity over a wide field. In order to archive an outstanding performance of OMEGA2000, many requirements must be met by the optical, mechanical, and the electronic components of the camera system. The first chapter reviews the set-up and operation of these carefully designed and produced mechanisms. In the first section we begin with a short account of the mechanical design of the dewar containing the camera system. The cryogenic optical system, consisting of a four-lens focal reducer located in

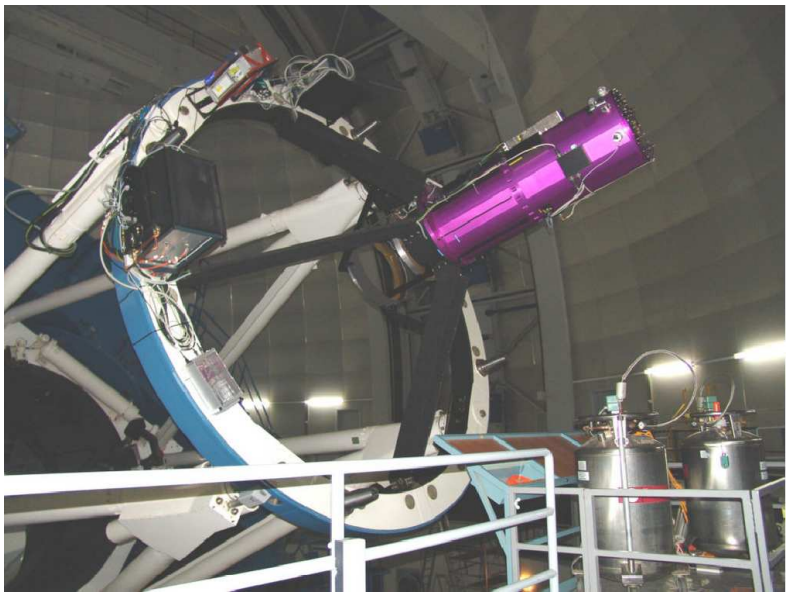

Figure 1.1: The OMEGA2000 NIR camera mounted on front ring (In Röser, 2004).

the prime focus, will then be discussed briefly in the second section. The third section presents the mechanical design of the filter wheels and the warm mirror baffle system as well. The chapter is ended with a concise description of the multi functional data acquisition system and control software of OMEGA2000, which performs the readout and the data saving simultaneously at a

high data rate.

1.1 Cryostat

One of the most important problems in ground based Infra Red (IR) imaging is to reduce the photon noise from the background. A significant part of this noise is from the bright sky, which is predominantly OH air-glow at nights in the wavelength regime below 3 μm. The thermal radiation from the warm telescope mirrors, structure, and dome is dominant longwards of about 2.2 μm, causing problems for the K-band imaging. In an effort to insulate the detector and the optics of OMEGA2000 from the latter, they are enclosed in a cryostat and cooled by liquid nitrogen to the operating temperature, 77 K (Baumeister et al., 2002). The cryostat contains three shields nested into each other whose purpose is to reduce the thermal radiation (Fig. 1.2). The liquid nitrogen is stored in two vessels, which can be filled on the telescope through the upper side of the dewar. The inner vessel is directly connected to the inner radiation shield and the outer one to the second shield. The outer shield is passive, since it is not thermally connected to the vessels. The lower end of the inner vessel also serves as a base for the cold plate of the detector unit. Both vessels are filled up to a level which allows a tilt angle of the telescope for taking the service position. After filling up the vessels, the dewar keeps the cold parts at thermal equilibrium for about 34 hours. In order to control the axial and radial shrinkage of the vessels and the shields, epoxy spacers carrying the axial loads are attached to the vessels. This allows the inner parts to be supported flexibly in the axial direction and rigidly in the radial one.

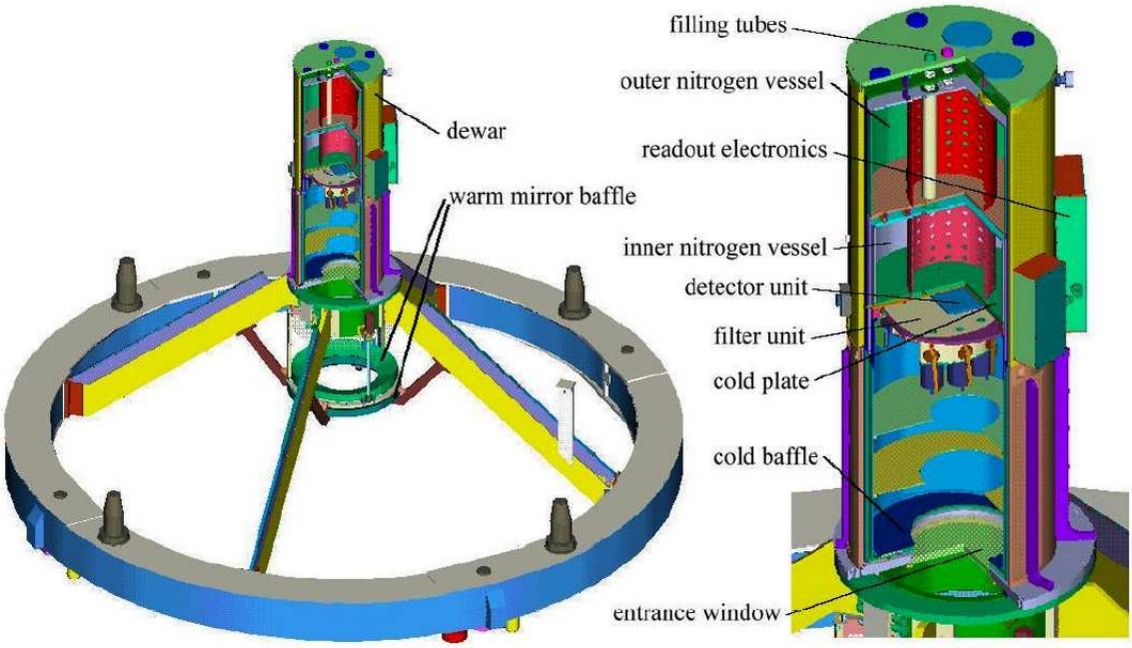

Figure 1.2: The OMEGA2000 cryostat mounted on front ring (In Baumeister et al., 2002).

1.2 Optics

Since the primary science goal was for OMEGA2000 to be a IR wide field imager, producing high quality images with the largest reasonable pixel scale, it is placed at the prime focus of the telescope. The optics consists of a cryogenic focal reducer providing a 15.4 × 15.4 arcmin field of view with a resolution of 0.45 arcsec/pixel (Baumeister et al., 2002). It has four corrector lenses made of CaF_2, fused silica (FS), BaF_2 and ZnSe with diameters between 106 and 150 mm, which are achromatic between 850 and 2500 nm (Fig.1.3). Each lens is fixed by a spring-loaded retainer ring in a single assembly. To achieve an excellent optical image quality and to minimize

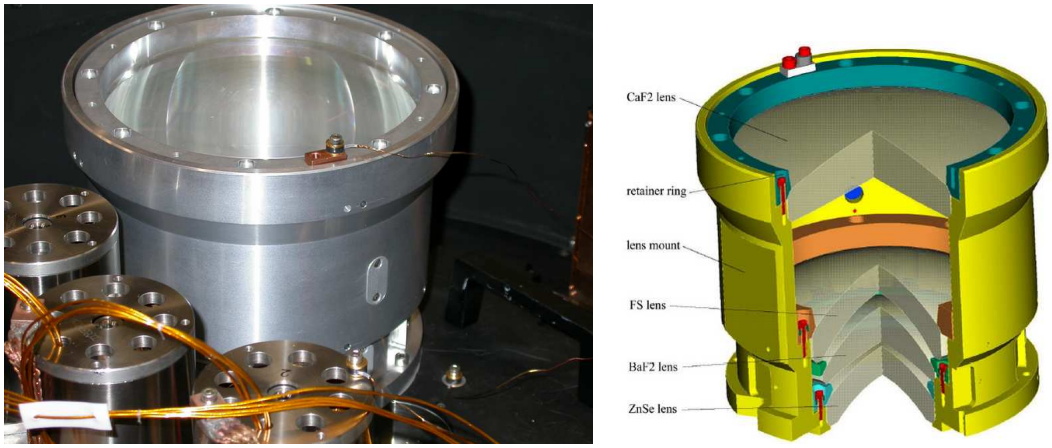

Figure 1.3: Four lens reducer with spring loaded cryogenic lens mount (In Baumeister et al., 2002).

the lens diameters, the focal reducer unit is located in the dewar, as close to the detector as possible. This means it is cooled down to a temperature of about 80 K, so the most difficult task of the lens mount design was to make sure that the lenses survive cooling and at the same time achieve the tight tolerances required for high optical quality. As a solution to this problem, chamfers with angle of 45° are used for both outer edges of each lens, the lens mount and the retainer ring. The lenses sit on the conical surfaces of the mount and the retainer keeps them in this position. Temperature changes result in diameter changes in the parts and lenses can slide on the chamfer surfaces relative to each other, which leads to an axial displacement. Tests have shown that changes in the accurately aligned lens positions (±0.01mm) caused by multiple cooling cycles and changes in dewar orientation cannot be measured down to the accuracy of ±0.005mm. With these tolerances, the optical quality produced by the focal reducer together with the dewar window completely fulfills the requirements. To determine the optical distortion, during the operation of the camera distances between a star at the center and all the other objects in the field of view were calculated both from the measured positions on the detector and directly from the differences of the RA and DEC positions. The ratio of the two distance measurements was plotted as a function of distance from the field center. The center to corner image distortion was measured to 0.12" for the maximum distance of 600", which is less than one pixel (Fig. 1.4). This is an exceptionally low distortion level. However scattered light and reflections could be seen in the flat-field images, which were attributed to the shining aluminum

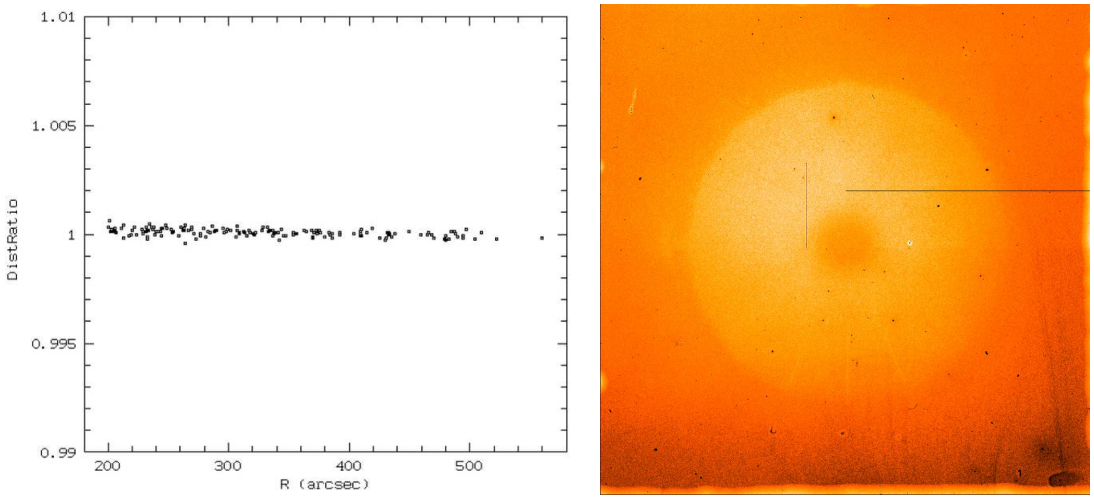

Figure 1.4: The left hand panel shows the center to corner image distortion of the OMEGA2000 optics (In Röser, 2004) and the right hand panel is a flatfield frame with the ghost image of the primary mirror.

surface of the optics mount. The largest accessible areas were covered to reduce the scattering but the bevels defining the lens positions could not be painted and they were still reflecting surfaces. There were also reflections between the filter surface and the innermost lens producing ghost images of the primary mirror in the flatfields (Fig. 1.4).

1.3 Baffle system

The OMEGA2000 was designed without a cold pupil or re-imaging optics. This means the camera has no cold-Lyot-stop, which would be able to prevent the detector from receiving the thermal radiation from the warm telescope structure and dome. While only the sky background is significant for J and H band imaging, the surrounding thermal noise causes problems in K band without re-imaging. As a solution, OMEGA2000 is equipped with a baffle system to minimize the amount of background radiation reaching the detector in the K band (Baumeister et al., 2002). The baffle system consists of one cold and two warm mirror baffles (Fig. 1.5). The cold baffle is located inside the dewar to reduce thermal background emitted by the surroundings of the telescope pupil. The position of the cold baffle is as far from the detector as possible but the distance between them is limited by the size of the dewar window, feasible dewar dimensions, and a maximum tolerated central obscuration. The warm baffles of the camera are annual sections of an oblate ellipsoid with the edges of the cold baffle as the foci. The first baffle (diameter 750 mm) is at a fixed position and does not vignette the field of view. The second baffle has a smaller inner diameter and it is designed to vignette the entire field of view uniformly. It prevents the detector from seeing the warm surroundings, which improves the S/N ratio in the K band. For J and H band observations, the baffle can be moved closer to the dewar to a position where it does not vignette at all (Bailer et al., 2000).

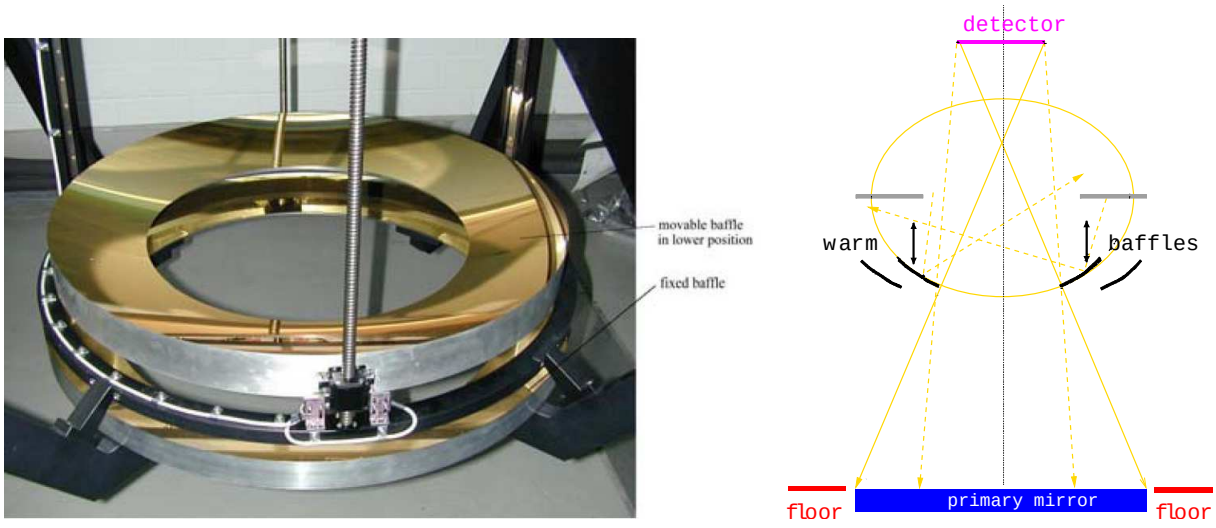

Figure 1.5: The warm baffles of OMEGA2000 (In Baumeister et al., 2002) and the working principle of the movable warm baffle (In Röser, 2004).

1.4 Filter Mechanism

The OMEGA2000 contains 17 filters of 3 inch diameter for wavelengths between 0.8 and 2.4 μm and one closed blank, which are distributed over three filter wheels. The filter unit containing the wheels, the cryogenic stepper motors and the locking/cooling mechanisms is placed between the detector and the focal reducer. Each wheel, mounted on a cryogenic ball bearing, contains seven equally spaced locking positions (six for filters and one free opening) and each filter position has a 3-bit magnet arrangement for determining the selected filter by three Hall sensors. The filters can be repositioned with an accuracy of less than 22 arcsec. With the pixel size of the HAWAII-2 detector of 18μm, this angle corresponds to 0.78 pixels at the outer edge of a filter.

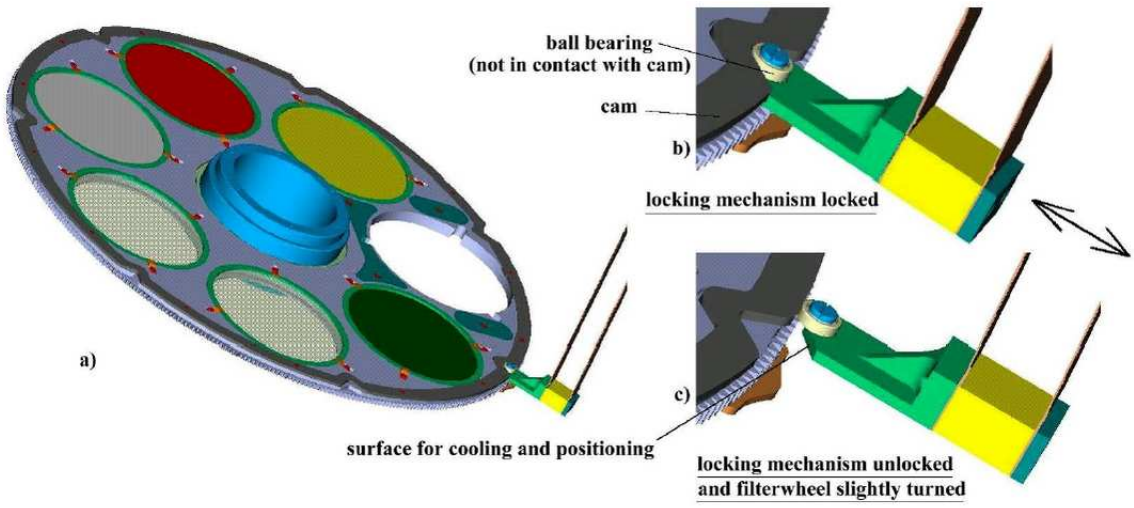

Figure 1.6: The filter wheel with its spring mechanism for positioning and cooling (a), mechanism locked (b) and unlocked (c) (In Baumeister et al. 2002).

1.5 Detector Mount

The detector fanout board holds a Zero Insertion Force (ZIF) socket mount for the HAWAII-2 detector, which allows us to connect the HAWAII-2 chip without any friction on the pins. Before the chip is inserted, a lever on the side of the ZIF socket is moved, pushing all the sprung contacts apart so that the chip can be inserted with very little force. The lever is then moved back, allowing the contacts to close and grip the pins of the FPA. The central pins of the chip carrier and the socket are used for thermal contact, whereas the outer two rows on each side are electrical contacts. The detector unit consists of a rigid aluminum base plate or "cold plate" which carries the fanout board on 12 identical cylindrical supports (Fig. 1.7). A spring-loaded cooling mechanism is used to cool the detector. A copper bar, which is preloaded by springs, presses an indium foil against the central detector pins.

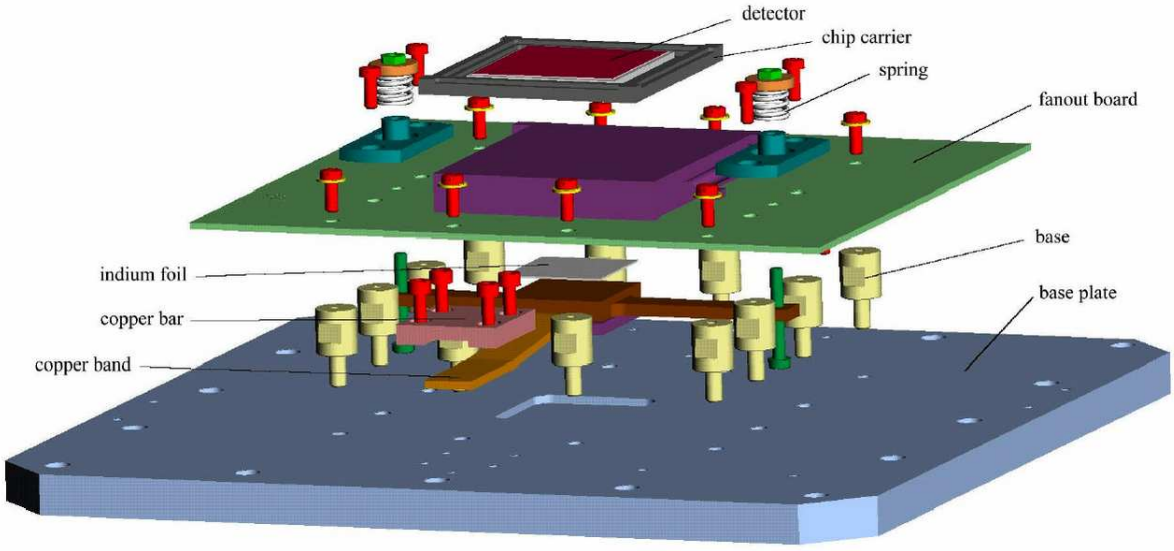

Figure 1.7: The detector unit with the base plate, fanout board, detector and its cooling mechanism (In Baumeister et al., 2002).

1.6 The Readout Electronics and Control Software

The general readout electronics at MPIA were designed not for only OMEGA2000 but a number of different instruments, including MIDI and LUCIFER. Although the electronics contain universal functional units, they were configured to fit the particular requirements. The data acquisition system of the OMEGA2000 consists of several hardware layers through which the data transfer is controlled: the hardware components located in the dewar, the detector front-end electronics, the data acquisition and control electronics, and a computer data interface connected to the network via I/O ports (Fig. 1.8). The video outputs of the HAWAII-2 FPA from the fanout board (first layer) go to the front-end electronics consisting of two preamplifier boards and clock drivers via 32 channels and the amplified signals organized in four cables are sent to the readout electronics containing eight boards of AD converters, which receive the video signals. The output range of the amplified video signal is 3.5 - 4.5 V. After the amplification, subtraction and an

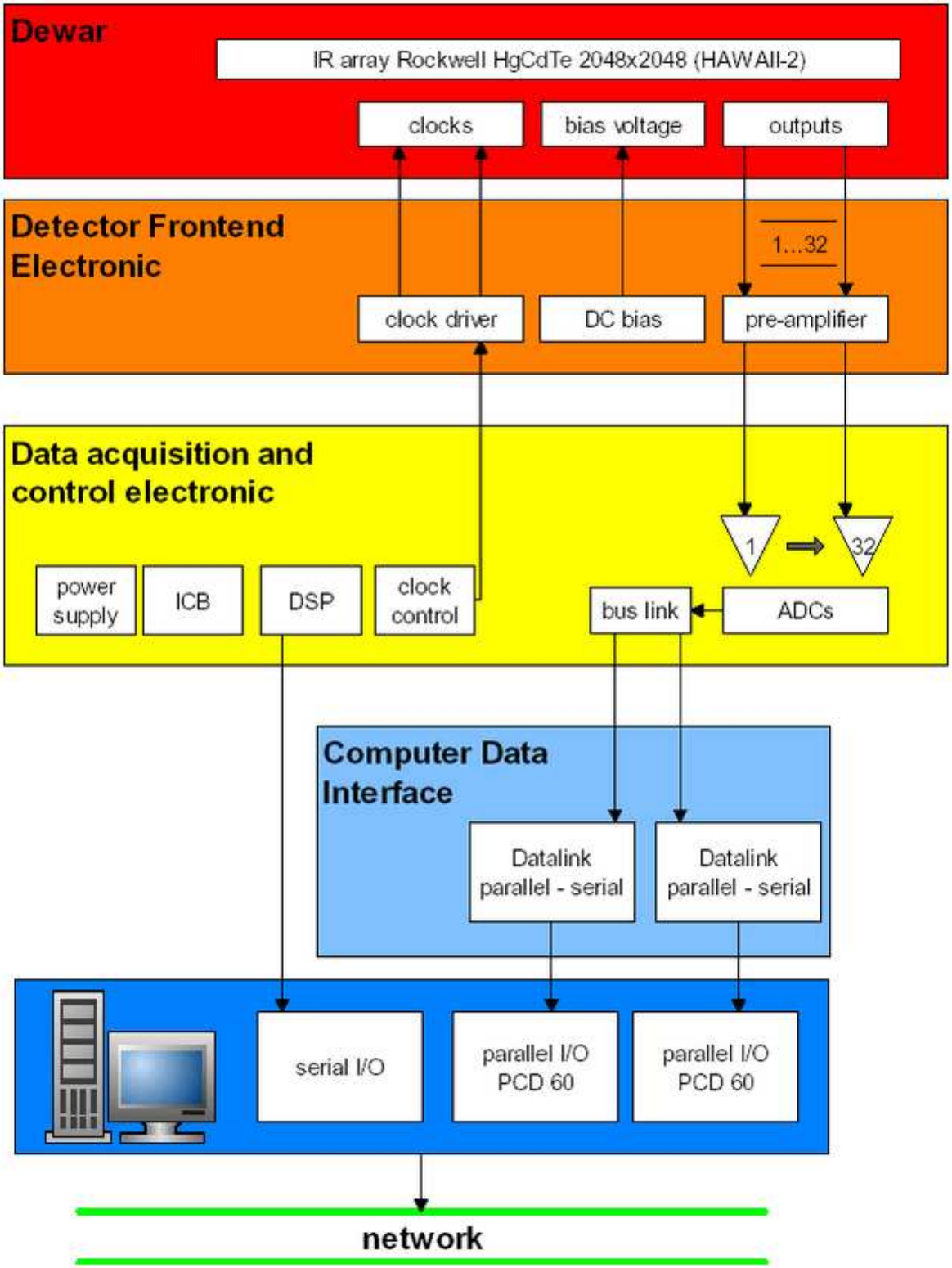

Figure 1.8: The block diagram of the read-out electronics of OMEGA2000 (In Röser, 2004).

AD conversion the range of the video output is ±32767, which is mapped into the range 0-65535 ADU. Thus, one count represents about 76 μV (Fig. 1.9).

A Digital Signal Processor (DSP) clocks the readout process of the chip and the timing of the data transfer through control channels and triggers the AD conversions. These tasks are implemented as control patterns in the instruction tables and macros handled by the DSP. The patterns are sequences of control signals of the chip and the instruction tables consist of linear sequences and loops of instructions which determine the timing and repetition of these patterns. The macros for the pattern generator contain instructions for more general purposes such as running instruction tables in the DSP memory or controlling the DSP itself. The digitized video outputs from two BUSLINK cards, via FDDI cables, arrive at a signal converter which transforms them to a proper data format for a Sun workstation. The DSP is controlled by a microprocessor

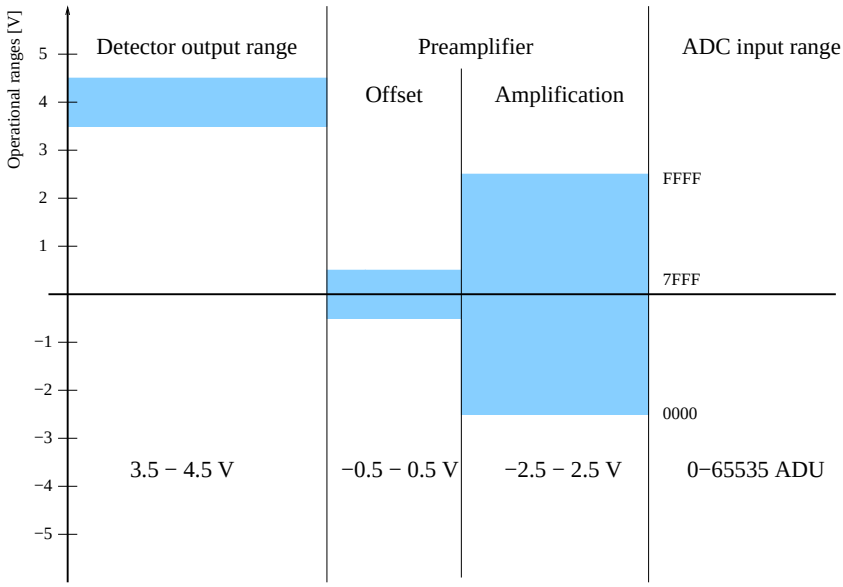

Figure 1.9: The conversion range between the analog output of HAWAII-2 detector, 3.5-4.5 V, and digitized data, 0-65535 ADU.

which communicates with the IR control software running on the workstation.

The data acquisition and control software used for OMEGA2000 is the Generic Infra-Red camera Software (GEIRS) developed for the general readout electronics. The software is able to sustain a high data transfer rate continuously, have data visualization control, and save the data in time to hard disks. These tasks have been implemented by efficient organization of shared data buffers and parallel processing with optimal usage of the multiprocessor capabilities. Besides the command line prompt, the control software has a graphical user interface with control panels and a display for the video output. The parameters of the readout process can be set and modified in the control panels (Fig. 1.10). Each readout mode is implemented in corresponding instruction tables, which the control software can load and send to the DSP. The parameter files of GEIRS contain these instruction tables, different clock and control patterns for the 1 and 8 output modes, and macros calling the instruction tables in different output, readout and idle/non-idle modes. The control software stores the parameters in variables, such as the integration time, the repetition number of readout, the actual readout and output mode or the filter and baffle

positions. During the initialization process of the clock and control patterns, the instruction tables and the macros required for the actual output and readout modes are sent to the DSP by the software.

If a parameter is changed via the control panel, the software reinitializes the electronics and sends the new instruction tables and macros to the readout electronics before starting any readout process. The readout frames are stored in a memory buffer and saved interactively or by GEIRS commands. The commands of the control software can be organized batches, i.e., in predefined series of readout commands with given integration times, repetition counter and other commands to synchronize the different steps or move the telescope. We used the environment of GEIRS to test and characterize different HAWAII-2 detectors but the observations were carried out with MIDAS utilities controlling the camera software.

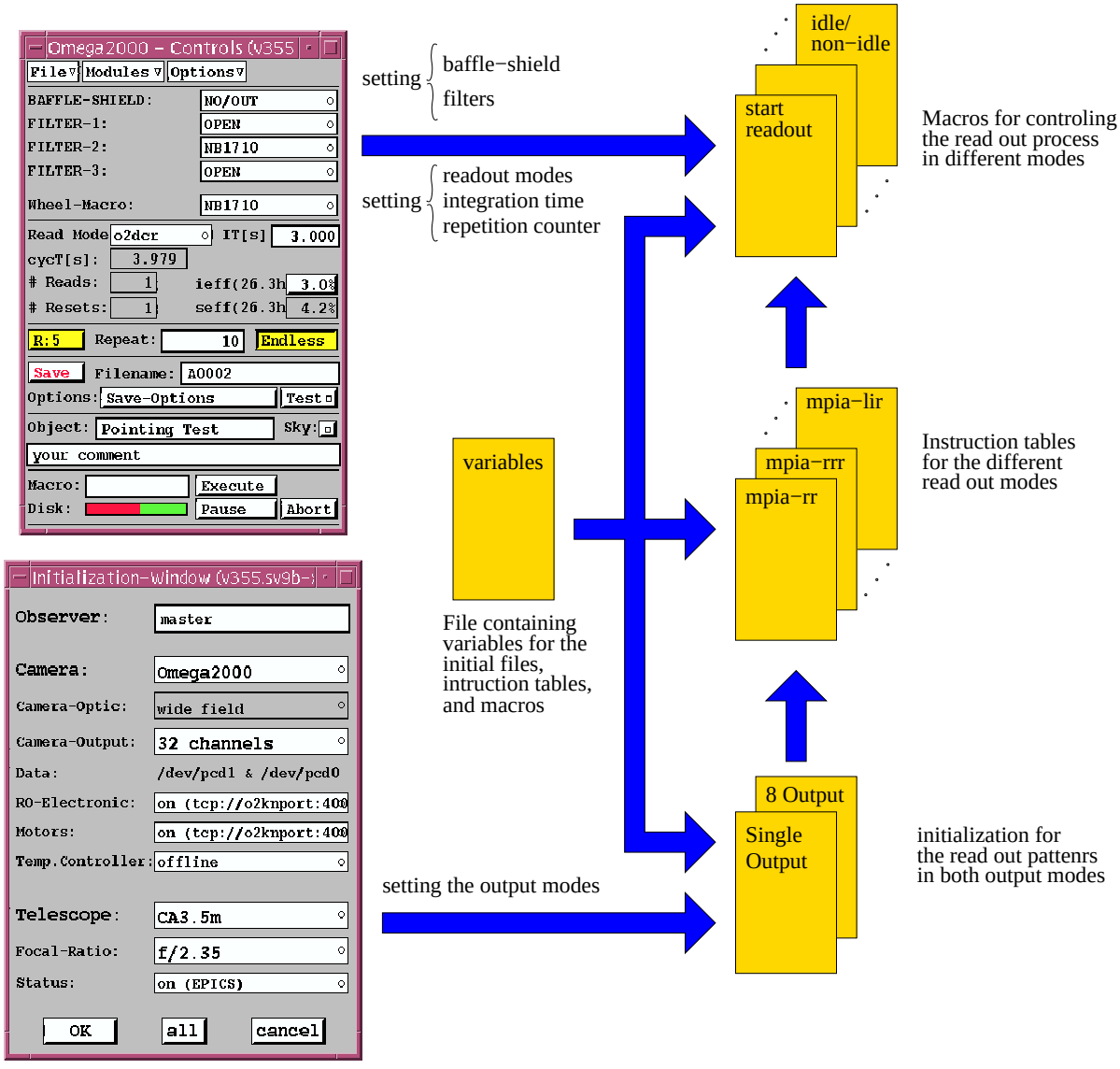

Figure 1.10: The scheme of the control interface of GEIRS. The two main control panels of GEIRS are shown in the left hand side. The files containing the macros, instruction tables, files for initialization, and variables for the readout electronics are represented with yellow boxes. whereas the blue arrows indicate their dependencies on each other.

Chapter 2

The HAWAII-2 Focal Plane Array

In the history of the developement of InfraRed (IR) image sensors several architectures of different properties and performances were born with various advantages and drawbacks. In this chapter we introduce the basic concepts of wide-spread IR detector families, considering their layouts and operations. This helps us to present the HAWAII-2 Focal Plane Array (FPA) applied for the OMEGA2000 instrument and understand the principles of its operation. The first section of this chapter starts with comparison of the Charged-Couple Device (CCD) and Complementary Metal Oxide Semiconductor (CMOS) architectures developed for the IR imagers and goes on to describe the layout and readout architecture of the HAWAII-2 sensor in details. In the second section, all the readout modes of the detector are presented which the team of the OMEGA2000 project implemented for engineering or scientific purposes. The optimization of the different readout modes will be discussed in the subsequent chapter, as an issue which determines the detector performance.

2.1 Design and Operation of the HAWAII-2 FPA

CCD sensors had been fairly widespread in IR imaging until the mid eighties when CMOS detectors started to supersede the traditional technology. It was due to the fact that CMOS technology allows simplification of the sensor interface and increase of on-chip integration while enhancing the performance of infrared detectors to a great extent. As a result of this development, a continuously broadening family of the HAWAII Focal Plane Arrays (FPA) has been brought to the market recently by Rockwell Science Center. The HAWAII-2 FPA, the latest member of this family, is the largest high-performance detector available for infrared astronomy at the moment (Fig. 2.1). With an array size of 36×36 mm^2 and 2048×2048 pixel format, it provides unrivaled spatial resolution and sensitivity and is a good candidate to satisfy the requirements of the next generation scientific projects.

Here, we present the setup and operation of the HAWAII-2 detector in three sections. In order to give an overview on the motivations which lead to the design of the HAWAII-2 FPA, we start with a short comparison of the CMOS technology that makes the HAWAII-2 image sensor so outstanding in its category within the traditional CCD paradigm. In the second section there is a brief summary on the design issues of the HAWAII-2 layout. In the last section we describe internal architecture of the chip circuits and their operation.

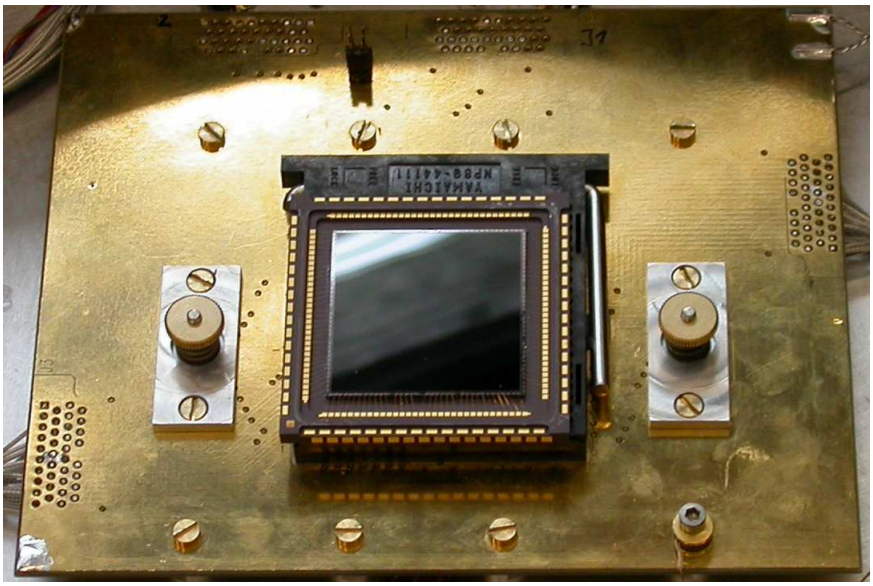

Figure 2.1: HAWAII-2 FPA mounted on its fanout board (Photo: Peter Bizenberger).

2.1.1 Infrared detectors

In a general setup of IR detectors a photosensitive semiconductor layer is grown on a transparent substrate. Incident photons are absorbed in this semiconductor material and generate charge carriers, which are collected in the well capacities of each pixel during the integration time. In the readout process the accumulated charge is transferred to the pixel row and column shift registers, where a sense node capacitance converts it to photo-voltage. The CCD chips, the traditional solution in the IR imaging, operate according to the above described passive pixel sensor (PPS) scheme. They absorb photons and store charge in the same bulk material with a simple pixel layout and use an external amplifier circuit for data acquisition.

However, this architecture has some drawbacks. The amplification of the video output by off-chip circuits causes the readout noise of the large format CCD chips to be dominated by the wide band thermal noise of the output amplifier and the excess noise of the video electronics. Both noise sources can be minimized by maximizing the conversion gain, i.e., minimizing the sense node capacitance but this approach has its limits. If the photo-voltage is read before and after the integration and only the difference of these values is sampled as a video signal, some the reset noise and the $1/f$ noise can be mitigated but the thermal noise remains the same. Another problem is the leaking of the collected charges from a pixel to the adjacent ones in case of saturation, which smears the photo-signal over the area of that pixel group. Normally the saturation of the whole chip is avoided during the operation of CCDs but pixel arrays alway contain hot pixels which can be saturated even if the exposure time is short enough to prevent the saturation of the normal pixels. It is hard for CCDs to avoid the smear-off effect caused by hot pixels. Besides these problems, the readout process of CCDs is destructive, i.e., the collector capacitance in pixels has to be recharged to measure the voltage of the pixels, which might affect the charge collection.

While CCD imagers use only passive pixel sensors (PPS), CMOS detectors can have either

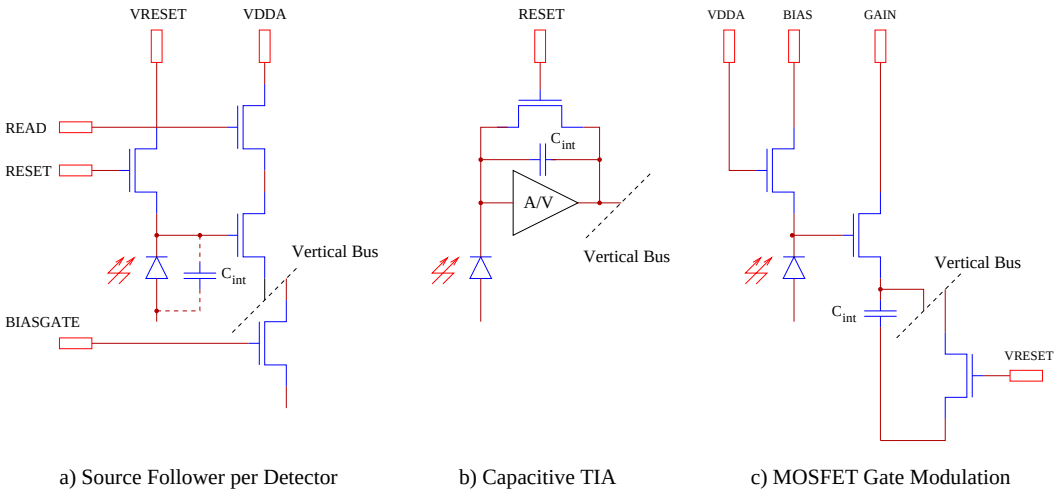

Figure 2.2: Low noise APS Circuits for hybrid and monolithic FPAs. SF detectors (a), CTI Amplifiers (b) and the solution of MOSFET Gate Modulation (c) (In Hodapp, 2000).

active or passive pixel based architectures. Active pixel sensors (APS) with a higher on-chip integration can amplify photo-voltage at each pixel before reading out. They therefore provide a more efficient readout noise reduction. Depending on the degree of on-chip integration there are three different types of APS (Fig. 2.2). The simplest is the source follower detector (SFD) using three transistors. Two of them are for accessing and reseting the pixel and the third provides amplification. Capacitive TransImpendance Amplifiers (CTIA) have a fourth transistor besides the SF amplifier to amplify voltage further and have a negative feedback to suppress the kTC noise generated by setting the detector. The resetting of the integration capacitance also produce kTC noise but a fifth transistor can reduce it by modulating the gain of the video signal. Hence the APS consisting of five transistors achieves the lowest output read noise, about 1 e^-, depending on the combination of detector, feedback and integration capacitance. Nevertheless, if the total capacitance consisting of the detector capacitance and input capacitance of a three-transistor APS is in the order of 10 fF the read noise produced in a double correlated read is only in the order of 10 e^-. It is therefore the most advantageous to implement a three-transistor SFD by the virtue of its relatively simple pixel layout and good performance (Hodapp et al., 1995).

The APS design allows for the usage of the reverse bias mode, where the capacitance of each pixel is completely charged by applying a constant reset voltage in the whole array. Incoming photons discharge the capacitances of pixels, reducing the voltage measured on them. The photo signal is inverse proportional to the remnant charges or voltages. Saturated pixels are completely discharged without causing any leakage in the adjacent pixels, which is a further advantage of the CMOS technology, compared to CCDs. Another advantage of using the APS scheme, is the non-destructive readout, i.e, the preservation of charges in the pixel capacitances, in which the voltage on pixels can be measured without affecting the charge collection. However, the simple pixel architecture is very important because it allows for minimazation of the gap between the optically sensitive regions of the pixels, called photo-sites. This increases the optical collection efficiency, characterized by the fill factor, to as high an extent as possible. The passive pixel based imagers have pixels consisting of only one photo-diode and a MOSFET switch, which allows for

a high fill factor. The pixels of APSs contains many components, making the gaps between them large. This bulkiness reduces the fill factor considerably, even in the case of the more compact three-transistor SFD. However, this problem can be solved by application of a hybrid layer structure for signal detection and readout functions, which separates them instead of using a single bulk material. The gap between the unit cells is thereby reduced, which results in a higher fill factor of the sensor. The HAWAII FPA family belongs to the first generation products of hybrid technology for IR imagers and the next sections will describe its latest member, the HAWAII-2 FPA, in details.

2.1.2 Layout of the HAWAII-2 FPA

Besides the capability to optimize the optical fill factor efficiently, there are other advantages of the hybrid structure. The photosensitive layer can be grown separately from the multiplexer layout itself, which allows fine tuning of the composition and thickness of the stratum. The properties of the detector material are optimized so that it could meet various requirements of the operation (Hodapp, 2000).

A CdTe layer is grown on a lattice-matched sapphire substrate by metal organic chemical vapor deposition and the result, due to Hg vacancies, is a p-type semiconductor material (Fig. 2.3). The band gap of HgCd can be adjusted by controlling the molar fraction of the Hg and Cd and the uniformity and thickness by controlling the melt temperature during the evaporation. This fine tuning also allows reduction of the number of defects in the photosensitive layer whose presence decreases the performance of the detector. The band gap determines the cut-off frequency of the detector and the spectral response of the HAWAII-2 is 0.85-2.6 μm (the sapphire substrate is transparent for visible and infrared radiation to beyond 5.5 μm). The photosensitive layer must be thick enough to absorb as much IR radiation as possible, i.e., few times greater than the absorption length of IR photons. Nevertheless, its thickness should be no more than the diffusion length of minority charge carries generated by absorbed photons in order to avoid diffusing of the minority carriers into neighboring pixels, which causes image blurring, or their recombination before they can be collected, reducing the quantum efficiency. HAWAII-2 has a

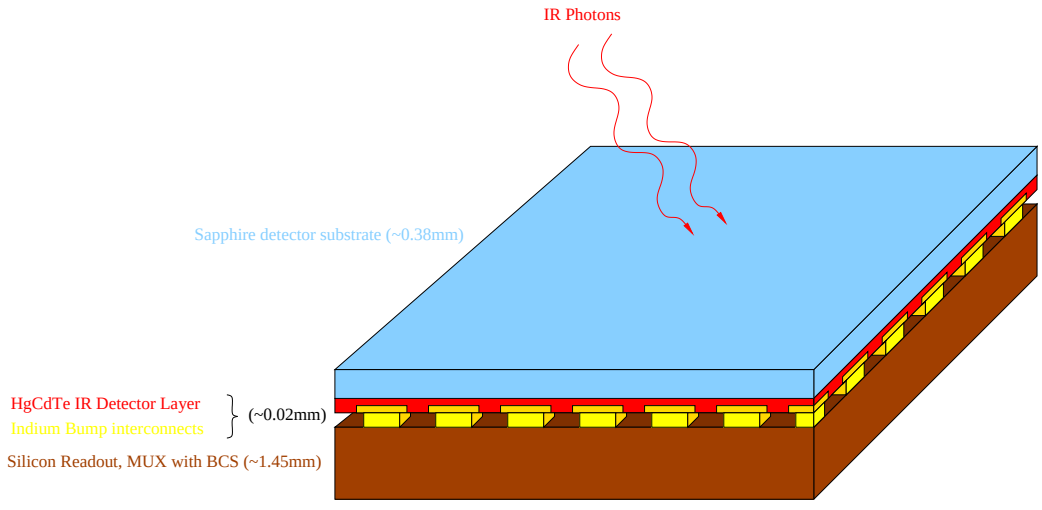

Figure 2.3: The cross-sectional view of HAWAII-2 (in Kozlowski et al., 1998).

~ 10 μm thick photosensitive layer, which meets these requirements.

An important issue is the thermal and mechanical interface between the detector array and the silicon multiplexer. As the chip is cooled down to its operation temperature (77K), high mechanical pressure allowing tight thermal contact between its two main parts can cause high mechanical stress between them owing to their different thermal expansion coefficients. Weak mechanical forces applied to clamp the two parts reduce thermal coupling, which makes the detector temperature difficult to control. The choice of sapphire as a substrate makes this problem less severe, since its thermal expansion coefficient matches that of the silicon MUX. reasonably well. The application of indium columns as inter-connectors and backfilling the hybrid with epoxy futher mitigates the problem. Additionally, the HAWAII-2 array is mounted on a pin-grid chip carrier. While its outer pins provide electric connection, all its inner pins are used to connect the chip carrier thermally. The hybrid sandwich structure also allows an optimal design of the multiplexer of HAWAII-2, which is an array of MOSFET switches with SF amplifiers separated by other MOSFET switches. This kind of architecture has a minimal glow during its operation because the voltage can be lowered below 5 V. The multiplexer contains SF amplifiers for all unit cells of the detector layer (Fig. 2.5).

The pixel array is organized in a CMOS read architecture, which consists of four electrically independent quadrants (1k×1k pixels) with either 1 or 8 outputs per quadrant (Fig. 2.4). Each quadrant contains a horizontal and a vertical shift register for addressing the pixels in the array. During the detector readout, the horizontal register is clocked in the fast direction and the vertical register in the slow direction. All of the four quadrants are operated in parallel (Haas, 2002).

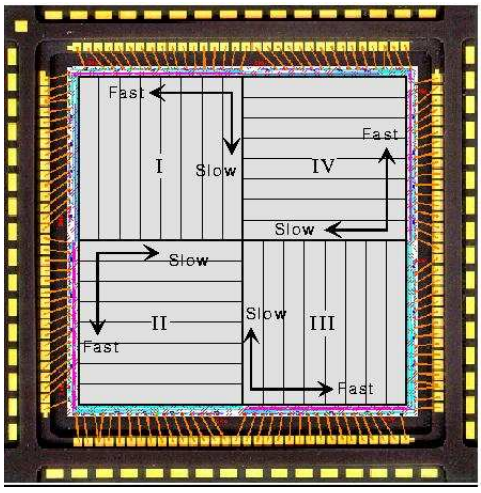

Figure 2.4: The quadrant and channel layout of HAWAII-2 (In Haas, 2002).

2.1.3 Internal Architecture and Operation of the HAWAII-2 FPA

The internal architecture of the HAWAII-2 FPA shown in Fig. 2.5 consists of three main parts: the unit cell, the shift registers, and the output SF amplifier. These functional units are controlled with thirteen logic signals and they also have two power supplies and three DC biases.

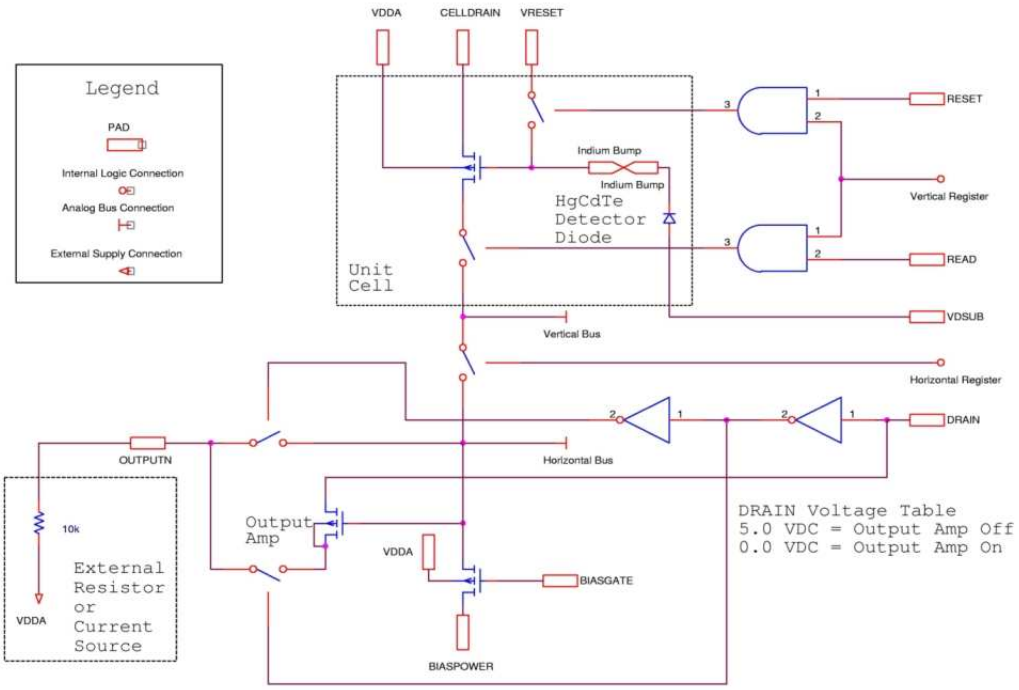

Figure 2.5: HAWAII-2 internal architecture (In Haas, 2002).

The unit cell consists of the HdCdTe detector diode, the drain transistor and MOSFET switches for reset and read and its basic control inputs are the digital signals READ and RESET and the bias voltage CELLDRAIN. The multiplexer is connected to the unit cell via the horizontal and vertical shift registers. The horizontal register has four basic clocks (CLK1/2 and CLKB1/2) and the control signal LSYNC for line synchronization. Two of the basic clocks (CLK1 and CLKB1) provide the same clock signals and the other two (CLK2 and CLKB2) are the complement of them. The readout of a pixel takes one full clock cycle, i.e., two clock edges per pixel. The register is reset by lowering LYSNC. When LSYNC goes high, the register is released and a single bit starts shifting down in the register. The vertical register is controlled by two external clocks, FSYNC and VCLK (frame synchronization and vertical clock). FSYNC has an active low state and it is pulsed once every frame. This pulse is propagated down in the vertical register by ticking of VCLK, i.e., a single positive pulse on VCLK addresses on row of the multiplexer for readout or reset. The control signals RESET and READ are for the line reset and read function of the multiplexer. RESET is an active high clock resetting all of the pixels in the selected row to the voltage set by VRESET. If READ is high then video signals from the current row are transferred to the vertical buses, which are inputs to the horizontal register. In turn, the horizontal register controlled by transmission gates produces input signals to the output SF amplifier.

There are two biases that can be adjusted for the SF amplifier, BIASGATE and VRESET. BIASGATE is the voltage gate of the "pull-up" P-FET for the SF amplifier and BIASPWR is the source voltage of the P-FET. The speed and the dynamical range of the unit cell SF can be adjusted by changing BIASGATE. VRESET is the reset voltage applied to the full array during the reset operation. Although external circuits can also be used instead of the output

Signal Name	Minimum	Nominal	Maximum	Comment
VDD	TBD	5.0	5.5	Digital Power Supply, must be $\leq$ VDDA
VSS	0.0	0.0	0.0	
MUXSUB	0.0	0.0	0.0	
VDDA	TBD	5.0	5.5	Analog and input protection network power supply, must be $\geq$ all other voltages
DSUB		0.0		
DRAIN	0.0	0.0,5.0	5.5	Output amplifier selection and amplifier drain voltage (5.0=Off chip amplifiers)
CELLDRAIN	0.0	0.0	5.5	
Bias Voltages				
BIASPOWER	TBD	5.0	5.5	
BIASGATE	0.0	3.5	5.5	Current control for unit cell
VRESET	0.0	0.5 to 1.0	5.5	PACE bias voltage range

Table 2.1: Nominal Bias Voltages for the HAWAII-2 (In Haas, 2002).

SF amplifier by raising the DRAIN signal, the latter is applied for OMEGA2000 configuration because of its more advantageous noise properties. When the internal SF amplifier operates, all the outputs are pulled up by using an external resistor so as to provide a proper bias for the amplifier.

The self-emission from these amplifiers can be minimized by turning them off during integration via the READ signal, which means the gate of the unit cell access P-FET is pulled "high" when not in use. This occurs when the READ input clock is "low", hence disconnecting all of the column buses from the gate of the SF amplifier. The gate will be pulled up via the BIASPWR bias input.

2.2 The Readout modes of HAWAII-2 FPA

There are three output modes available for the chip, which can be controlled via the readout patterns. In the *Single Output Mode* all data is routed to only one channel per quadrant. If the chip is set to *Eight Output, Unshuffle Mode* the data is spread across all the output channels of the detector, namely eight per quadrant. Each output provides data from 128 consecutive columns. The *Eight Output, Shuffled Mode* is similar to the previous one, except the data from each block of 128 columns is cyclically shifted to the next output bus. In normal operation of OMEGA2000 the *Eight Output, Unshuffled mode* is preferred because of its high speed. These output modes are controlled by the digital inputs O1 and O2, which can be set at the initialization of the whole readout process (Tab. 2.2). The background limit will be reached in broad-band imaging with HAWAII-2 array on OMEGA2000 in a few seconds. Series of images are therefore required to achieve sufficient S/N, so it is very important that the array can be read out with minimal dead time. The minimal integration time is given by the duration time of readout for a complete frame, which is on the order of one second for all readout modes. There are several readout

Output Mode	**O1**	**O2**
Single Output Mode	1	0
Eight Output, Unshuffled Mode	0	0
Eight Output, Shuffled Mode	0	1

Table 2.2: Output Mode Control Signals for HAWAII-2 (In Haas, 2002).

modes feasible for OMEGA2000 but some of them are used only for engineering function. This section will describe all of these modes in details. First we give an overview on how the readout process of the HAWAII-2 FPA is organized. Then we present the readout modes of the FPA which were to be implemented for the operation of the OMEGA2000.

2.2.1 The General Readout Scheme of the Detector

The HAWAII-2 chip is built up in electrically independent quadrants and they are controlled in parallel. This means the sequence of the control signals sent the HAWAII-2 chip by the readout electronics contains a readout patten only for one quadrant and this sequence is distributed in multiplexer to each quadrant in parallel. Therefore, the basic scheme of a readout mode consists of a reset and readout of a full quadrant and not the whole array. The implementations of all the readout modes are based on this general scheme for each quadrant, as shown in the timing diagrams in Figs. 2.6 and 2.7. Here, the frame synchronize signal, called FSYNC, has a pulse (negative logic) before starting the readout of the frame, indicating its beginning. The line synchronize signal, called LSYNC, is set high (positive logic) at the beginning of each row, which shifts the vertical shift register (slow direction) and allows to scan through the lines in the vertical direction. The pixel clocks CLK1, CLKB1, CLK2, and CLKB2 are clocking the vertical shift register (fast direction), scanning the actual row addressed by the horizontal register. The algorithm implementing this basic timing can be written as:

$$
\begin{array}{llll}
1. & \textit{once} & & \textbf{FSYNC} \ \& \ \textbf{LSYNC} \ \& \ \textbf{RESET} \\
2. & 1024/128 & \textit{times} & \textbf{Pixel CLK} \ \& \ \textbf{SCON} \\
3. & 1022 & \textit{times} & \textbf{FSYNC} \ \& \ \textbf{LSYNC} \ \& \ \textit{jump to step } 2. \\
4. & 1024/128 & \textit{times} & \textbf{Pixel CLK} \ \& \ \textbf{SCON}
\end{array}
\tag{2.1}
$$

This sequence of control patterns contains a loop scanning through each row of the array (the second and the third line), in which the clocking and pixel readout are repeated 1024 or 128 times according to the *Eight* or *One Output Mode*. Here, SCON denotes the pixel readout, that is the input signal of the A/D converter for starting the conversion of the video signal.

The readout process of the HAWAII-2 chip is organized in *readout cycles*, which are defined as sequences of control patterns providing a complete image. Of course they have different timing patterns for different readout modes. In the non-correlated modes the readout cycle is a complete readout of the full array with or without resetting the array. Whereas for the modes applying double correlated sampling the readout cycle refers to two frames which are needed to produce a complete image: the readout of the reset level and the readout of the integrated signal. The readout cycles therefore consist of different control sequences, depending on the readout mode.

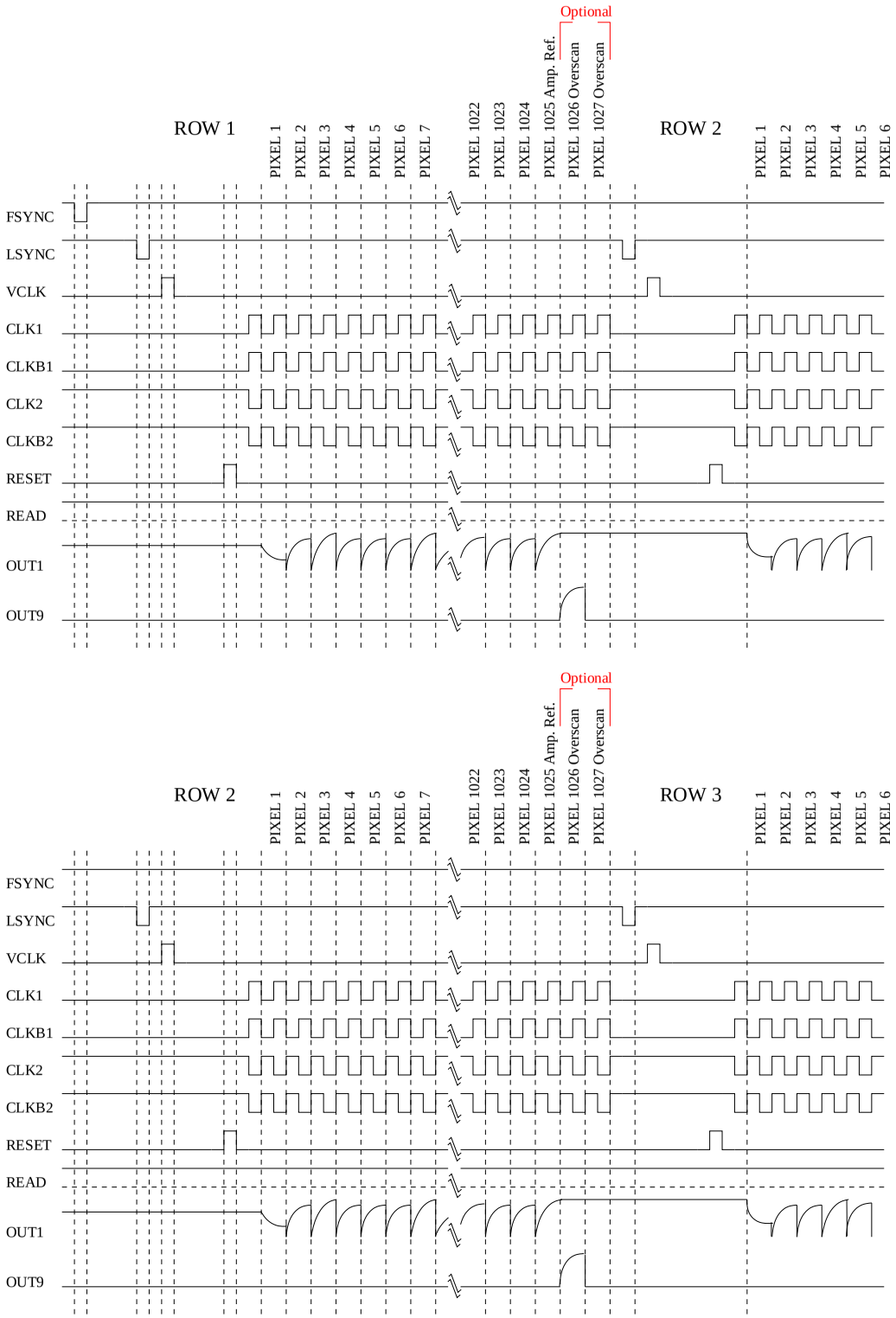

Figure 2.6: Timing diagrams for the readout of the first and second rows of HAWAII-2 FPA quadrant (In Haas, 2002).

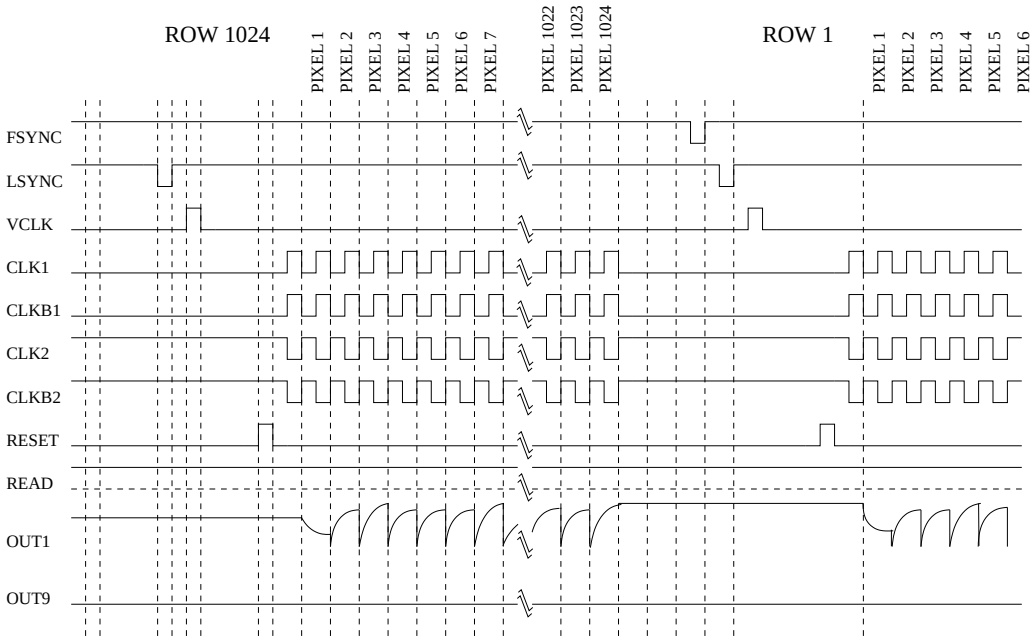

Figure 2.7: Timing diagram for the readout of the last and first rows of HAWAII-2 FPA quadrant (In Haas, 2002).

Each mode can be characterized with its efficiency, that is the ratio of integration time to the duration time of the readout cycle.

In order to increase the efficiency of the readout modes, we tried to maximize this ratio. There are three readout modes, the single pixel read, the reset level read and single correlated read, which are non correlated modes and used only for testing the operation of the chip. The double correlated read with two different implementation of the resetting, the line interlace read, and multiple end point read provide different solutions to operate the chip for scientific applications. We describe these read out modes in the following and compare them with each other in terms of their advantages and disadvantages.

2.2.2 Single Pixel Read (spr)

The read out cycle starts a full frame reset then only one pixel is read out in each channel or quadrant depending on whether the *Four* or *Eight Output Mode* is used. As a result, the data of a full channel or a quadrant consists of the value of only one arbitrarily chosen pixel. This mode is only for engineering purpose and used to test the stability of the readout process, comparing the data transfer of the same pixel value with that of the abruptly changing video signal due to the transient states in beginning the readout process of a whole quadrant.

2.2.3 Reset Level Read (rlr)

The readout of the reset level of a complete frame has the simplest readout scheme: we reset the full array then read it out. For HAWAII-2 FPA a line reset is implemented, which means that one reset pulse always resets each pixels in a line of the array and the chip needs 1024 pulses to reset the full array while clocking through the horizontal shift register. It allows the reset-readout

cycle to be accomplished in two ways. Either the whole array is reset and then read out or the reset-readout cycle is run line by line: one line is reset and then read out and the next line is reset and read out and so on up to the last line. The latter way means the whole array is reset and read quasi-simultaneously. In the first case the elapsed time between resetting and reading out of the same pixel is equal to the resetting time of the full array. The reset-readout scheme is faster in the second case, where each row is read out immediately after being reset (Fig. 2.8). The timing diagram of the integrated signal represents only the theoretical reset-readout scheme where the reset means a complete frame reset which is followed by the readout of the full array. As the video signal is sampled after resetting contains the reset noise and reset bias this readout mode has only engineering purpose for studying the the line reset scheme in a simple readout process of one frame.

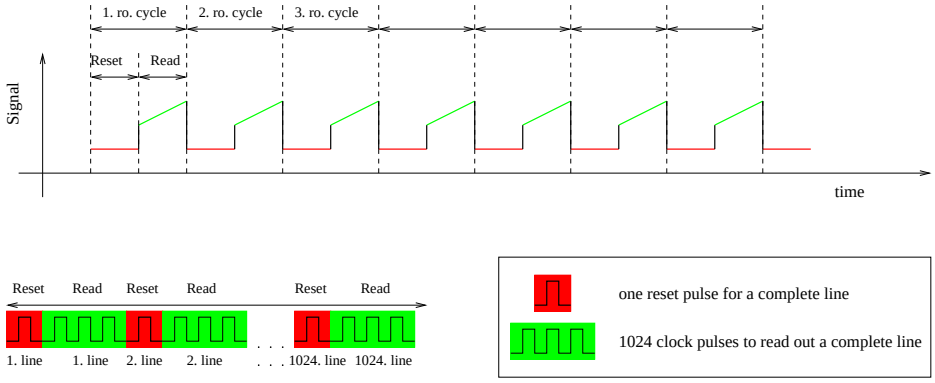

Figure 2.8: The timing diagrams of the signal (upper) and the control pattern (lower) for the reset level read (reset-read).

2.2.4 Non-correlated Sampling or Single Correlated Read (rr)

In the normal operation of the image sensor there is some exposure time between the frame reset and the readout of the full array so that more photo signal can be collected. The readout cycle of non-correlated sampling implements this reset-integration-read scheme (Fig. 2.9). Here, the reset is separated from the readout process by integration, which prevents the application of the fast reset method. Since the exposure lasts from the resetting of the first line of pixels until their readout, the resetting time of the full frame should be added to the integration time to obtain the total exposure time. The integrated frame contains not only the signal collected during exposure but also the reset bias and noise as in the previous mode, therefore this readout scheme is also applied only for engineering function.

2.2.5 Correlated Double Sampling or Double Correlated Read (o2dcr)

The Correlated Double Sampling (CDS) is introduced to eliminate reset bias which is present in any image taken in the previous readout mode. This scheme consists of a complete frame reset, a readout of the full array, an integration and a readout of the complete integrated frame. The reset and the first readout of the frame are not simultaneous, i.e., a slow reset is applied (Fig. 2.10). The output signal is obtained by the subtraction of the reset frame from the integrated

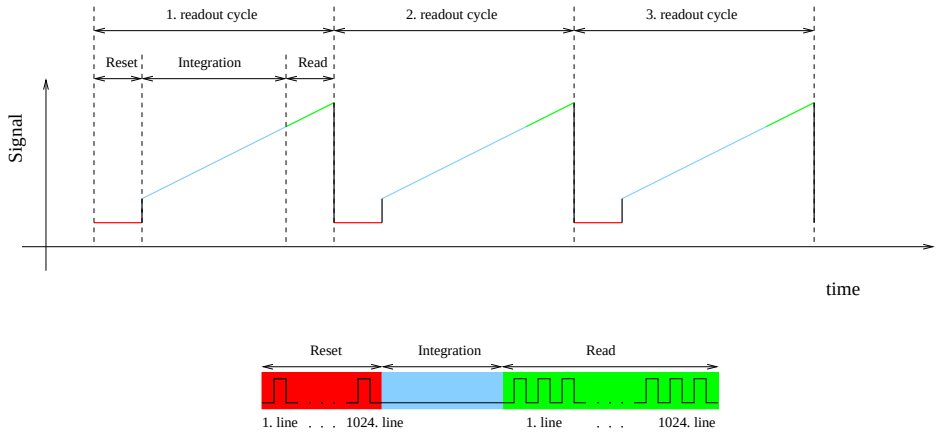

Figure 2.9: The timing diagrams of the signal and the control pattern for non-correlated sampling (reset-read).

one, which eliminates the reset bias from the signal value. Since the whole array must be clocked three times (one full frame reset and two readouts of the full frame) the efficiency of this readout scheme is only 33% at the minimum integration time.

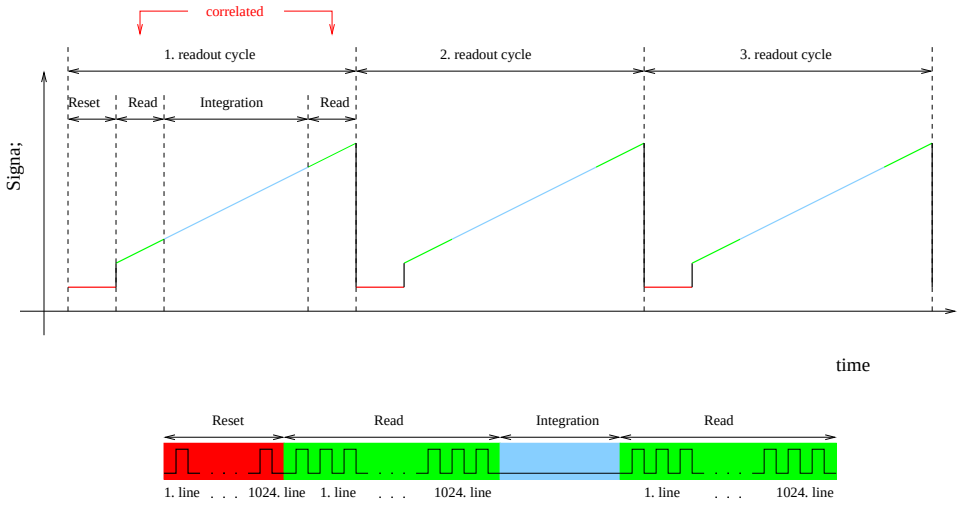

Figure 2.10: The timing diagrams of the signal and the control pattern for CDS (reset-read-read).

2.2.6 Correlated Double Sampling with Fast Reset (fcr)

The CDS can also be implemented with the fast reset scheme. This means that the reset and the readout of the reset level are carried out simultaneously and followed by the integration and the readout of the integrated video signal (Fig. 2.11). The result frame is provided by subtraction of the reset level from the integrated signal. Since the whole array is clocked only two times - once for the reset with the first readout and once for the second readout, the efficiency of this readout scheme is 50% for the minimal integration time. This readout mode was planned for scientific operation

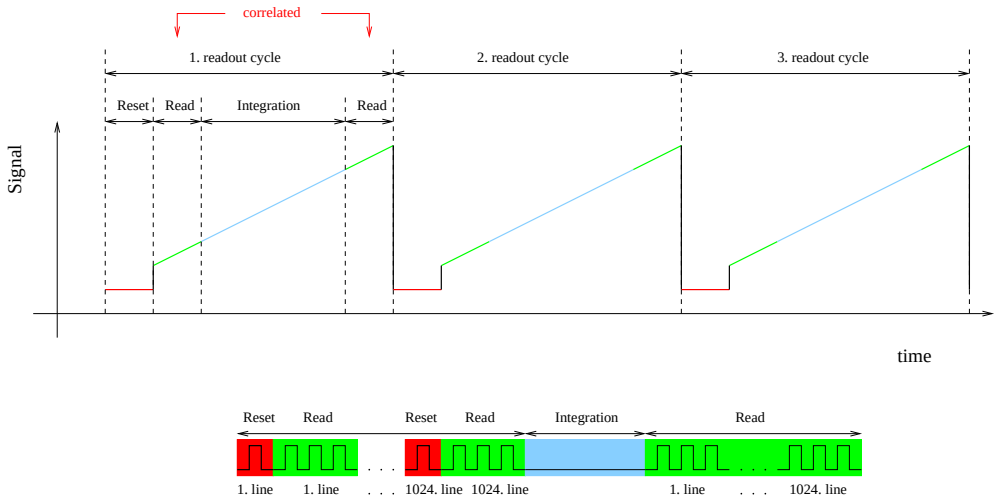

Figure 2.11: The timing diagrams of the signal and the control pattern for CDS with fast reset (reset-read-read).

2.2.7 Line-interlaced Read (lir)

The technique of the line interlaced read should guarantee the a more stable operation of image sensors because each line in the frame is read out twice before and after the integration. The readout cycle of this mode consists of two main parts: the clocking through the full array with a read-reset-read scheme and the integration (Fig. 2.12). The read-reset-read scheme means that each line in the complete frame is read out, reset and read out again, where the second readouts provide the reset level of the detector. The integration completes the first readout cycle then the second readout cycle starts with its read-reset-read scheme. The integrated photo signal is obtained by the first readouts of this scheme and the second readouts, after resetting, provide the reset levels for the next readout cycle. The result frame is produced by subtracting the reset level obtained in the first cycle from the integrated signal read out in the second one. The second cycle is also completed by integrating of the photo signal and a third readout cycle starts, which provides the integrated signal for the second cycle. Concerning the result frames, the reset level of the first frame comes from the first readout cycle and its integrated signal value form the second cycle. The reset level of the second frame comes from the second cycle and its integrated signal value from the third cycle, etc. As can be seen, the readouts of the lines in the adjacent readout cycles are interlaced in contrast to the previous modes, where each cycle carried out a complete readout of a frame line by line. After reading the whole array there is a pause if the integration time is above the minimal value and the cycle is repeated for as many images as required. Essentially no time is wasted, and for any integration time the efficiency of this mode is almost 100%. Since the line-interlaced mode also provides correlated double sampling, it is also used for scientific purpose.

2.2.8 Multiple End-point Read (mep)

This read out mode is similar to the double correlated read but here the readout cycle contains $2 \times n$ readouts instead of two. After the complete frame reset the full array is read out n times

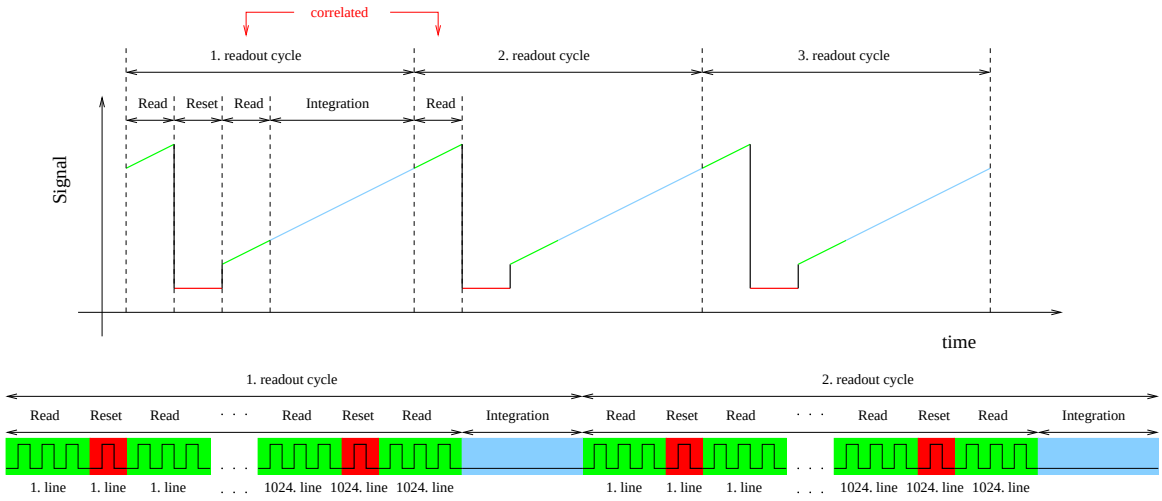

Figure 2.12: The timing diagrams of the signal and the control pattern for the line-interlaced read.

and the average of the n frames provides the bias values of the pixels after reset. After the integration the complete array is read out n times again and the average of these frames is taken as the integrated signal (Fig. 2.13). The video signal is the difference of the two averaged frames. Since the averaging of more frames helps to reduce the readout noise in the image, this read out mode provides a more accurate flux detection, which is advantageous for scientific purpose. This solution allows the chip to have a stable operation as well but the duration of one readout cycle is on order of seconds even if a fast reset is implemented, which may cause the minimal integration time to be too long.

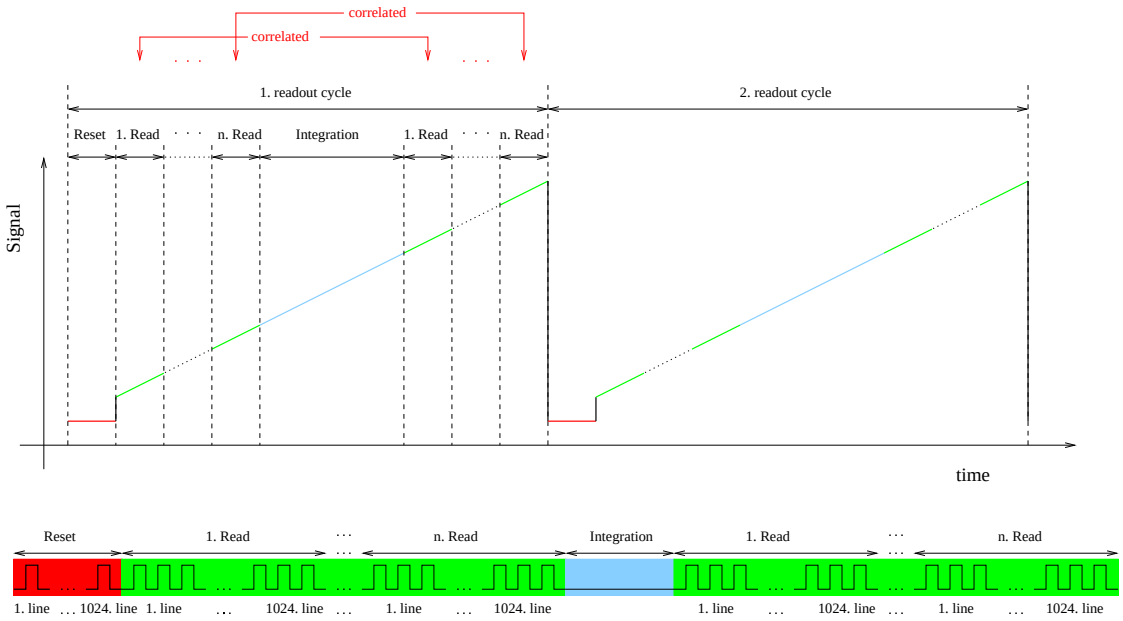

Figure 2.13: The timing diagrams of the signal and the control pattern for the multiple end-point read.

2.2.9 The choice of the readout modes for scientific operation

The aim of the technical part of this doctoral thesis was to implement and test the readout modes for HAWAII-2 FPA descried above. Since there were various readout modes available for scientific purposes, we tested them in order to choose the one of them allowing for the best performance of the detector. We used several criteria to measure the performance. The most important criterion we used to compare the different solutions with each other was the image quality produced in these readout modes. The multiple-end point read with the averaging of the measured pixel vaules provides a stable operation of the HAWAII-2 chip and the best image quality, comparing with the other readout modes in the same conditions.

Considering the efficiency of the readout modes, the line-interlaced read is the favorable with its almost 100 % efficiency comparing with the Correalted Double Sampling with normal reset and fast reset providing efficiencies of 33% and 50% for the minimal readout time. The multiple-end point read have also only an efficiency of 33% or 50%, depending on the realization of normal or fast reset. However, the readout time of the full array is a critical parameter as well and its length depends on the scheme of the readout mode. The minimal readout time is longer in the line-interlaced mode than that of the CDS with and without fast reset which may be enough to saturate the detector in K-band imaging. This problem is more pronounced for the multiple-end point read, where the readout time is even longer. Therefore the implementation of these readout modes involves an optimization of the readout process aiming for the reduction of the readout time of the full array as much as possible. The efficiency and the readout time together give the effective time needed to produce an image during observations. By increasing the efficiency and the reducing the readout time, we also reduce this effective time, which is important for an optimal usage of the telescope time.

Thus the performance of the HAWAII-2 image sensor operating in these readout modes is measured in terms of the three criteria, the image quality produced in a stable detector operation, the efficiency of the detector operation, and an optimal readout time of the FPA. A compromise between the best image quality, the maximal efficiency, and the shortest readout time results in the best choice of the readout modes. In the next chapter we present our solutions to the implementation of these readout modes together with their tests, where we consider the techniques which can facilitate the optimal performance of the detector with respect to the three criteria mentioned above.

Chapter 3

Optimizing of the Operation of HAWAII-2 FPA

In this chapter we present results related to the optimization of the camera operation for the OMEGA2000 instrument. The aim of this optimization was to achieve the best possible performance of the HAWAII-2 FPA installed in the camera. The OMEGA2000 NIR wide field imager was designed for a background-limited operation, which determined the possibilities for the implementation of its optimal readout process. A very slow operational mode of the imager could not be a goal, even if it would assure a stable operation with favorable noise-properties, since a readout of full HAWAII-2 array taking too long might saturate the detector with the incident signal, especially in the K-band imaging. Therefore, the main task was to achieve as fast and stable operation of the HAWAII-2 detector as possible while keeping its readout noise below the photon shot noise of the background and producing the best possible image quality. This task constituted the technichal part of this dissertation and we will discuss it in this chapter. In the fist section of the chapter we concentrate on the optimal design of the readout process and investigate how the maximal attainable frame rate for the HAWAII-2 FPA can be realized. In the second section, we present the techniques applied for optimization of the camera operation and consider the problems related to the image quality produced at high data rate and then describe the solutions to these problems. As a result of these optimizing techniques, the OMEGA2000 camera could operate at an appropriate frame rate, i.e., the $K-$band imaging was feasible, and the image quality was also satisfactory for scientific purposes. MPIA had the opportunity to test the operation of OMEGA2000 camera with three different HAWAII-2 focal plane arrays with the serial numbers #37, #48 and #77. Here, we describe the probelms occurred in the operation of these specimen installed in the OMEGA2000 camera and discuss their solutions. The tests of the camera performance with the various image sensors after optimization of readout process will be presented in the next chapter.

3.1 Optimizing of the Detector Readout

In the previous chapter presenting the HAWAII-2 FPA, we saw that the operation of the chip is based on several factors. Its different output modes or the different implementations of the readout process provide some free parameters for the optimization of the camera operation. In an

optimal design of the control of HAWAII-2 FPA, all the free parameters in readout process of the array had to be fine-tuned so that the best performance of the image sensor could be achieved. These free parameters are incorporated in different possibilities to implement the operation of the chip, such as the choice of the output mode, application of different mode of the idle cycles of the image sensor, adjustment some of the *analog signals* operating the chip and implementing of an optimal timing of the readout process, i.e., design an optimal pattern for its *digital control signals*. In the followings these possibilities will be discussed. We start with the considerations related to the choice of the output mode of the data transfer from the HAWAII-2 chip. Then we present the solution of the handling of idle cycles in the readout process of the FPA. It is followed by a brief summary on the on fine-tuning of the analog controls signals of the chip and we finish this section with the discussion how we found the optimal design of the clocking of the digital control signals of the HAWAII-2 FPA.

3.1.1 The Choice of the Output Mode

The first step for the optimal design of the readout process was and the choice of the output mode. As described in the previous chapter, the HAWAII-2 chip has three output modes, the Single Output Mode, the Eight Output, Unshuffle Mode and the Eight Output, Shuffled Mode. Since in the Single Output Mode only one channel is used for the data transfer, the array operates at a lower data rate than in the other two modes. In the specifications obtained from the Rockwell Company the maximal data rate (or frame rate) of the HAWAII-2 FPA is 100 kHz (or 0.25 Hz) for the Eight Output Modes. This gives a readout time of 4 s for a full frame with CDS and it is even more in the Single Output Mode. The Shuffled Mode with eight outputs was provided for the detector so that accidental stripe patterns in the images due to systematic effects could be eliminated. However, the shuffling increases the data transfer time and we expected the systematics effects will be suppressed by the dominating background noise.

Therefore we implemented only the Single Output Mode and the Eight Output, Unshuffled Mode for the purpose of the detector test. We created two sequences of instructions initializing the readout process of the detector for both the modes. The digital inputs O1 and O2 of the HAWAII-2 FPA for controlling its output modes are set to the proper values (see Tab. 2.2) in these sequences sent to the HAWAII-2 chip by the readout electronics.

Although we preferred the Eight Output Modes to the Single Output Mode for scientific operation of the HAWAII-2 FPA by virtue of its speed, some artifacts due to the higher data transfer rate appeared in the frames and these unwanted effect could only be reduced by applying the Single Output Mode. This was the case during the scientific operation of HAWAII-2 FPA #77, where a gradient appeared in its each quadrant in the Eight Output Mode. This will also be discussed in the last section of this chapter.

3.1.2 Application of different modes for the idle cycles

We saw in the previous chapter that the readout process of the HAWAII-2 chip is organized in units, so called readout cycles. Each readout cycle provides a complete image information, i.e., one or two frames depending on the readout mode. However, the control patterns of these cycles can implemented without reading the pixel values as well, where the full array can be clocked

through without sampling the video signal. The difference between the implementations of the control patterns is the presence or the absence of the start of conversion signals (SCON) sent to the A/D converters. The other control signals are all the same in the both cases so they operate the chip in the same way. The readout cycles implemented without the sampling of the video signal are called *idle cycles*. Since the HAWAII-2 FPA can run in idle cycles between the readouts without any interrupt, the idle cycles are useful to stabilize the state of the image sensor. If the readout of the FPA is started and finished without changing its operation, we can avoid the transient feature in the video signal due to the modifying the state of chip circuits.

There are two solutions applied to start of the readout process in idle-mode: the idle-wait and idle-break mode. In the first mode the software waits for the end of the current idle-cycle before starting the readout of the chip while in idle-break mode it interrupts the running of the actual idle-cycle and starts the readout immediately. The camera uses the idle-wait mode for normal operation, which assures the stable operation of the chip. However, if a series of frames with long integration times are taken the idle cycles between the readouts have also long duration times, which causes a long dead time in the readout process. In order to avoid this dead-time, the idle break mode should be used, in which the control software always stops the long idle cycles and starts the readout. We used idle-break mode to take series of dark frames of the HAWAII-2 chips with longer integration times increased up to 1000 s.

3.1.3 Fine tuning of the Analog Signals

In the previous chapter on the operation of the HAWAII-2 FPA the role of the analog control signals of the chips are discussed, among others. These analog signals, namely the bias voltages of the detector, can also be used to optimize the operation of the image sensor. The task is then to adjust them in the range of their nominal values and check performance of the detector with different timings of the digital control signals.

As seen in the Table 2.1, two of the bias voltages, BIASPWR and BIASGATE, have nominal values of 5 V and 3.5 V, respectively. In fact, BIASPWR should not be changed since it is the source voltage of the P-FET for accessing the unit cell. Nevertheless, BIASGATE can be modified in its nominal range (0-5.5V) without any problem, which changes the current control for the unit cell. By fine-tuning the current control, the speed and the dynamical range of the SF amplifier can be adjusted. The other analog input is VRESET, the reset level of the unit cells, which has a nominal range between 0.5 and 1 V. This means the BIASGATE and VRESET can be used together to find an optimal range of the operation of the detector. In order to assure a fast operation, the speed of the discharging of the unit cell should be increased. If fact the P-FET with BIASPWR and BIASGATE is a voltage driven current source and the current is proportional to the difference in the voltage between BIASPWR and BIASGATE (Fig. 2.5). By decreasing BIASGATE with constant BIASPWR, e.g. 5 V, the current discharging the unit cell capacitance can be increased. As a consequence, if BIASGATE is adjusted to a lower value, it increases the speed of the operation. The minimal value of BIASGATE could be 0V in its nominal range. However, at about its nominal value, 3.5 V, the P-FET starts to saturate and cannot increase the discharging current. Thus its optimal value must be in the near of the nominal one. Besides increasing the rate of the discharging, a smaller reset value could also make

shorter the discharging time. It means the value of VRESET should be set as small as possible. On the other hand the video signal must have a maximal dynamical range which allows us to measure the video signal more precisely. This requirement maximizes the value of VRESET. A trade-off between these two requirements gives roughly the values of the analog inputs. An optimal dynamical range, which takes about 4 μs, VRESET is set its maximal value, 1V, and BIASGATE is adjusted to 3.2 V. These values were used for the operation of the HAWAII-2 FPA in the OMEGA2000 camera.

3.1.4 Optimal Design of the Basic Timing

Besides the choice of the output mode with the fastest data transfer and the fine-tuning of the bias voltages, the main task was to design an optimal basic timing for the readout of HAWAII-2 sensor. As a goal of this task, we wanted to ensure a detector limited operation of the OMEGA2000 camera, i.e., we reduced the time needed for the readout of the full FPA while the operation of the chip had to remain stable. Hence, the main purpose for optimizing the pixel readout cycle was to increase the sampling frequency of the video signal to an upper limit beyond which the sampled signal would be distorted due to the interference and the transient behavior of the circuit components. Here, we discuss the solutions we applied to achieve this detector limited operational mode.

As already described in the previous chapter presenting the HAWAII-2 FPA, it operates in reverse bias mode. It means the capacitance of each pixel in the array is charged by applying a reset voltage and the charge carriers induced by the incident IR photons discharge these capacitances in an amount proportional to the number of the photo charges. The video signal is the voltage measured on the capacitances after discharging. The theoretical upper limit of the sampling and clocking frequency of the video singal of the HAWAII-2 FPA is determined by its transient time. After pulling the video signal up with the reset voltage at the beginning of the readout cycle of a pixel, we cannot sample the signal until it has reached its stable value, which takes about 4 μs with an optimal dynamical range adjusted with 1 V reset voltage and 3.2 V bias-gate voltage. The readout cycle time of one pixel is therefore altogether minimum 6 μs corresponding to a clock frequency of 166 kHz. Since the readout cycle of a pixel starts at the rising edge of the clock signal but the video signal is pulled up only at the falling edge, it allow us to increase the clocking frequency. We can use not only the time period of the low state of the clock signal (between the falling and rising edges) but also that of the high state of the clock signal (between the rising and falling edges) in the next cycle to cover the whole transient time of the video output. By applying a shorter low state of the clock signal, the next readout cycle will start earlier and the video output can be sampled before the falling edge of the clock signal in the next readout cycle. As a result, we have a readout cycle with a shorter duration time.

Fig. 3.1 compares the original readout process using the normal triggering with this solution. The FSYNC pulse (plotted with magenta in both the oscilloscope screens) controls the start of the readout of the full array with negative logic. The cycle time of a pixel readout spans the time axis from the first rising edge of the clock signal (plotted with green color) to the second one. The left hand panel shows the normal triggering where the cycle time covers the whole time needed for the video signal (plotted with yellow color) to decrease to its stable value after its

pulling-up. The transient time of the video output is delimited with the orange vertical markers. Here, the SCON signal (plotted with purple color) triggers the sampling of the video output at the end of the first readout cycle. The right hand panel displays the triggering delayed until the second falling edge of the clock signal. In this case, the video singal is also sampled in its stable state (SCON pulse plotted with magenta) but the next readout cycle starts (rising edge of the second clock pulse) before the video signal reaches its stable value. The only difference between the two pictures in Fig. 3.1 is the position of the FSYNC pulse. By positioning the trigger of the sampling in the second readout cycle, we eliminate the dead time between the sampling and the pulling up of the video output. As a result, we can decrease the cycle time in the second case.

Figure 3.1: The left hand panel displays the normal triggering of the video signal conversion of the first pixel in the FPA and the right hand one the triggering with delay. The clock signal (CLK1) is plotted with green color, the output singal of the video amplifier with yellow, the start signal of the sampling (SCON) with purple, and the frame synchronization signal (FSYNC) with magenta.

Another possibility to minimize the cycle time is to decrease the transient time of the video signal. It is about 4 μs when the signal RESETEN is high, i.e., we reset the column bus to cell-drain while there is no readout. If RESETEN is low the voltage difference between the pixels and the cell-drain becomes smaller, which decreases the transient time to roughly 2 μs. Thus, a minimal value of symmetric clock signal is reduced to $2 \times 2\mu\text{s} = 4\mu\text{s}$, i.e. the clock frequency can be 250 kHz. Although a stable video signal is sampled with all the methods, we used a pixel readout time of 6 μs (166 kHz) because ramps and stripes appeared at the edge of the frames taken with higher clock frequency. This problem will be discussed in the next section.

With a pixel readout time of 6 μs, the readout time of a full quadrant is $128 \times 1024 \times 6$ μs $= 786{,}432$ $\mu\text{s} \approx 0.79$ s in the Eight Output Mode and eight times more in the Singe Output Mode. This gives the minimal time needed to readout the HAWAII-2 FPA since its quadrants are read in parallel. However, the readout modes implemented for the OMEGA2000 camera contain more steps than a simple readout of the full array. Thus, the minimal readout time of the camera's readout modes is inherently longer than a read of the full array. In order to determine the time elapsed in a readout cycle of a given readout mode, we had to sum up the duration times of all the instructions used in that readout cycle. Since it was an important criteria to avoid the usage of any built-in interpeter making more complicated GEIRS (the control software of the OMEGA2000 instrument), this task had to be implemented with an externally runing program. I wrote a simple interpreter which processed the content of the instruction tables

Readout Mode	Min. readout time [s] Single Output Mode	Min. readout time [μs] Eight Output Mode
Single pixel read (spr)*	15.9	2,065,076
Reset level read (rlr)	6.31	799,945
Non-correlated sampling (rr)	6.31	792,249
CDS (o2dcr)	6.32	799,970
CDS with fast reset	6.32	799,945
Line interlaced read (lir)	12.6	1,599,771

Table 3.1: The minimal redout times of the implemented readout modes of HAWAII-2 FPA. * For the single pixel read this value depends on the position of the pixel to read out. Here, we read out the 10.-th pixel located in the 6.-th line of each quadrant.

used for the various readout modes and calculated the total duration time of the readout cycle from the duration times of the instructions organized in loops. We could determine the minimal integration times for each implemented readout mode with this interpeter, which are shown in Tab. 3.1. In the table, the first three readout modes are for engineering purposes. The minimal readout times of the reset level read and the non correlated sampling are only negligibly higher than the theoretical limit. We need much longer time for the single pixel read depending on the position of the pixel specified to read out. The series of the line synchronization signals applied for reaching a given pixel of the array in each quadrant is very time-demanding, which increases the minimal readout time considerably for this mode. However, this time is critical only for the other three readout modes as they are to be used for scientific applications. CDSs with and without fast reset in the Eight Output Mode have minimal integration times of about 0.8 s, which are short enough to avoid the saturation of the FPA in K-band imaging. These readout modes in the Single Output Mode with ~ 6.3 s provide acceptable readout times for J- or H-band observations but cannot be applied in K-band surveys. In spite of that, the line-interlaced read is the most efficient readout mode and produces the minimal overhead between the frame readouts. The minimal frame readout time is 1.6 s in the Eight Output Mode, which still allows us to use this mode in J- and H-band imaging but might cause problems in K band. The Singe Output Mode is not available for the the line interlaced read because its minimal readout time is very long, 12.6 s, and during this time the HAWAII-2 FPA will saturate in all broad NIR bands. Altough the multiple end-point read with its frame averaging provides the most accurate photon flux detection, we did not implement it since this mode has the longest readout time. In the multiple-end point mode we need to read out at least four frames in order to produce one averaged image, which, considering the theoretical limit of the minimal frame readout time, gives a readout cycle time of 4×0.79 s $= 3.16$ s for the Eight Output Mode. This long duration time would make the application of this readout mode difficult even in J and H bands.

In this section we have considered how to design the basic timing of the readout process of the HAWAII-2 chip optimally. With the techniques described above, we minimized the duration time of the frame readout cycles of each readout mode implemented for the FPA. For the optimal design, there are three readout modes available for the OMEGA2000 camera for the scientific observations. In the Eight Output Mode the readout using CDS with or without fast reset can be applied in all NIR bands, while in the case of the line interlace read we must check if the properly

positioned baffle reduces the background noise enough to avoid the saturation of the detector in K-band imaging. The OMEGA200 instrument is still able to operate with both types of CDS in Single Output Mode but only for J and H-band surveys. The line interlaced read cannot be used in Single Output Mode. In the next section we present the test result of the operation of the HAWAII-2 FPA in these available readout modes and examine the quality of the imaging the camera produces. This will help us to chose the optimal configuration of the readout and output modes, thereby providing the best image quality for scientific purpose, without any feature or artifact.

3.2 Improving of the Image Quality

Even if the video signal is sampled correctly, artifacts might appear in the images, due to the transient effects in electric circuits operating at high clock frequency. Other unwanted couplings between the different parts of the electrical circuits can also degrade the image quality. In this section we consider these problems together with the techniques applied to eliminate these artifacts. The first part presents the problems due to the transient behavior of the electrical circuits of the HAWAII-2 FPA and the solutions to eliminate the artifacts related to the transient phenomena. In the second part we describe the problems caused by internal couplings between the electrical circuits of the FPA and the readout electronics. We also describe the solutions to this problem.

3.2.1 Transient Features in the Images

We saw in the previous section that the transient phenomena of the electrical signals limit the time resolution of the readout process. The video signal cannot be sampled until it reaches its stable value and this imposes a time constraint on the pixel readout. Besides this transient feature, there is another effect related to the video signal which must also be considered. In the beginning of each line, indicated by a pulse of LSYNC, a drift in the video signal can be measured, even if we sample the signal in the stable range. Fig. 3.2 showing the control singals and the video output of the HAWAII-2 FPA demonstrates this feature. The left hand panels shows the start of a frame readout after resetting the full array. In the left hand side of the oscilloscope screen we can see the video signal measured in the last few pixels in the whole frame to be reset. The FSYNC pulse, plotted with magenta, starts the readout of the next frame. The right hand side of the screen shows this readout process, where the video signal of the first few pixels are increasing only gradually up to the average value of the local area in the next frame. The right hand panel shows the same phenomena but after the integration of the video signal. Here, the video output is not active during the integration and has a gradual increase in its value for the first few pixels, as in the previous case.

Since the same drift occurred both after reset and after integration, it should not cause any problem for the readout modes with CDS. By subtracting the reset frame from the integrated one, the gradient in the pixel values could be eliminated if the rate of the drifts were the same in both frames. However, narrow stripes appeared at the border of the image as a result of the subtraction, indicating that the drift rates were different. Since the amplitude of this difference

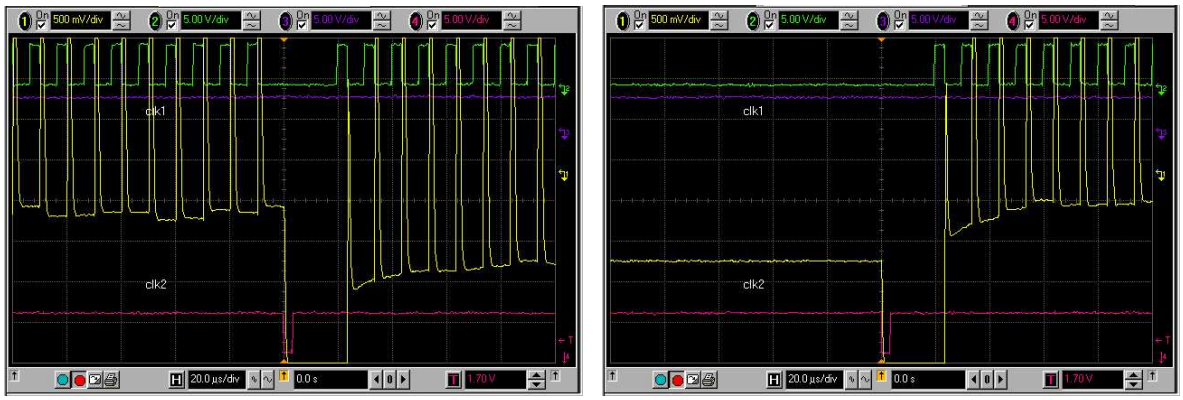

Figure 3.2: The left hand panel shows the drift in the video signal after reset and the right hand one displays it after integration. The clock signal (CLK1) is plotted with green color, the output singal of the video amplifier with yellow, and the frame synchronization signal (FSYNC) with magenta.

was on the order of 100 mV, representing about 1300 ADU, it became dominant only in low signal level, as demonstrated in Fig. 3.3.

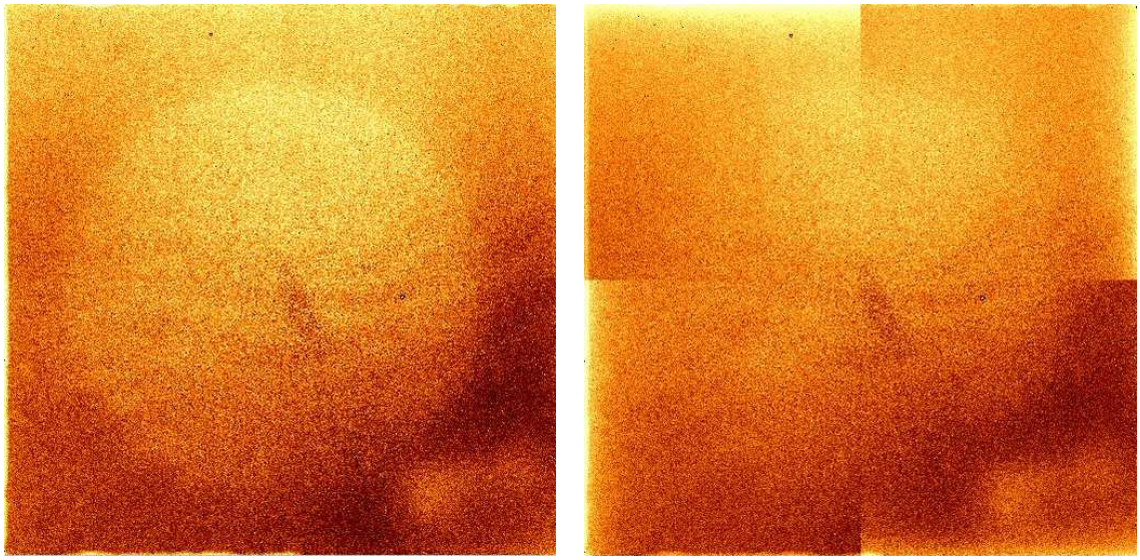

Figure 3.3: The left hand panel shows a frame taken with the FPA #37 with higher incident flux, 20,000 ADU on the average, and the right hand one displays a frame taken with the weakly irradiated detector, producing only $\sim$ 5000 ADU. The latter exhibits drifts at the outer edges of the quadrants.

A similar behavior was observable for the last pixels in each row, where the signal value was considerably higher than the average signal of the previous pixels. Fig. 3.4 shows the readout of the last few pixels in a row. The last pixel value is on the order of 100 mV, i.e., $\sim$ 1300 ADU, higher the those of the previous pixels in the same row. The origin of this anomaly is hard to explain. While in the previous case, the drift was due to the transient features of the electrical circuits after changing their state, this explanation does not apply to this situation. The triggering of line synchronization signal at the end of readout cycle of the last pixel cannot

effect on the pixel value already at the beginning of the readout cycle. In any case, this difference did not cause any feature in the frames taken in the readout modes with CDS, since it was only a bias value superposed in the reset frame, which could be eliminated by subtracting it from the integrated frame.

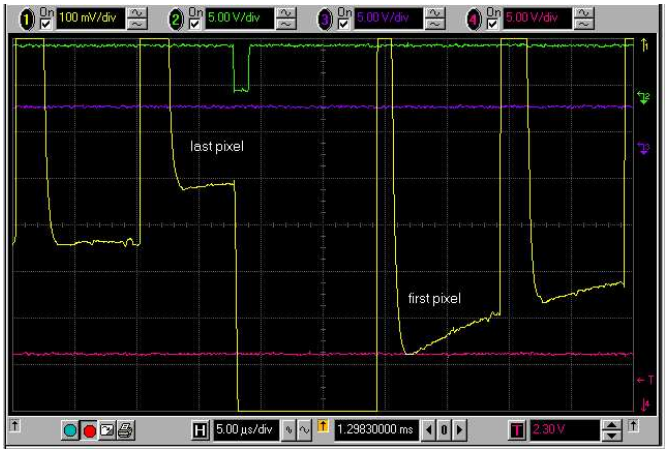

Figure 3.4: The deviation of the value of last pixel from those of the previous pixels in an arbitrary row of the array. The the line synchronization signal LSYNC is plotted with green color, the output singal of the video amplifier with yellow.

3.2.2 Artifacts caused by internal Couplings

All the implemented readout modes were tested with the three HAWAII-2 FPAs operating . with clock frequencies between 150 and 250 kHz and we checked the quality of the images they produced. The noise statistics of the frames taken with different clock rates did not change dramatically but some artifacts degrading the image quality appeared at higher clock frequencies. In the case of FPA #37 and FPA #77 , a typical problem was that the different groups of channels had different offsets in the frames of low signal level taken in CDS mode with fast reset (Fig.3.5). With slow reset or in line-interlaced mode, only a gradient or a ramp in the pixel values appeared in the quadrants but this artifact had a non-linear behavior, i.e., it did not scale with the average signal level. We used slower clock rates down to 150 kHz but the ramps could not be eliminated. This phenomenon might be caused by some unknown coupling problem between the multiplexer of the detector and the data bus of the readout electronics. Whatever the cause, we did not observe any similar feature in the images produced with the FPA #48 in the traditional CDS with the clocking frequency of 166 kHz.

In the case of the specimen #48 another issue emerged. Here, the readout in CDS mode with fast reset also caused some drift in the dark fames which could be observed in each channel (Fig. 3.6). This indicated that there is drift in the reset level along the rows of the pixel array in all the quadrants. The drift was not present in the traditional CDS mode, so we used this mode in the the science run, even though it is more time-consuming because of its less efficient readout scheme.

The observations carried out with two of the HAWAII-2 detectors are listed in Tab. 3.2. FPA #48 was used for the observations in September 2003 and OMEGA2000 provided data of good

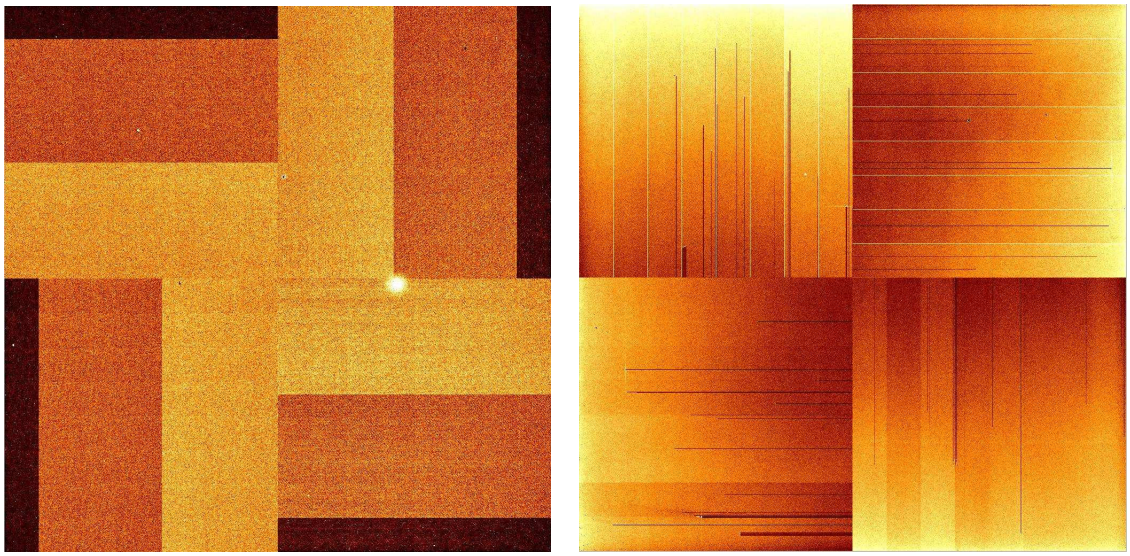

Figure 3.5: Dark frames produced by the FPA #37. The left hand panel shows a image taken with fast reset and the right side one displays an image taken in conservative CDS mode.

Observation	Used filters	FPA
September 2003	J_1, H, K	#48
November 2003	J_1, H	#77
April 2004	J_1, J_2, H	#77

Table 3.2: Observations with two specimen of the HAWAII-2 FPA in the OMEGA2000 camera.

quality. In November 2003 and in April 2004, the camera was operating with the FPA #77 in the Single Output Mode because the ramps present in the frames were less steep in this mode. The ramps could not be completely flatfielded out, but the preliminary results of the data reduction were satisfying. The one drawback was the increased overhead due to the slower output mode.

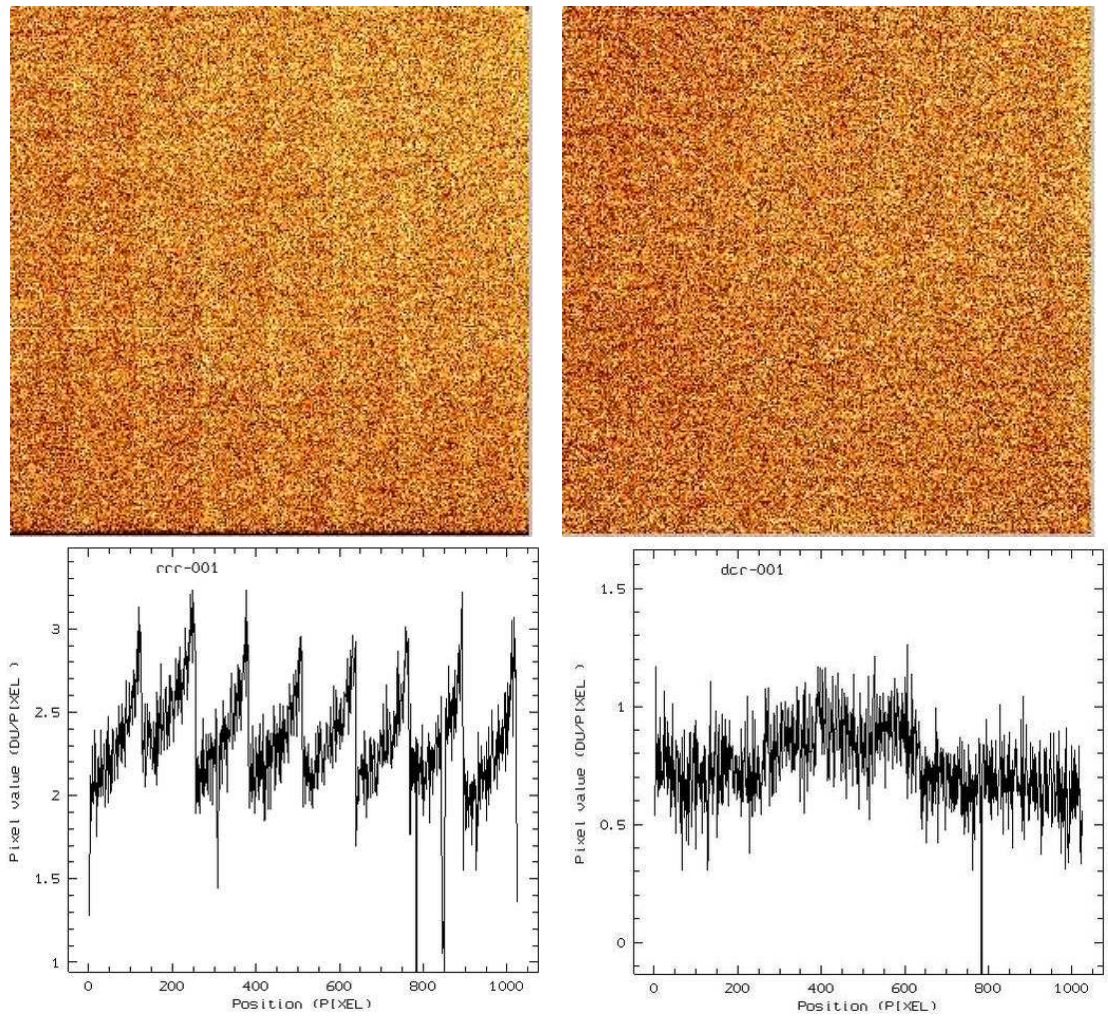

Figure 3.6: The two upper panel display the right lower quadrants of the dark frames taken in CDS mode with fast reset (left hand panel) and in conservative CDS mode (right hand panel) with FPA #48. The lower panels give cross sectional views of the summed signal values over the whole arrays for the same frames.

Chapter 4

Performance of the HAWAII-2 FPA

In this chapter we present the results of the detector tests and discuss the performance of the HAWAII-2 FPAs operating in the OMEGA2000 camera. In order to give a comprehensive view of the performance of a detector, we have to test its operation by measuring its various properties. As we optimized the operation of the HAWAII-2 FPA in the OMEGA2000 camera, we carried out a series of tests with the three specimen of HAWAII-2 FPAs, #37, #48, and #77, to characterize their most important properties. During the tests, we measured and compared their noise properties, dark current statistics, quantum efficiency and linearity, providing a more comprehensive view on the performance of this detector family.

4.1 Noise Properties of the Image Sensor

In astronomy the goal of the imaging is to measure the photon flux, i.e., the rate at which photons impinge on each point in the field of view. Focal plane arrays are therefore designed and manufactured in that way to reach as maximal sensitivity to illumination as possible. However, there is always a wide variety of features and artifacts appearing in the captured images, which was not present in the incoming photon flux. These unwanted features and artifacts superimposed on the input signal by the imaging system are specified as noise degrading the image quality. Besides the sensitivity, another aim of the detector design is to minimize or control the sources of noise, since noise is what ultimately limits the overall performance of a camera. In an ideal digital camera, the performance is limited by the photon noise or the noise of the image sensor and not by that of the system electronics.

The noise sources are usually classified in two categories: *temporal or random noise sources* and *spatial or pattern noise sources*. The temporal or random noise is not constant from frame to frame in the image and it can be reduced by applying longer exposure time for a frame, i.e., increasing the signal-to-noise ratio, or averaging successive frames. Statistical momenta, such as the average, root mean square and median, are useful tools to describe the statistical properties of random noises. Typical temporal noises are the shot noise, reset noise, output amplifier noise and dark current shot noise. The spatial noise does not change significantly from frame to frame and it cannot be reduced by increasing the exposure time or averaging successive frames. However, frame subtracting and gain or offset correction techniques are able to reduce some kinds of spatial noise. The pattern noise is described in terms of the variation in the signal values of

the individual pixels under uniform illumination. This kind of noise has major components, such as fixed pattern noise, photo-response non-uniformity and dark current non-uniformity. In this section we give a short overview on some of the noise types

4.1.1 Photon Shot Noise

There exists a noise source which is not associated with the intrinsic properties of light detection systems but with the discrete nature of photons. The random arrival of the photons at any detector causes a random generation of the photo-electrons in the detector material and therefore an inevitable statistical fluctuation in the rate of the photo-charge accumulation and in turn in the video signal. The shot noise of the photons draws a fundamental limit on the performance of imagers and it is important to determine its contribution to the total noise of the system. This type of noise does not depend on the frequency of the light illuminating the detector, so it is a white noise.

If the photon flux incident on a unit area of the sensor during a unit time is $I(t)$, then the number of photons received on that unit area during the exposure time between t_0 and t_1 is

$$n = \int_{t_o}^{t_1} I(t)dt \ . \tag{4.1}$$

Since the shot noise has a Poisson statistical distribution, i.e., the time between photon arrivals is specified by Poisson statistics, the uncertainty in the number of photons collected during the given period of time is

$$\sigma_{shot} = \sqrt{n} \ . \tag{4.2}$$

The useful data range of HAWAII-2 resides between 0 and 65535 and its linear regime is measured to be up to about 40,000 ADU for each specimen, as we will see it in the Section 4.4. Since the output signal conversion gains of the detectors are roughly $5e^-$/ADU, their linear full well capacities are about $200,000e^-$. If we take the quantum efficiency of the photo sites to be almost unity, the average number of photons in the incoming flux has the same order and the shot noise will be $\sigma_{shot} = \sqrt{200,000} = 400$ ($\sim$ 100 ADU). We use only about two third of the full dynamical range of the detector for the observations. Therefore, the shot noise of the signal coming from the target objects typically $\sqrt{2/3}$ times smaller than σ_{shot} derived for the full dynamical range, which gives about 80 ADU. This value should be compared with the infrared background noise so that we could determine whether the observations will be limited by the shot noise of the singal or by the background.

4.1.2 Reset Noise

As mentioned in the previous chapter, a typical active pixel sensor applies a source-follower amplifier with a sense node capacitance to convert the photo-generated signal from the charge domain to the voltage domain. In the beginning of every readout cycle each pixel of the camera is reset to some reset level, V_{res}. It means that the sense node capacitance is charged through the resistance of the reset MOSFET channel to reach the voltage V_{res}. Nevertheless, there is always an uncertainty in this voltage due to thermal noise generated by the MOSFET channel

resistance. This uncertainty is referred to as the reset noise and it depends on not only the temperature but also the noise equivalent bandwidth (NEB) Δf of the channel. The latter is defined defined by the expression

$$\Delta f = \frac{1}{|A(0)|^2} \int_0^\infty |A(f)|^2 df \quad , \tag{4.3}$$

where $A(f)$ the transfer function of the cannel, and it gives the cut-off frequency of an ideal filter with a power spectral density equivalent to a real one. Any real filter can be replaced by its ideal pair if its response to the white noise superimposed on its input has the same power spectral density as the real filter. The definition of the noise equivalent bandwidth can be seen in Fig. 4.1, where this cut-off frequency of the ideal filter has the value for which the two shaded areas are equal. Then the RMS of the reset voltage is expressed as

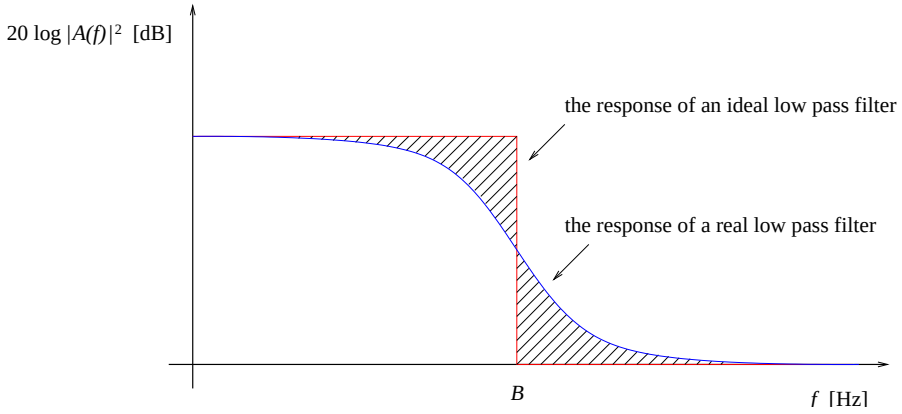

Figure 4.1: The definition of the noise equivalent bandwidth. The shaded areas are equal.

$$\sigma_{res} = \sqrt{4kT\Delta f R} \quad , \tag{4.4}$$

where k is Boltzmann's constant, T is the temperature and R is the effective channel resistance. Normally a RC low pass filter with the transfer function

$$A(f) = \frac{1}{1 + j(f/f_0)} \qquad f_0 = \frac{1}{2\pi RC} \quad , \tag{4.5}$$

provides a good approximation of the noise channel models for resetting of the output nodes of CCDs or Active Pixel Sensors. Its noise equivalent bandwidth has the simple form

$$\Delta f = \int_0^\infty \left| \frac{1}{1 + j(f/f_0)} \right|^2 df = \int_0^\infty \frac{1}{1 + (f/f_0)^2} df = \frac{\pi}{2} f_0 \tag{4.6}$$

that is

$$\Delta f = \frac{1}{4RC} \quad , \tag{4.7}$$

which can be substituted in Eq (4.4) and we obtain that

$$\sigma_{res} = \sqrt{\frac{kT}{C}} \quad . \tag{4.8}$$

It is more convenient to express this value in terms of electrons so that we can compare it with the number of electrons accumulated in the well capacitance. Since the accumulated charge in the sense node capacitor is $nq = CV_{res}$, where n is the number of electrons, q is the fundamental charge and C is the sense node capacitance, the RMS of the reset noise in terms of electrons is

$$\sigma_{res} = \frac{\sqrt{kTC}}{q} \quad . \tag{4.9}$$

Because the two free parameters are only the temperature and the sense node capacitance in this equation, the reset noise is also called kTC noise. By reducing the free parameters, the reset noise can be decreased. The tradeoff is that the lower the sense node capacitance, the smaller the dynamical range of the photo-sites. According to the specification of HAWAII-2 detector, its unit cells have a sense node capacitance of 28-35 fF (Haas, 2002). Therefore, at the temperature of 77K we expect a maximal reset noise generated on the sense node capacitance to be $\sigma_{res} \approx 40e^-$, i.e., about 10 ADU. This value is one order less in magnitude than the expected photon shot noise, hence it is negligible in the background limited operation of the imagers.

4.1.3 Readout Noise

The two primary sources of the readout noise of the imaging sensors are the *thermal* and the *flickering noise* generated in the output amplifier. The thermal noise is a white noise, i.e., it is independent of the operation frequency of the circuit, while the flickering noise is frequency dependent. This means their contribution to the total readout noise is varying in different domains of the frequency scale.

Thermal or White Noise

Not only the reset MOSFET but also the transistor of the output amplifier of the detector has a resistance that causes thermal noise. This kind of white noise, sometimes called Johnson noise, can be described with a similar expression in volts as the reset noise,

$$\sigma_{th} = \sqrt{4kT\Delta f R_{out}} \qquad [\mathrm{V}] \ , \tag{4.10}$$

but here the resistance R_{out} denotes the output impedance of the source follower amplifier. If the g is the gain of the image sensor, then the thermal noise in electrons can be written as

$$\sigma_{th} = \frac{\sqrt{4kT\Delta f R_{out}}}{g} \qquad [e^-] \ . \tag{4.11}$$

With the output impedance of a few Ohms and about the same noise equivalent bandwidth as the reset noise has, this noise for the HAWAII-2 detector with a gain of $\sim 4\mu\mathrm{V}/e^-$ has the same order as its reset noise.

Flicker or $1/f$ noise

Another natural noise source in electrical circuits produces a noise with an amplitude approximately inversely dependent on the frequency. It is called flicker or $1/f$ noise because of its

frequency dependence. The higher clock frequency a system is driven on, the lower the noise, hence it causes no problem for fast readout circuits and it can only be the dominant noise component for the imagers operated with low pixel rate. Quantitatively, if we increase the clock frequency by one order of magnitude then the noise power decreases also by a factor of 10 and the RMS of the noise current is

$$\sigma_{1/f} = i_s \sqrt{\frac{\Delta f}{f}} \quad , \tag{4.12}$$

where i_s is the signal current, Δf is the noise equivalent bandwidth of the output amplifier and f is its operational frequency. The typical source of the 1/f noise is any junction in the circuits, namely the traps of electron states at the silicon-oxide interface of the MOSFET switches. The variations of the electron states exhibit different characteristic time constants related to the different charge traps and the superposition of these variations, each with its own time constant, generates the $1/f$ noise spectrum.

If the detector is clocked slowly the 1/f noise is the natural noise limit but by increasing the frame rate at the 1/f corner frequency the device becomes white noise limited.

4.1.4 The Photon Transfer Curve

An efficient analysis for the noise characteristics of an imager is to determine its photon transfer curve, which provides the read noise floor, the conversion gain, the full well capacity and the dynamical range of the detector. Such a plot can be obtained by taking a series of flatfielded images with different exposure times, or with different signal intensities, and measuring the mean and the variance of the pixel values in a fixed area of all the images. The photon transfer curve then, is the graph of the variance as a function of mean pixel values. The method of determination of the read noise and the gain from this plot is very simple. The conversion gain of an image sensor is defined as the ratio of the number n_e of the photo generated electrons to the video signal s in ADU,

$$g = \frac{n_e}{s} \qquad \left[\frac{e^-}{\mathrm{ADU}}\right] \quad . \tag{4.13}$$

Since the number of the photoelectrons also exhibits a Poisson's distribution caused by the photon shot noise, its variance can be expressed in the term of the gain and the video signal

$$\sigma_e^2 = n_e = gs \quad . \tag{4.14}$$

The major noise components of a bias subtracted image should be this random noise exhibiting Poisson statistics and the readout noise of the detector. By adding their standard deviations in quadrature, we obtain the noise of the total signal in electrons,

$$g\sigma_s = \sqrt{\sigma_e^2 + \sigma_{ro}^2} \quad , \tag{4.15}$$

or the the variance of the total signal

$$\sigma_s^2 = \frac{1}{g} s + \frac{1}{g^2} \sigma_{ro}^2 \quad , \tag{4.16}$$

which is a relation between the variance and average signal intensity. In fact, the photon transfer

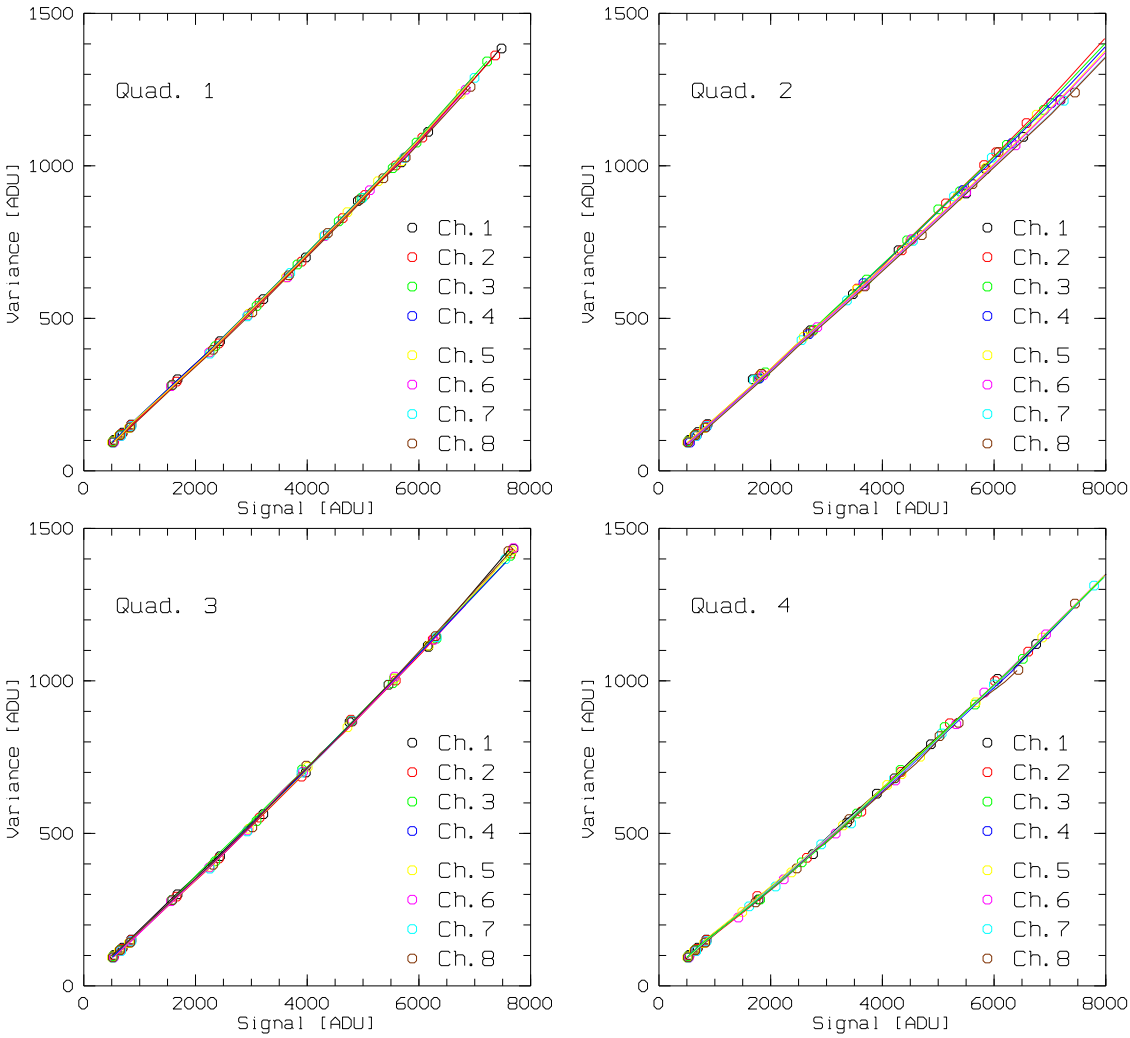

Figure 4.2: The photon transfer curve for each quadrant of the FPA #37.

curve is not linear but it has different characteristic regimes. In the first regime, at lowest signal values, the operation of image sensors is dominated by the readout noise and the curve is flat. The intersection of the transfer curve and ordinate axis gives the theoretical value of the readout noise floor, $(\sigma_{ro}/g)^2$. As the signal level increases, the camera operation becomes shot noise or background limited. This is the second regime, where the photon transfer curve has a slope of g^{-1}, i.e., its tangent determines the signal conversion gain of the detector. The third range represents the pattern noise limited operation of the imager. Here, the noise is proportional to the signal level, which means the slope of the photon transfer curve is unity in the log-log plot.

In order to determine the readout noise and the gain of the HAWAII-2 detectors, flatfield images were taken with constant illumination through a narrow band filter (NB1083) with different exposure times. After flatfielding them, the median and the variance of the pixel values in each channel of the arrays were measured in the frames and averaged for each quadrant. These values gave the photon transfer curves of the imager. The first, readout noise limited regime was very small compared to the shot noise limited one. Even if the detectors were very weakly illuminated, on the order of 1000 ADU, the operation of the imagers were shot noise limited.

Quad./Ch.	Fitted $(1/g)$	g (e^-/ADU)	Fitted $(\sigma_r/g)^2$	σ_r^2 (ADU)
Quad. 1				
Ch. 1.	0.1786	5.60	1.7130	53.7
Ch. 2.	0.1773	5.64	2.1369	67.98
Ch. 3.	0.1751	5.71	3.5764	116.65
Ch. 4.	0.1755	5.70	2.9699	96.42
Ch. 5.	0.1733	5.77	3.9987	133.14
Ch. 6.	0.1679	5.96	4.5716	162.17
Ch. 7.	0.1775	5.63	1.9586	62.17
Ch. 8.	0.1713	5.84	3.5667	121.55
Quad. 2				
Ch. 1.	0.1966	5.09	-2.0739	-
Ch. 2.	0.1892	5.29	1.1052	30.87
Ch. 3.	0.1843	5.43	3.1954	94.08
Ch. 4.	0.1882	5.31	0.7883	22.26
Ch. 5.	0.1849	5.41	1.4673	42.92
Ch. 6.	0.1905	5.25	-2.1159	-
Ch. 7.	0.1815	5.51	1.4328	43.49
Ch. 8.	0.1826	5.48	0.6488	19.46
Quad. 3				
Ch. 1.	0.1864	5.36	5.9957	172.56
Ch. 2.	0.1818	5.50	0.2913	8.81
Ch. 3.	0.1883	5.31	3.8819	109.48
Ch. 4.	0.1862	5.37	2.9250	84.37
Ch. 5.	0.1849	5.41	2.7540	80.55
Ch. 6.	0.1908	5.24	-1.0344	-
Ch. 7.	0.1862	5.37	0.7624	21.99
Ch. 8.	0.1813	5.52	2.2328	67.93
Quad. 4 3				
Ch.1.	0.1945	5.14	2.4648	65.15
Ch.2.	0.1934	5.17	1.9898	53.2
Ch.3.	0.2007	4.98	-2.1223	-
Ch.4.	0.1976	5.06	-1.9213	-
Ch.5.	0.1874	5.34	3.3340	94.94
Ch.6.	0.1922	5.20	1.9204	51.99
Ch.7.	0.1933	5.17	-1.2340	-
Ch.8.	0.1924	5.20	-3.2398	-

Table 4.1: The gain g and the readout noise σ_r measured for each channel of the HAWAII-2 FPA #37.

Quad./Ch.	Fitted $(1/g)$	g (e^-/ADU)	Fitted $(\sigma_r/g)^2$	σ_r^2 (ADU)
Quad. 1				
Ch.1	0.2344	4.27	1.9979	36.35
Ch.2.	0.2301	4.35	1.8634	35.20
Ch.3.	0.2201	4.54	1.8648	38.51
Ch.4.	0.2330	4.29	1.7869	32.90
Ch.5.	0.2415	4.14	1.8383	31.53
Ch.6.	0.2418	4.14	1.8636	31.87
Ch.7.	0.2202	4.54	1.6704	34.46
Ch.8.	0.2482	4.03	1.8523	30.06
Quad. 2				
Ch.1.	0.2029	4.93	1.5180	36.86
Ch.2.	0.2121	4.72	1.7969	39.96
Ch.3.	0.2039	4.90	1.7956	43.19
Ch.4.	0.2352	4.25	1.7484	31.60
Ch.5.	0.2404	4.16	1.6821	29.12
Ch.6.	0.2451	4.08	1.6565	27.57
Ch.7.	0.2489	4.02	1.6740	27.03
Ch.8.	0.2476	4.04	1.7355	28.32
Quad. 3				
Ch.1.	0.2130	4.70	1.0705	23.60
Ch.2.	0.2143	4.67	1.0794	23.52
Ch.3.	0.2037	4.91	1.1203	27.00
Ch.4.	0.2304	4.34	1.2721	23.97
Ch.5.	0.2013	4.97	1.3732	33.88
Ch.6.	0.2258	4.43	1.5482	30.36
Ch.7.	0.2114	4.73	1.5859	35.49
Ch.8.	0.2169	4.61	1.3775	29.29
Quad. 4				
Ch.1.	0.2077	4.81	1.5186	35.20
Ch.2.	0.2483	4.03	1.1290	18.32
Ch.3.	0.2319	4.31	1.4456	26.87
Ch.4.	0.2067	4.84	1.4966	35.04
Ch.5.	0.2444	4.09	1.5238	25.52
Ch.6.	0.2451	4.08	1.6973	28.25
Ch.7.	0.2465	4.06	1.7926	29.50
Ch.8.	0.2306	4.34	1.8150	37.60

Table 4.2: The gain g and the readout noise σ_r measured for each channel of the HAWAII-2 FPA #48.

Quad./Ch.	Fitted $(1/g)$	g (e^-/ADU)	Fitted $(\sigma_r/g)^2$	σ_r^2 (ADU)
Quad. 1				
Ch.1.	0.2059	4.86	2.1565	50.8
Ch.2.	0.2102	4.76	1.4323	32.48
Ch.3.	0.2166	4.62	3.2364	69.01
Ch.4.	0.2084	4.8	0.2134	4.92
Ch.5.	0.2041	4.9	-2.2312	-
Ch.6.	0.2066	4.84	3.8764	90.83
Ch.7.	0.2200	4.54	2.3432	48.4
Ch.8.	0.2082	4.8	5.6544	130.41
Quad. 2				
Ch.1.	0.1883	5.31	1.3214	37.26
Ch.2.	0.1872	5.34	-2.4325	-
Ch.3.	0.1957	5.11	3.2784	85.59
Ch.4.	0.1921	5.21	2.4324	65.93
Ch.5.	0.1983	5.04	6.3476	161.45
Ch.6.	0.1946	5.14	1.7654	46.63
Ch.7.	0.1887	5.3	8.5436	239.82
Ch.8.	0.1971	5.07	-1.3221	-
Quad. 3				
Ch.1.	0.1942	5.15	4.5435	120.45
Ch.2.	0.1956	5.11	3.4656	90.54
Ch.3.	0.2059	4.86	-1.4324	-
Ch.4.	0.2105	4.75	2.4343	54.92
Ch.5.	0.1966	5.09	0.8776	22.71
Ch.6.	0.2043	4.90	2.3243	55.7
Ch.7.	0.2028	4.93	1.4355	34.91
Ch.8.	0.2102	4.76	4.3463	98.35
Quad. 4				
Ch.1.	0.2234	4.48	1.9615	39.32
Ch.2.	0.2352	4.25	2.7455	49.63
Ch.3.	0.2256	4.43	6.8767	135.07
Ch.4.	0.2101	4.76	-1.2423	-
Ch.5.	0.2089	4.79	4.3651	100.01
Ch.6.	0.2122	4.71	2.5433	56.5
Ch.7.	0.2132	4.69	3.1213	68.66
Ch.8.	0.2274	4.40	1.6456	31.81

Table 4.3: The gain g and the readout noise σ_r measured for each channel of the HAWAII-2 FPA #77.

The transfer curves for all the three arrays had very similar characteristics. Fig. 4.2 shows the photon transfer curve for each channel of the FPA #77. The gain and the readout noise statistics derived from this curve are listed in Tab. 4.1, whereas Tabs. 4.2 and 4.3 display these values for the specimen #48 and #77. The gains of the detectors were 4-5 e^-/ADU and their values at zero gave a readout noise of 10 e^- on the average, as expected (Hodapp, 2000).

4.1.5 Feedthrough and crosstalk

Although the flicker noise is not a problem for the electric circuits driven with high frequency, unwanted signals might appear in data transfer of one part of the circuit due to the operation of another part. The feedthrough of digital signals from the clock and the control lines into the analog parts of the circuit can deform the output waveform. The feedthrough is normally the result of the varying loads due to the different signal levels and the variability in the clock edge placement due to jitter. Besides the high frequency control and clock signals the high data transfer rate also causes similar problems: the crosstalk between some analog channels can produce moderate distortion in the waveform of the video output. The noise associated with the feedthrough and crosstalk is roughly a function of square root of the clock frequency.

The pixel clock of HAWAII-2 FPA operates at 160kHz, which is high enough to produce some crosstalk events. Although bright stars can saturate the detector during its operation, resetting of the full array prevents this high excess in the pixel values from causing any residual image effects in the following image of the dithering. Nevertheless, the saturated pixels generate a crosstalk between the data transfer lines of the different channels of the quadrant in which they are situated. The data lines of the channels are organized in parallel and there might be an interference between the data lines transferring the high video signal and the neighboring ones. As a result of this crosstalk, a series of spots with the distances of 128 pixels from each other appears in the whole quadrant, corresponding to each channel. The average values of the spots were lower than the background signal and their difference was a few percent, which is large enough to degrade the photometric correctness at the places they are situated. These spots could not be measured in the raw images but they were well discernible in the reduced frames (Fig. 4.3). This effect was a general feature of the operation of all the HAWAII-2 detectors which were tested and it should be considered for the choice of pointing positions in any field of the observations.

4.1.6 Fixed Pattern Noise (FPN)

There is a noise type which does not depend on the illumination of the detector and exhibits fixed patterns instead of random properties. This type of noise, called *fix pattern moise*, is normally due to operation of the sensor circuitry. In spite of the carefully performed growing process of the sensor layer structure, there may be variations in the detector dimensions, the doping concentrations, the contamination during the fabrication and the characteristics of the MOSFETs. These non-uniformities in the physical properties of the photo-sites also cause variations in the voltage between the MOSFET components in the unit cells and in the column circuits. The output voltage can further distorted by repeating irregularities in the array clocking and, in very large arrays, resistive drops in the reset buses may lead to a fall in the reset voltage. As a result

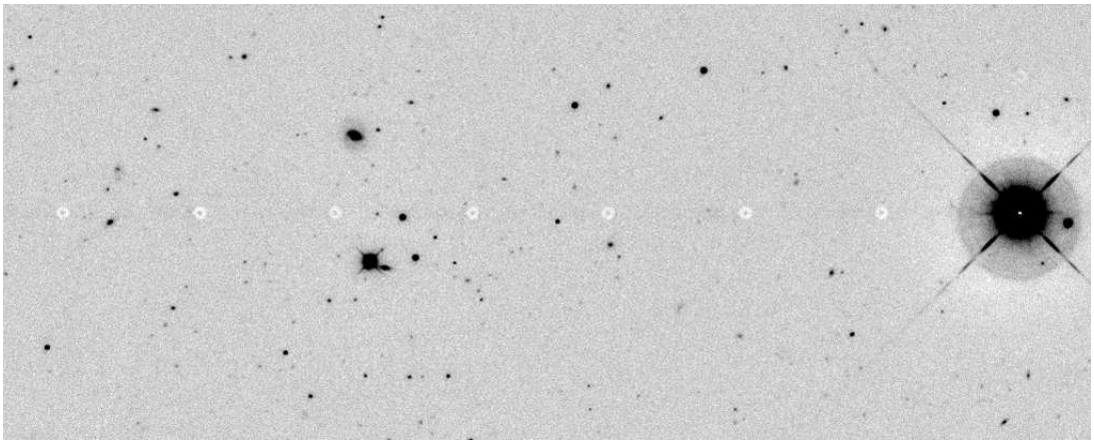

Figure 4.3: A series of pots caused by the cross talk during the transfer of the high signal values of saturated pixels.

of all these effects, a spatial variation can be measured in the output voltage produced by the pixels over the entire array even if in the absence of illumination. This spatial noise has a fixed pattern, which does not change appreciably image to image.

A typical fixed pattern noise of the HAWAII-2 FPAs is the difference of the bias levels in the 32 channels after resetting the detector, which appears in the frames taken in uncorrelated readout mode. This spatial noise besides other the noise features superimposed on the reset level can be eliminated by applying the double correlated readout mode.

4.1.7 Photo-Response Non-Uniformity and Quantum Efficiency

The non-uniformity of the pixel properties also results in a variation of their sensitivity to light. Besides the properties, such as the detector dimension, the doping concentration and the thicknesses of the over-layers, the sensitivity of the photo-sites depends on the illumination, both on its intensity and its frequency. This variation in the response of the pixels to the photo signal is called *photo-response non uniformity* (PRNU).

The image sensor technology uses some important quantities for the adequate characterization of the sensitivity of the detectors. The first one is the *responsivity* R, defined as the ratio of the electrical output signal i_s of the detector to the IR incident radiation power P,

$$R(\lambda, f) = \frac{i_s(\lambda, f)}{P(\lambda, f)} \quad , \qquad [\mathrm{AW}^{-1}] \quad , \tag{4.17}$$

where λ and f are the wavelength and the modulation frequency of the irradiation of the imager, respectively. For unmodulated signals (f =const.), the responsivity is called *spectral response*, which describes the wavelength dependence of the response function of detectors. For a fixed wavelength of the incident radiation, i.e., when photons fall in with the same energy, the *Responsive Quantum Efficiency* η (or RQE) of the image sensors can also be introduced as the ratio of number of the detected photons to the number of the incident ones. It gives the relative efficiency in which incident photons are collected and converted into electrons or an electric output signal.

In Figs. 4.4, 4.6, and 4.6 we show the RQE of HAWAII-2 FPAs #37, #48, and #77 mea-

sured in J, H, and K bands by the Rockwell company together with the histograms of flatfield images taken with the same detectors mounted in the OMEGA2000 camera. We used dome flats which were taken with the $J_1(\lambda/\Delta\lambda$=1190/80nm), H and K filters installed in the OMEGA2000 instrument. Since the IR sources illuminating a screen for the flatfielding in dome of the 3.5 m telescope were not calibrated and we cannot measure the incident photon flux needed to derive the RQE of the image sensors. We therefore give the histrograms of the dome flats normalized with their median for a qualitative comparison between the sensitivies of the three detectors. When the histograms of the flatfield frames are compared with each other, the difference between the distribution of the sensitivity of the imagers can be established: the narrow peak of the histogram belonging to FPA #48 shows that this chip has the most uniform distribution of the sensitivity. The left wing of the histogram of FPA #37 indicates a higher non-uniformity in its upper left quadrant while the broad, less pronounced bump in the histogram of FPA #77 is caused by a global variation of the quantum efficiency in the whole array.

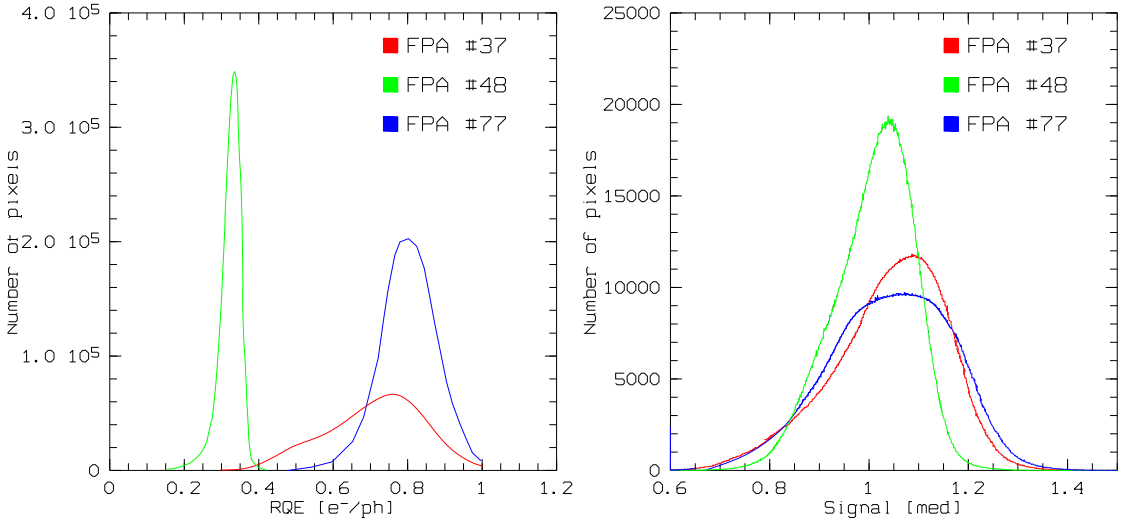

Figure 4.4: The left hand panel shows the Responsive Quantum Efficiency (RQE) of the HAWAII-2 FPAs, #37, #48, and #77 measured in J band by the Rockwell company. Theright hand panel displays the histograms of the flatfield images taken in J_1 band with with the same detectors installed in the OMEGA2000 camera.

By comparing the histograms of the normalized flatfield images with those of the RQE for each detector in each NIR band, we see the characteristics of RQE measured by the Rockwell company are similar to the distributions of the pixel values in the dome flats. The RQE histograms exhibit similar shapes and broadenings to those of the measured intensities in normalized flatfield images. In Fig. 4.7 we illustrate the different distributions of the pixel values by presenting the the flat field images for each detector.

However, neither the responsivity nor the RQE gives any information about the noise properties of image sensors, hence they cannot indicate their sensitivity. We need a quantity which can characterize not only the sensitivity of the detectors but also describe the noise degrading the quality of the measured signal. In an ideal imager the noise of the input signal, i.e., the photon shot noise σ_{ph} of the incident radiation is the only one noise source. The S/N of the

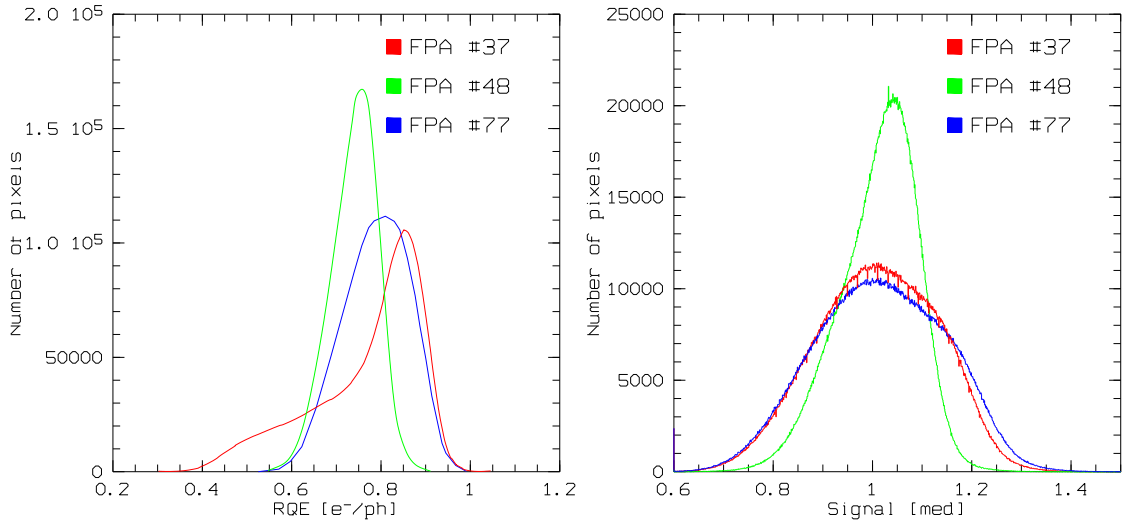

Figure 4.5: The left hand panel shows the Responsive Quantum Efficiency (RQE) of the HAWAII-2 FPAs, #37, #48, and #77 measured in H band by the Rockwell company. The right hand panel displays the histograms of the flatfield images taken in H band with the same detectors installed in the OMEGA2000 camera. .

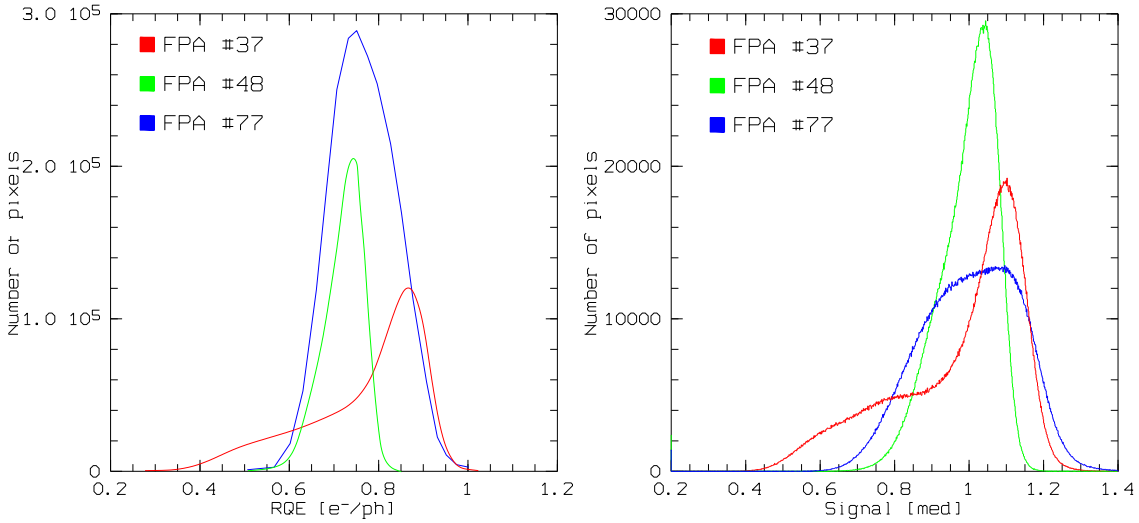

Figure 4.6: The left hand panel shows the Responsive Quantum Efficiency (RQE) of the HAWAII-2 FPAs, #37, #48, and #77 measured in K band by the Rockwell company. The right hand panel displays the histograms of the flatfield images in K band with the same detectors installed in the OMEGA2000 camera.

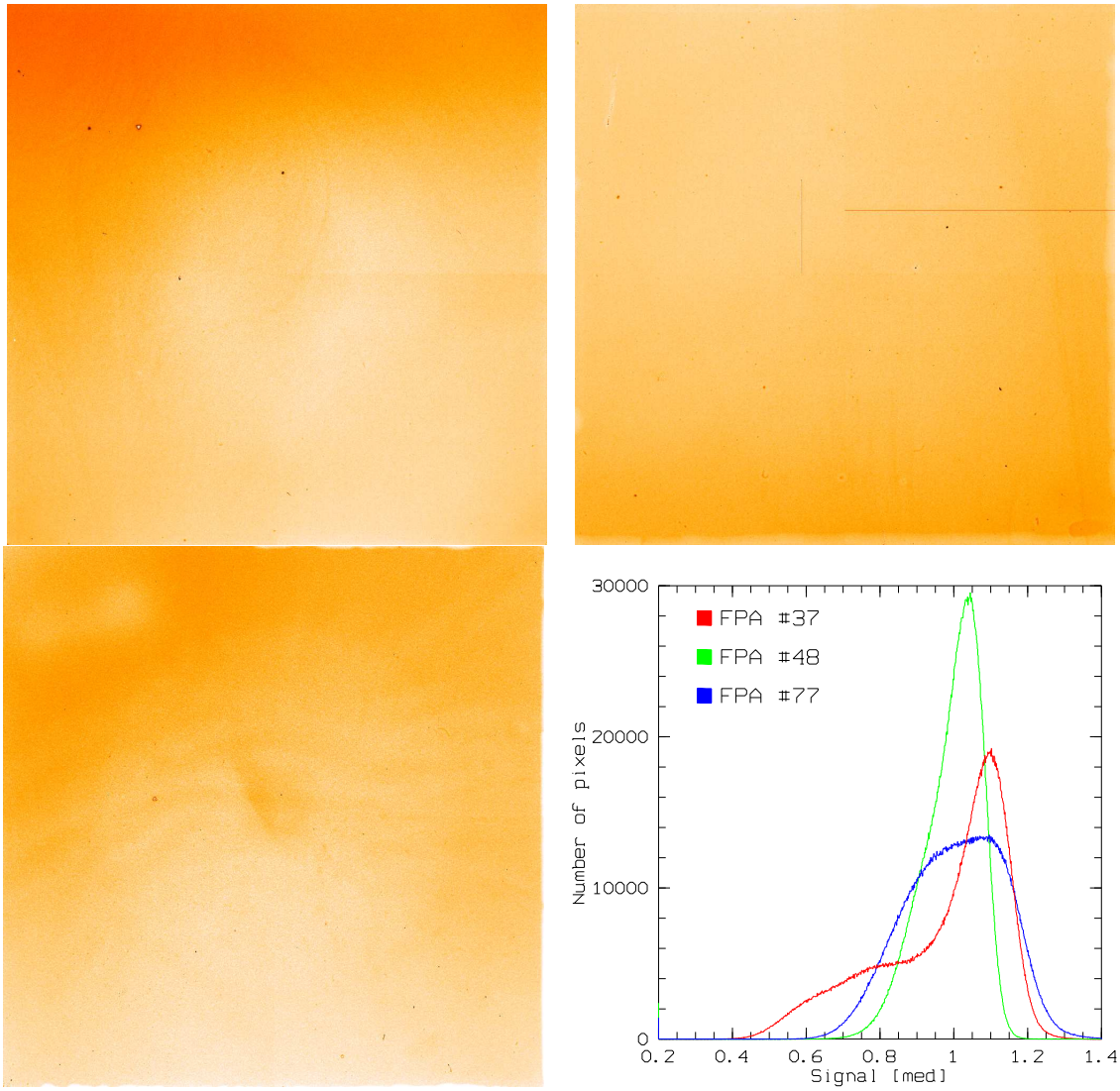

Figure 4.7: Flatfield images of FPA #37 (upper-left), #48 (upper-right) #77 (lower-left) taken with K filter and their histograms (lower-right)

ideal detector, by virtue of the Eq. (4.2), is given by

$$S/N_{ph} := s/\sigma_{ph} = n/\sqrt{n} = \sqrt{n} \tag{4.18}$$

where n is the number of the incident photons. A real image sensor has other noise sources, such as the dark current, reset, and readout noise, all of which decrease the theoretical S/N. The *Detective Quantum Efficiency* (DQE) of a real detector is defined as the square of the ratio of two S/Ns, the S/N of the output singal S/N_{out}, and that of the input radiation S/N_{in},

$$DQE := \left(\frac{S/N_{out}}{S/N_{in}}\right)^2 = \left(\frac{S/N}{S/N_{ph}}\right)^2 \tag{4.19}$$

which measures the effectivity of a real image sensor relative to that of idealized, noiseless photon-detecting system. If a calibrated IR source is used to adjust the incident flux, then the photon shot noise S/N_{ph} is also given and the average DQE can be calculated by measuring the S/N of the output signal.

Since the European Space Observatory (ESO) is determined the wavelength dependency of the RQE of the HAWAII-2 family. The quantum efficiency in the measurements was obtained by varying the temperature of a blackbody and measuring the photon response of the detector for different levels of photon flux. The filter transmission curves used to derive the photon fluxes were also measured at 77 K, the operational tempererature of a HAWAII-2 detector. For the known photon flux with Poissonian noise statistics, S/N_{ph} could be derived. The photon transfer curves of HAWAII-2 imagers were also determined, which provided their readout noise floors and gains. The gains were used to convert the detector singal to electrons. The ratio of the measured singal to the readout noise provided the S/N of the output. In Fig. 4.8, the average RQE of each FPA was measured in J, H and K broad bands and more detailed wavelength dependence of the RQE measured by ESO, which are consistent with the histograms

The average RQE given here is only an integrated value of the RQE distribution over the whole HAWAII-2 arrays. In order to obtain a more detailed characterization of quantum efficiency over the full pixel arrays, DQE maps have to be created for the NIR broad bands. Perhaps the most effective technique for mapping the DQE is to apply celestial signal sources. The OMEGA2000 camera needs only to scan a specified field containing many calibrated sources in a fine grid of pointings, i.e., with small offsets for each NIR filter, and the variation of these sources over the series of frames taken with different pointings can be used to create a high resolution DQE map over the whole detector area in each band. Since a detailed DQE map needs to have a great number of frames, the observations for this purpose demand a large amount of telescope time in nights when the weather allows for photometric observations.

4.2 Dark current

Dark current in image sensors is the result of imperfections and impurities occurring in the bulk material or at the Si-SiO_2 interface of the detector. These defects produce energy levels in the forbidden gap of the semiconductor which can be filled by thermally excited valence electrons. From this intermediate state the electrons with enough thermal energy jump to the

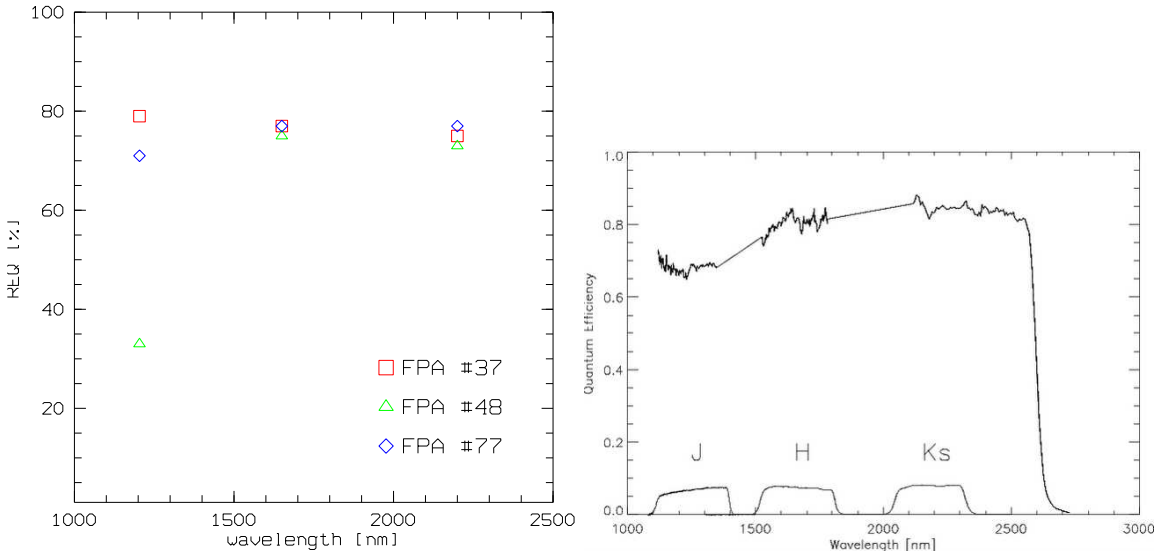

Figure 4.8: The left hand panel shows the average RQE in J, H, and K bands for the HAWAII-2 FPAs #37, #48, and #77 measured by Rockwell. The right hand panel displays the RQE vs. wavelength plot of a HAWAII-2 imager reported by ESO (Finger, 2002).

conductive band and produce a measurable signal in the well of the unit cells even in absence of illumination. The dark current due to the thermal excitation of the electrons located in the valence band strongly depends on the temperature of the detector,

$$I_{dark} = \text{const} \cdot A \cdot I_{300K} \cdot T^{1.5} \cdot e^{-\frac{Eg(T)}{2kT}} \quad , \qquad [e^-/\text{pixel} \cdot \text{s}] \quad , \tag{4.20}$$

where A is the pixel area in cm^2, I_{300K} the reference dark current measured at 300K (nA/cm^2), and E_g is the band gap energy at temperature T. The band gap energy can also be expressed in terms of the cut-off frequency λ_c of the detector material

$$E_g = \frac{hc}{\lambda_c} \quad , \qquad \text{or} \qquad E_g(eV) = \frac{1.24}{\lambda_c(\mu m)} \quad . \tag{4.21}$$

There is an empirical expression for the energy band gap of $Hg_{1-x}Cd_xTe$ as a fit function of temperature and the mol fraction x,

$$E_g(eV) = -0.302 + 1.93x + 5.35 \cdot 10^{-4}T(1-2x) - 0.81x^2 + 0.832x^3 \quad , \tag{4.22}$$

which is valid over the full composition range and for temperatures from 4.2 to 300K (Hansen et al. 1982). Therefore, the band-gap energy and in turn the cut-off wavelength can be adjusted by controlling the mol fraction of Hg and Cd, as mentioned in the previous chapter. For the HAWAII-2 chip the cut-off wavelength λ_c is 2.5 μm, which needs a band-gap energy of 0.496 eV. According to the empirical formula, the mol fraction $x = 0.458$ provides the required energy band gap at 77 K, the operational temperature of the HAWAII-2 FPA. At $\lambda_c = 2.5$ μm the energy gap of the HgTeCd semiconductor does not exhibit strong temperature dependence, hence E_g can be considered at constant band-gap wavelength (Hodapp et al. 1995). At lower temperatures and longer cut-off wavelengths the tunneling currents between defect states and the

HgTeCd valence and conduction bands increase with decreasing temperature according to the temperature dependence of the HgTeCd band-gap. The tunneling current has, in fact, relatively weak temperature dependence but it depends on bias voltage strongly. Nevertheless, the cut-off wavelength of the HAWAII-2 FPA is relatively short and any changing in the bias voltage does not really effect the contribution of tunneling current to total amount of dark current.

In this section we discuss both the temporal and spatial noise associated with dark current. The dark current shot noise, as a random and temporal noise, is negligible for the HAWAII-2 FPA and will be considered briefly. Then we characterize the dark current non-uniformity for the three HAWAII-2 chips. We present the measurements of the dark current statistics for each FPA and explain how to eliminate the contribution of dark current in the frames.

4.2.1 Dark current shot noise

Shot noise arises not only from the photon statistics but also from the presence of thermal electrons within the depletion region. The dark current shot noise also has Poisson statistics, so its amount can be expressed as

$$\sigma_{dark} = \sqrt{n_{dark}} \ , \tag{4.23}$$

where n_{dark} is the integrated dark current over a give time and measured in electrons. It is a temporal noise and averaging of more frames can reduce this effect. As will be seen in this section, the mean dark current of each specimen of HAWAII-2 FPA is about 0.03-0.04 e^-/s which gives σ_{dark}=0.17-0.20 e^-/s. These values are less then one ADU and much smaller than the net current from other noise sources, therefore the shot noise arisen from the statistical fluctuation in the dark current is negligible for integration times on the order of 10 s..

4.2.2 Dark current non-uniformity

On account of the variation in the physical properties of the unit cells, the same thermal energy excites valence electrons in the semi-conductor layer, producing varying amounts of dark current in each pixel. This dark current non-uniformity, due to the global variation of the physical properties of the individual unit cells, has a fixed spatial variation. In other words, the fixed pattern noise is the same in all the frames and can be eliminated by subtracting a dark reference frame from the illuminated image if both of them are taken with same exposure time and at the same temperature. Of course, this method has as an expense that subtraction of two images increases the dark current shot noise by factor of $\sqrt{2}$ and the readout noise.

The left hand panel of Fig. 4.9 shows the dark current histograms for HAWAII-2 FPAs #37, #48, and #77, measured by the Rockwell company. We also present the statistical momenta of the dark current characteristics of these detectors in Tab. 4.4. The dark current of these detectors is reported to be only about 0.02 e^-/s at 77 K (Hodapp et al., 1995) and the median values of the dark current provided by Rockwell for these specimen are in the interval 0.03-0.04 e^-/s, i.e., they are a factor of 1.5-2 larger than the specified value. However, these detectors still have negligible dark currrent contribution for integration times of 1-5 sec, which are in the range of the typical exposure times for scientific imaging. We also determined the dark current statistics for these HAWAII-2 chips under the control of the readout electronics of OMEGA2000. We took

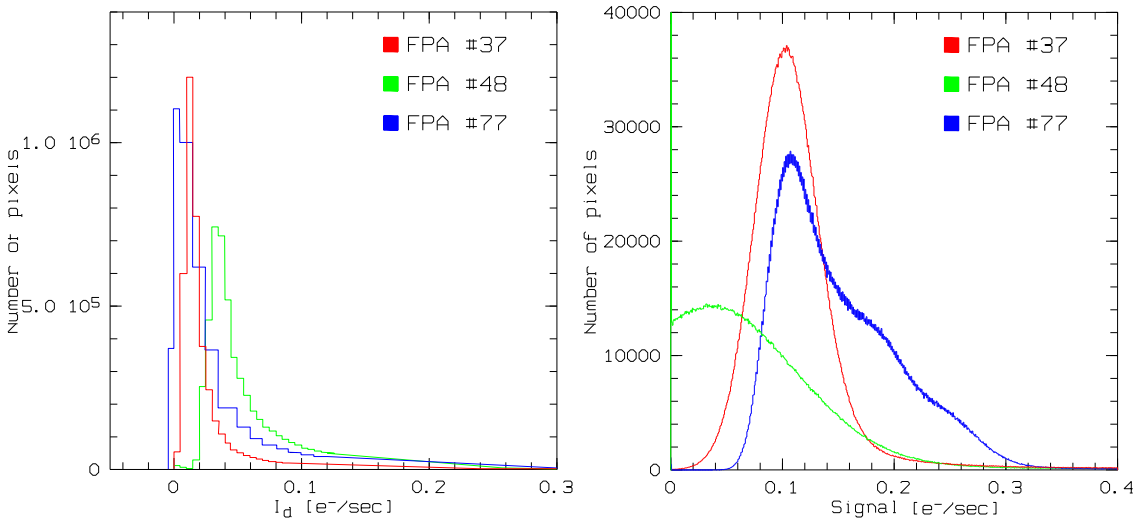

Figure 4.9: The left hand panel shows the dark current characteristics of the HAWAII-2 FPA #37, #48, and #77, measured by the Rockwell company. The right hand panel shows the histograms of dark frames taken with the detectors #37, #48, and #77 installed in the OMEGA2000 camera.

FPA No.	Min. value (e^-/sec)	Max. value (e^-/sec)	Mean value (e^-/sec)	Median value (e^-/sec)	Std. dev. (e^-/sec)
#37	0.000	1.000	0.035	-	0.065
#48	0.000	1.000	0.059	0.043	0.065
#77	-0.50	1.000	0.050	0.032	0.075

Table 4.4: Dark current statistics of the HAWAII-2 FPAs #37, #48, and #77 measured by the Rockwell company.

FPA No.	Min. value (e^-/s)	Max. value (e^-/s)	Mean value (e^-/s)	Median value (e^-/s)	Std. dev. (e^-/s)
#37	-1.11	1.09	0.163	0.15	0.21
#48	0.000	3.35	0.069	0.212	0.075
#77	-4.71	1.22	0.191	0.087	0.09

Table 4.5: Dark current statistics of the HAWAII-2 FPAs #37, #48, and #77 measured by MPIA.

dark frames for each HAWAII-2 imager with different integration times from the minimal frame readout times up to 2000 s by using a blank disk inserted in the filter wheel. As an example, Fig. 4.10 shows a dark frame of the FPA #48, which demonstrates the high uniformity of the dark current generated in the HAWAII-2 detector family. In the color coded figure, the areas with lowest measured counts are represented with dark blue color, while the lighter colors indicate the highest pixel values. The most prominent features are the glowing output transistors of each channel at the borders of the of the pixel array and the group of hot pixels with a dead core in the upper left quadrant. Aside from these artifacts, the dark current has a rather uniform characteristic over the whole array. The histograms of the dark frames, shown in the left hand panel in Fig. 4.9, have different characteristics from the ones specified by the Rockwell company. This is demonstrated with the statistical momenta of the distribution of the measured signal as well, which we present in Tab. 4.5. The median values we measured for the three detectors were one order of magnitude higher than the specified values and the distribution of the dark current histograms are broader than those measured by the Rockwell company. With the median value of dark current of 0.03-0.04 e^-/s for these detectors, the median of the dark signal with the integration time of 2000 s is expected to be 60-80 e^-. However, the median values in the dark frame histograms of each FPA were normally measured to 200 e^- for the integration time of 2000 s. This means the the dark signal of the image sensor was completely dominated by other noise sources (Fig. 4.9). Besides the non-uniformities of dark current, the individual channels building up the quadrant structure were also well discernible due to slightly different offset voltages in amplifier circuits. Other typical noise features were the periodic noise patterns over all the frame caused by a coupling between the pre-amplifiers and the power supply and the glowing of the output transistors. The glowing gave only a small excess on the right wing of dark frame histograms and did not change their mean values, which were determined by the noise of the external amplifiers. In fact, it is possible to eliminate their thermal radiation by switching the output transistors of the HAWAII-2 FPA off during the integration time but a more stable operation of the chip can be ensured without switching the transistors off and on in each readout cycle. The glowing for exposure times of some minutes is small and it can easily be subtracted from the video signal.

There are two basic methods for the subtraction of the dark frame from the raw images. If the exposure time is fixed, it is enough to take a series of dark frames with the same integration time as the scientific frames, average them to reduce the dark current shot noise and the result can be subtracted from the image frames. For raw frames taken with different exposure times, it may be more convenient to produce a *thermal frame* from a stack of dark frames with different

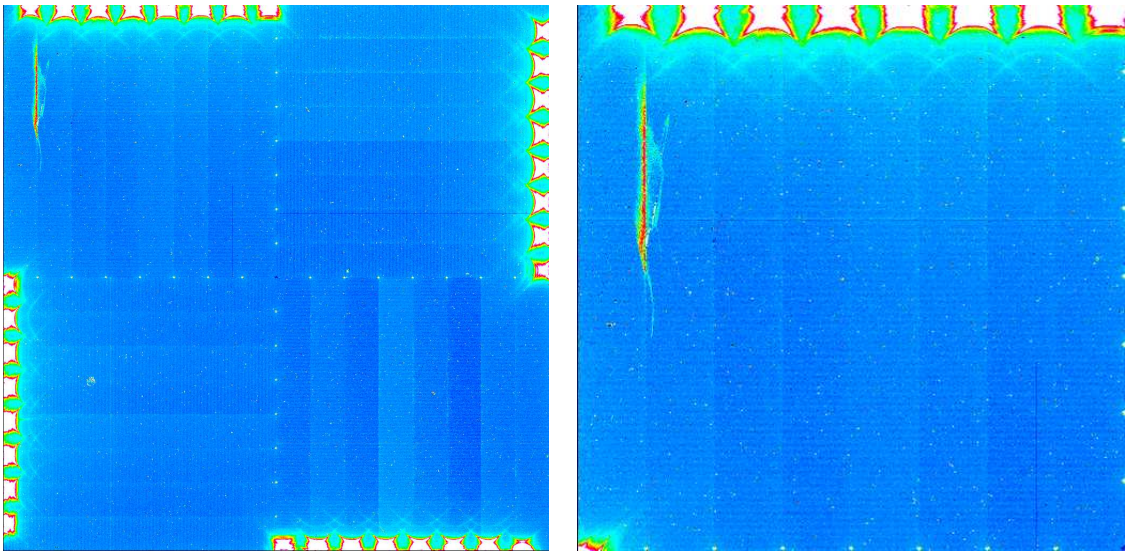

Figure 4.10: A dark frame of the FPA #48 taken with an integration time of 320 s. The left hand panel shows the whole array whereas the right hand one displays the upper left quadrant. The glowing of the eight output transistors can be seen in all the quadrants.

integration times. Since the signal measured in healthy pixels is proportional to the integration time, we can make a linear fit on the series of pixel values of each good pixel in the stack of frames. Then we can produce a map by taking the slope of the linear fit for each pixel. This map is the *thermal frame* of the image sensor, which contains the distribution of its dark current in ADU/(pixel · s).

The linear fit fails for those pixels which exhibit a highly non-linear response to the illuniation. The signal of these pixels will have a large scatter around the linear fit and they can be clipped out from the thermal frame by defining a threshold of the scatter, as we will discuss in the next section. The more dark frames we use for fitting, the more efficiently the dark current shot noise is suppressed in this map as in the case of the averaging dark frames. Then the thermal frame can be scaled according to the different exposure times of the raw images and subtracted from them. For the data reduction in the scientific applications thermal frames were used, which will be described in the next chapter.

4.3 Bad and hot pixels

In scientific-grade imagers the dark current is low and more or less uniform but some photo-sites, called *hot pixels*, always produce a dark current of some orders of magnitude higher than the average value. They are represented by the wider right wing of the dark current histogram in Fig. 4.9. Although the rate of accumulation of the thermal electrons in these photo-sites is much higher than the one of other pixels, it is constant in time. This means the hot pixels have also a linear response, which allows us to subtract the dark level from the photo signal as in the case of the normal pixels. Nevertheless, every image sensor contains a few photo-sites which have a highly non-linear response. They are considered to be *dead* or *bad pixels* because their non-linear behavior prevents us from subtracting the dark level correctly from the photo signal. Hot pixels

scatter in the array of the photo-sites individually or form groups but individual bad pixels are very rare and they compose particularly the cores of hot pixel groups. Sometimes a complete column or line of a quadrant is also dead. These features appear in a typical bias subtracted dark frame of a HAWAII-2 chip taken with long integration time at 77K. The upper left quadrant in Fig. 4.10, there is a large group of hot pixels with dead cores and all the quadrants contain some bad columns and lines.

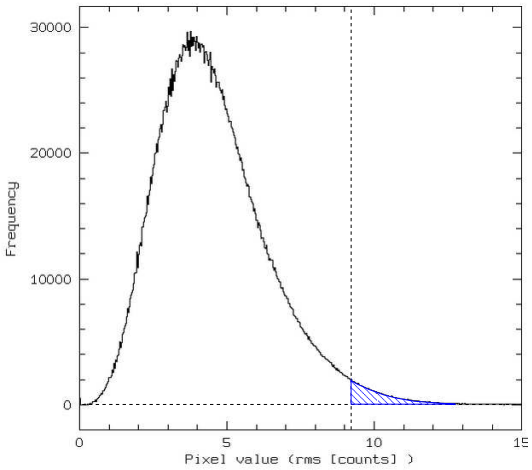

Figure 4.11: The histogram of RMS map calculated form the the fitting of a stack of dark frames taken different integration times for the HAWAII-2 FPA #48. The vertical dashed line denotes the upper limit of the RMS value above which the pixels are defined to be bad pixels. The latter are represented by the blue shaded area of histogram.

Besides the dark current subtraction, the thermal frames of the detectors also served to separate bad pixels from healthy ones. For each pixel in a stack of dark frames taken with different integration times, a root mean square map of the deviation from the values in the scaled thermal frames can be computed. Since a thermal frame is the result of a linear fitting, an RMS map contains the scattering of the signal values around the scaled fit. Its histogram at high values represents the pixels for which the linear fitting failed because of their highly non-linear response, so the map helps to discriminate the bad pixels from the hot and the normal ones. The histogram of the RMS map contains a well pronounced peak of the healthy pixels (Fig. 4.11). The wing of the peak at the right hand side is less steep because the major part of it represents the hot pixels. By defining an upper and lower limit in the histogram so that the chosen interval contains the peak and the wing representing the hot pixels, the pixels which have RMS values out of this interval can be considered as bad ones. The bad pixel masks created by using this method contained about 1000, 3600 and 5000 bad pixels for FPA #37, #48 and #77, respectively. This means more than 99.8% of the pixels could be corrected by dark current subtraction and flatfielding for all the three detectors.

4.4 Linearity

Besides the map containing the slope of the linear fitting, it is also useful to create another one with the additive constant of the fitting and third one with the root mean square describing the

scattering of the pixel values around the fit line. These maps together characterize the linearity of response of the photo-sites satisfactorily and provide a simple method to separate the bad pixels from the healthy ones. The histograms of the slope and the constant maps have a peak representing the great number of well-behaving pixels. Its tails at the left and right hand side consist of the cold, hot and bad pixels. The histogram of the RMS map also has a similar shape but its tail at high values contains only the pixels with very non-linear responses. Therefore this map can be used to estimate the number of pixels which still have a linear response. However, the saturation of the unit cells at high gives a limit, which determines the linear dynamical range of image sensors.

The linearity of the HAWAII-2 detectors is measured by taking flatfields with different integration times and constant illumination through a narrow band filter (NB1083). Since the dark current of the HAWAII-2 chips is very low and the maximal exposure time was 2000 s, the dark current contribution had a negligible effect on the measured signal. We measured the non linearity of the signal with increasing exposure time, i.e., the deviation of the signal value from the linearly scaled values with time. All of the detectors #37, #48 and #77 were linear within 1% of the signal up to about 40000 ADU, which means the linear full well capacity of each FPA is $\sim 200000\ e^-$ (Fig. 4.12).

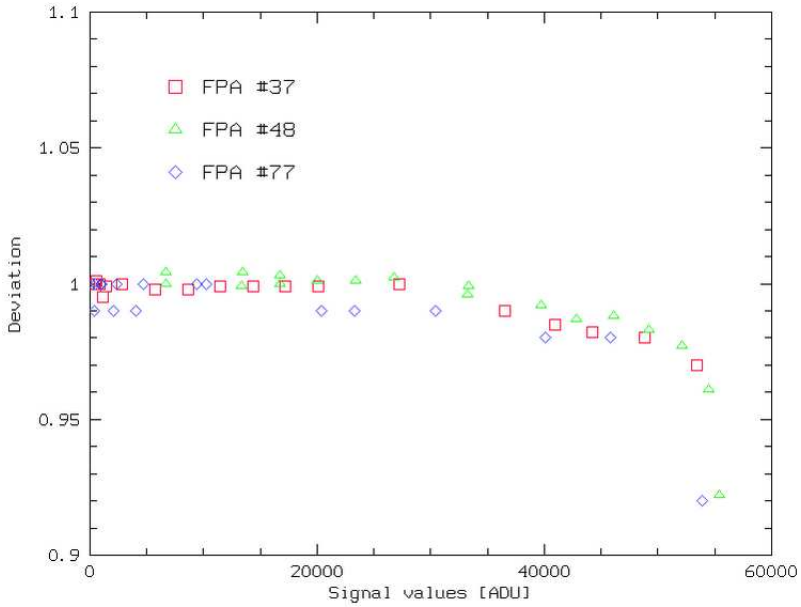

Figure 4.12: Linearity tests for the three HAWAII-2 FPAs.

Part II

Using OMEGA2000 for the MANOS Deep Field Survey

Chapter 5

The MANOS Deep Field Galaxy Survey: COMBO-17+4 NIR

Observational cosmology is a study of all the astrophysical phenomena using astronomical instruments which are relevant for developing and testing theoretical models on the origin, structure and evolution of the Universe. Some of these phenomena, such as the matter distribution in large co-moving volumes or the patterns in the cosmic background radiations, indicate that, although our space-time can be considered homogeneous and isotropic above length scales of about 100 Mpc, at lower distances the structure of matter exhibits a hierarchical clustering. It constitutes galaxies, clusters of galaxies and clusters of galaxy clusters, so called super-clusters. If we consider galaxies as the fundamental building blocks of this hierarchy, it is obvious that the studying of the formation and subsequent evolution of galaxies is essential in understanding the organization of the matter in the Universe. For the last ten years, several extragalactic surveys have aimed to obtain a comprehensive statistical description of the physical properties observed in the galaxy samples. Two of them, the CADIS (Calar Alto Deep Image Survey) and the COMBO-17 survey ("Classifying Objects by Medium-Band Observations in 17 Filters"), were projects at MPIA and their results served as a basis to start a new extragalactic survey. This new project, called MANOS (**M**PI**A** **N**IR-**O**ptical **S**urvey), is the extension of the wavelength range beyond that of the old surveys from optical to the near infrared, combining a relatively deep field survey, the MANOS Deep or COMBO-17+4 NIR, with a shallower but much wider cluster survey, MANOS Wide or the HIROCS (Röser et al., 2003). The near infrared data is provided by the OMEGA2000 instrument for both the MANOS Deep and MANOS Wide surveys. From these two sub-projects, the COMBO-17+4 NIR deep field galaxy survey was chosen as an astrophysical application of the NIR wide field imager OMEGA2000, presented in the second part of the thesis. However, technical difficulties and bad weather prevented us from obtaining the complete NIR data set for the deep field survey. Hence, we restrict the discussion of the MANOS-deep project to a description of the improvements due to the extension of the wavelength regime to the NIR bands and make a case study on luminous infrared objects. The second part of the thesis compares the results based on the optical COMBO-17 data set with the NIR supplemented data. It consists of two chapters. In the first chapter, we describe the COMBO-17+4 NIR project and then present the preliminary scientific results of this galaxy survey. We start with a short overview on the COMBO-17 project by discussing the basic concepts along

Field	α_{J2000}	δ_{J2000}	l_{gal}	b_{gal}	E_{B-V}
CDFS	$03^h32^m25^s$	$-27°48'50''$	$223°.58$	$-54°.45$	0.01
A 901	$09^h56^m17^s$	$-10°01'00''$	$248°.04$	$+33°.59$	0.06
S 11	$11^h42^m58^s$	$-01°42'50''$	$270°.45$	$+56°.78$	0.02
SGP	$00^h45^m56^s$	$-29°35'15''$	$328°.80$	$-87°.26$	0.02
A 226	$01^h39^m00^s$	$-10°11'00''$	$183.60°.60$	$-77°.20$	0.02

Table 5.1: Positions and galactic reddening for the three COMBO-17 fields. Fields shown in bold face are already completed in optical regime.

with the observations, multi-color classification, and results and limitations of the survey. Then follow the details of the COMBO-17+4 NIR project, where we summarize the observation and describe the strategy of data reduction and photometry and the multi-color classification based on the NIR-band-extended data. The first chapter will be closed by an analysis of the survey from a technical viewpoint, comparing the results derived from the pure optical COMBO-17 and the COMBO-17+4 NIR data set.

5.1 The COMBO-17 Project

Traditionally, multi-color surveys applying broad-band photometry to obtain spectral information have only been used to search certain types of astronomical objects, e.g. high-redshift galaxies or AGNs, and always needed follow-up spectroscopy to specify the nature of these objects and measure their redshifts. The latest multi-color surveys carried out by MPIA, such as the CADIS or the COMBO-17 projects, are usually equipped with 15-20 filters, which allows them to sample the visual spectrum with a resolution comparable to that of low resolution spectroscopy. These deep field surveys can detect objects above high S/N (typically 10-σ limits) and measure their photometric redshifts accurately enough that follow-up spectroscopy is not needed for deriving sample properties, e.g. the clustering statistics or the galaxy luminosity functions. The COMBO-17 survey running since January 1999 has already covered 0.8 deg^2 of the sky and produced detailed statistics of the objects detected in that area. The aim of the COMBO-17 project was to provide precise photometric redshifts with an accuracy of $\sigma_{z,gal} \approx 0.03$ and $\sigma_{z,QSO} \lesssim 0.1$ based on 17 colors for a sample of $\sim 50,000$ galaxies and $\lesssim 1,000$ quasars. Its morphological and spectral data set is primarily intended for studies of gravitational lensing and evolution of galaxies and quasars. In this section we will give a short overview of the COMBO-17 project, describing the observation, photometry, multi-color classification, and results of this survey compared with that of other galaxy surveys. We close this section with a summary of the limitations of the COMBO-17 survey. These limitations were one of the factors which motivated the extension of the project to include a NIR band survey.

5.1.1 The COMBO-17 Survey

5.1.1.1 Observations

The COMBO-17 survey has produced multi-band data using 17 optical filters in three fields, the Chandra Deep Field South (CDFS) and the fields of the super-clusters Abell 901 and S 11. Another two, covering the super-cluster Abell 226 and the South Galactic Pole (SGP), are yet to be completed (Tab. 5.1.1.1). All five together cover an area of 1.4 deg^2 of the sky. The filter set applied for the survey consists of five broad-band filters ($uBVRI$) and 12 medium band filters covering the wavelength range between 400 and 930 nm (Fig. 5.1). All the observations were carried out with the Wide Field Imager (WFI) at the MPG/ESO 2.2-m telescope on La Silla, Chile. The total exposure time per field was about 160 ksec. The field of view of WFI is $34' \times 33'$ on an array of eight 2k×2k CCDs with about 67 million pixels altogether and a scale of $0''.238$/pixel. Observations and data analysis have been completed for three fields covering an area of 0.78 deg^2. A catalogue of about 200,000 sources was compiled as a result of the photometry with SExtractor on the deep, high-resolution R-band images of ~ 20 ksec exposure, which have 5σ point source limits of $R \approx 26$ (Vega mag.). The photometry of COMBO-17 is based on this R-band selected source catalogue.

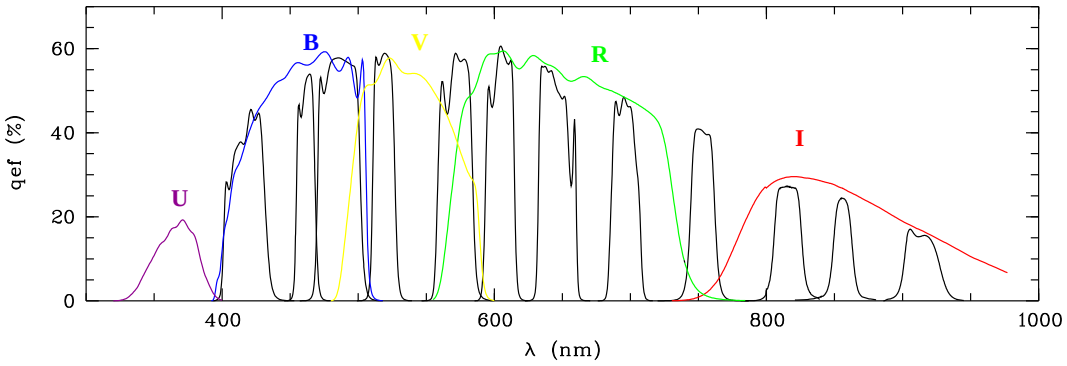

Figure 5.1: COMBO-17 filter set: Total system efficiencies are shown in the COMBO-17 pass-bands, including two telecope mirrors, WFI instrument, CCD detector and average La Silla atmosphere. Combining all observations provides a low-resolution spectrum for all objects in the field (In Wolf et al. 2003).

5.1.1.2 Photometry

The photometry of COMBO-17 sources from the R-band selected catalog was obtained in the 17 bands by projecting the object coordinates into the frames of reference of each image and measuring the fluxes at the locations of objects. The seeing variation during the observations is a typical problem for ground-based telescopes, hence the measured fluxes must be corrected so as to avoid color offsets. Instead of the flux correction, the seeing-adaptive weighted aperture photometry is used in the COMBO-17 survey, as implemented in the package MPIAPHOT (Röser & Meisenheimer 1991). The method first determines the Point Spread Functions (PSF) of stars on each individual input frame and smoothes them with a Gaussian of a FWHM corresponding to an effective PSF of $1''.5$ diameter. This technique, providing a common effective PSF of $1''.5$

diameter for all the frames in all bands, guarantees that always the same fraction of the light distribution of an object is probed in the measurement of its central surface brightness in an aperture of $\sim 1''$ diameter. Therefore, it represents a measurement of the peak brightness in an aperture of $\sim 1''$ diameter in $1''.5$ seeing for all objects.

The photometric calibration is based on a system of faint standard stars in COMBO-17 fields, which were established by spectrophotometric calibration with respect to spectrophotometric standard stars in photometric nights.

5.1.2 Multi-color Classification

We give a short overview on the multi-color classification, deriving some astrophysical properties of the detected objects in the COMBO-17 fields. We then discuss the library of the model spectra applied in the classification for different classes of celestial objects.

5.1.2.1 Classification Scheme

Multi-color surveys provide fluxes and colors on objects measured in different filters together with their morphology. All the astrophysical information (like redshift, spectral energy distribution, dust extinction etc.) are extracted from these data. The method applied for extracting this information is the multi-color classification of the detected sources. Here, we give a brief summary on the scheme of this classification method and describe its implementation in the COMBO-17 survey.

The multi-color classification scheme essentially compares the observed colors of each object with a color library of known objects. Objects are classified by locating them in the n-dimensional color space and comparing the probability for each class. Given the photometric error ellipsoid in the color space, each library object can be assigned a probability to cause an observation of the measured colors. For a whole class, this probability is assumed to be the average value of the individual class members, resulting in relative likelihoods for each object to belong to the various classes. The scheme assigns to an object the class which provides the largest sum over all probabilities for each members within that class (see details in Wolf et al., 2001).

The reason the classification method of the COMBO-17 uses local color indices as input rather than fluxes themselves is that the influence of the overall flux normalization is minimized in this way and the color-based classification still has the same performance as a flux based algorithm for the case of high S/N.

The classes for the multi-color surveys are defined as the classes of galaxies, stars, and quasars and the task of the classification in the COMBO-17 survey is to sort the objects in the R-band source catalog into these classes by using their measured colors. Besides the colors, morphological information is also available for galaxies but it is only used to estimate their total flux. The internal structure of each object class is spanned by its individual parameter set, which consist of the redshift, spectral energy distribution (SED), and the extinction for galaxies and quasars.

The COMBO-17 survey applies five broad bands, $uBVRI$, and as well as observations in 12 medium bands, which together give a low resolution spectra of the observed sources. Two sets of color indices are calculated from the measured fluxes. The first set consists of the colors derived from only the broad bands which were neighboring one another on the wavelength axis, ($u - B$,

$B-V$, $V-R$, and $R-I$), while the second one contains the colors combined from a broad band (taken as a base filter) and some medium bands most nearby it in terms of wavelength. These color definitions allow the classifier to apply the deep broad bands to fit the global shape of predefined spectral templates, then use a few groups of medium bands around each deep broad band to fit the smaller-scale shape of the model spectra.

As a result of the spectral template fitting for each class member, a likelihood function, depending on redshift z, a spectral energy distribution and a flux normalization parameter, will be calculated from the squared photometric distance between the observation and the model in the color space. The likelihood function gives the probability that the spectral energy distribution of a source producing the measured colors can be best represented by a given spectral template. The classifier sorts the sources into classes which provides the largest sum over all probabilities for each spectral fit within that class. The choice of the best spectral template fit for a given object in the source catalog is based on the minimization of the χ^2-parameter derived from the squared photometric distance. Such a simple χ^2-minimization prevents unreliable assignments of any class when it has only one well matching template with a high probability value but all its other templates fit very poorly. Therefore the choice of spectral templates is very important for an unambiguous classification and a correct parameter estimation.

5.1.2.2 The Classification Libraries

The spectral templates are organized in libraries, which contain star, galaxy and quasar templates for sorting the objects into these three classes. The libraries are expected to contain a representative variety of objects covering a complete class. The classes cover as many odd members as possible but there is a trade-off between classifying the odd ones right and introducing more spatial overlap between the classes, i.e, causing more confusion among normal objects. The spectral libraries employed in the COMBO-17 multi-color classification are based both on observations and model calculations. In this passage we describe briefly the latest version of these libraries.

The star library was compiled from the UK spectra of the Pickles catalogue (1998 PASP 110, 863). It contains 96 stars of spectral types F,G,K and M having luminosity classes I to V from the spectral atlas of Pickles. In addition to the original library derived from the catalogue, template spectra of white dwarfs, subdwarfs, and blue horizontal branch stars are also included. Since the atlas is not structured as a regular grid in stellar parameters, the resulting color library is also unsorted set without internal structure.

The galaxy library used in the COMBO-17 multi-color classification contains a sequence of model spectra calculated with the stellar population synthesis code PEGASE (Fioc & Rocca-Volmerange 1997). The sequence of spectral templates spans a two dimensional grid with a range of ages and a range of extinction levels. The input parameters of the PEGASE code are chosen as suggested by simple star population models with a Kroupa (1993) IMF, an initial metallicity of 0.01 dex, and no extinction. The star formation rate (SFR) follows an exponential decline with a timescale of τ =1 Gyr. The SEDs are calculated by PEGASE for various time steps since the beginning of the first star formation. As templates, a sequence of spectra for galaxies is used with 60 logarithmically spaced ages, i.e., elapsed time since onset of star formation, form

50 Myr to 15 Gyr. These templates cover typical local galaxy SEDs from elliptical galaxies to starbursts and their scale form 0 to 59 can be mapped onto the Kinney et al. (1996) templates used in the older version of the galaxy library. The extinction is applied afterwards as a screen following the SMC law from the 3-component model by Pei (1992) with six equidistant levels of $E_{B-V} = [0.0, 0.1, \ldots 0.5]$. With $R_V \sim 3$ for the SMC law, the color excess A_V has values in the interval $[0 - 1.5]$ of the extinction given in V-band magnitudes. The redshift range $0.0 \leq z \leq 1.4$ of the templates is covered by 177 steps with a 0.005 resolution on a $\log(1 + z)$ scale.

5.1.3 Scientific Results of COMBO-17 and Other Deep Field Surveys

The COMBO-17 survey produced a very deep imaging over an area approaching 1 deg^2, reduced field-to-field variations. It allowed the survey to give a comprehensive picture about the galaxy formation and evolution in the last half of the age of Universe. As a result, the COMBO-17 galaxy survey derived a detailed statistics on the redshift evolution of the galaxy number density and luminosity function, which provide strong constraints on the evolution of galaxies and mean efficient tests of galaxy formation models (Wolf et al. 2003).

Since the survey sample was divided into four classes via the parameter of the galaxy spectral templates used in the multi-color classification, i.e., a fixed, present-day spectral sequence for galaxies from ellipticals to starburst, all the results are phrased in terms of these four spectral types. These are the early-type galaxies, defined as redder than a present-day reference Sa spectrum, the galaxies resembling present-day Sa-to Sbc-colors, the galaxies with SEDs similar to the present-day spectral templates between Sbc-SB6, and starburst galaxies (SB6-SB1). The survey established that the luminosity function (LF) depends strongly on the spectral energy distribution (SED) of galaxies at all redshift covered. Although the shape of the LF is similar for all spectral types, the characteristic luminosity above which the number of galaxies falls sharply is different. There is a steep increase in the number density of the early-type galaxies by factor of 10 towards low redshifts from $z = 1.1$ and by a factor of 4 in their contribution to the co-moving r-band luminosity density j_r. The starburst galaxies decrease towards low redshift both in luminosity and density, and by a factor of 4 in their contribution in j_r, while these quantities for the second (Sa-Sbc) and third (Sbc-SB6) classes of galaxies do not vary much with redshift. The COMBO-17 survey also provided more precise constraints for the trend of the global star formation rate (SFR) in the Universe. Although the survey measured a SFR declining by the order of five to ten from $z \sim 1$ to now, it appears gentler compared to the result of CDFS, where near-UV luminosity density used as a tracer for young stellar population, is found to drop by a factor of five from $z \sim 1$ to now. These findings confirm earlier results that the epoch of galaxy formation, or star formation of galaxies, has been declining over the last half of the cosmic evolution with a strong decrease of starburst galaxies and a similar emergence of older galaxies, whose SED is redder than an Sa template spectrum.

However, the multi-color classification of COMBO-17 is based on a set of non-evolving templates, which are not well suited to early spectral types and particularly at visible wavelengths, where passive evolution results in significant color evolution. The non-evolving spectral types correspond to constant rest-frame color cuts at all redshifts, where the early types galaxies have the colors of present day luminous elliptical and lenticular galaxies, but are significantly redder

than the reddest galaxies at higher redshifts. Therefore, the fact that these galaxies are extremely rear in the distant Universe and exhibit a rapid evolution in the luminosity density is due mainly to the passive evolution of their colors. Bell et al. (2004), using the COMBO-17 survey to derive evolving luminosity functions, separated the galaxy population into blue and red components on the basis of an empirically determined color distribution. The red field population shows a color-magnitude trend similar to the that seen in clusters, and this red sequence evolves as expected from passive evolution. They found little evolution in the red galaxy LF, particularly at the bright end and showed that the large decline in the number of red galaxies as reported by Wolf et al. (2003) is heavily influenced by passive evolution in the colors of the earliest spectral types. As a consequence of the usage of the color based definition for the red sequence instead of the one based on non-evolving spectral templates for the early type galaxies, the result stating that galaxies redder than a fixed threshold have a rapidly evolving luminosity density from $z \sim 1$ to now is consistent with the statement of a roughly non-evolving rest-frame B-band luminosity density in the red-sequence galaxies.

This picture on the passive color evolution of the red sequence is confirmed in other surveys as well. Lilly et al. (1995), studying the evolution in the LF of galaxies with colors redder than a present-day Sbc galaxy, also measured very little evolution but they had large uncertainties from small number statistics and cosmic variance. Pozzetti et al. (2003) used the K20 spectroscopic sample to derive J- and K-band LFs for galaxies and estimated the evolution of the red galaxies out to ~ 1. They found mild evolution in the number of the luminous red galaxies to the highest redshifts, implying that the space density of these systems has declined in a limited extent. Chen et al. (2003) in the Las Campanas Infrared Survey derived the rest-frame R-band co-moving luminosity density of the E/S0 and Sa galaxy population and found that the early-type galaxies exhibit only moderate evolution with redshift. It was at most a factor of two in red galaxy density, so the passive evolution of this sample cannot be ruled out. According to these results there appears to be a consensus that the LFs of the red galaxies show little apparent evolution to $z \sim 5$, which is in some disagreement with the predictions of hierarchical merging models for galaxy formation and evolution.

Besides the LF and the co-moving luminosity density, the mass evolution of the stellar content of galaxies is also a useful ingredient in the studies of the galaxy evolution because it provides a key gauge of the process of galaxy building and imposes a constraint on models of the cosmic star-formation history, the synthesis of heavy elements, and merger rates. In the COMBO-17 analysis of the red sequence, Bell et al. (2003) obtained a modest evolution in M/L (about a factor of 2) since $z \sim 1$ and from this they inferred an increase in the total stellar mass in red galaxies since $z \sim 1$ by a similar amount. Rudnick et al. (2003) measured the mass evolution in the red sample of the Faint IR Extragalactic Survey (FIRES) and concluded that there has been a factor of ~ 3 growth in the stellar mass of galaxies since $z \sim 2.5$. A more dramatic increase in stellar-mass density since $z \sim 3$ was found in the Hubble Deep Field Data (HDF) by Dickinson et al. (2003), measuring only 3-14% of the present density at $z \sim 2.7$.

At $z \gtrsim 1$ the difference between the stellar masses of elliptical galaxy progenitors in the hierarchical and monolithic collapse models becomes substantial. At sufficiently large redshifts there should be few or no massive red galaxies in the hierarchical models since these models

predict both a decline in the total stellar-mass density to high redshift and a decline in the maximum mass observed in galaxies. The analysis of stellar-mass evolution for the COMBO-17 galaxy sample, together with the results obtained from the FIRES and HDF samples, confirmed the latter model. The increase of the stellar mass in the red sequence since $z \sim 1$ is consistent with the rate expected from the hierarchical build-up of stellar mass via galaxy mergers in a ΛCDM Universe.

5.1.4 Limitations of the COMBO-17 Survey

As a main result of the COMBO-17 project, redshifts for $\sim 25,000$ galaxies with $R \lesssim 24$ were determined together with their SED classifications in three independent fields of 0.26 deg^2 each. The redshifts are derived from high-precision photometric redshift estimates using the multi-color method with 17 filters. However, the filter set employed in the COMBO-17 survey lies entirely in the optical regime and this restricts the results of the survey for various reasons.

The first problem is the limitation of the available redshift range for the optical survey. Since the multi-color method for the reliable redshift determination requires at least 2 filters placed longwards of the redshifted 4000 Å break, the second reddest filter of COMBO-17 centered at $\lambda_c = 865$nm restricts the maximal reliable redshift to $z \sim 1.1$.

The other restriction comes from the fact that galaxies containing a significant population of old stars at $z > 1$ become too faint in the optical regime to be measurable with optical filters alone. Their flux keeps rising into the NIR regime and we can measure them only with an extended filter set.

Considering these basic limitations, it is immediately clear how the COMBO-17 survey should be extended. In order to extend the redshift range, the existing optical data base of COMBO-17 should be supplemented with infrared data which are deep enough to detect a typical early-type galaxy at higher redshifts with comparable signal to noise ratio over the whole extended wavelength range. In fact, this was the main motivation for MPIA to start the MANOS project with its two parts, the deeper COMBO-17+4 NIR survey and a shalower HIROCS project.

5.2 The COMBO-17+4 NIR Project

In the previous section we gave a short overview on the COMBO-17 project and in this section we discuss the COMBO-17+4 NIR project extending this optical survey to the NIR regime. We start with some remarks on its motivation and we describe the details of the new project from the observations obtained with the OMEGA2000 camera in the NIR regime via the data reduction of the NIR data to the photometry of the optical+NIR data.

5.2.1 Motivations for COMBO-17+4 NIR Project

As discussed above, the main goal was to extend the range of reliable multi-color redshifts beyond the current limit of COMBO-17 survey, $z \simeq 1.1$. The NIR-band filter set of COMBO-17+4 NIR consists of three medium-band filters $Y(\lambda/\Delta\lambda = 1040/80\text{nm})$, $J_1(1190/130\text{nm})$, $J_2(1320/130\text{nm})$, and one broad-band filter, $H(1650/300\text{nm})$, covering the wavelength range between 1 μm and 1.8 μm (Fig. 5.2). The J_2 filter, centered on $\lambda_c = 1320$ nm, extends the

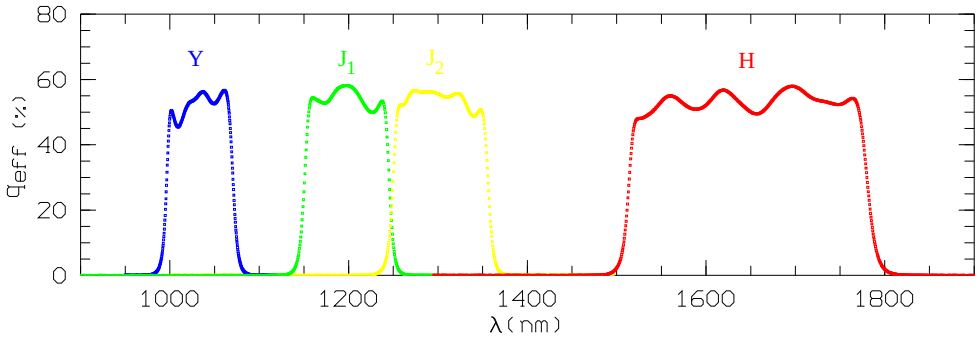

Figure 5.2: The NIR filter set of COMBO-17+4 NIR: Total system efficiencies are shown in the NIR passbands, including the telecope mirror, OMEGA2000 instrument, CCD detector, and average Calar Alto atmosphere.

available redshift range to $z \simeq 2.1$. From the results of COMBO-17, 1400 galaxies with $R \lesssim 24$ and $1.1 < z < 2$ are expected on average per survey field. About the same number of galaxies is expected at $R > 24$ in the extended redshift range for which the multi-color classification could derive reliable redshift from the combination of the optical and NIR data sets. Hence, the COMBO-17+4 NIR will provide a large sample of galaxies at $1 < z < 2$.

Besides this main motivation, there are other promising advantages of the supplement of the COMBO-17 data set in NIR regime. The first one is related to the improvement of the stellar mass estimation in galaxies. Back-tracing the assembly history of stars and determining the mass growth of the stellar component in galaxies are very important issues for studying galaxy evolution. Since the blue-band luminosity may depend on short burst of star formation, we need also information on old stellar populations containing most of the mass to obtain a comprehensive picture of the stellar evolution in galaxies. Even in the redshift range $0.7 \lesssim z < 1.1$, the old stars have a dominant contribution for galaxy spectra only in the NIR regime, hence the optical data cannot provide the best tracers of the old stellar component in galaxies. Therefore, the NIR filter combination introduced for COMBO-17+4 NIR will significantly improve the determination of the stellar mass in galaxies.

The extended wavelength range of the measurement between 700 nm and 1300 nm also covers the most interesting part of the spectra for Extremely Red Objects (EROs), which may help to answer the question of whether the extreme colors of these objects can be attributed to the dust-extinction in starburst galaxies or they are early-type galaxies dominated by an old stellar population.

The NIR-band filters of COMBO-17+4 NIR with the broad I-band filter seem useful for searching AGNs at redshits $z > 6.5$, but the survey area of 0.77 deg^2 may be too small to detect these rare objects. However, the photometry of COMBO-17+4 NIR data helps to measure the quasar rest-frame B-band luminosity function out to $z \simeq 2.6$ or the 250 nm rest-frame luminosity in the range $0.5 < z < 5.5$. This will be useful for studying the redshift evolution of AGNs in the Universe.

Besides the extra-galactic projects, the COMBO-17+4 NIR survey has prospects for the detection of extremely red stars (brown dwarfs), as a consequence of the improvement in the object classification due to inclusion of the NIR bands.

Field	α_{J2000}	δ_{J2000}	l_{gal}	b_{gal}	E_{B-V}
A 226	$01^h39^m00^s$	$-10°11'00''$	$183.60°.60$	$-77°.20$	0.02
A 901	$09^h56^m17^s$	$-10°01'00''$	$248°.0$	$+33°.6$	0.06
S 11	$11^h42^m58^s$	$-01°42'50''$	$270°.5$	$+56°.8$	0.02

Table 5.2: Positions and galactic reddening for the three COMBO-17+4 NIR survey areas.

5.2.2 Observations

The NIR extension of the COMBO-17 survey was planned to produce multi-band data in 4 NIR filters on three equatorial fields covering 0.77 deg^2 which have been or are going to be observed by COMBO-17 (Tab. 5.2.2). Since each of these fields measures 31×30 arcmin^2, a mosaic of 2×2 OMEGA2000 pointings is required to cover one entire COMBO-17 field. The quadrants of the COMBO-17 fields, denoted with the letters A, B, C, and D, have overlaps for preventing the dithering of the OMEGA2000 pointings to cause too much loss in intergration time for the stripes at the boundaries of the four OMEGA2000 pointings inside the COMBO-17 field (Fig. 5.3). As already mentioned, the survey is designed to use a filter set of the medium-band Y, J_1, J_2 filters and the broad-band H filter. In order to combine the existing optical database from COMBO-17 with observations in the four NIR bands, 10σ magnitudes in the four NIR bands, $Y = 22.0$, $J_1 = 21.2$, $J_2 = 21.0$, and $H = 20.5$ (Vega mag.) have to be obtained. Based on the experience with CADIS, where broad J-band observations with OMEGAprime reached a 10σ-magnitude $J = 21.5$ after 10 ksec integration time, it is expected that about 10ksec integration time in each of the medium bands Y, J_1 and J_2 will be enough to obtain this source point limit. An integration of $\lesssim 20$ ksec should suffice to reach the target magnitude limit in the H band. Thus, the four NIR bands add up to 50 ksec per pointing, and the 2×2 mosaic necessary to cover one entire COMBO-17 field needs 200 ksec.

The observations with the 3.5m telescope equipped with the OMEGA2000 wide field imager in Calar Alto, Spain started in September 2003. Because of technical difficulties, only the medium-band J_1, J_2 and the broad-band H filters were available for the observations. The project had guarantee times in the fall and winter of 2003 and in the spring of 2004 for the observation of the Abell 226 and S 11 fields. The weather conditions allowed us to obtain data with an integration of $\sim$ 3ksec on average for both fields in each session (Tab. 5.2.3). The J_1- and H-band data provided in the Abell 226 field in September 2003 has a very good quality with a seeing of ~ 1 arcsec on average. The observations of the same field in November 2003 could produce only data with poor quality because of the bad weather conditions. In April 2004 the COMBO S11 field was surveyed but we could obtain data with a quality fulfilling the requirements of COMBO-17+4 NIR only in the third quarter of the total field, in the quadrants B, C, and D. Since that time optical data was not available for the Abell 226 field we were restricted our analysis to the optical and NIR-band data of COMBO S11 field. We used only the NIR-band data provided by the observations in April 2004, (see Tab. 5.2.3).

In the preliminary observations of the COMBO-17+4 NIR project using the OMEGA2000 camera, the J_1- and H-band imaging is not as deep as planned, which restricted our possibilities further. We will give some accounts on the consequences of this restriction in the next chapter.

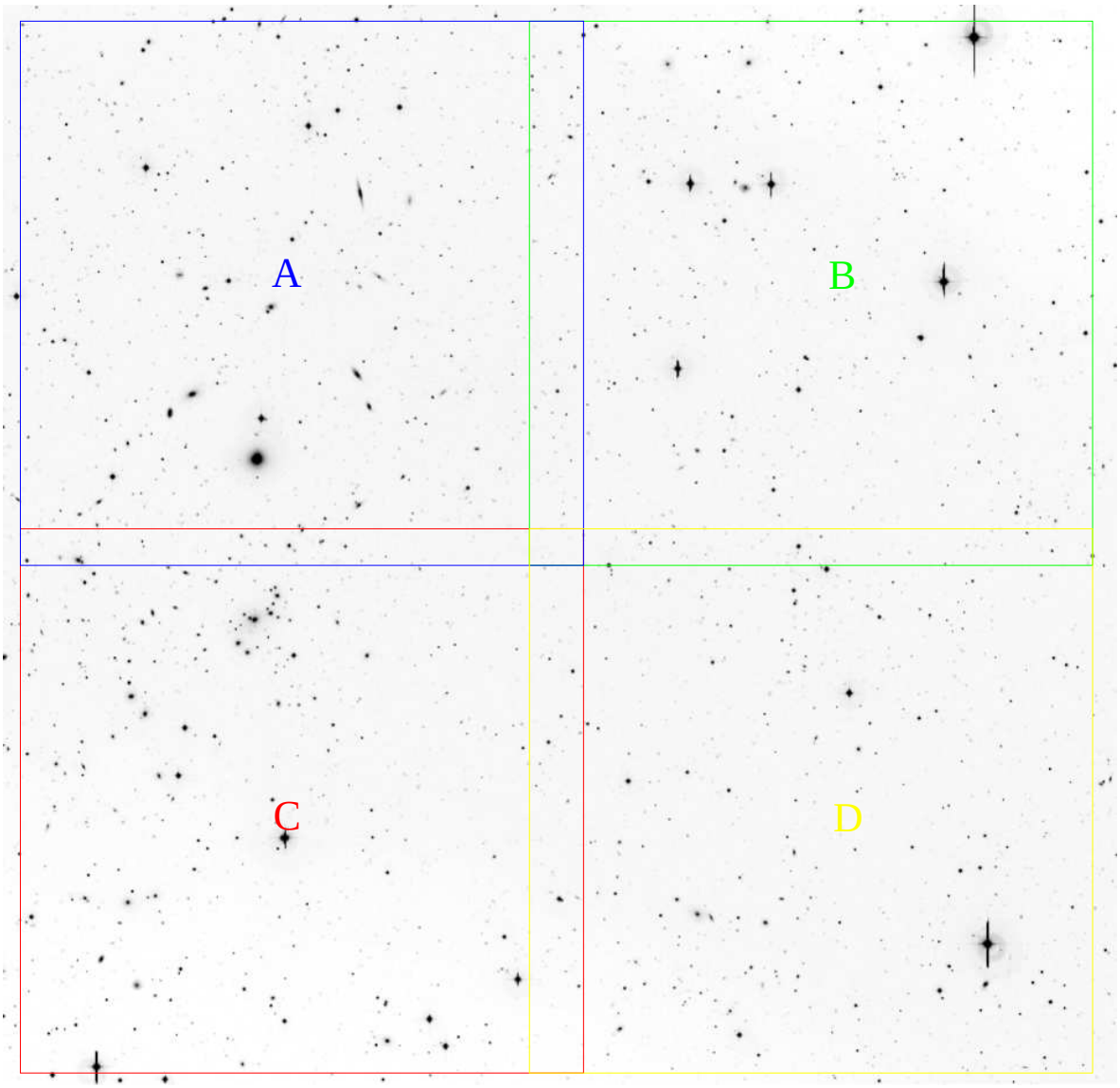

Figure 5.3: The COMBO S11 field (deep R-band image form the COMBO-17 survey) covered by the four OMEGA2000 pointings A, B, C and D.

Field	Observation	Filter	Δt [sec]	Seeing [arcsec]
A 226 (A)	September 2003	H	3000	1.0
	November 2003	H	3000	0.9
A 226 (B)	September 2003	H	3000	1.1
	November 2003	H	6000	1.1-1.2
A 226 (C)	September 2003	H	3000	0.6
	November 2003	H	5700	1.2-1.6
	September 2003	J_1	2520	0.9
A 226 (D)	September 2003	H	3000	0.9
	September 2003	J_1	3000	0.9
S 11 (A)	April 2004	H	3000	1.7
	April 2004	J_1	3000	1.5
S 11 (B)	**April 2004**	H	3000	1.1
	April 2004	J_1	3000	1.2
S 11 (C)	**April 2004**	H	3000	1.2
	April 2004	J_1	3000	1.1
	April 2004	J_2	3000	1.1
S 11 (D)	April 2004	H	3000	1.1
	April 2004	J_1	4500	1.3

Table 5.3: NIR-band observations in the A 226 and the S 11 fields with 3.5m telescope equipped with the OMEGA2000 camera carried out for COMBO-17+4 NIR survey between September 2003 and April 2004. We used the NIR-band data which were provided by the observations shown in bold face letters.

Moreover, because the currently available data in the COMBO-17+4 NIR project are limited to only two of the four NIR bands, J_1- and H, we shall henceforth refer to the survey as, "COMBO-17+2 NIR".

5.2.3 Data Reduction

For the reduction of the data produced by the OMEGA2000 camera, we applied the MPIAPHOT package, as was also the case in the COMBO-17 project. This package, developed for the MIDAS environment, provides complete facilities for handling bad pixels, eliminating dark current and flatfielding stacks of frames converted into a MIDAS specific data format (Röser & Meisenheimer 1991). The OMEGA2000 data indeed required both additive and multiplicative corrections and these tasks could be carried out efficiently with MPIAPHOT. The standard scheme implemented in MPIAPHOT was used in the data reduction process, which consists of bad pixel correction and dark current subtraction of the raw frames, a subtraction of the reflected image of the primary mirror of the 3.5 telescope, flatfielding for global and pixel-to-pixel variation of the detector sensitivity and fringe pattern correction. This section gives an overview of these steps of the data reduction, presented in the block diagram in Fig. 5.4, together with the calibration and photometry of the OMEGA2000 data.

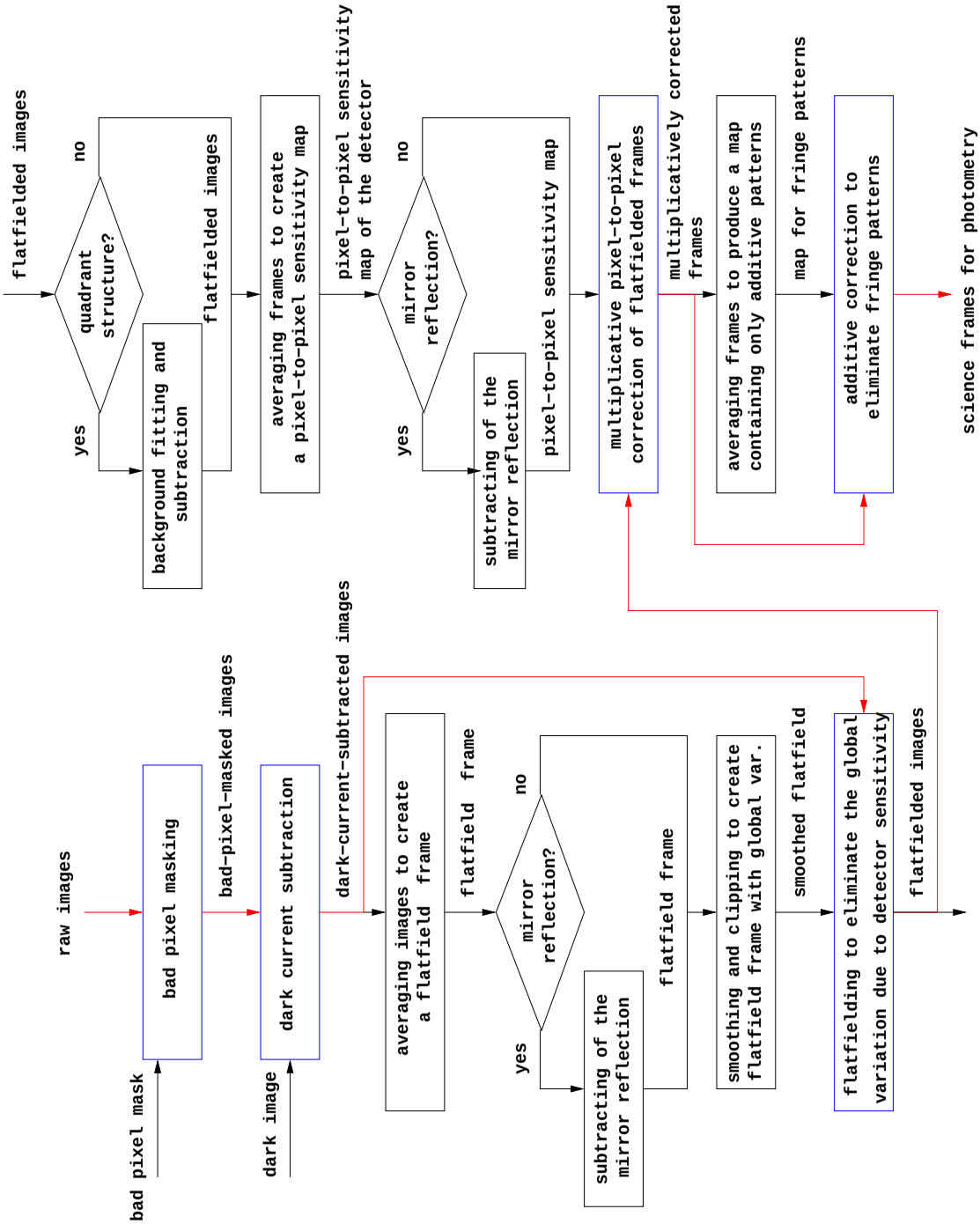

Figure 5.4: Block diagram for presenting the reduction of the NIR-band data provided by OMEGA2000 wide field imager. The blocks plotted with blue color represent the main steps of the reduction process, such as the dark current subtraction, the global and flatfielding with the pixel-to-pixel correction of the detector sensitivity, and the fringe subtraction with the correction of other additive noise corrections. The red lines follow the path of the science frames in the reduction process, whereas the black color indicates the preparatory steps, such as creating flatfield images or frames for the additive correction.

5.2.3.1 Bad Pixel Correction

As already seen in the first part of the thesis describing the performance of the HAWAII-2 FPA, the yield of the HAWAII detector family is extremely high. About 98% of the pixels in arrays are useful for imaging and only the remaining 2% have to be considered as bad pixels. However, even a small number of pixels with incorrect values can cause problems for the photometry, hence they have to be handled properly in the data reduction. The standard method is to mask them out from the original images, i.e., drop their values and substitute them with the median value of the neighboring pixels. The preparation of bad pixel masks for each HAWAII-2 sensors tested for the OMEGA2000 project was already discussed in the first part. We use these masks to mask the bad pixels out in the frames by setting their value above the threshold of the $\kappa\sigma$-clipping applied for the images in flatfielding. As a result, the bad pixel values are replaced with the median of that in predefined array neighboring the given bad pixel.

5.2.3.2 Dark Current Subtraction

In order to eliminate the dark current of the images, we subtracted a thermal frame from them. In the first part of the thesis we already described how the thermal frames for the HAWAII-2 detectors are derived from a series of dark frames, i.e. exposed images without input signal. A linear fit is produced on the values of the dark signal for each pixel in the dark frames taken with different integration times. Each pixel of the thermal frame contains the value of the linear fits for the integration time of 1000 s. The thermal frame was scaled according to the exposure time of the science frames and subtracted from all of the images, as the first additive correction in the data reduction.

5.2.3.3 Correction of Mirror Reflection

In the short overview on the performance of the optics in the OMEGA2000 camera we mentioned the problem of the ghost images in each frame which are identified as the reflection of the primary mirror. Since this reflection is an additive pattern superposed on the incoming photon flux, it must be subtracted from the signal. However the superposed signal of the reflected and the emitted radiation has also a variation due to the photo-response non-uniformity of the detector. In order to remove the mirror reflection in the images, we have to correct this variation in the image as well. However, only the flatfielding can eliminate this effect, which is a multiplicative correction. We need flatfield frames for this correction, which are free from any additive noise, such as the mirror reflection, but all of the images produced with the OMEGA2000 camera contain the mirrors reflection, as do the series of flatfield images. Therefore we made only an additive correction of the ghost images without flatfield correction. As a simple method for the reduction of the mirror reflection, we modelled the mirror image as a disk with a hole in the center. The edges at the boundaries of the disk are smoothed to avoid any abrupt changes in the pixel values which could cause problems for the photometry. Then we subtracted the disk with different amplitudes from the images and sample the subtracted images in both sides of the disk boundary. We adjusted the amplitude for the disk by minimzing the standard deviation of the differences between the juxtaposing points at the outer and the inner part of the disk. The

global variation, due to the residues of the ghost images after this correction, remains below 1 % of the background of the flatfielded images. So this additive correction works well.

5.2.3.4 Flatfielding

The flatfield correction was carried out in two steps for the J_1 and H-band images provided by the OMEGA2000 camera. The first step is the correction of a global deviation in the frames due to the photo response non-uniformity of the HAWAII-2 detector and the second one is the correction of pixel-to-pixel variation of the detector sensitivity. For the correction the global photo-response non-uniformity, we created a median frame of a series of images from the observation of the S11 field and smoothed it with a $\kappa\sigma$-clipping. The pixel values were set by the bad pixel masking so that they exceed the κ-threshold and therefore they were dropped, preventing any bias in the median filtering caused by the bad pixels. We divided the result by its median value to obtain a normalized flatfield image. The result was used to make a multiplicative correction on each dark current subtracted science image, which eliminated the large scale deviations in the images due to the global variation of the detector sensitivity. If the sky variation is very strong because the moving clouds in the field of view a strong quadrant structure, i.e, gradients in the quadrants might still remain in the frames after the global sensitivity correction. We reduced this effect for each globally corrected frame by fitting two dimensional surfaces to the variable backgrounds and subtracting them from the images. The median value of the surface was added to the result for preserving the norms of the images.

In the next step we corrected the pixel-to-pixel variation of the detector sensitivity in the frames. The stack of frames corrected for the global sensitivity were used to create a local sensitivity map containing only the average pixel-to-pixel variation of the frames. If there was a mirror image in the averaged frame we subtracted it by applying again the simple disk model of the primary mirror. We used as many images for the local sensitivity map as needed to keep the reduction of the S/N below 1%. The flatfielding can be described by the function $f(F_{raw}, F_{ff}) = F_{raw}/F_{ff}$, where F_{raw} and F_{ff} denote the fluxes measured in the raw frame and the flatfield frame with the standard deviations σ_{raw} and σ_{ff}, respectively. Thus the standard deviation of the flatfielded image can be written as

$$\sigma_{raw/ff} = \sqrt{\left(\frac{\partial f}{\partial F_{raw}}\right)^2 \sigma_{raw}^2 + \left(\frac{\partial f}{\partial F_{ff}}\right)^2 \sigma_{ff}^2} = \frac{1}{F_{ff}} \sqrt{\sigma_{raw}^2 + \left(\frac{F_{raw}}{F_{ff}}\right)^2 \sigma_{ff}^2} \quad . \tag{5.1}$$

If n raw images with the same integration time and standard deviation σ_{raw} are used to create a flatfield image the noise of the result will be

$$\sigma_{ff} = \frac{\sqrt{n}\sigma_{raw}}{nF_{raw}} = \frac{\sigma_{raw}}{\sqrt{n}F_{raw}} \quad , \tag{5.2}$$

which, together with the Eq. (5.1), gives

$$\sigma_{raw/ff} = \frac{\sigma_{raw}}{F_{ff}} \sqrt{1 + \frac{1}{nF_{ff}^2}} \approx \sigma_{raw} \sqrt{1 + \frac{1}{n}} \tag{5.3}$$

for a normalized flatfiled frame, $F_{ff} \approx 1$. Let ϵ be represent the increase in noise of the flatfielded images,

$$\sigma_{raw}(1+\epsilon) = \sigma_{raw/ff} \quad , \tag{5.4}$$

then we obtain from the Eq. (5.3)

$$n = \frac{1}{(1+\epsilon)^2 - 1} \quad . \tag{5.5}$$

For $\epsilon \approx 0.01$ n is equal to 50. Therefore we used 50 dithered science frames to create a flatfield image for the pixel-to-pixel correction, which increases the noise of the flatfielded images only by 1%. After normalizing the pixel-to-pixel variation map by its median, we used it for a multiplicative correction of the globaly flatfielded images.

5.2.3.5 Sky Subtraction or Fringe Pattern Correction

After the multiplicative correction of the images, they might contain additive fringe patterns mainly due to the many narrow nightsky emission lines. They do not affect the object signal itself only the sky background and thus are to be subtracted from the images. If the science frames also contain the additive pattern of the mirror reflection it is subtracted from them in this step. In order to eliminate them we created an average image from the flatfielded frames taken in different dither positions and subtracted the result from them. For this additive correction we also applied as many images as needed to keep the degradation of the S/N of the averaged frame below 1%. The sky subtraction of the a raw image can be written as $f(F_{raw}, F_{sky}) = F_{raw} - F_{sky}$, where F_{raw} and F_{sky} are the fluxes measured in the raw image and the averaged image containing only the sky background. Then the noise of sky subtracted frame is

$$\sigma_{raw-sky} = \sqrt{\left(\frac{\partial f}{\partial F_{raw}}\right)^2 \sigma_{raw}^2 + \left(\frac{\partial f}{\partial F_{sky}}\right)^2 \sigma_{sky}^2} = \sqrt{\sigma_{raw}^2 + \sigma_{sky}^2} \quad , \tag{5.6}$$

where σ_{raw} and σ_{sky} are the noise of the pixel values in the raw and the sky background, respectively. Similarly to the formule (5.2), the noise of n averaged raw images used to extract the average background of them is

$$\sigma_{bgd} = \frac{\sigma_{raw}}{\sqrt{n}} \quad , \tag{5.7}$$

which can be substituted in the Eq. (5.6):

$$\sigma_{raw-bgd} = \sigma_{raw}\sqrt{1 + \frac{1}{n}} \quad . \tag{5.8}$$

Since this equation has the same form as the Eq. (5.3), for $\sigma_{raw}(1+\epsilon) = \sigma_{raw-sky}$ we obtain the same formula as in Eq. (5.5). For $\epsilon = 0.01$ we averaged 50 dithered science images to create a frame containig only additive noise, i.e, the fringe and the mirror patterns. We subtracted the result from the science images and added the median value of the sky background to them. After the sky and the mirror pattern subtraction of the science frames, they are prepared for the flux measurement.

5.2.4 Photometry

For the photometry of the J_1- and H-band imaging of the COMBO-17+2 NIR survey we used the MPIAPHOT package. Since the R-band frame is deeper than the NIR-band images of the COMBO S11 field, the flux measurement is based on the R-band selected catalogue of the COMBO-17 data base. The object coordinates were projected into the frames of reference of each single exposure, and the object fluxes were measured at the given location. We employed the seeing adaptive, weighted aperture photometry as for the optical bands of COMBO-17. We also chose a common effective PSF of $1''.5$ as in the case of the optical data and convolved each frames with it in order to obtain the same seeing in every images. We used the spectra of nine faint star for the calibration of the fluxes in the quadrants B, C, and D in the S11 field. The measured J_1- and H-band fluxes in the different quadrants were united in one data table and then inserted into the optical data base of COMBO-17.

5.2.5 Multi-color Classification Including 2 NIR Bands

In multi-color surveys, the reliability and precision of the derived galaxy properties depend on many factors, such as the number of bands, the wavelength coverage of the observed data, the measurement uncertainties, and the degeneracies between different features of galaxy spectra. By increasing the number of filter bands and wavelength coverage, we can extend the color space of the observed objects and impose more constraints on the galaxy properties derived from the color information. This helps to disentangle different types of degeneracies which are present due to the smaller amount of information extracted from the smaller color space. The color degeneracies entangle astrophysical properties such as the age of galaxies (defined as the epoch at which a galaxy has started to form stars), the extinction caused by the dust content of galaxies, and stellar mass and metallicity measured in galaxies, which have already been studied for broadband photometry in multi-color surveys by Gil de Paz & Madore (2002).

The COMBO-17 survey uses a filter set covering only the optical regime ($uBVRI$), which introduces a significant age uncertainty for galaxies even though the medium band filters can probe the finer features of galaxy spectra. The optical data do not give information about the spectral contribution of the old stellar population containing most of the mass in galaxies for $z \gtrsim 0.7$. By supplementing the optical data with NIR-band data (YJ_1J_2H), we can sample galaxy spectra in the wavelength range dominated by old stars up to $z \sim 2.1$. The new color information derived from the optical and NIR fluxes allows us to measure the abundance of the old stars in early-type and evolved spiral galaxies at the redshift range $0 \lesssim z \lesssim 2.1$. The COMBO-17+4 NIR survey increases the number of bands and extends the wavelength regime of the original COMBO-17 data base by using the three medium band filters Y, J_1, and J_2, and the broad band H filter. Although the first observations of the COMBO S11 field for this survey produced only J_1- and H-band imaging, it enlarged the color space of the measurement enough to produce redshift evaluation for the galaxies detected in this field up to $z \sim 2.1$. Therefore, we expect the introduction of the NIR bands to reduce the uncertainties in measurement of the physical properties of galaxies and disentangle the degeneracies between these properties.

In this section, we will analyse the improvements in the measurement caused by the better detection of the old stellar content in galaxies for $z > 0.7$. These improvements are studied for

the redshift measurement, the determination of the spectral types of galaxies in the extended redshift range $0 \lesssim z \lesssim 2.1$, and the break of the age-extinction degeneracy. We begin the analysis with a comparison of the redshifts based on the optical and the optical+NIR data sets for the same galaxy sample. Then we study the improvements in the redshift measurements and select some interesting groups exhibiting significant differences between the redshifts derived from the optical and the NIR-supplemented fluxes. These groups can demonstrate the influence of the introduction of the NIR colors in the multi-color classification. The rest of this section analyses the spectral template fitting via examples chosen from each group, comparing the redshifts, spectral types, and extinctions, based on the two data sets. We finish this section with an overview on the impact of NIR-extention of the data set of the COMBO S11 field and conclude that the improvements in the redshift measurement and the spectral classification of galaxies live up to the expectations, which makes the COMBO-17+4 NIR survey a promising extension of the already successful COMBO-17 survey.

5.2.5.1 Comparison of the Redshift Measurements

The COMBO S11 field (see Tab. 5.1.1.1) covering 4×OMEGA2000 pointings contains more then 50,000 galaxies with 5σ point source limits of the aperture magnitude $R = 25.8$ but NIR band data were available for only three quarters of this field, as described in the previous section. Since the H-band imaging is the relevant for the NIR-band extension of the optical data set, we use an R- and H-band selected sample with the limits $R = 25.8$ and $H = 21.4$. This sample of ~ 8700 galaxies is further restricted to the galaxies which have errors in their NIR fluxes small enough to derive reliable color indexes for spectral template fitting. By considering the error limits $\sigma_H < 0.2$ and $\sigma_{J1} < 0.2$ for the aperture magnitudes in the two NIR bands, we obtain a sample with better template fits but reduce the number of the available galaxies for the analysis to ~ 4300. This R- and H-band selected galaxy sample is used to study the improvements of the spectral template fitting.

We measured the redshifts and determined the spectral energy distributions in our sample by using the optical and the optical+NIR data. The multi-color classifier provided redshifts, spectral energy distribution, and extinction levels extracted from both data sets by chosing the best fitting spectral templates for the measured colors of each object in the sample. We compared the results obtained from the optical and the enlarged data bases and tested how well the spectral templates match on the measured fluxes, i.e., how much the measurement was improved by increasing the number of bands and extending the wavelength coverage from the optical regime to the NIR one. The analysis also involved checking how significant the differences in the redshifts, SEDs and extinction parameters derived from the two data sets are. The comparison of the figures derived from the two data sets allowed us to describe how the detection of the old stellar content is improved and how the age-extinction degeneracy in the determined galaxy properties is disentangled by introducing the NIR colors.

Before studying the improvement in the redshift evaluation due to the introduction of NIR colors, we have to consider the error propagation of the measurements in order to restrict our statements to the examples fulfilling some reasonable criterion related to the quality of the measured data. As a result of the spectral template fitting, the photometric redshifts z_{opt} and

$z_{opt+NIR}$ with their standard deviations $\sigma_{z(opt)}$ and $\sigma_{z(opt+NIR)}$ are calculated for each object in the R-band selected sample of the whole S11 field. Here, z_{opt} and $z_{opt+NIR}$ refer to the photometric redshifts based on optical and optical+NIR fluxes, respectively. For the comparison of the redshift values coming out of the two data set, we take their difference,

$$\Delta z_{gal} = |z_{opt+NIR} - z_{opt}| \ , \tag{5.9}$$

and use it to give a criterion for limiting the galaxy sample further to the interesting cases. If we derived this redshift difference for any galaxy from two independent measurements, then the error of the redshift difference Δz_{gal} would be given by the expression

$$\sigma_{\Delta z,gal} = \sqrt{\sigma^2_{z(opt)} + \sigma^2_{z(opt+NIR)}} \ . \tag{5.10}$$

In fact, the two measurements are not independent since all the information used for determining z_{opt} were also needed for the measurement of $z_{opt+NIR}$. This means that $\sigma_{z(opt)} > \sigma_{z(opt+NIR)}$ for each galaxy in the subsample. Therefore, the formula (5.10) provides a conservative estimation of the error for Δz_{gal}. By applying the ratio of the redshift difference to its error, we introduce the criterion

$$\frac{\Delta z_{gal}}{\sigma_{\Delta z,gal}} > 3 \tag{5.11}$$

for selecting galaxies with large redshift differences and small errors in their redshift measurements. This criterion provides a galaxy sample which exhibits a significant improvement in spectral template fitting caused by the inclusion of NIR-band colors in the data set. In the following subsections we will study the effect of the NIR extension of the optical data base on the redshift, SED, and extinction evaluation for this group of galaxies.

Fig. 5.5 compares the photometric redshifts z_{opt} and $z_{opt+NIR}$ in our sample consisting of ~ 4300 galaxies. In the left $z_{opt+NIR}$ vs. z_{opt} diagram of Fig. 5.5, the majority of the galaxies form a diagonal branch up to $z \sim 1.4$, which is plotted with black color. Its small spread for $z_{opt} \lesssim 0.7$ indicates that the redshift measurement could not be considerably improved in that interval. Nevertheless, the diagonal branch broadens for $z_{opt} \gtrsim 0.7$, and a prominent group scattering above it over the interval $0.8 \lesssim z_{opt} \lesssim 1.1$ exhibits considerable differences between the redshifts based on the original and NIR-extended data sets. By applying the criterion (5.11), this interesting group can be found together with other small ones plotted with different colors, as the right hand panel of Fig. 5.5 shows. The groups plotted here with blue, yellow, red, and green colors will be used for the analysis of the improvement in the redshift measurements. The selected galaxy population consits of three prominent groups and contains some objects scattering around the diagonal branch as well. The most important group, designated with blue circles in Fig. 5.5, is the one above the broadening diagonal branch for $0.6 \lesssim z_{opt} \lesssim 1.2$. These objects obtained higher redshifts from the measurements on the extended data set, compared with the results of the redshift determination based on optical data. A smaller group, plotted with yellow color in the Fig. 5.5, can be found below the broadening diagonal branch for $0.7 \lesssim z_{opt} \lesssim 1.1$. This shows a counter tendency - the redshifts of the galaxies in this group are derived to be greater than 1 based on the optical colors alone but less than 1 when we apply the NIR-band-extended data set. Another group, denoted with red circles in Fig. 5.5, is located in the top left

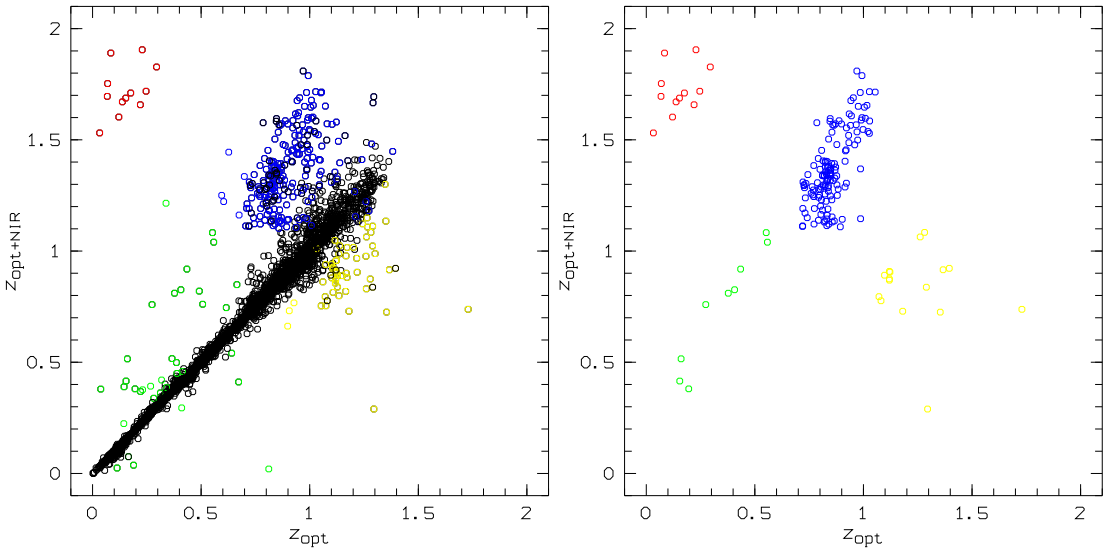

Figure 5.5: The plots of redshifts based on optical colors vs. the ones based on optical and NIR band data for galaxies in COMBO S11 field. The left hand panel shows the R- and H-band selected sample, which is further restricted by the criteria $\sigma_H < 0.2$ and $\sigma_{J1} < 0.2$. The different colors designate the interesting groups for the improvement analysis. The right hand panel displays all the galaxies from the same sample which satisfy the criterion (5.11). The colors designate the group members found by applying the criterion.

corners of the $z_{opt+NIR}$ vs. z_{opt} plots and represents objects with enormous variations in their photometric redshifts. They are identified as low-redshift galaxies by using only the optical data but the measurement with NIR fluxes assigns high redshifts to them. Some objects, designated with green circles in Fig. 5.5, scatter above the diagonal line too, according to the moderate variations in their redshifts.

If we compare the redshift distribution of the galaxy sample in Fig. 5.6 derived from the two databases we find noticeable differences over the whole available redshift range, as a consequence of the improvement of the redshift evaluation. Both the redshift histograms in Fig. 5.6 have local maxima at $z \sim 0.1$, 0.6, and 0.8, since the optical data set is also enough to find galaxy cluster canditdates up to ~ 1.2. However, the number of galaxies has an excess from $z \sim 1.1$ for the optical+NIR measurement compared with that for the pure optical data. In return for this excess, the redshift bins between $z \sim 0.8$ and 1.1 contain less galaxies for the evaluation of the NIR-band-extended data set. This redistribution in the redshifts comparing the two data sets with each other is another representation of the dominant group of galaxies (denoted by blue circles) above the diangonal branch in Fig. 5.5.

As already mentioned, the extension of the optical data with NIR fluxes has a twofold impact on the photometric redshift measurement. On the one hand, it makes the multi-color classification capable to detect the spectral features due to the old stellar population up to $z \sim 2.1$ and on the other hand, it can also disentangle the age-extinction degeneracy in the galaxy colors. These capabilities enhance the determination of the spectral properties, i.e., improve the quality of the spectral template fitting and increase the reliability of the redshift measurement in the interval $0.7 < z < 2.1$.

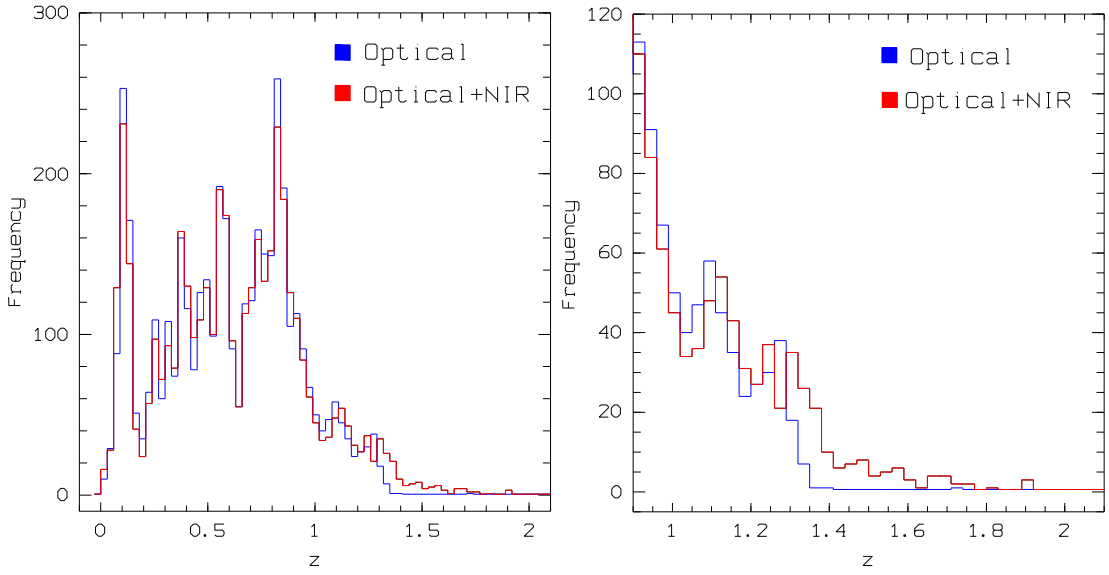

Figure 5.6: The redshifts distributions of galaxies derived from the optical and optical+NIR band data. The left hand panel shows the R- and H-band selected sample, which is further restricted by the criteria $\sigma_H < 0.2$ and $\sigma_{J1} < 0.2$. In the right hand panel, only the interval $0.9 < z < 2.1$ can be seen, which is the most interesting redshift domain for the analysis.

Hence, the next step of the analysis is to study the spectral properties of the groups located in the $z_{opt+NIR}$ vs. z_{opt} plots in Fig. 5.5. In the COMBO-17+2 NIR multi-color classification the spectral properties of galaxies are represented by two parameters, the spectral energy density (SED) and the dust extinction. They together give the proper characteristics of the spectral types of galaxies, which can be associated to the morphological types. The $z_{opt+NIR}$ vs. z_{opt} diagrams of the total galaxy sample in Figs. 5.7 and 5.8 binned by the SED parameter and extinction derived from the optical+NIR data set show the most noticeable difference between the two redshift measurements in the intervals 20<SED<50 and $A_V < 0.6$. Here, the range of SED parameter just maps the Kinney et al. (1996) templates onto a sequence of values from 0 (SB1 starburst template) to 59 (E galaxy template). There is a limited range of the SED and extinction parameters, over which the groups defined in the $z_{opt+NIR}$ vs. z_{opt} plots in Fig. 5.5 concentrate. This indicates the correlation between the improvement of redshift measurements and the SED/A_V parameter evaluation for these groups . In the next section we will study this correlation by giving an analysis on the evaluation of the astrophysical properties and the quality of the spectral template fittings for both the optical and the optical+NIR data sets.

In the SED vs. extinction plot of our galaxy sample for the measurement on the optical+NIR data the galaxies are not distributed uniformly, as shown in the left hand panel in Fig. 5.9. They form a diagonal stripe located between the upper left and the bottom right corners, following the trends of the SED vs. extinction relation of the spectral templates (the diagonal light blue lines) derived from Kinney spectral tempates of galaxies in the local Universe. The comparison of the SED vs. A_V relations for the data and the template spectra suggests that E/S0 galaxies with lower extinction are almost missing and we can find hardly any dust-free starburst galaxies in the sample.

The differences between the spectral properties based on the two data sets can be seen well

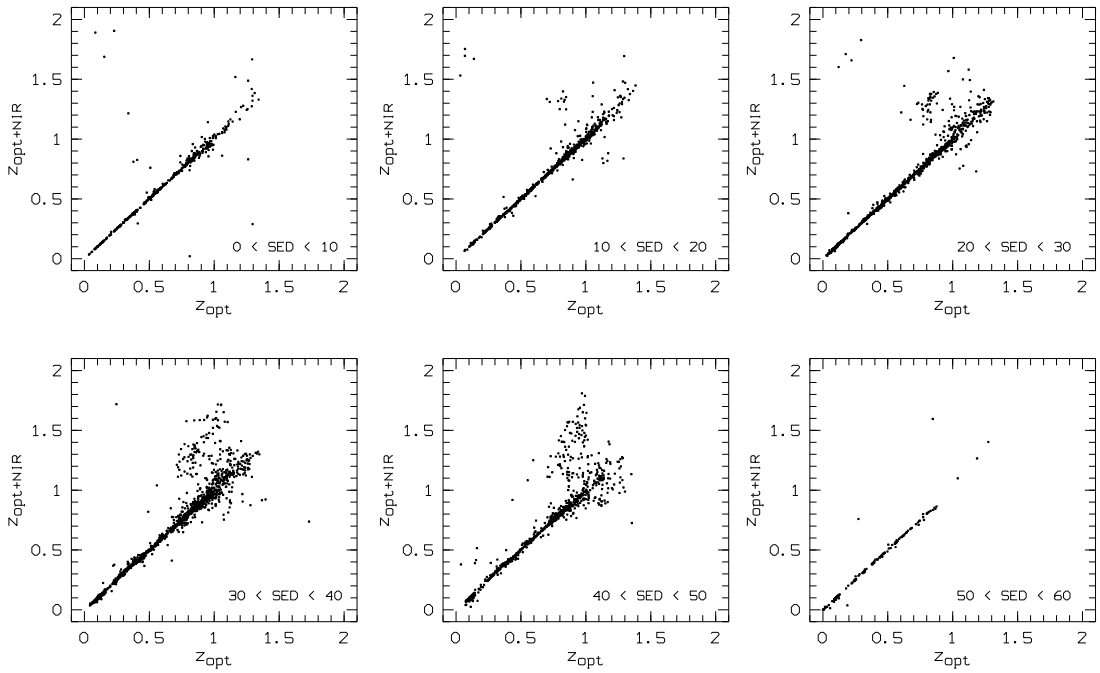

Figure 5.7: $z_{opt+NIR}$ vs. z_{opt} plots of the R- and H-band selected galaxy sample split by bins of different spectral types derived from the optical+NIR-band data ($\sigma_H < 0.2$ and $\sigma_{J1} < 0.2$).

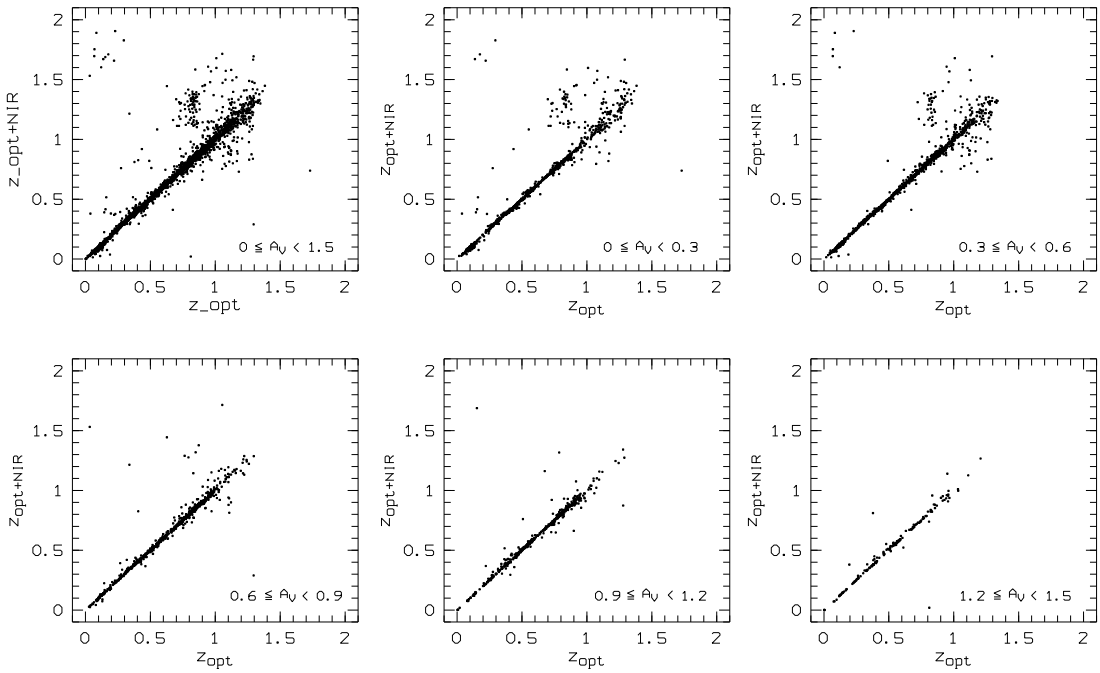

Figure 5.8: $z_{opt+NIR}$ vs. z_{opt} plots of the R- and H-band selected galaxy sample split by bins of extinction parameter derived from the optical+NIR-band data A_V ($\sigma_H < 0.2$ and $\sigma_{J1} < 0.2$).

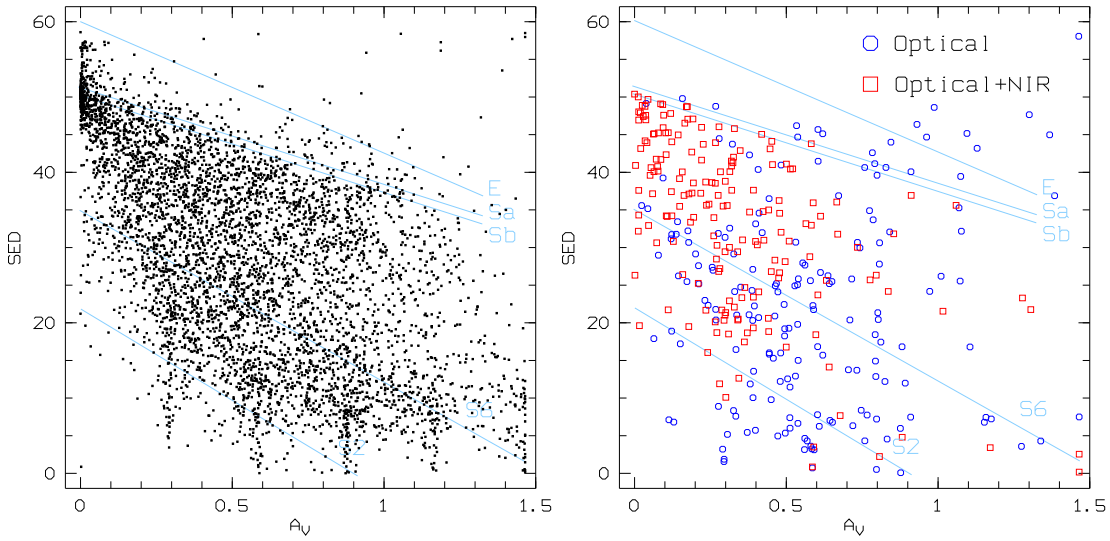

Figure 5.9: Distribution of galaxies in the SED vs. extinction plot. The left hand panel shows the R- and H-band selected sample with $\sigma_H < 0.2$ and $\sigma_{J1} < 0.2$. Here, the SED and extinction values are derived from the optical+NIR colors. The panel in the right hand side displays only the galaxies selected with the criterion 5.11. The blue circles denote galaxies with SEDs and extinctions based on the optical data while the same galaxies are represented with red squares for the parameteres derived from the NIR-band-extended data set. The light blue lines show the SED range vs. extinction relations of the present-day spectral templates ($z = 0$) used in the COMBO-17+2 NIR multi-color classification.

in the SED vs. A_V plot in Fig. 5.9, which displays only the objects fulfilling the criterion $\Delta z_{gal}/\sigma_{\Delta z,gal} > 3$. By comparing the SED vs. A_V distributions derived from the optical and the optical+NIR data for the same galaxies, we see that the measurement on the optical data (blue circles) identified a great number of objects as starburst galaxies with a wide range of dust extinction while the evaluation of the NIR-supplemented data (red squares) produced a large quantity of evolved spirals with low extinction. This general tendency along with other subtle trends in the parameter evaluation will be associated with the groups of galaxies denoted with blue, yellow, red and green colors in the z_{opt} vs. $z_{opt+NIR}$ plot in Fig. 5.5. Henceforth we study the distribution of these groups in SED vs. extinction diagrams for both the optical and the optical+NIR data sets and check the improvement of their spectral template fittings.

We continue this section with an analysis of the most prominent group located above the diagonal branch at high z_{opt}, denoted with blue dots in Fig. 5.5. Then we analyze the group scattered below the diagonal branch, represented by yellow dots in Fig. 5.5. The group in the top left corner of the diagram 5.5, plotted with red color, will be discussed afterwards. Finally, we consider the small group denoted by green dots, which is scattered above the diagonal branch at lower z_{opt}. In the concluding remarks the results of this analysis are extended to the galaxy sample in the whole COMBO S11 with deeper NIR-band imaging.

5.2.5.2 High-redshift Galaxies with an Increase in the Redshift

The most dominant group plotted with blue color in the z_{opt} vs. $z_{opt+NIR}$ diagram in Fig. 5.5 consists of about 500 galaxies and it can be found in the redshift domain $0.7 \lesssim z_{opt} \lesssim 1.1$ and

$1.1 \lesssim z_{opt+NIR} \lesssim 1.8$. By applying the selection criterion (5.11), we chose ~ 180 objects from this group, represented by blue dots in Fig. 5.10, for studying the impact of the NIR-band extention of the measurement. If we compare the redshift diagram and SED vs. extinction plots of these galaxies in Fig. 5.10 derived from the optical data set (blue circles) and the NIR-supplemented one (red squares), we see a general tendency of the differences in the spectral types and the extinction levels, represented with the arrows A, B and C. According to the evaluation of the purely optical data, most of the objects are identified as starburst galaxies (S1-S6 types) with moderate or high extinctions in the redshift range $0.7 \lesssim z_{opt} \lesssim 0.9$. After the combination of the optical and NIR bands, these galaxies become spirals with lower extinction levels and are located at higher redshifts, $1.1 \lesssim z_{opt+NIR} \lesssim 1.7$.

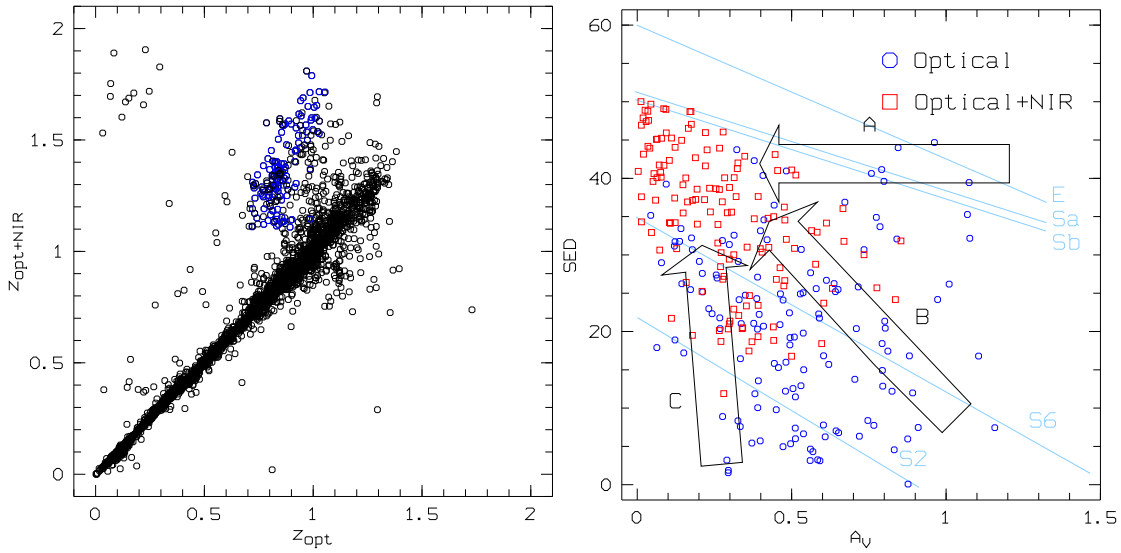

Figure 5.10: The left hand panel shows the $z_{opt} - z_{opt+NIR}$ plot for the R- and H-band selected sample with $\sigma_H < 0.2$ and $\sigma_{J1} < 0.2$. The blue dots denote the galaxies for which $\Delta z_{gal}/\sigma_{\Delta z,gal} > 3$ in the domain $z_{opt} > 0.7$ and $z_{opt+NIR} > 1.1$. The right hand panel is the SED vs. extinction plot for these galaxies derived from the optical data set (blue circles) and the optical+NIR colors (red squares), respectively. The arrows A, B, and C indicate the general tendencies in their relocations due to the inclusion of the NIR colors in the measurement.

This general tendency in the differences between the SED parameters and extinction values derived from the two data sets is an expected consequence of the NIR-band extention of the optical color information. We access the wavelength regime of galaxy spectra which is dominated by old stars only up to $z \lesssim 1.1$ with optical filters. By applying the NIR-band colors in addition to the optical ones, we can sample the galaxy spectra in the wavelength regime as well, which is relevant for measuring the spectral contribution of the old stellar population in the redshift range $0.7 \lesssim z \lesssim 2.1$. The above shown trend indicates the three medium-bands filters in Johnson I band along with the I-band filter itself are not enough to correctly detect the presence of the old stellar content of quite a few objects for $z \gtrsim 0.7$ and the multi-color classification identifies them as less evolved spiral or starburst galaxies. The spectral types derived from the NIR-supplemented data set indicate that we already measure the contribution of old stars to the total fluxes of these galaxies, which allows us to identify these object as more evolved systems.

We demonstrate this improvement in the measurement in more details with three pairs of

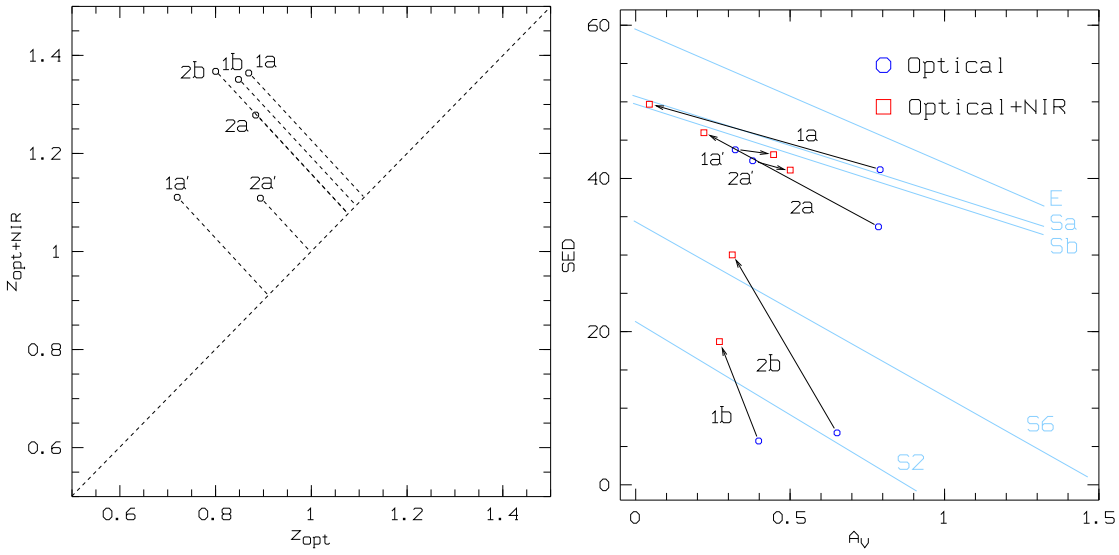

Figure 5.11: The $z_{opt} - z_{opt+NIR}$ and the SED vs. extinction plots of the galaxies given here as examples for the demonstration of the improvement of the spectral template fitting. The dashed lines connecting the data points with the diagonal in the left hand plot measure the difference between z_{opt} and $z_{opt+NIR}$. The arrows in the right hand plot indicate the direction of the relocation made by the objects, compared the optical data (blue circles) with the NIR-extended one (red squares). The galaxies moving along the SED-A_V relations of the spectral templates Sa/Sb (the light blue lines) to lower extinction values in the SED vs. extinction plane are denoted with (1a) and (2a), while (1a') and (2a') sign the galaxies obtaining higher extinctions. The two examples referred by (1b) and (2b) are starburst galaxies with lowered dust content and increased mean age.

examples of the spectral template fitting of galaxies. Fig. 5.11 shows the $z_{opt} - z_{opt+NIR}$ and the SED vs. extinction plots of the galaxies chosen as examples, where they are denoted by (1a)-(2a), (1a')-(2a'), and (1b)-(2b). We display and compare the results of the spectral template fitting based on the optical and the optical+NIR data sets for each pair of galaxies in the followings.

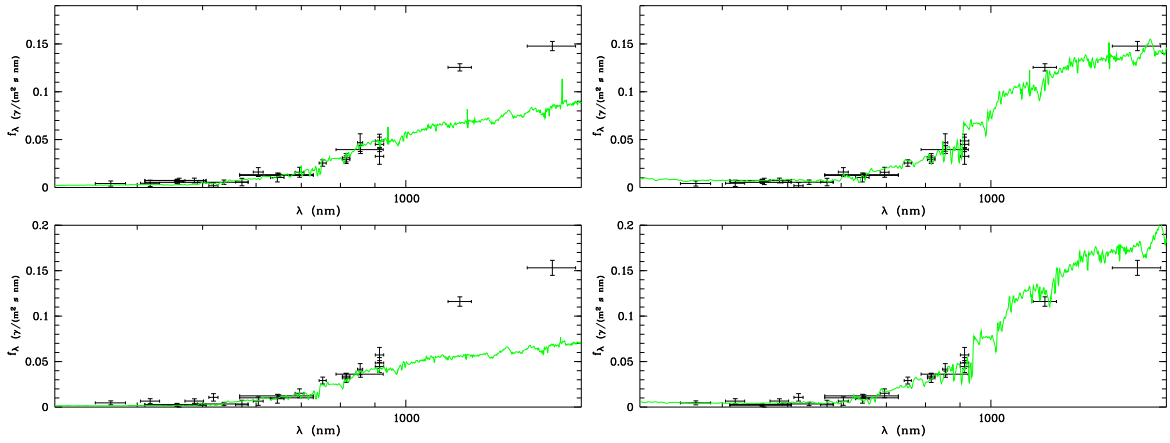

Figure 5.12: Two examples of the spectral template fittings for spiral galaxies, which are denoted with (1a) and (2a) in Fig. 5.11. The fits on the optical data are displayed in the left hand side and they represent the spectra of dusty Sa (upper plot, 1a) and Sbc (lower plot, 2a) type galaxies with high dust extinctions, $A_V \approx 0.8$, at redshifts $z \approx 0.8$. The plots in right hand side are the results of the data evaluation in the optical+NIR bands. The spectral type of the example (1a) in the upper plot exhibits no changes while the example (2a) in the lower plot is identified as an Sa/b galaxy. The dust extinction are drastically reduced for both of them, $A_V \lesssim 0.3$ and higher redshifts were measured for them at $z \approx 1.3$.

The first pair, denoted with (1a) and (2a), is chosen to demonstrate the tendency indicated with the arrow A in the SED vs. extinction plot in Fig. 5.10. Fig.5.12 shows the results of the spectral template fitting for this pair of galaxies. The left hand plots contain the fittings of model spectra based on the optical fluxes. In both cases the filters in the optical bands can sample the redshifted Balmer jump only in the redward part, below $\lambda \lesssim 900$ nm, which is not enough to detect the increase in the spectrum caused by the old stellar content of the galaxies. As a result, the sources of these optical fluxes are identified as dusty Sa (upper plot, 1a) and Sbc (lower plot, 2a) galaxies at redshifts below 1, which have spectral shapes poorly matching the J_1- and H-band fluxes. By supplementing the optical data with the NIR-band colors, we will detect the redshifted 4000 Å break and a considerable part of the galaxy spectra dominated by the old stars up to $z \sim 2.1$. Therefore the multi-color classification results in synthetic spectra which fit on the J_1- and H-band fluxes, as shown in the right hand side plots in Fig 5.12. The spectral types here are of Sa/b galaxies with a mild decrease (upper plot, 1a) and increase (lower plot, a2) in the mean age but the dust extinctions are reduced drastically and the redshifts have values of $z \approx 1.1$. These modifications in the results of the measurements are represented with the arrows belonging to (1a) and (2a) in Fig. 5.11.

For the most part the inclusion of the NIR colors in the measurement causes the members of the group plotted with blue color in Fig. 5.10 to have the usual decrease in the extinction value. There are, however, some objects from this group exhibiting a counter tendency. The plots in

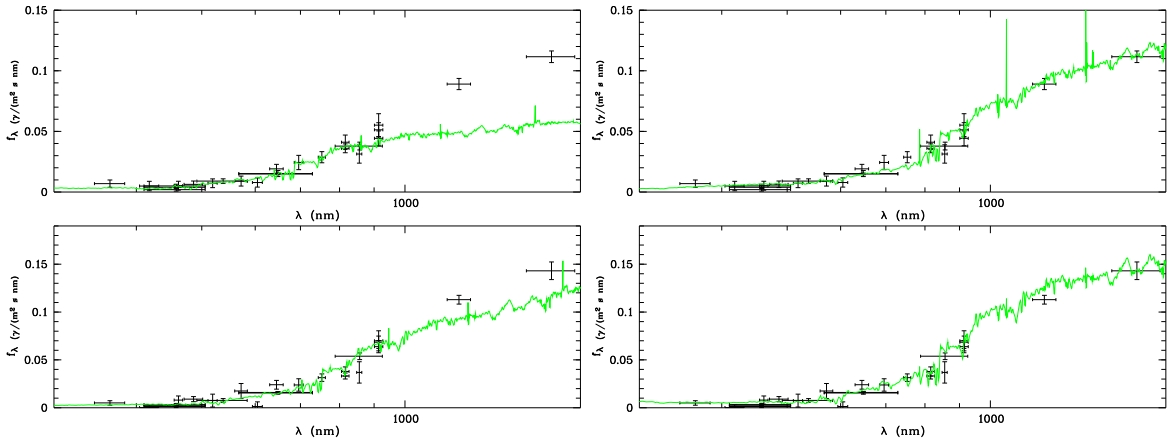

Figure 5.13: Template fittings of spiral galaxies, where the upper two plots belong to the object denoted by (1a') and the lower two plots belong to the object denoted by (2a') in Fig. 5.11. The plots in the left hand side, derived from the optical data, show two spectral templates for a Sb galaxies with low dust extinctions, $A_V \approx 0.3$, at redshifts $z < 1$. By supplementing the optical data with the NIR-band colors, we obtain template fits, shown in the right hand side, which have the same spectral types but higher extinction levels, $A_V \approx 0.5$, and are located at higher redshifts, $z \approx 1.1$

Fig. 5.13 show the spectral template fitting for two of them at $z < 1$, denoted with (1a') and (2a') in Fig. 5.11. The template spectra in the left hand side are derived from the optical data and belong to Sb type galaxies with low extinction values. The right hand plots in Fig. 5.13 contain the model spectra fitted on the optical+NIR colors. These templates also represent Sb galaxies but at redshifts higher than 1 and with slightly increased dust extinctions, as seen in Fig. 5.11.

The third example describes the improvement of the template fitting for starburst galaxies. This pair of galaxies, denoted by (1b) and (2b) in Fig. 5.11, are identified as S2 galaxies with moderate extinctions and redshifts greater than 1 in left hand plots in Fig. 5.14 showing the results of the measurement on the optical data. Here, the local maxima of continuum spectra due to the younger stellar content are redshifted to the redward part of the optical regime but the templates do not match the reddest optical fluxes around 800 nm. Because of the slow fall-off of the continuum spectra, the discrepancy between the measured fluxes and the model spectra even becomes more considerable in the NIR band. By including the J_1- and H-band data, we can better determine the position of the local maxima of the continuum spectra. The right hand plots in Fig. 5.14 show spectral templates with these maxima redshifted to the NIR band, at $z \approx 1.3$, which belong to more advanced S3-type starburst (upper plot, 1b) and Sc-type spiral galaxies (lower plot, 2b). The dust extinction levels are also reduced indicating the disentanglement of the age-extinction degeneracy of the colors for these galaxies.

5.2.5.3 High-redshift Galaxies with a Decrease in the Redshift

If we consider the z_{opt} vs. $z_{opt+NIR}$ diagram in Fig. 5.5, we also find a less prominent group below the diagonal branch in the redshift interval $0.7 \lesssim z_{opt} \lesssim 1.1$, plotted by yellow color. The galaxies in this group have a tendency in the redshift differences calculated from the two

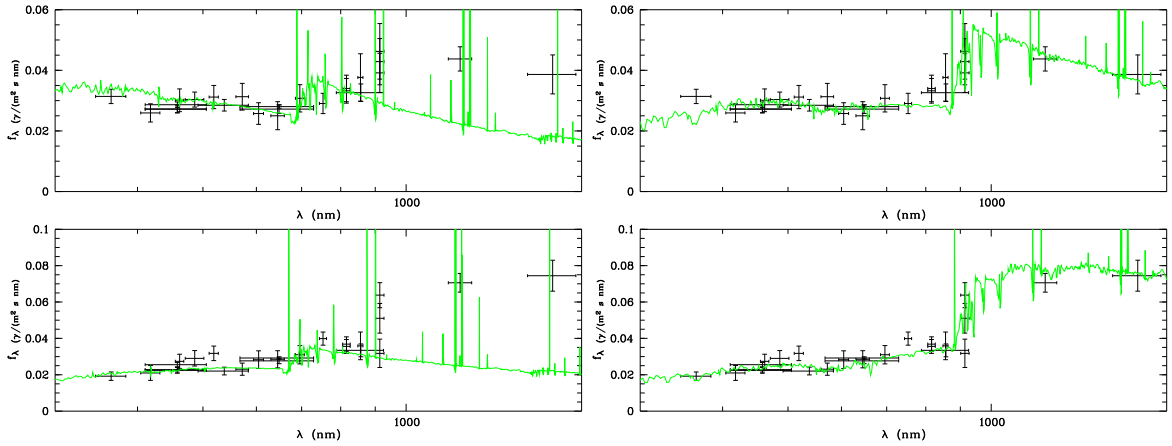

Figure 5.14: Two examples of the spectral template fittings for starburst galaxies, which are denoted with (1b) and (2b) in Fig. 5.11. The plots in the left hand side, based measurements in optical bands, show model spectra of S2-type galaxies with moderate extinctions, $A_V \approx 0.4$ and 0.7, and at $z \approx 0.8$. With the extension of the wavelength range of the measurement the mean age of the systems is considerably increased and they are identified as S3 (upper plot, 1b) and S6 (lower plot, 2b) types, as seen in the right hand plots. At the same time their dust extinctions were reduced, while the redshifts evaluations provided higher values, $z \approx 1.3$, than those derived from the optical fluxes.

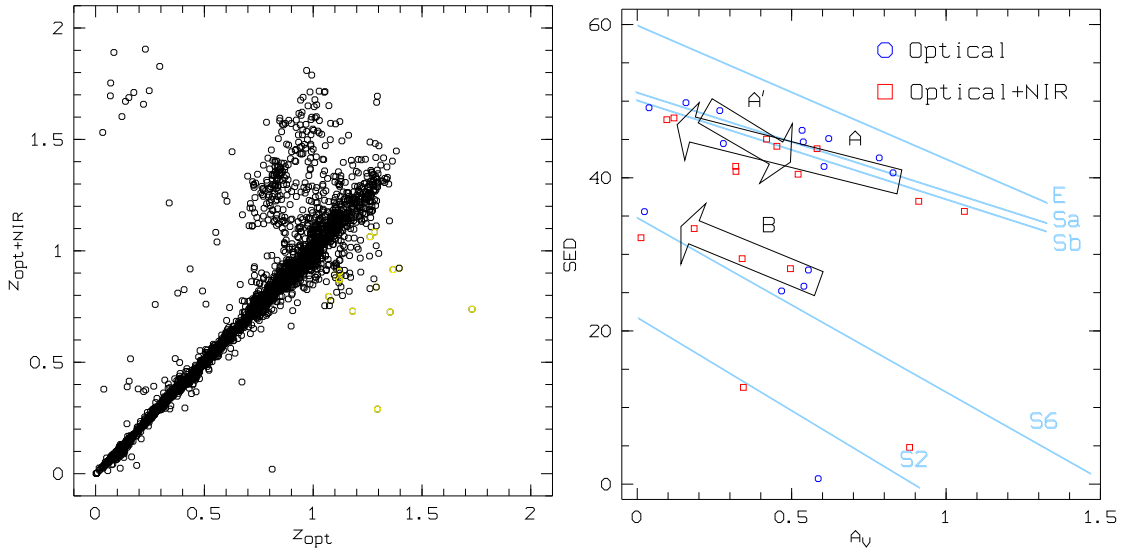

Figure 5.15: The left hand panel shows the $z_{opt} - z_{opt+NIR}$ plot for the R- and H-band selected sample with $\sigma_H < 0.2$ and $\sigma_{J1} < 0.2$ in the COMBO S11 field. The yellow dots denote the galaxies fulfilling the criterion (5.11) in the domain $z_{opt} > 0.7$ and $z_{opt+NIR} < 1.1$. The right hand panel is the SED vs. extinction plot for these galaxies derived from the optical data set and the optical+NIR colors, respectively. The arrows indicate the general tendencies in their relocations due to the inclusion of the NIR colors in the measurement.

measurements opposite to that of the most prominent group discussed in the previous section. They are identified as galaxies located at redshifts higher than ~ 1 in the measurement applying only optical data but they obtain redshifts only up to ~ 1 in the evaluation of optical+NIR data. In this section we compare their spectral properties and extinction levels derived from the two data sets.

The SED vs. extinction plot in Fig. 5.15 of the 13 objects selected from this group, with the criterion (5.11), suggests that the majority of them are evolved spiral galaxies and some are Sbc- or S6-type systems in both of the measurements. The right hand panel in Fig. 5.15 shows similar trends in the variation of the SED and A_V values, represented here by the arrows A and B, to those of the prominent group. The evaluation of optical+NIR data provides older stellar populations and lower dust extinction for the galaxies than the ones coming from the optical colors only. The trend denoted with the arrow A in the SED vs. extinction diagram follows the main stream of the prominent group, but with lowering of the redshifts. The measurement based on the optical data identifies these objects as Sa and Sb galaxies and the NIR-band-extension of the wavelength regime modifies only slightly their spectral types by decreasing the mean ages of their star populations to a small extent. Only their high dust reddening together with the redshifts are reduced considerably. As described in the previous section, this tendency indicates that the measurement of the NIR fluxes can sample the spectral contribution from the old stellar components in galaxies, which helps to determine the correct SEDs of systems with older mean age. Since the galaxies following the tendency in the direction of the arrows A and B in Fig. 5.15 have only minor changes in their spectral types, only the lowering of their redshifts and extinction levels can produce better fits on their J_1- and H-band fluxes. In SED vs. extinction plot in Fig. 5.15, the tendency represented by the arrow A is the mainstream of the Sa and Sb galaxies in the group discussed here. However, there are some galaxies in this plot following a counter tendency. The direction of this tendency is denoted by the arrow A', which illustrates the galaxies which have slightly redder rest-frame colors and an increase in their extinction level caused by the inclusion of the NIR colors in the data set.

The examples given in the $z_{opt} - z_{opt+NIR}$ and the SED vs. extinction plots in Fig. 5.16 illustrate these trends for both the groups of evolved spirals and starburst galaxies. The pair of galaxies denoted with (1a) and (2a) is an example for the redistribution in the direction of the arrow A while the pair denoted with (1b) and (2b) follows the trend represented with the arrow B in Fig. 5.15. The last examples, referred to as (1a') and (2a') in Fig. 5.16, are given for the counter tendency indicated with the arrow A' in Fig. 5.15. The plots in Fig. 5.17 show the results of the spectral template fittings for the first pair of galaxies, (1a) and (2a). The model spectra in the left hand plots are fitted on only the optical data and match them well. In the NIR regime both of the templates have an excess, which is reduced in the right hand plots by including the NIR colors in the measurement. As the galaxies in the example obtain only slightly bluer rest-frame colors in SED vs. extinction plot in Fig. 5.16, the cumulative effect of the reduction in redshift and extinction level caused the spectral template to fit on the J_1- and H-band fluxes.

The plots in Fig. 5.18 display the results of the spectral template fittings for the next examples denoted with (1b) and (2b) in Fig. 5.16. In the left hand plots derived from the optical

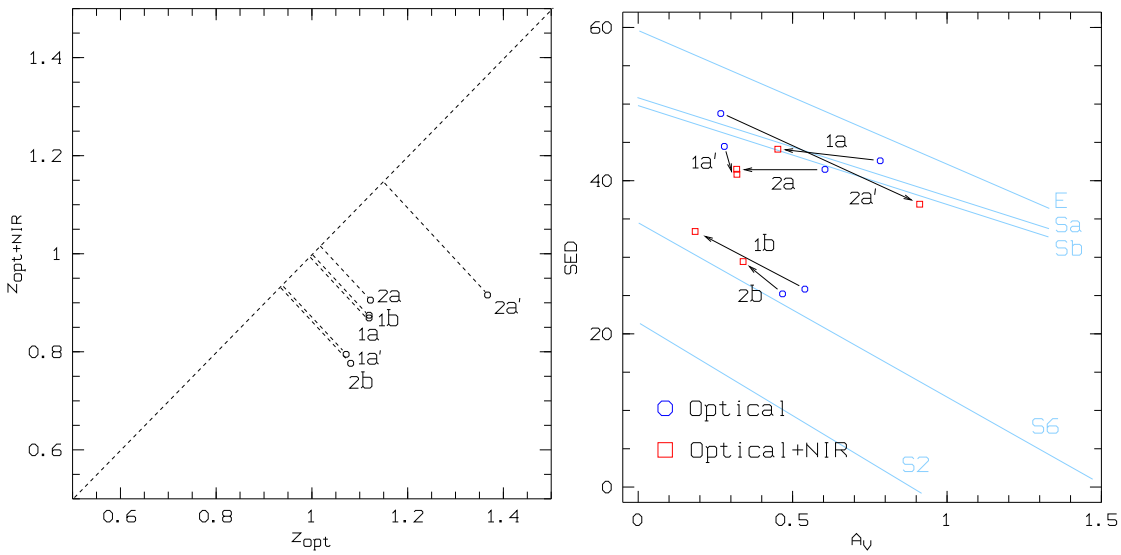

Figure 5.16: The $z_{opt} - z_{opt+NIR}$ and the SED vs. extinction plot of the galaxies - given as examples for comparing the spectral template fittings derived from the optical and optical+NIR data sets. The left hand plot measures the difference between z_{opt} and $z_{opt+NIR}$ with the dashed lines connecting the data points to the diagonal for each galaxy. The right hand panel is the SED vs. extinction plots for these galaxies derived from the optical data set (blue circles) and the optical+NIR colors (red squares), respectively. The arrows indicate their relocations due to the inclusion of the NIR colors in the measurement. The pair of galaxies denoted with (1a) and (2a) are examples for the redistribution in the direction of the arrow A while the pair denoted with (1b) and (2b) follows the trend represented with the arrow B in Fig. 5.15. The galaxies referred to as (1a') and (2a') are examples for the counter tendency indicated with the arrow A' in Fig. 5.15.

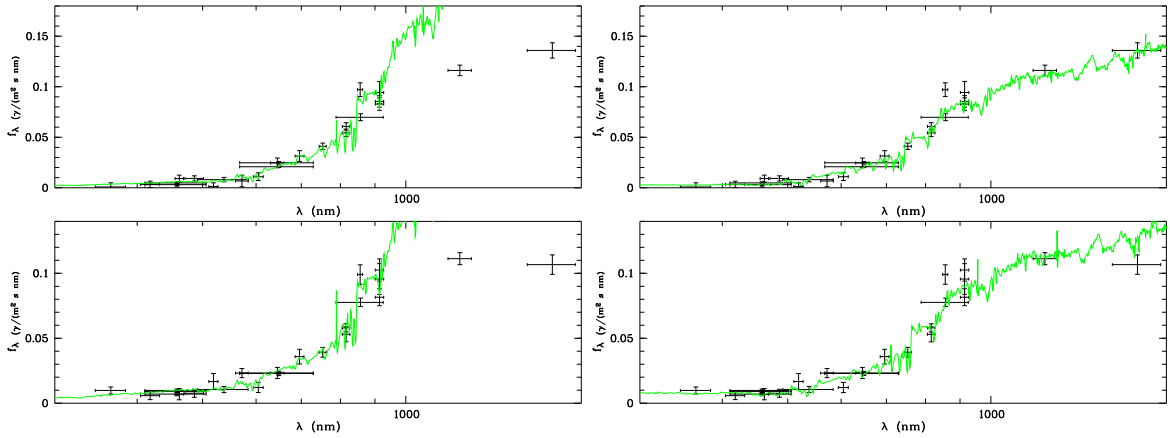

Figure 5.17: Two examples of the spectral template fittings for galaxies following the trend represented by the arrow A in the SED-A_V plot in Fig. 5.16. The fits on the optical data are displayed in the left hand side where we see spectra of dusty Sa/Sb galaxies, $A_V \approx 0.6 - 0.8$ at the redshifts $z \approx 1.1$. The templates have a high excess in the NIR regime, which has been corrected in the right hand plots displaying the results of the evaluation of optical+NIR data. The galaxies here have a slightly younger stellar content but obtain much lower extinction levels, $A_V \lesssim 0.4$, and redshifts, $z = 0.78$ and 0.91.

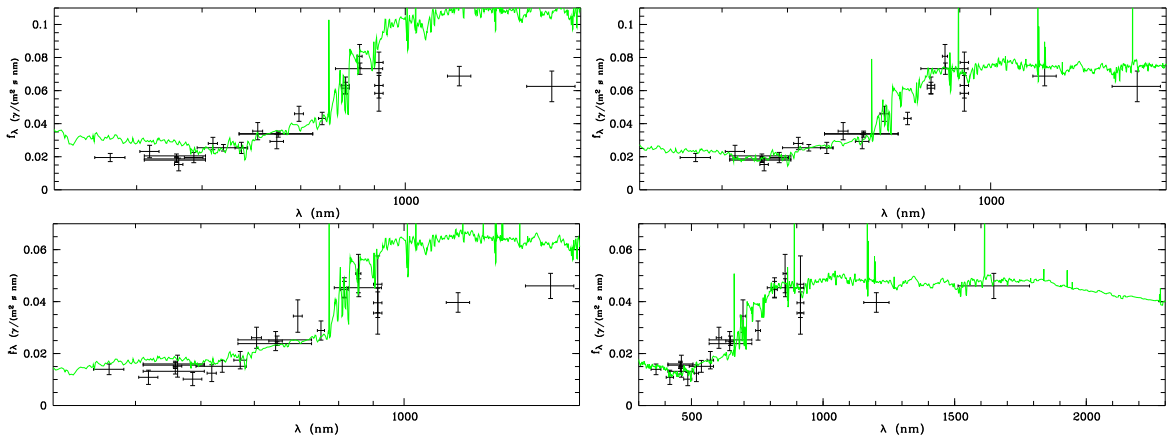

Figure 5.18: Two examples of the spectral template fittings for galaxies following the trend indicated with the arrow B in in the SED-A_V diagram in Fig. 5.16. The plots in the left hand side, derived from the optical data, show two spectral templates of S6- (upper left plot, 1b) and Sc-type (lower left plot, 2b) galaxies with moderate extinctions at redshift $z \sim 1.1$. By supplementing the optical colors with the NIR ones, the right hand plots display templates of Sc-type galaxies with much lower extinctions and redshifts, $z \sim 0.8$.

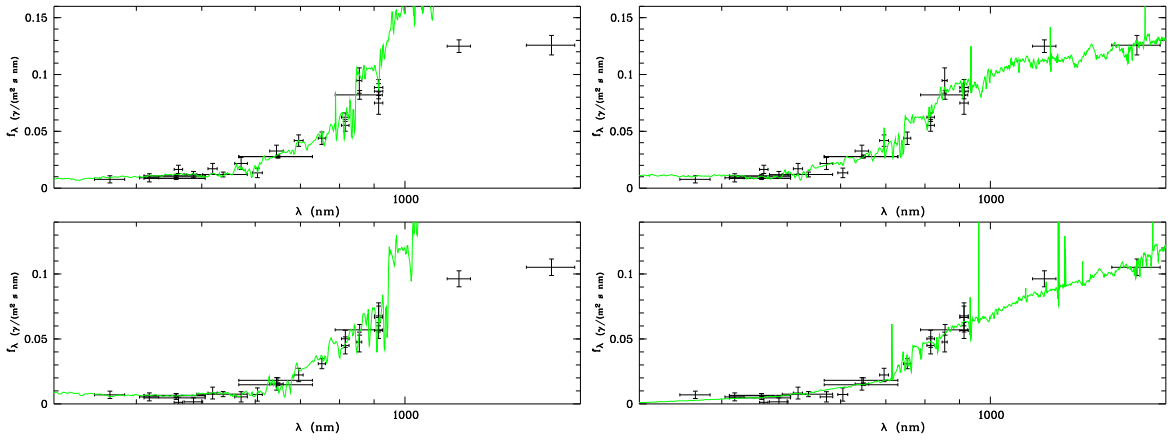

Figure 5.19: The spectral template fittings for galaxies given as examples for the tendency indicated with the arrow A' in in the SED-A_V diagram in Fig. 5.16. The fits on the optical data are displayed in the left hand side where the templates represent spectra of Sa galaxies with moderate dust extinctions, $A_V \approx 0.2$, at redshifts $z \gtrsim 1.1$. The plots in right hand side are the results of the data evaluation in the optical+NIR bands. The spectral types exhibit moderate changes, as the objects were identified as Sa/b galaxies with older stellar content, higher extinctions, $A_V \approx 0.3$ and 0.9, and lower redshifts, $z = 0.76$ and 0.92.

data, the spectral templates of Sc/S6 galaxies also exhibit an excess in the NIR band as in the previous example. The right hand plots show its correction due to the NIR-band-extention of the optical data, which is not so considerable since these galaxies are less abundant in old stars. Their spectral types remain the same, whereas the redshift and extinction values are reduced moderately.

The last examples, referred to as (1a') and (2a') in Fig. 5.16, demonstrate the improvement of their spectral template fittings. The left had plots in Fig. 5.19 are the results of the fitting on the optical data and show model spectra of Sa/Sb galaxies with similar overshots in the NIR regime as in the case of the first pair of examples. The J_1- and H-band fluxes give proper constraint for the abundance of the old stellar content in the host galaxies and their application results in better fits in the NIR regime, as seen in the right hand side plots. However, these fits have slightly lower values in the J_1 medium band than the measured fluxes, which could indicate imperfections in the templates of the galaxy spectral library.

5.2.5.4 Galaxies with Large Redshift Variation

In our R- and H-band selected galaxy sample, the group plotted with red color in Fig. 5.5 is completely isolated from the rest of the galaxies in the $z_{opt} - z_{opt+NIR}$ plane. The members of this group are determined as less evolved spirals or starburst galaxies for $z_{opt} \lesssim 0.4$ by the evaluation of the purely optical data but the inclusion of the NIR bands redistributes them in the redshift interval $1.5 \lesssim z_{opt+NIR} \lesssim 1.9$, as shown in Fig. 5.20.

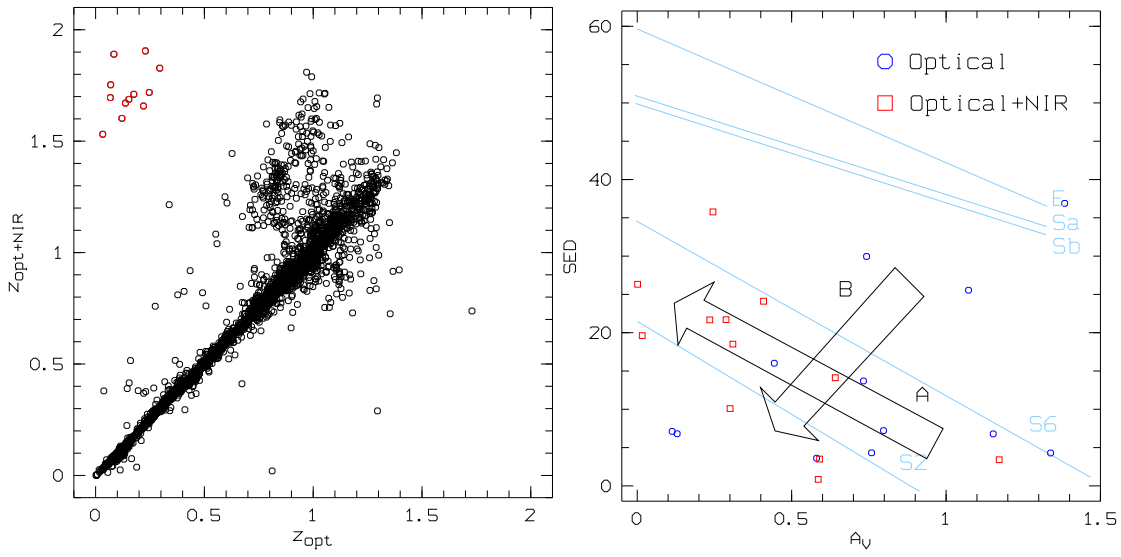

Figure 5.20: The left hand panel shows the $z_{opt} - z_{opt+NIR}$ plot for the R- and H-band selected galaxy sample, which is further restricted by the criteria $\sigma_H < 0.2$, $\sigma_{J1} < 0.2$ and $q = 3$. The red dots denote the group of the galaxies with $\Delta z/\sigma_{\Delta z,gal} > 3$ in the domain $z_{opt} < 0.5$ and $z_{opt+NIR} > 1.3$. The right hand panel is the SED vs. extinction plot for these galaxies derived from the optical (blue circles) and the optical+NIR colors (red squares), respectively. The arrows A and B indicate the general tendencies in their relocations due to the inclusion of the NIR colors in the measurement. The blue lines represent the SED vs. A_V relations of the galaxy spectral templates used in the COMBO-17+2 NIR multi-color classification.

As in the case of the previous groups, we study this enormous variation in the redshift determination of these galaxies by associating it with the trends of the differences between the spectral types and extinction levels derived from the two data sets. These trends, denoted by the arrows A and B in the SED vs. extinction diagram in Fig. 5.20, separate the objects into two groups. Some objects, following the direction of the arrow A in the SED-A_V plane, are identified as starburst galaxies in the measurement on the optical data and they become less dusty systems with older stellar content at much higher redshifts in the evaluation of the optical+NIR fluxes. Other objects follow the tendency denoted by the arrow B in the SED vs. extinction diagram in Fig. 5.20. These are evolved starburst and Sc galaxies, considering their spectral types derived from the optical fluxes. They obtain younger star populations while their extinctions are reduced in the measurement based on the optical+NIR data. The $z_{opt} - z_{opt+NIR}$ and SED vs. extinction diagrams in Fig. 5.21 show the data of two pairs of galaxies chosen as examples for the demonstration of the improvement in the fitting of the model spectra. Here, the objects denoted with (1a) and (2a) follow the tendency represented by the arrow A and the ones with (1b) and (2b) are examples for the tendency referred by the arrow B in the SED-A_V plane in Fig. 5.21. We can see the spectral template fitting for the first pair of galaxies (1a and 2a) in Fig. 5.22, where the left hand plots are derived from the optical colors and the right hand ones display template fits on the optical+NIR data set. Both of the model spectra in the left hand plots

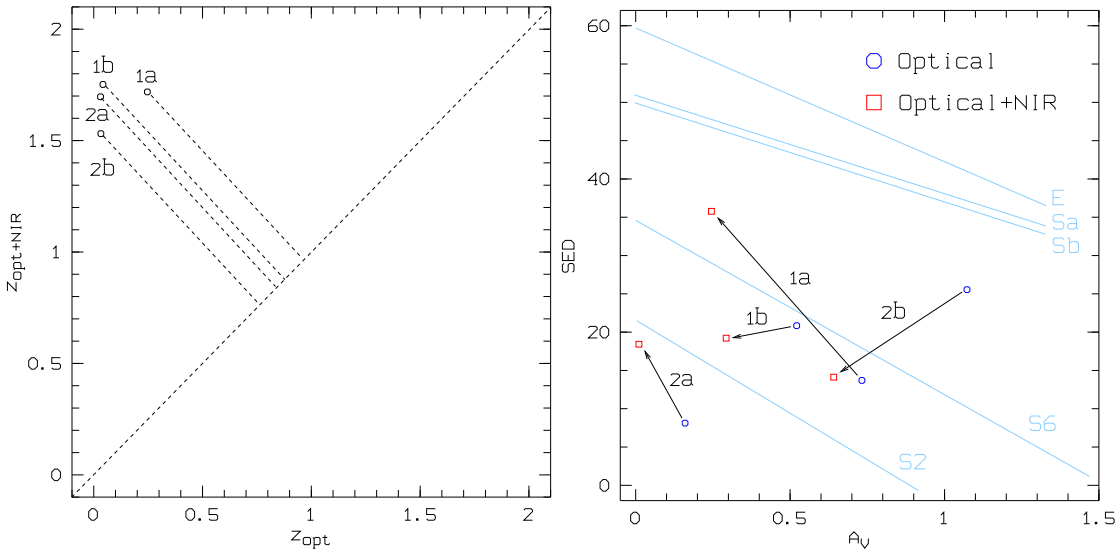

Figure 5.21: The $z_{opt} - z_{opt+NIR}$ and the SED vs. extinction plot of the galaxies given here as examples comparing the spectral template fittings derived from the optical and optical+NIR data sets. The left hand plot measures the difference between z_opt and $z_{opt+NIR}$ for each galaxy with the dashed lines connecting the data points to the diagonal. The right hand panel is the SED vs. extinction plot for these galaxies derived from the optical data set (blue circles) and the optical+NIR colors (red squares), respectively. The arrows indicate their relocations due to the inclusion of the NIR colors in the measurement. The galaxies with an increase in the mean age of their stellar content are denoted with (1a) and (2a), whereas the other pairs obtaining younger star populations are referred by (1b) and (2b).

belong to starburst galaxies with moderate (upper plot, 1a) and small dust extinctions (lower plot, 2a) for which the continuum spectra with the emission lines are not redshifted out from the

optical regime. These templates match the optical fluxes but have much lower values in the NIR regime than the measured fluxes. In the first example (upper right plot, a1) the introduction of the J_1- and H-band fluxes helps to detect the old stellar content in the host galaxy and, as a result, provides the spectal template of an Sc-type system with a lower extinction level at much higher redshift. In the second example (lower right plot, 2a), the NIR filters sample the fluxes dominated by the high-redshifted continuum spectrum, and we obtain here a dust free S2-type starburst galaxy at $z \sim 1.8$.

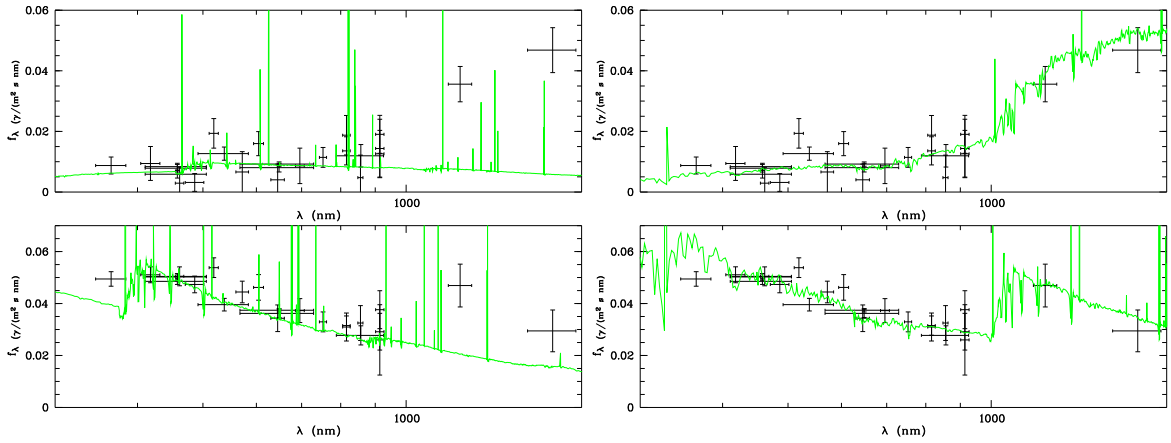

Figure 5.22: Spectral template fitting for the galaxies denoted with (1a) (upper plots) and (2a) (lower plots) in Fig. 5.21. The fittings based on the optical fluxes provide spectral templates corresponding to starburst galaxies with a relatively moderate and low dust extinctions, $A_V = 0.73$ and 0.15, with low redshifts, $z = 0.25$ and 0.03, which are shown in the left hand side. The plots in the right hand side derived form the optical+NIR data display spectral template fits corresponding to Sa/b galaxies with reduced extinction, $A_v = 0.26$ and 0.1, and with a raise of the redshifts to $\lesssim 1.7$.

The other two examples, plotted in Fig. 5.23, demonstrate that the NIR extension will help in case the multi-color classification using only the optical data fails and cannot find any matching spectral template on the optical fluxes. Both the examples are starburst galaxies, where the left hand side plots show incorrect fits, while we see starburst galaxies with moderate dust content at high redshift in the right hand side plots derived form the optical+NIR data set.

5.2.5.5 Galaxies at $z \lesssim 1$ with Moderate Redshift Variation

The last group we analyze is denoted by green dots in the $z_{opt} - z_{opt+NIR}$ diagram in Fig. 5.5 and contains galaxies scattered above the diagonal branch for $z_{opt} \lesssim 0.7$. The members of this group have moderate differences between their redshift values derived from the optical and the NIR-band-supplemented fluxes. Since the criterion $\Delta z_{gal}/\Delta\sigma_{z,gal} > 3$ selects only 9 objects in this group, their presence could have been considered as a noise in the measurement. However, the evaluation of the optical+NIR data provided satisfying spectral templates matching better on the NIR fluxes for these galaxies, compared with the fits derived only from the optical colors. Therefore, they are worth being studied in more details.

In the SED vs. extinction diagram of this group, shown in Fig. 5.24, most of the objects are identified as early-type galaxies and evolved spirals with high dust extinction by the evaluation

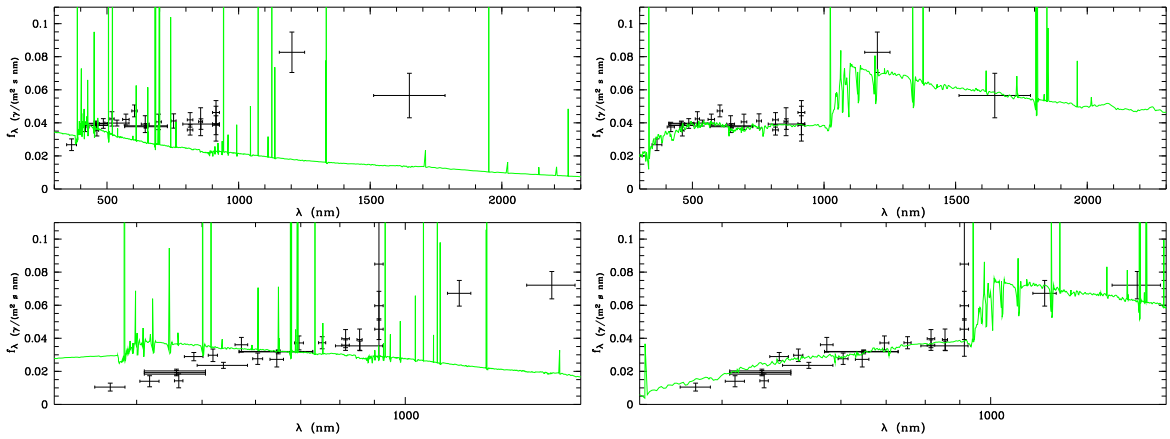

Figure 5.23: Two examples, where the fittings with the optical fluxes provide spectral templates corresponding to Sb2 galaxies, shown in the left hand side. The galaxies obtain a relatively moderate or lower dust extinction, $A_V = 0.52$ and 1.07, and are located lower redshifts, $z = 0.04$ and 0.03. The plots in the right hand side, derived form the optical+NIR data, display spectral template fits corresponding to galaxies with bluer rest-frame colors and reduced extinctions, $A_v = 0.29$ and 0.1, at higher redshifts, $z = 1.75$, 0.64.

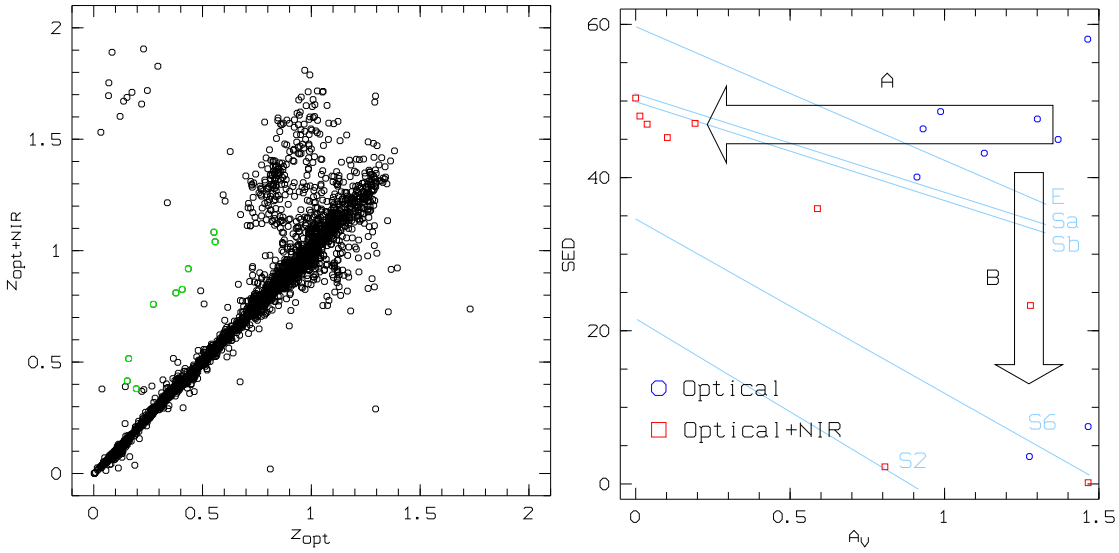

Figure 5.24: The left hand panel shows the $z_{opt} - z_{opt+NIR}$ plot for the R- and H-band selected galaxy sample with $\sigma_H < 0.2$, $\sigma_{J1} < 0.2$. The green dots denote the group of the galaxies with $\Delta z_{gal}/\sigma_{\Delta z,gal} > 3$ in the domain $z_{opt} < 0.7$ and $z_{opt+NIR} < 1.1$. The right hand panel is the SED vs. extinction plot for these galaxies, derived from the optical data set (blue circles) and the optical+NIR colors (red squares), respectively. The arrows A and B indicate the general tendencies in their relocations due to the inclusion of the NIR colors in the measurement. The light blue lines represent the SED vs. A_V correlation of the galaxy spectral templates applied in the COMBO-17+NIR multi-color classification.

of the optical data (blue circles). These objects exhibit two tendencies with respect to the differences in their spectral types and extinction levels comparing the results from the two data sets. The first one, denoted with the arrow A in the SED - A_V plot in Fig.5.24, is typical for the objects which are identified as early-type galaxies with extremely high extinctions in the measurement based on the optical fluxes and become dust-poor Sa/Sb galaxies at higher redshifts (red squares). The galaxies following the tendency indicated by the arrow B in the SED vs. A_V plot in Fig.5.24 are dusty early-type systems, spirals or starbursts in the evaluation of the optical fluxes. The measurement on the optical+NIR data determines all of them as starburst galaxies at higher redshifts while their dust reddenings undergo only slight variations or even remain the same.

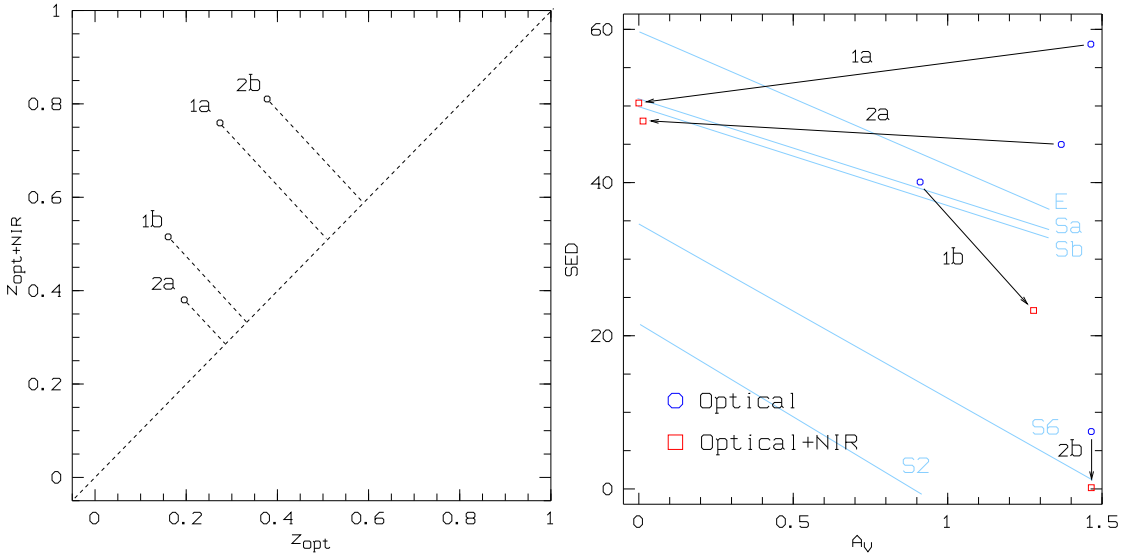

Figure 5.25: The $z_{opt} - z_{opt+NIR}$ and the SED vs. extinction plot of the example galaxies comparing the spectral template fittings derived from the optical and optical+NIR data sets. The left hand plot measures the difference between z_{opt} and $z_{opt+NIR}$ with the dashed lines connecting the data points to the diagonal for each galaxy. The right hand panel is the SED vs. extinction plots for these galaxies derived from the optical data set (blue circles) and the optical+NIR colors (red squares), respectively. The arrows indicate their relocations due to the inclusion of the NIR colors in the measurement. The galaxies with extremely large decrease in their extinctions are denoted with (1a) and (2a) and the other pair with moderate changes in their dust extinction are referred by (1b) and (2b).

As examples of the spectral template fitting, we show two pairs of galaxies for each tendency to demonstrate an improvement of the redshift mesaurement due to the NIR-band-extension of the optical colors. The $z_{opt} - z_{opt+NIR}$ and the SED vs. A_V diagrams in Fig. 5.25 characterize the differences of the astrophysical properties of the galaxies chosen as examples, comparing their data derived from the two data sets. The first pair of galaxies, designated with (1a) and (2a) in Fig. 5.25, provides examples for the tendency represented by the arrow A in the SED - A_V plot in Fig. 5.24. The plots in Fig. 5.26 show the fittings of the model spectra for the examples based on the optical and optical+NIR fluxes in the left and right hand plots, respectively. The left hand plots display spectral templates of dust-shrouded E/S0 galaxies at $z \sim 0.2$ and 0.3. The templates match the optical fluxes well but have an excess in the NIR band, which is caused

by the abundance of the old stellar content associated to these model spectra. By applying the J_1- and H-band data, we can measure the spectral contribution of the old stars in the NIR band and chose templates with younger mean age. These already match the fluxes measured in this wavelength regime, as demonstrated by the right hand plots in Fig. 5.26. The objects here are identified as Sa/Sb galaxies and their redshifts are increased by a factor of three. Although, these spirals are completely free from dust, it has no effect on galaxy spectra in the NIR regime. The matching of data and the model spectra in that wavelength range is due to the improved detection of the old stellar population up to $z \sim 2.1$.

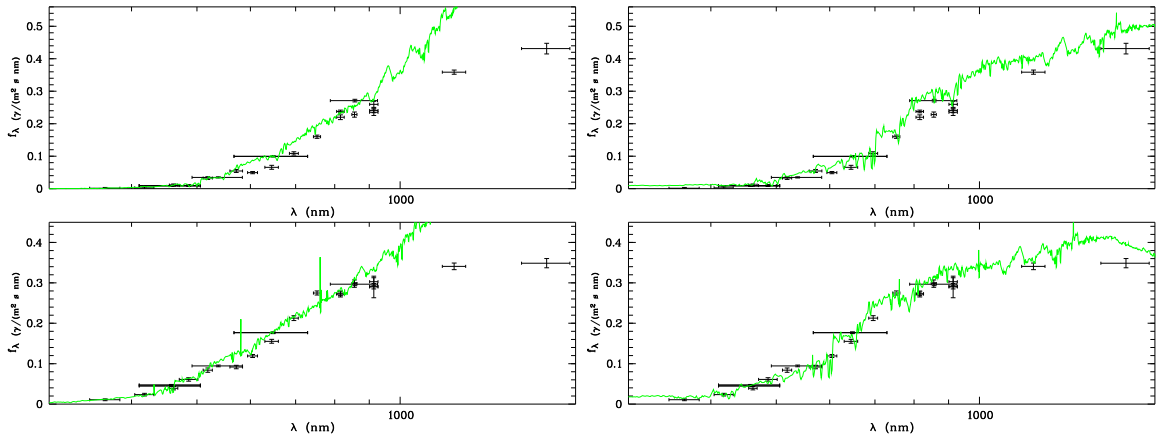

Figure 5.26: Two examples for spectral template fittings for the galaxies denoted with (1a) and (2a) in Fig. 5.25. The plots in the left hand side, derived from the optical data, show two spectral templates for E/S0 galaxies with very high extinction levels, at redshifts lower than 0.3. By supplementing these data with the NIR-band colors, we obtain template fits, shown in the right hand plots, which represent galaxies with the same spectral type but without dust, $A_V \approx 0$ and at higher redshifts, $z > 0.5$.

Another pair of galaxies is also given as an example for the other tendency represented by the arrow B in the SED vs. extinction diagram in Fig. 5.24. The $z_{opt} - z_{opt+NIR}$ and the SED vs. A_V plots in Fig. 5.25 denote this pair of galaxies as (1b) and (2b) and show that they are identified as dusty spiral and starburst galaxies, respectively. The plots in Fig. 5.27 display the spectral template fittings for these galaxies based on the optical fluxes (left hand plots) and on the optical+NIR data (right hand plots). Even though only optical fluxes are used for the fitting, there is no significant discrepancy between the measured fluxes and the spectral templates of the Sa- (upper left hand plot, 2a) and Sc-type (lower left hand plot, 2b) galaxies. However, the NIR-extension of the wavelength regime in the measurement provides better fits in the NIR band, as the right hand plots show in Fig. 5.27. Since the J_1- and H-band fluxes of the Sbc type galaxy (upper right hand plot, 2a) at $z \sim 0.4$ are still dominated by old stars, the improvement in the template fitting is considerable in the NIR regime. In the case of the S6 starburst galaxy (lower right hand plot, 2b), which is less abundant in old stars, the inclusion of NIR-band information in the optical data set does not have such a significant effect on the template fitting.

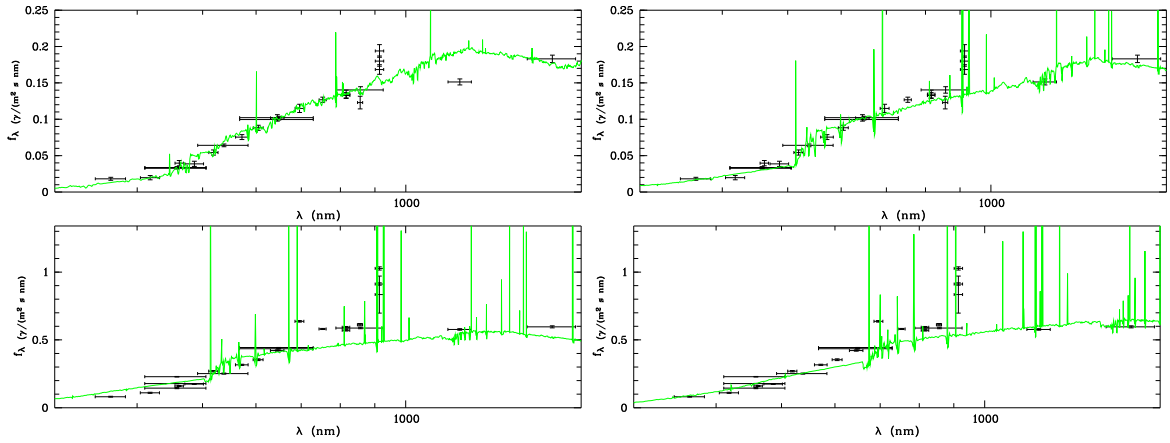

Figure 5.27: Two examples of the spectral template fittings for the galaxies denoted with (1b) and (2b) in Fig. 5.25. The plots in the left hand side, based on the measurements in optical bands, show model spectra of E/S0- (upper plot, 1b) and Sb-type (lower plot, 2b) galaxies with old stellar populations and high dust extinctions, at redshifts lower than ~ 0.4, respectively. The NIR-extention of the wavelength range of the measurement provides templates of galaxies with bluer rest-frame colors, as seen in the right hand side plots. The extinction level is increased in the first case to and does not change at all in the second one, while the redshifts evaluations provides higher values, $z > 0.4$.

5.2.6 Concluding Remarks

In this section, we have studied the improvement in the redshift determination and the fitting of the synthetic spectra on the measured fluxes for galaxies due to the supplement of the optical data with the NIR-band colors. We chose a population from the R- and H-band selected galaxy sample in the COMBO S11 field for which the variation in the astrophysical properties derived from the optical and the optical+NIR data sets was significant. We split this galaxy population into smaller groups with respect to the trends observed in the differences between their photometric redshifts, z_{opt} and $z_{opt+NIR}$, and analyse the results of the SED and extinction evaluation based on the optical and the NIR-band combined fluxes for the galaxies in each group.

The most significant group contains galaxies with the 4000 Å break in their spectra redshifted to the redward end or even out of the optical regime, i.e., at $z \gtrsim 1.2$. The measurement based on only optical bands could not detect the spectral features of their old stellar content at these redshifts. They were identified mainly as actively star-forming systems with large variation in their dust reddening and some of them as dusty early-type or evolved spiral galaxies. By including the NIR colors, we obtained mainly spiral galaxies in this population from Sa to Sbc with low extinction and some starburst galaxies with more dust as well. Hence, the improvement in the determination the physical properties can be summarized in the following statement. If we compare the redshifts, spectral types, and extinction levels measured in the optical band with the ones measured in the optical and NIR bands, we find a prominent group of galaxies for which the redshifts are redistributed from the interval $0.7 \lesssim z \lesssim 1.1$ to $1.1 \lesssim z \lesssim 1.8$ while their mean ages are increased or remained the same and their dust reddenings are reduced.

Other minor trends in the redshift variation caused by the NIR-band-extension correspond to a moderate decrease, an enormous increase, or a similar increase in z - but at lower redshifts.

These trends are either associated with the main tendency or with other patterns in the SED and extinction variation. The latter means that there are some galaxies in the population we analyzed which exhibit lowering in the mean age, i.e., they obtain bluer rest-frame colors, or their extinction level are increased, as a result of the improvement in the measurement.

However, considering the statistics of the different groups in the discussed population, the minor trends are far less important than the main tendency. We studied about 4300 galaxies in this section and found ~ 500 of them belonging to the dominant group and the number of the objects in the smaller groups is on the order of 100. This means about 14% of the studied population has a significant improvement in the measurement where $\sim 12\%$ shows the main tendency and only $\sim 2\%$ follows other trends, when the properties obtained from the optical and the NIR-supplemented data set are compared with each other.

We can extrapolate these numbers for the whole COMBO S11 field with a NIR band data deep enough to assure that the multi-color classification could produce reliable redshifts, SEDs, and extinction levels for each galaxy with $R < 24$ in the R-band selected catalogue. For $R < 24$ and $0.2 < z < 1.2$, the S11 field contains $\sim 13,400$ galaxies of the catalogue with photometric redshifts derived from optical colors. If we have enough NIR band data to produce reliable redshifts for these objects in the range $0.2 < z < 2.1$ then ~ 1600 galaxies or $\sim 12\%$ of the them, mainly starburst or Sbc galaxies in the redshift range $0.7 \lesssim z \lesssim 1.1$, will be identified as evolved spirals (Sa-Sb) at higher redshifts, $1.1 \lesssim z \lesssim 1.8$. Only a small number of the entire population, less than ~ 270, transforms from spiral galaxies to actively star-froming system or obtains higher dust reddening.

The detection of more faint red galaxies in the deeper NIR-band imaging might increase these numbers but we expect a lot of systems with small fluxes in the NIR bands to have bluer rest-frame colors or to be located at higher redshifts than ~ 2.1. This makes the measurement of their astrophysical properties relatively insensitive to the introduction of the NIR colors in the data evaluation. However, these raw statistics are derived from the analysis of the data set supplemented only with the J_1- and H-band fluxes. We suppose that the quality of the spectral template fitting will be further improved by including the other NIR-band filters, Y and J_2, as well. As a net effect, we therefore expect the extension of wavelength coverage and the increase of the number of bands will have a deep impact in the redshift and SED determination for at least 15% of the entire galaxy population.

According to our prediction the COMBO-17+4 NIR survey can achieve a significant improvement in the redshift measurement for $\sim 15\%$ of the R-band selected galaxies in the COMBO S11 field, compared to the data provided by the COMBO-17 optical survey.

Chapter 6

Scientific Results of the COMBO-17+2 NIR Project

The previous chapter was devoted to the analysis of the first results obtained in the COMBO-17+2 NIR survey from a technical viewpoint, as it focused on the improvement of the redshift measurement due to the extension of the wavelength coverage and the increase of the number of the bands in the NIR regime. In this chapter we consider the results of the first NIR-band observations carried out in the COMBO S11 field for the COMBO-17+2 NIR project from scientific viewpoint. Here, we discuss our results in two steps. The first section of this chapter gives a general overview on the evolution of the astrophysical properties derived from the survey data for the galaxy population in the target field, whereas the second section concentrates on a special application of this results. There we study the Extremely Infrared Objects detected in the S11 field on the basis of the information from the new NIR-band data.

6.1 Astrophysical Discussion of the Results

In the COMBO-17 survey the evolution of the galaxy luminosity function and the stellar luminosity density was derived for galaxies of different SEDs over the last half of the Universe's age ($0.2 < z < 1.2$). Since the NIR-band imaging of COMBO-17+2 NIR is still not deep enough to produce reliable luminosity functions and densities we cannot extend the results of the COMBO-17 survey to higher redshifts. Here, we restrict our discussion on the redshift evolution of the red galaxy counts measured in COMBO-17+2 NIR and compare it with the results of other surveys.

We begin with a short description of the R- and H-band selected galaxy sample of the COMBO S11 field. Some extrapolations are made for the expected number of galaxies which can be detected with the planned 10σ point source limit in the NIR bands for the whole survey volume of the S11 field. We give a modified definition of the galaxy SED types used in COMBO-17 and present the co-moving number counts of the total sample and of these SED types. This section is completed with the comparisons of our findings with the results of previous work in the K20 and MUNICS surveys and the other studies of Hubble Deep Field.

6.1.1 The Galaxy Sample

The available area to collect a sample of galaxies in the COMBO S 11 field for the MANOS deep project consists of three OMEGA2000 pointings (B), (C) and (D) and contains almost 27 000 galaxies with fluxes in the optical and the NIR bands. In order to extend the COMBO-17 data set with the NIR band data for that area, we have to adapt the selection criteria for the sample used for the analysis of the COMBO-17 data, which is defined by limits in aperture magnitude, in redshift and in luminosity. Objects are selected to have an aperture magnitude of $17 < R < 24$ so that the saturated or the noise affected faint sources with lower fluxes than 10σ-limit should be excluded from the sample. Since the NIR band observations could not produce significantly deeper imaging than that obtained in R band, this aperture magnitude cut is kept for the COMBO-17+2 NIR data as a selection criterion. The redshift range studied in the COMBO-17 survey was limited to $0.2 < z < 1.2$, where the lower limit is used to avoid working with too small co-moving volume and the higher one to restrict the sample to the objects whose spectroscopic information was available for checking the accuracy of the redshift measurements. This higher limit is raised to ~ 2.1 by supplementing the optical data with the NIR band fluxes, therefore the criterion $0.2 < z < 2.1$ is applied for restricting the R-band selected COMBO-17+2 NIR sample further.

The COMBO S11 field contains about 13,400 galaxies with $17 < R < 24$. The aim is to measure the redshifts of all galaxies in this sample which have redshifts lower than 2.1. The OMEGA2000 pointings B, C, and D in the S11 field produced optical- NIR-band imaging over an area of 710 arcmin^2, giving a co-moving volume of 1.89×10^6 h_{70}^3 Mpc^2 in the redshift range $0.2 < z < 2.1$ for the standard ΛCDM cosmology ($\Omega_M = 0.3, \Omega_\Lambda = 0.7$). About 9000 galaxies are located in the three quarter of the S11 field with NIR-band data from the 13,400 galaxies in the R-band selected catalogue but there are only $\sim$ 6000 object with 5σ source point limit of $H = 21.4$. Therefore we restrict our analysis in the following sections to the R- and H-band selected population with $R < 24$ and $H < 21.4$ in the S11 field.

The aim is to supplement the optical data set of COMBO-17 with medium and broad-band NIR data which are deep enough to detect a typical early type galaxy at $z \simeq 0.8$ with comparable S/N in all filters between $\lambda = 600$ and 1650 nm. In order to fulfill this requirement, we have to reach the 10σ limits $R = 24.0$, $Y = 22.0$, J=21.0, H=20.5. If more data are delivered with the OMEGA2000 instrument we will achieve deeper NIR-band imaging for the correct extention of the COMBO-17 optical data set. Then we obtain data in each NIR band for all the galaxies in the R-band selected catalogue with 10σ point source limits at $R = 24$, which allows us to provide good spectral template fittings on the measured fluxes of all the selected objects and derive more reliable astrophysical properties for them. This means if we can increase the deepness of the J_1- and H-band imaging with the specified 10σ-limiting magnitudes in the B, C, and D quadrants of the S11 field, we can determine the redshifts for almost 9000 objects over the area of 710 arcmin^2. Considering the redshift distributions for galaxies derived in deep surveys, such as the Las Campanas IR Survey or the K20 survey, we expect that the dominant part of these 9000 galaxies has redshifts below 2.1. Thus we can provide reliable redshifts for these galaxies. If we extend the NIR-band imaging over the whole S11 field, covering a co-moving volume of 2.52×10^6 h_{70}^{-3} Mpc^3 for $0.2 < z < 2.1$, we can extend the redshift evaluation to the 13,400 galaxies with

$R < 24$ detected in the S11 field. The quality of the redshift determination will be increased further if the medium Y- and J_2-band data with the specified 10σ-limiting magnitudes is also available, besides the J_1- plus H-band imaging for the whole S11 field. With the complete optical and NIR data set of the COMBO S11 field, we will be able to give a more comprehensive analysis of the evolution of different galaxy properties measured in the S11 field.

6.1.2 The Distribution of Infrared Bright Galaxies above $z \sim 1.1$

The determination of the redshift range over which the most massive galaxies were assembled can give a clue if the hierarchical merging scenario or the pure passive luminosity evolution should be preferred for the models of the galaxy formation and evolution. According to recent observations, the effects of the merging in the build up of galaxies are minor at late epochs. The luminosity function of the red galaxies (defined as redder than a present day Sbc galaxy) shows a very little change in either number density or luminosity over the redshift range $0 < z < 1$ as reported by the Canada-France Redshift Survey (Lilly et al. 1995). This indicates that their luminosity function has gone predominantly through a passive evolution since $z \sim 1$. The spectroscopic studies with the LRIS spectrograph on Keck of HAWAII deep survey fields also found that the substantial fraction of the galaxies formation occurred between $z = 0.8$ and 1.6 (Cowie et al. 1996). The more massive galaxies formed at higher redshift while the late galaxy formation accounts for the rapid evolution galaxy colors, confirming the PLE model at lower redshifts. As summarized in Sect. 5.1.3, a dramatic decline in the number and luminosity density was reported for extreme early-type galaxies form $z \sim 1$ to the present in the COMBO-17 survey (Wolf et al. 2003). By separating the galaxy population into blue and red components on the basis of an empirically determined color distribution, Bell et al. (2004) showed that the red sequence in the COMBO-17 galaxy sample evolves as expected from passive evolution. They established that the galaxies with colors of present-day luminous elliptical and lenticular galaxies are significantly redder than the reddest galaxies at higher redshift. Consequently, the rapid evolution of the galaxies with colors of present-day early-types is due to the fact that the passive evolution of their colors makes them extremely rare in the distant Universe. Therefore Bell et al. (2004) concluded the large decline in the number of red galaxies detected by Wolf et al. (2003) is heavily influenced by passive evolution in the colors of the earliest spectral types. The first analysis of the infrared data with redshifts and rest-frame luminosities from the observations of the *Spitzer Space Telescope*, combined with colors from COMBO-17, and with morphologies from *HST* images for ~ 1500 galaxies, also confirm the rapid evolution in the number of luminous infrared galaxies at intermediate and high redshift and the drastic decline in the space density of intensely star-forming galaxies. The COMBO-17+2 NIR survey with its NIR-supplemented optical data provies a possibility to back trace the redshift evolution of these types of galaxies as well.

In the following, we analyze the bright infrared galaxy counts in terms of redshifts in the COMBO S11 field. We split the galaxy sample into the four types defined by SED and the extinction level of the non-evolving spectral templates of COMBO-17+2 NIR. We study the redshift evolution of the relative fraction of these types in terms of co-moving number densities. The results are discussed in the next section, where we compare them with the finding of other

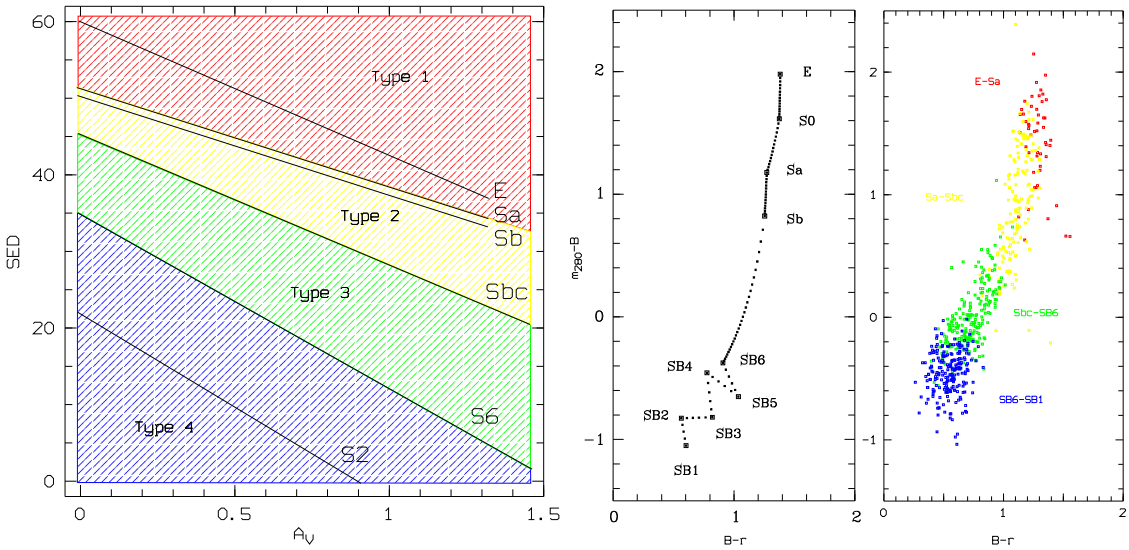

Figure 6.1: Type definition and rest-frame color of spectral templates. The left hand side plot shows SED vs. extinction relations of the present-day spectral templates, where the domains shaded with different colors represent the four ranges of morphological types of the synthetic spectra. The E-Sa range is color coded with red, the Sa-Sbc range with yellow, the Sbc-SB6 range with green, and the SB6-SB1 range with blue color. The two plots in the right hand side shows the rest-frame colors $m_{280} - B$ vs. $(B - r)$ of the template sequence (left hand panel) and those measured for the galaxy sample with $R < 25.8$, $H < 21.4$, and $z = [0.2, 0.4]$ (right hand panel). Here, the four types are also rendered in different colors.

.

surveys.

Since the distribution of the SED values in the COMBO-17 samples shows no obvious structures suggesting particular bins, Wolf et al. (2003) derived a set of four SED types by comparing the observed evolutionaly patters for the study of differential behavior between these types. The four SED types were mapped into four ranges of spectral templates from E/S0 to SB1 by dividing the SED parameter of the spectral template library into four intervals and assigning the ranges E-Sa, Sa-Sbc, Sbc-SB6, and SB6-SB1 to them. However, the analysis of dusty star-forming galaxies in the red-sequence defined by Bell et al. (2004) showed that the dust reddening is a second independent factor besides the age in galaxy colors (Wolf et al. 2005). We therefore use both the SED parameter and the extinction levels to define the four types in the two-parameter family of spectral templates. The lines representing the SED vs. extinction relations of the present-day synthetic spectra of galaxies divide the SED vs. extinction plane into different regions, as seen in the left hand panel in Fig. 6.1. If we consider the areas separated by the lines belonging the Sa, Sbc, and SB6 templates, respectively, we obtain four domains of SED-extinction value pairs, which are considered to be typical for four ranges form E/S0 to SB1. These domains are color-coded with red (E-Sa), yellow (Sa-Sbc), green (Sbc-SB6), and blue (SB6-SB1) colors in the SED vs. A_V plane. The two small plots in the right hand side in Fig.6.1 show the relationship between the four types and the rest-frame color indices, demonstrating that the definition of the four ranges E-Sa, Sa-Sbc, Sbc-SB6, and SB6-SB1 based on two parameters is still consistent with the galaxy library, as the template sequence (left hand panel) covers the color distribution

of the observed galaxies (right hand panel).

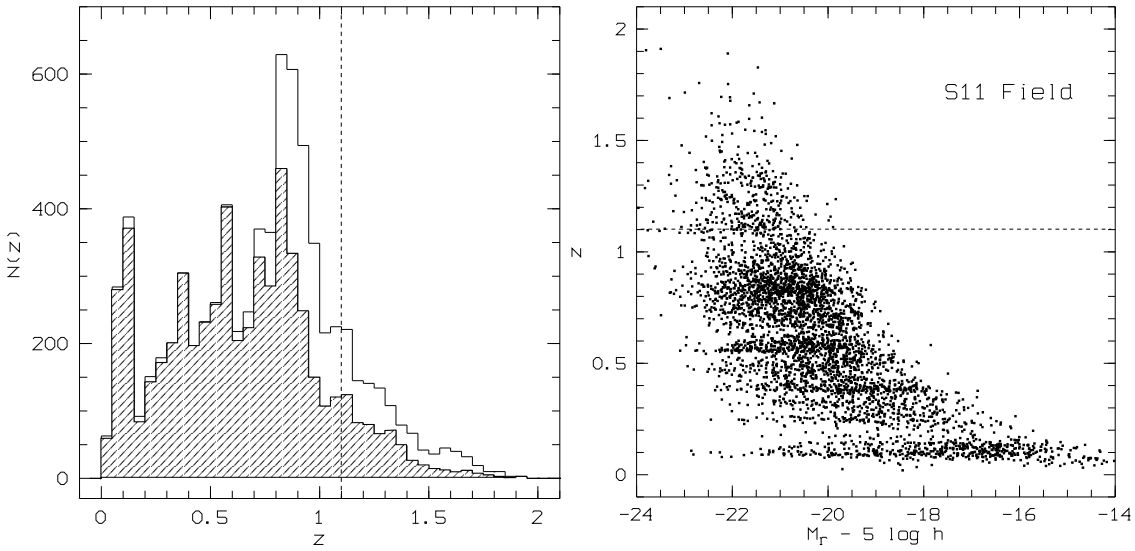

Figure 6.2: The left hand panel shows the redshift distribution for the galaxy sample for R<25.8 and H<21.4 (hollow histrogram) and for R<24 and H<21.4 (shaded histrogram) in the COMBO S11 field. The right hand panel shows the redshift over luminosity M_r in the rest-frame SDSS-r band for the COMBO S11 galaxy sample for R<24 and H<21.4. The photometric redshifts for this sample are derived from 17 optical and 2 NIR fluxes. The dashed lines at $z = 1.1$ denote the upper limit of the reliable redshift determination of the COMBO-17 survey.

.

We begin the statistical properties of the total galaxy sample in the S11 field and then split the population into the four types defined above. The observed $N(z)$ for $\sim$ 6000 galaxies with photometric redshifts and the redshift evolution of the luminosity in the rest-frame SDSS-r band for $R < 24$ and $H < 21.4$ are shown in Fig. 6.2. The peaks in the reshift histrogram at $z \approx 0.11$, 0.46, 0.58 and 0.82 are due to clusters or prominent filaments in the large scale structure. The median redshift of $N(z)$ for this galaxy sample is $z_{med} = 0.59$. We can identify finer structures in the redshift vs. luminosity diagram as well, such as the galaxies concentrating at the redshifts of 0.24, 0.32. 0.38, 1.1 and 1.4. These groups are good candidates for the cluster searching in the HIROCS project, the shalower but much wider part of MANOS survey.

Fig. 6.3 shows the sample in terms of redshift over the rest-frame SDSS r-band luminosity, but split by SED type. Here, the faint selection limit of the rest-frame color exhibits a strong dependence on the spectral type. The faint limit is the very flat for the E-Sa galaxies, whereas it is steepest for the SB6-SB1 population. The lower number of the detected fainter red galaxies at higher redshifts may be due to the that the $R < 24$ limit suppresses the red galaxies at high redshifts. This effect may also be enhanced by redshift effects on the galaxy rest-frame colors. At higher redshifts the redder galaxies are selected in their fainter rest-frame UV and need to be intrinsically more luminous to enter the sample. Therefore we are able to observe starburst galaxies at $M_r \approx 21.5$ up to $z \approx 1.7$, but in contrast, E-Sa galaxies with the same brightness limit can be traced only to $z \approx 1$. This effect is demonstrated in the redshift distributions of the different types in Fig 6.4.

Since the definition of the spectral types here are based on galaxy colors, it is interesting to

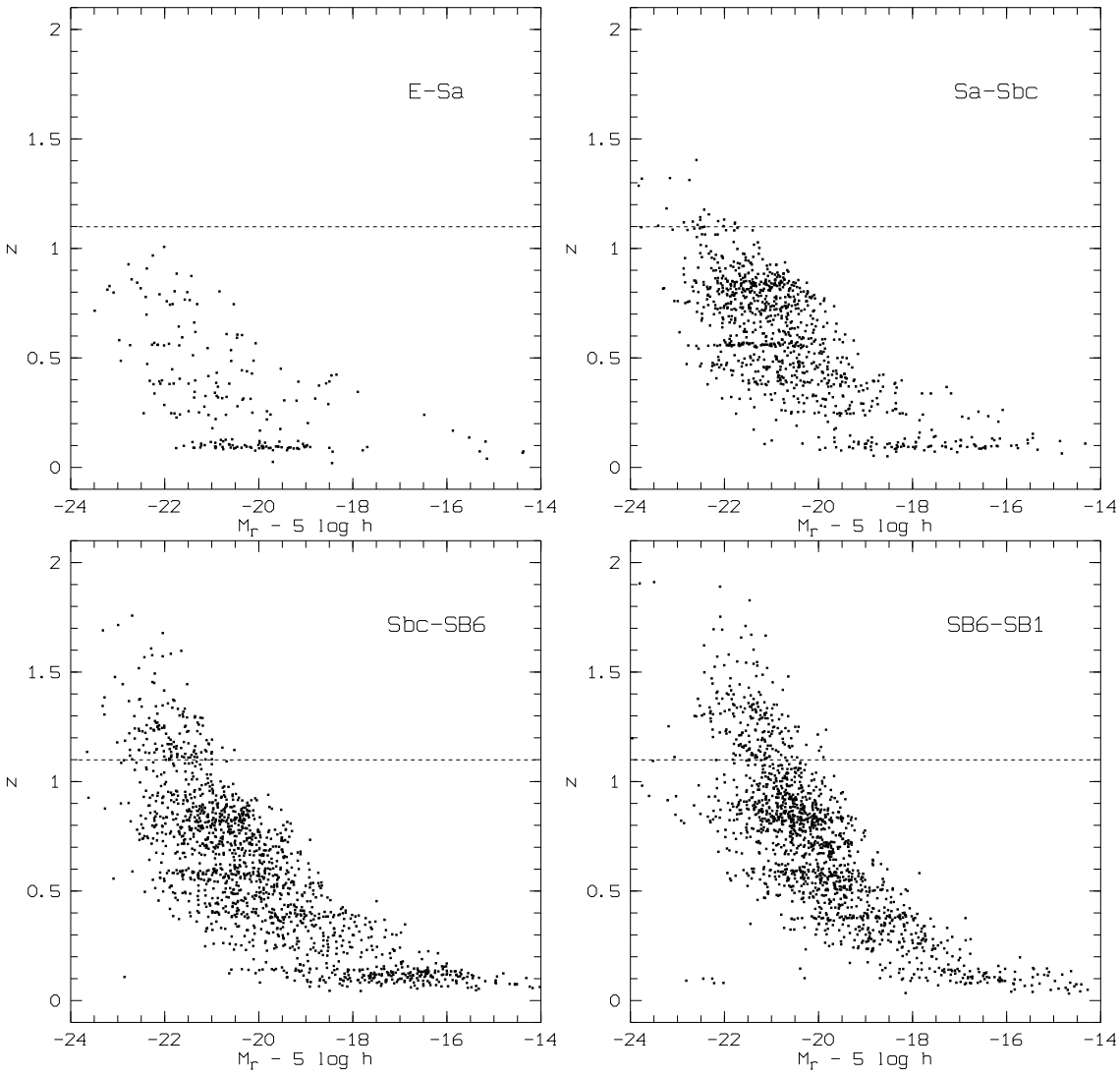

Figure 6.3: The redshift over luminosity M_r in the rest-frame SDSS-r band for the the galaxy sample with R<24 and H<21.4 in the COMBO S11 field. The photometric redshifts for this sample are derived from 17 optical and 2 NIR fluxes. The dashed lines at $z = 1.1$ denote the upper limit of the reliable redshift determination of the COMBO-17 survey.

compare their evolutional properties with those of types based on morphological classification. The nearby bright galaxy population, defined as galaxies brighter than $M_B < -20$, is becoming morphologically well characterized with recent surveys such as the Two-Degree Field Survey (2dF) and the Sloan Digital Sky Survey (SDSS) (e.g. Bell et al. 2003). An analysis of the largest morphological catalog of galaxies, the Third Reference Catalogue of Bright Galaxies (de Vaucouleurs et al. 1991), shows that approximately 75% of nearby bright galaxies are spirals, while about 23% are ellipticals and the remainder are irregular galaxies (Marzke et al. 1998). The nearby bright galaxy population is clearly bimodal, with two large populations of old massive systems and less massive galaxies with younger stellar content (Kauffmann et al. 2003, Baldry et al. 2004). We investigate how the relative fractions of the spectral types in the COMBO S11 galaxy sample with $M_B < -20 + 5\log h$ has been evolved from $z \sim 2$ to present, comparing with the development of the morphological distribution observed in other surveys at $z \sim 0$, and how this is related to the mass assembly history of these systems.

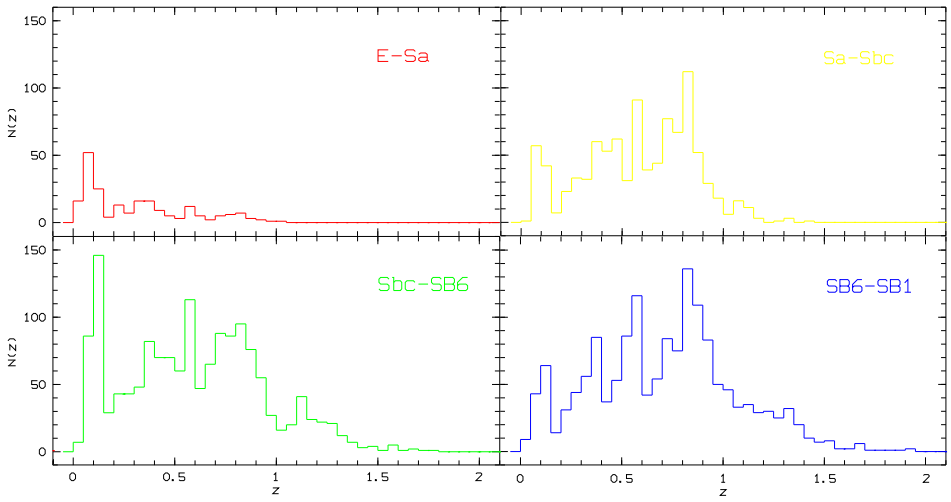

Figure 6.4: The redshift distribution for the galaxy sample with R<24 and H<21.4 in the COMBO S11 field split by SED types defined in Fig. 6.1.

.

To determine the faint end limit we can use in our analysis without missing objects, in Fig. 6.5 we check how the rest-frame Johnson B-band luminosity varies with redshift for each spectral type. Here, the steepness of the faint end limits for the different spectral types, showing similar tendencies as seen in Fig. 6.3. The faint end limit intersects the brightness limit $M_B = -20 + 5\log h$ between $z \approx 1.0$ and 1.5. Since we can detect only few E-Sa galaxies with redshifts above ~ 1 and the number of the galaxies with bluer rest-frame colors decreases considerably above ~ 1.5 as well, all the galaxies brighter than $M_B = -20 + 5\log h$ appear to be detected without a significant incompleteness at redshift $z \lesssim 1.8$.

Fig. 6.6 displays the number densities of the galaxies brighter than $M_B = -20 + 5\log h$ for the total S11 galaxy sample with $R < 25.8$ and $H < 21.4$ and for each SED types. We computed the galaxy counts in the redshift slices $\Delta z = 0.05$ from $z = 0.05$ to 2 over the area of 710 arcmin^2, covering a co-moving volume of 8.54×10^6 h_{70}^{-3} Mpc^3. It is listed in Tab. 6.1.2. The redshift evolution of number counts of the total sample rises from present to $z \sim 0.8$, exhibits

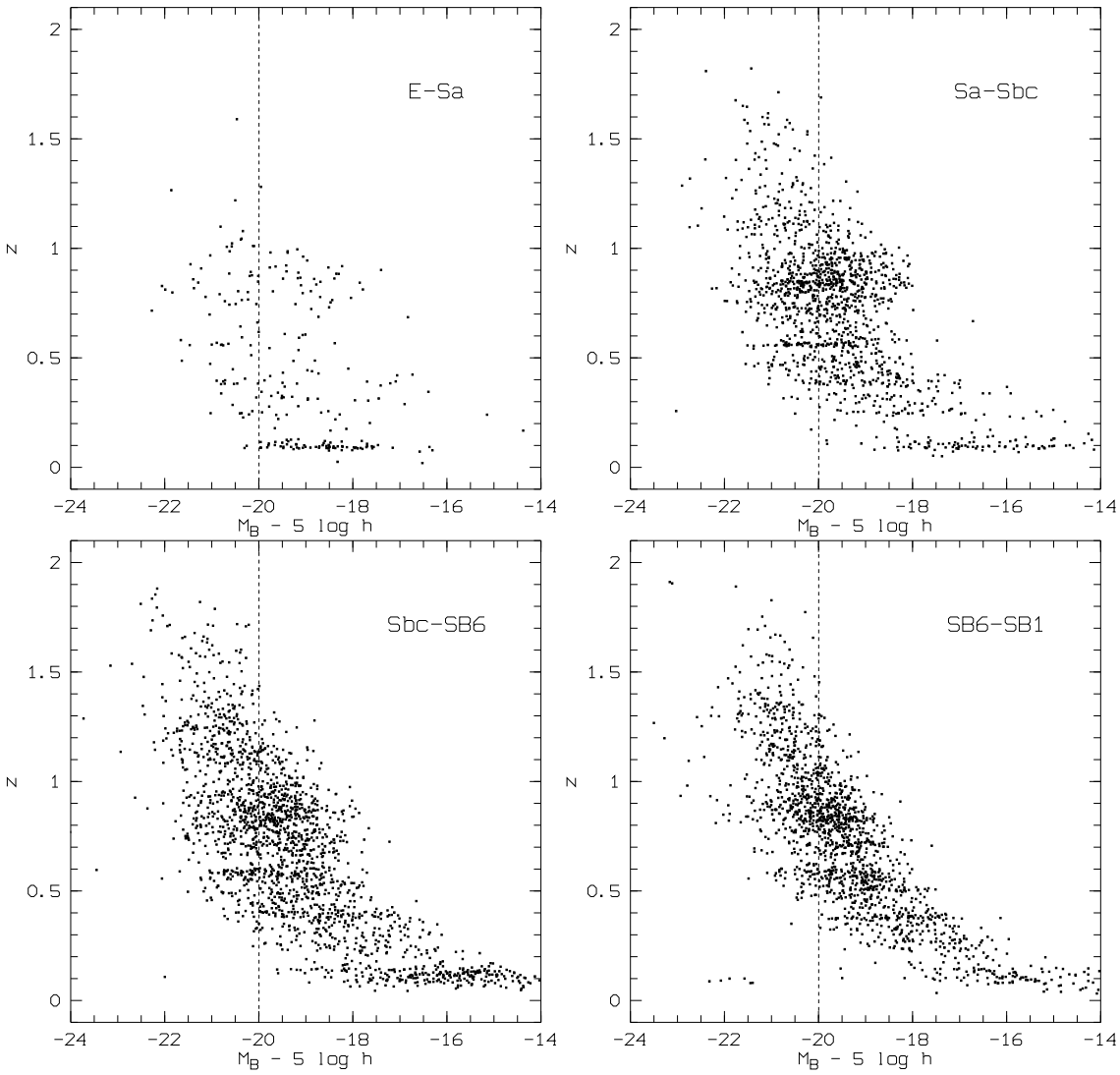

Figure 6.5: The redshift over luminosity M_B in the rest-frame Johnson band for the the galaxy sample split by spectral types with $R < 25.8$ and $H < 21.4$ in the COMBO S11 field. The vertical dashed lines indicate the absolute magnitude limit that we use for the analysis.

a maximum in the redshift range $0.8 \lesssim z \lesssim 1.3$ and declines from 1.3. Examining the galaxy counts for the E-Sa and Sa-SBc type systems reveals a deficit of ellipticals and evolved spirals and a moderate decline of less evolved spirals at redshifts larger than $z \sim 1.1$. The decline in the number of Sbc-SB6 and SB6-SB1 galaxies is milder and their relative fractions are increasing at $z > 1$, which makes them the dominate population at higher redshifts. The difference between their number densities is smaller over the whole redshift range from $z = 0.5$ to 2, compared with those of the two redder spectral types. The counts of Sbc-SB6 galaxies have stronger decrease only above $z \approx 1.5$. However, the relative number densities of the Sa-Sbc, Sbc-SB6, SB6-SB1 are quite similar, as $N(z)$ for these types is between 40 and 50 $h_{70}^3 10^4$ Gpc^{-3} in the redshift bin $z = [1.4, 1.45]$.

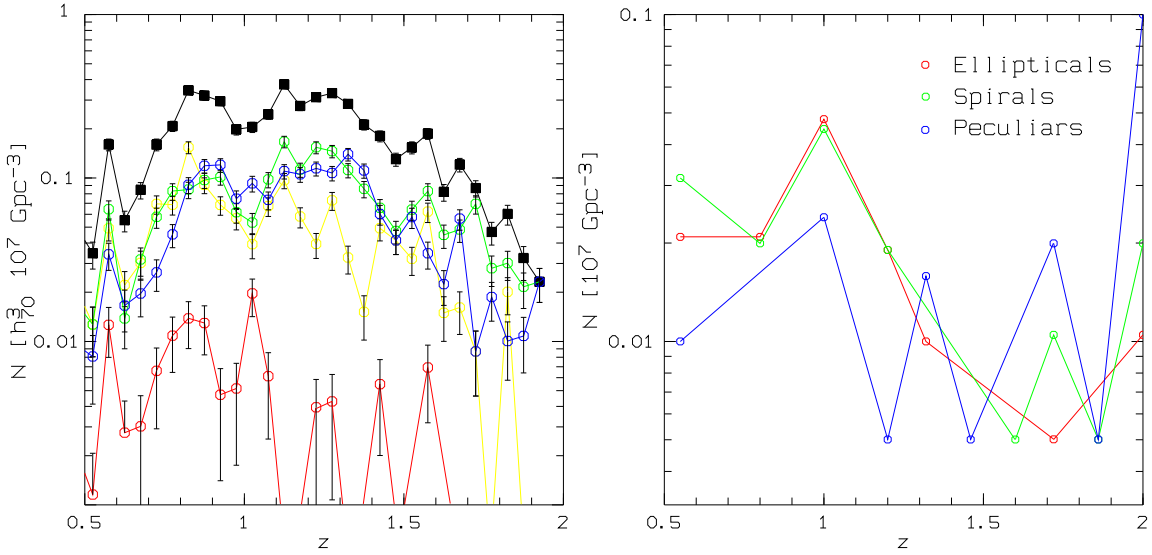

Figure 6.6: Co-moving number density evolution of galaxies brighter than $M_B = -20 + 5 \log h$. The left hand panel shows the R- and H-band selected COMBO S11 sample for the total galaxy population and the different by SED types defined in Fig. 6.1. The black squares represent the total sample while the red, yellow, green, and blue circles refer to the E-Sa, Sa-Sbc, Sbc-SB6, and SB6-SB1 type of galaxies, respectively. The error bars show the 95% confidence interval assuming Poisson statistics. The right hand panel shows the HDF-N I-band selected galaxy sample for $M_B < -20$ analyzed by Conselice et al. 2005. Here, the sample is split by morphological classes such as ellipticals, spirals, and peculiars.

.

The redshift evolution of IR bright galaxy counts derived from the optical and NIR data of COMBO-17+2 NIR can be considered as a consistent extension of the results COMBO-17 up to $z = 2.1$. The drastic decrease of E-Sa galaxies continue above $z = 1.2$, which may partly be attributed to the passive evolution of their colors and to the R-band limit, as mentioned formerly. The number of Sa-Sbc systems do not vary much in the redshift range $0.5 \lesssim z \lesssim 1.2$, also shown in the analysis of the COMBO-17 data, but their number density has a continuous increase from $z \approx 2.1$ to $z \approx 1.2$. A milder increase in the counts of the Sbc-SB6 and SB6-SB1 type galaxies can be seen in this reshift range as well, but the number of these systems starts to decrease at lower redshifts, as already found in the COMBO-17 survey.

These trends in the co-moving number densities of the four spectral types can be interpreted

Redshift	Total	E-Sa	Sa-Sbc	Sbc-SB6	SB6-SB1
			$[h_{70}^3 10^4$ Gpc$^{-3}]$		
0.05-0.10	$03.84^{+3.12}_{-1.87}$	$1.10^{+2.32}_{-0.88}$	-	-	$2.74^{+2.84}_{-1.55}$
0.10-0.15	$01.18^{+2.35}_{-0.93}$	-	-	$0.59^{+2.12}_{-0.56}$	$0.59^{+2.12}_{-0.56}$
0.15-0.20	$00.64^{+2.14}_{-0.59}$	-	$0.64^{+2.14}_{-0.59}$	-	-
0.20-0.25	$04.83^{+3.34}_{-2.12}$	$3.45^{+3.02}_{-1.76}$	$00.69^{+2.16}_{-0.63}$	$00.69^{+2.16}_{-0.63}$	-
0.25-0.30	$02.25^{+2.70}_{-1.38}$	$1.50^{+2.47}_{-1.08}$	$00.75^{+2.19}_{-0.67}$	-	-
0.30-0.35	$07.34^{+3.82}_{-2.64}$	$1.63^{+2.51}_{-1.14}$	$03.26^{+2.98}_{-1.71}$	$02.45^{+2.76}_{-1.45}$	-
0.35-0.40	$21.31^{+5.68}_{-4.58}$	$7.10^{+3.78}_{-2.60}$	$07.99^{+3.94}_{-2.76}$	$05.33^{+3.44}_{-2.23}$	$0.89^{+2.24}_{-0.76}$
0.40-0.45	$22.27^{+5.79}_{-4.68}$	$1.94^{+2.61}_{-1.26}$	$09.68^{+4.21}_{-3.05}$	$10.65^{+4.36}_{-3.21}$	-
0.45-0.50	$49.69^{+8.09}_{-7.02}$	$2.11^{+2.66}_{-1.33}$	$21.15^{+5.67}_{-4.56}$	$16.92^{+5.19}_{-4.07}$	$9.52^{+4.19}_{-3.03}$
0.50-0.55	$34.66^{+6.94}_{-5.86}$	$1.16^{+2.35}_{-0.91}$	$12.71^{+4.65}_{-3.51}$	$12.71^{+4.65}_{-3.51}$	$8.09^{+3.95}_{-2.78}$
0.55-0.60	$160.42^{+13.69}_{-12.65}$	$12.63^{+4.64}_{-3.50}$	$049.26^{+8.06}_{-6.99}$	$064.42^{+9.07}_{-8.00}$	$034.11^{+6.89}_{-5.81}$
0.60-0.65	$055.26^{+8.48}_{-7.41}$	$02.76^{+2.85}_{-1.55}$	$022.10^{+5.77}_{-4.66}$	$013.82^{+4.80}_{-3.67}$	$016.58^{+5.15}_{-4.03}$
0.65-0.70	$084.63^{+10.23}_{-09.18}$	$03.02^{+2.91}_{-1.63}$	$030.23^{+6.55}_{-5.46}$	$031.74^{+6.69}_{-5.60}$	$019.65^{+5.50}_{-4.39}$
0.70-0.75	$160.35^{+13.69}_{-12.65}$	$06.61^{+3.69}_{-2.50}$	$069.43^{+9.37}_{-8.31}$	$057.86^{+8.65}_{-7.58}$	$026.45^{+6.20}_{-5.11}$
0.75-0.80	$207.92^{+15.44}_{-14.41}$	$10.85^{+4.39}_{-3.24}$	$068.70^{+9.33}_{-8.27}$	$083.17^{+10.15}_{-9.10}$	$045.20^{+7.77}_{-6.70}$
0.80-0.85	$343.97^{+19.56}_{-18.54}$	$13.84^{+4.80}_{-3.67}$	$154.19^{+13.44}_{-12.40}$	$085.00^{+10.25}_{-9.20}$	$090.93^{+10.57}_{-9.52}$
0.85-0.90	$319.76^{+18.90}_{-17.87}$	$12.96^{+4.69}_{-3.55}$	$090.74^{+10.56}_{-9.51}$	$097.22^{+10.89}_{-9.84}$	$118.83^{+11.93}_{-10.88}$
0.90-0.95	$295.02^{+18.19}_{-17.17}$	$04.72^{+3.32}_{-2.09}$	$068.44^{+9.31}_{-8.25}$	$101.49^{+11.11}_{-10.06}$	$120.37^{+12.00}_{-10.95}$
0.95-1.00	$198.40^{+15.11}_{-14.07}$	$05.15^{+3.41}_{-2.19}$	$056.69^{+8.57}_{-7.50}$	$061.84^{+8.90}_{-7.84}$	$074.72^{+9.68}_{-8.62}$
1.00-1.05	$205.21^{+15.35}_{-14.31}$	$19.68^{+5.51}_{-4.39}$	$39.36^{+7.32}_{-6.24}$	$053.41^{+8.35}_{-7.28}$	$092.77^{+10.66}_{-9.61}$
1.05-1.10	$245.17^{+16.68}_{-15.65}$	$06.13^{+3.60}_{-2.40}$	$67.42^{+9.25}_{-8.19}$	$098.07^{+10.93}_{-9.88}$	$073.55^{+9.61}_{-8.55}$
1.10-1.15	$373.91^{+20.35}_{-19.33}$	-	$96.82^{+10.87}_{-9.82}$	$166.92^{+13.94}_{-12.91}$	$110.17^{+11.53}_{-10.48}$
1.15-1.20	$276.16^{+17.64}_{-16.61}$	-	$58.14^{+8.67}_{-7.60}$	$112.65^{+11.64}_{-10.60}$	$105.38^{+11.30}_{-10.25}$
1.20-1.25	$312.19^{+18.69}_{-17.66}$	$03.95^{+3.14}_{-1.90}$	$39.52^{+7.34}_{-6.26}$	$154.12^{+13.44}_{-12.40}$	$114.60^{+11.73}_{-10.69}$
1.25-1.30	$330.62^{+19.20}_{-18.17}$	$04.29^{+3.22}_{-1.98}$	$72.99^{+9.58}_{-8.52}$	$145.99^{+13.11}_{-12.07}$	$107.34^{+11.39}_{-10.34}$
1.30-1.35	$284.32^{+17.88}_{-16.85}$	-	$32.63^{+6.77}_{-5.68}$	$111.86^{+11.61}_{-10.56}$	$139.83^{+12.85}_{-11.81}$
1.35-1.40	$212.31^{+15.59}_{-14.56}$	-	$15.17^{+4.97}_{-3.85}$	$085.94^{+10.30}_{-9.25}$	$111.21^{+11.58}_{-10.53}$
1.40-1.45	$180.75^{+14.47}_{-13.43}$	$05.48^{+3.47}_{-2.26}$	$49.30^{+8.07}_{-6.99}$	$065.73^{+9.15}_{-8.08}$	$060.25^{+8.80}_{-7.74}$
1.45-1.50	$130.44^{+12.45}_{-11.40}$	-	$41.50^{+7.49}_{-6.41}$	$047.43^{+7.93}_{-6.86}$	$041.50^{+7.49}_{-6.41}$
1.50-1.55	$153.89^{+13.43}_{-12.39}$	-	$32.06^{+6.72}_{-5.63}$	$64.12^{+9.05}_{-7.98}$	$57.71^{+8.64}_{-7.57}$
1.55-1.60	$187.05^{+14.70}_{-13.66}$	$6.93^{+3.75}_{-2.56}$	$62.35^{+8.94}_{-7.87}$	$83.13^{+10.15}_{-9.10}$	$34.64^{+6.94}_{-5.85}$
1.60-1.65	$082.25^{+10.10}_{-9.05}$	-	$14.96^{+4.95}_{-3.82}$	$44.87^{+7.75}_{-6.67}$	$22.43^{+5.80}_{-4.70}$
1.65-1.70	$120.96^{+12.03}_{-10.98}$	-	$16.13^{+5.09}_{-3.97}$	$48.38^{+8.00}_{-6.93}$	$56.45^{+8.55}_{-7.49}$
1.70-1.75	$086.87^{+10.35}_{-9.30}$	-	$08.69^{+4.05}_{-2.89}$	$69.50^{+9.37}_{-8.31}$	$08.69^{+4.05}_{-2.89}$
1.75-1.80	$046.75^{+7.88}_{-6.81}$	-	-	$28.05^{+6.36}_{-5.26}$	$18.70^{+5.40}_{-4.28}$
1.80-1.85	$060.33^{+8.81}_{-7.74}$	-	$20.11^{+5.55}_{-4.44}$	$30.17^{+6.55}_{-5.46}$	$10.06^{+4.27}_{-3.11}$
1.85-1.90	$032.41^{+6.75}_{-5.66}$	-	-	$21.61^{+5.72}_{-4.61}$	$10.80^{+4.38}_{-3.23}$
1.90-1.95	$023.19^{+5.88}_{-4.78}$	-	-	-	$23.19^{+5.88}_{-4.78}$

Table 6.1: Co-moving number densities and their Poissonian confidence intervals of 95% for galaxies brighter than $M_B = -20 + 5 \log h$ in the in the COMBO S11 sample with $R < 25.8$ and $H < 21.4$.

as a gradual decline in the numbers and the relative numbers of normal galaxies, i.e., morphologically defined ellipticals, early- and late-type disks, at $z > 1.5$. At the same time peculiar galaxies become the dominating population at $z > 1$ (van den Bergh et al. 2001, Kajisawa & Yamada 2001). Since we defined the galaxy spectral types in terms of colors and not of morphology, the SB6-SB1 type consisting of actively star-forming systems and even the Sbc-SB6 type might easily contain peculiar or irregular galaxies as well. The deficit in the number of our E-Sa type galaxies at $z > 1$ and the growing relative fraction of the Sbc-SB6 and SB6-SB1 at $z > 1.5$ is therefore consistent with the general statement about the decline of the normal types at $z > 1.5$.

In the case of the morphologically defined types, it should be examined how much of the drop of normal galaxies is due to redshift effects. The morphological classification is able to identify lower fraction of ellipticals and spirals at higher redshift and with lower resolution and S/N, which might cause significant difference between the number of Hubble types expected and those found. This is not a problem for the four spectral types defined in terms of SEDs and extinction levels.

Now we compare our result with the findings of other surveys and analyse its consequences in the light of previous work.

6.1.3 Comparison to the Previous Results

The census of bright IR galaxies from $z = 2.1$ to present in COMBO-17+2 NIR survey is in broad agreement with the results of other comprehensive IR surveys, such as K20 and MUNICS, or that of other studies of galaxy samples selected in Hubble Deep Field. In this section, we compare our findings with their results and draw some conclusions on the galaxy evolution from $z \sim 2$ to present. If we associate our SED types with the Hubble sequence of galaxies, we can compare the evolutional patterns derived from surveys using galaxy classification based on morphology with that of our SED types.

In the analysis of the galaxy population with $M_B < -20$ in the Hubble Deep Field North and South (HDF-N and HDF-S), Conselice et al. (2005) recognized similar tendencies in the evolution of the co-moving densities of ellipticals, spirals, and peculiars to those we found in the case of the four spectral types. They showed a gradual decrease of peculiar galaxies at the expense of the normal Hubble types and considered it as circumstantial evidence that at least some fraction of ellipticals and spirals at lower redshifts originate from peculiar galaxies. The same tendencies were observed both in HDF-N and HDF-S, thus they are unlikely to be purely the result of cosmic variance. In these survey fields the galaxy population is also found to be evenly distributed in co-moving number densities for all types at $z \sim 1.5$. This appears to be some equilibrium point between the number of ellipticals, spirals, and peculiars, which breaks down at higher and lower redshifts. We obtained similar results at at $z \sim 1.4$ but only for the types with rest-frame colors redder than the present day Sa galaxies. Conselice, et al. (2005) also studied the relation between the change in relative number and luminosity densities of peculiars and normal galaxies and the evolution of stellar mass as a function of morphological type. They found that the most massive galaxies are ellipticals, with disks generally of lower mass, and peculiars having the lowest masses at redshifts $z \sim 1$. At $z > 2$, the most massive galaxies are peculiars and contain the 50 - 80% of total stellar mass in the Universe. At $z < 1$, this fraction

drops close to zero with a corresponding rise in the fraction and density of mass in ellipticals and disks, suggesting that peculiar galaxies have evolved into modern galaxies.

Large IR surveys like K20 and MUNICS, tracing the mass assembly history in galaxies out to $z \sim 2$, provided a similar picture on the redshift evolution of Hubble types. The K20 survey derived the spectroscopic redshift distribution of about 550 K-selected objects with $K_s < 20$, in a 52 arcmin^2 area. Giallongo et al. (2005), using a composite sample of I, H, and K selected galaxies from the K20 and Hubble Deep Field samples, also confirmed that the volume and luminosity densities of early and late populations with $M_B < -20.6$ appear to have a bifurcation at $z > 1$. While the star-forming galaxies slightly increase or keep constant their luminosity density, early-type galaxies decrease in luminosity density by a factor of $\sim 5-6$ from $z \sim 0.4$ to $z \sim 2.5-3$.

The evolutionary patterns of the bright IR galaxy counts for our spectral types in the COMBO S11 field show similar features as the those of the morphologically defined types, hence our results appears to be consistent with the findings of other surveys. Therefore, we can draw similar conclusions on the galaxy evolution from $z \sim 2$ to present as in the other IR surveys. The change of the relative fraction of E-Sb-type galaxies and the actively star-forming systems defined via their bluer rest-frame color probably indicates that some massive early-type galaxies originate from peculiars at high redshift. The dramatic decline of the E-Sb type systems with increasing redshift also demonstrates the important role of the passive evolution of galaxy colors besides the merging processes in the variation of the relative fractions of different spectral types.

6.2 Studying of Extremely Red Objects in the COMBO-17+2 NIR Project

The extragalactic objects with extremely red optical-NIR colors are among the most interesting topics in the modern cosmology and their nature is still controversial. The Extremely Red Objects (hereafter EROs) were discovered in the K-band survey of Elston, Rieke & Rieke (1988) and at that time thought to be good candidates for primeval galaxies at extremely high redshifts. Subsequent observations (Elston, Rieke & Rieke 1989), however, showed these objects are elliptical galaxies at $z \approx 0.8$. Although many groups also confirmed that bright objects with extremely red colors are old ellipticals (Spinrad et al 1997; Cimatti et al. 1999; Soifer et al. 1999; Liu et al. 2000), other surveys identified them as dusty starburst galaxies (Spinrad et al. 1997, Cimatti et al. 1999; Smail et al. 1999; Gear et al. 1999). Indeed, such red colors, originally defined by high $R-K$ values, are consistent with the SEDs of both types of systems and can be explained by two mainly opposing scenarios of galaxy evolution. The relative fraction of these two classes in the ERO population is therefore very important for the modeling of the galaxy formation in the Universe and more and more studies reporting the results of the latest (mainly) infrared surveys are also devoted to the analysis of the nature of their ERO sample.

The development of large format and high resolution NIR cameras with wider field instrumentation, such as OMEGA2000, has enabled systematic field surveys to cover enough area to assemble significant samples of EROs, which has given new prospects for their study. However, we focus on only objects which are bright in the NIR regime, mainly because the H and J_1 band

data collected in the COMBO-17+2 NIR survey is not yet as deep as aimed for the extension of the optical data set of COMBO-17. The COMBO-17+2 NIR project, using the OMEGA2000 camera, indeed detected a population of galaxies with very red colors in the COMBO S11 field. In this section we study some properties of these objects, such as their redshift distribution and SEDs, by exploiting the facilities of the COMBO-17 multi-color classification. Before the detailed analysis, we give the selection criterion used to define our ERO sample. Then we describe the results of the quality test of the spectral template fitting for these extremely red galaxies, which helped us to characterize the reliability of their redshift measurement together with their SED and extinction determination. In the first part of the analysis of our ERO sample, we present the redshift distribution of EROs and compare it with the results of other surveys. This is completed with the classification of the ERO types by applying color-color selection methods based on both models and observations. Based on this information there is a discussion on the old elliptical-dusty starburst dichotomy in the last part, where describe the nature of the ERO population detected in the COMBO 11 field, and draw some conclusion on the constraints which it imposes on cosmological models.

6.2.1 ERO Selection

Elston, Rieke & Rieke (1988) found a new class of extragalactic objects in the K band selected sample of their deep 2 micron survey which had $R-K$ colors of about 5 at $K \approx 17$ (in Vega magnitudes). In the $R-K$ vs. K diagram these objects are located above the group of red elliptical galaxies at moderate redshifts. They are separated from the red ellipticals by a "red envelope" representing a passively evolving brightest cluster galaxy without ongoing star formation (taken from Bruzual's model 1983). Since the color $R-K=5$ means considerably redder spectra than that of the "normal galaxies" scattered below the red envelope, the selection criterion for Extremely Red Objects was introduced as $R-K>5$ and $K \leq 18.5$. In the last decade this criteria became a general definition of very red galaxies with slightly different color cuts and luminosity thresholds, $R-K \leq 4-6$ and $K \leq 20-22$, e.g. in the K20 survey (Cimatti et al. 2002) or the Subaru/XMM Deep Field Survey (Miyazaki et al. 2002).

Besides these traditional ERO definitions based on the $R-K$ color, other galaxy surveys also used other NIR band filters for ERO selection. In the NIR observation of CDF/HDF, Saracco et al. (2001) selected EROs as objects redder than $J-K_s=2.3$ at $K \leq 22.0$, which would in principle be a color threshold for passively evolving galaxies at $z>2$. The Las Campanas Infrared (LCIR) Survey provided H band imaging, hence the color cuts $R-H>4-5$ and $I-H>3-3.5$ were applied in the magnitude range $19<H<20$ in the survey sample (Firth et al. 2002). These colors are still considered to be characteristic of elliptical galaxies at $z \gtrsim 1$, high-redshift star-forming galaxies reddened by dust at high redshift, and obscured AGNs. Nevertheless, the filter pairs $R-H$ and $I-H$ are closer together than the more traditional $R-K$ and they are therefore less sensitive to the smoother break in spectra of dusty galaxies compared with the strong Balmer jump in those of evolved galaxies at $z \sim 1$. The $I-H$ cut is also more sensitive to evolved galaxies which, as a result of small amounts of residual star formation following late merger events, would be missed from an $R-K$ color cut.

The ERO population studied in the COMBO-17+2 NIR survey was chosen from an R- and

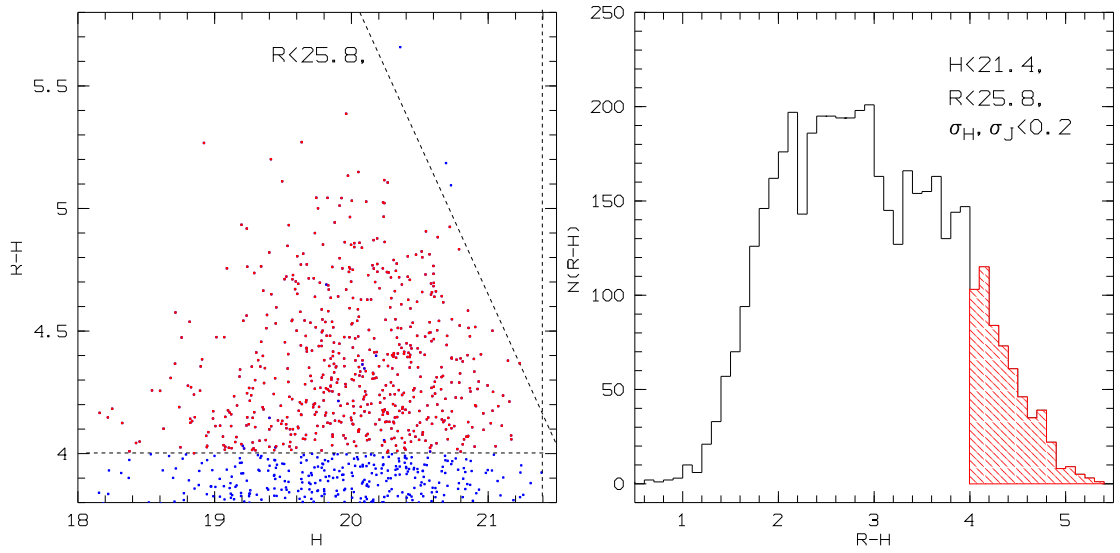

Figure 6.7: In the left figure the color $R-H$ plotted against H for the galaxies with low measurement error in their NIR-band fluxes, $\sigma_H, \sigma_{J1} < 0.2$ in the COMBO S11 field. The dashed horizontal line corresponds to the threshold $R-H=4$ for selecting EROs. The dashed skew and vertical lines indicates the $R=25.8$ and $H=21.4$ limiting magnitudes, respectively. The red dot denotes the EROs selected with this criterion. The right figure shows the $R-H$ color distribution of the galaxy sample with $R<25.8$, $H<21.4$, and $\sigma_H, \sigma_{J1} < 0.2$. The red shaded area represents the ERO population in the S11 field.

H-band selected galaxy sample of the COMBO S11 field. For the deep imaging in R band the 5σ detection limit is 25.8 mag while the shallower H-band imaging produced an 5σ limit of 21.4 mag. Therefore we restricted the galaxy population with $R<25.8$ in the S11 field to $\sim$ 4700 objects by applying the natural magnitude limit $H<21.4$ together with the criteria $\sigma_{J1}, \sigma_H < 0.2$. In this R- and H-band selected sample we defined our ERO population with the color cut $R-H>4$ which provided 620 objects for our analysis (Fig. 6.7). The $R-H$ color distribution of the total sample with a median of ~ 2.5 demonstrate that the selection criterion applied here probes about the 13% of the galaxies with the reddest SEDs

6.2.2 Testing of the Spectral Templates for EROs

Since the techniques applied to classify EROs as early-type ellipticals or dusty starburst galaxies are based on the measured colors, it is crucial to know if the result of this method is consistent with the statistics of the astrophysical properties derived from the COMBO-17+2 NIR multi-color classification for the ERO population. The reliability of the redshift measurements and SED and extinction determinations highly depends on the quality of the spectral template fitting. This means the model spectra have to match the measured data in order for the data analysis to provide reliable redshift information for all the galaxies in the COMBO S11 field, including the ERO population. In Section 1.2.5 we have already investigated the improvement in the quality of the spectral template fitting due to the extension of the wavelength range into the NIR regime. In this section we check whether it applies for the ERO sample as well, by studying the improvement in the redshift measurement and the SED determination.

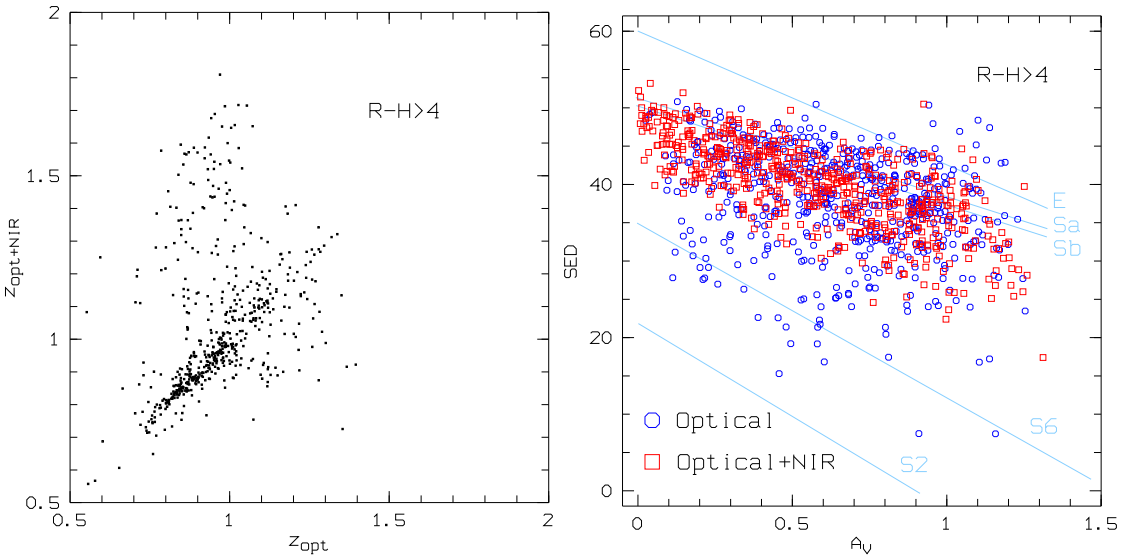

Figure 6.8: The redshift and SED vs. extinction diagrams based on optical and optical+NIR data for the ERO population defined by the $R-H>4$ in the COMBO S11 field. The light blue lines in the left diagram represent the galaxy spectral templates for various Kinney types used in the COMBO-17 multi-color classification.

We start again with a comparison of the redshift measurements of EROs based on optical and optical+NIR data. In the $z_{opt+NIR}$ vs. z_{opt} plot of the ~ 600 EROs detected in the S11 field the vertical branch between $z \sim 0.8$ and 1.2 and the diffuse group above it are the two characteristic features which have already been studied in the previous chapter (Fig. 6.8). Almost 100 objects in the diagram belong to the group above the diagonal branch, indicating the influence of the inclusion of NIR colors on the redshift determination. The different distributions of the ERO population plotted in the SED vs. extinction diagram for both the optical and optical+NIR data also demonstrate this impact on the determination of the spectral types.

The measurement based only on optical data identified the objects in the ERO sample mainly as early-type galaxies (Sa) and evolved spirals (Sb) but numerous younger spirals (Sc) and starburst galaxies were also detected among them. The extension of the wavelength range of the measurement to the NIR regime reduced this broad variation in the SEDs. The galaxies in ERO sample represent more evolved galaxies (Sa-Sb type) without star-forming systems. So the inclusion of NIR band data results in a more uniform distribution of the spectral types. This is consistent with the expectation that the ERO definition based on the $R-H$ color selects galaxies with older stellar population to dusty starbursts.

Comparing the two results, we see the NIR-supplement of the optical data base has a double influence on the measurement. The old stellar population dominating galaxy spectra in the NIR regime became detectable with the extension of wavelength coverage to the NIR bands. This allowed us to identify early-type galaxies or Sa/Sb-type spirals, which were erroneously detected as starburst galaxies on the ground of the optical colors. Furthermore the additional color information also helps to disentangle the age-extinction degeneracy. That is, several objects which had been determined as dust shrouded spirals in the analysis based on the optical data are identified as early-type galaxies with lower extinction with the inclusion of NIR data.

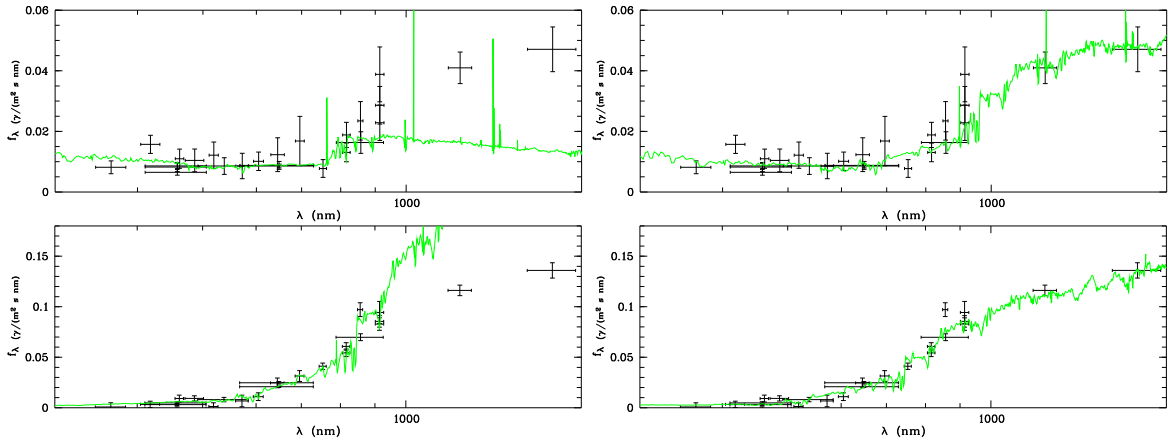

Figure 6.9: The upper and the lower pairs of the plots are two examples of the template fittings for EROs. In the first example the plot in left hand side, derived from the optical data, show a dust poor S6-type galaxy, $A_V = 0.1$, at the redshift of 1.05. By supplementing the optical data with the NIR-band colors, we obtain a template fit, displayed in the right hand side, which belongs to an extinction free Sb galaxy ($A_V \approx 0$) but at a higher redshift, $z = 1.41$. In the second example we can see a spectral template for an Sa galaxy with a higher extinction, $A_V = 0.7$, at $z = 1.12$ in the left hand side plot, as a result of the measurement on the optical colors. The NIR-band extension of data set produced a template fit, plotted in the right hand side, which represents an early-type galaxy but with a lower extinction, $A_V = 0.4$, and a lower redshift, $z = 0.87$.

We demonstrate these two characteristic improvements in the measurement with the examples of the spectral template fitting for EROs, shown in Fig. 6.9. Here, the upper plots give an example how the appearance of old stellar population influenced the template fitting. The left plot shows a model spectrum of a starburst galaxy. This result of the template fitting is based on the optical data and therefore matches to the optical fluxes well but is not consistent with the redshifted 4000 Å break in the J_1 and H bands. With the new information in the two NIR bands, we can also probe the fluxes in the NIR regime too and detect the bump for $\lambda \gtrsim 800$ nm caused by the old stellar population in the host galaxy, as shown in the right hand panel. The second pair of plots is a typical example for the disentangling of age-extinction degeneracy. Here, the spectral template fits on the optical fluxes. The rise from $\lambda \approx 500$ nm in the spectrum due to the old stars is also detected since the Balmer jump is not redshifted out from the optical regime completely. However the measurement based only on optical colors cannot determine the steepness of the rise and the model spectrum has an excess in the J_1 and H bands, caused by the high dust extinction. By including the two NIR bands in the measurement, we can adjust the fitting in that regime, which produces a template spectrum of a galaxy with less dust content and a more advanced stellar population.

Before analyzing the redshift distribution of the ERO samples in the COMBO S11 field, we have to check if the objects with mismatching spectral templates cause any artifacts in the redshift measurement.

In order to characterize the quality of the χ^2-fitting, we use a distance function d calculated in the multi-color classification as follows: The classifier determines the differences between the template values and measured fluxes for each filter. These differences are then weighted with

respect to color errors and added in quadrature providing the square of the distance function. The quality of a fit is considered satisfactory for $d < (4-5)\sigma$, where σ is the dispersion of the differences between the fit and the data points. In the case of the ERO sample, we checked the result of the template fittings fulfilling the criterion $d < 4\sigma$ and found the quality of the fittings evaluated by eye inspection was satisfactory for $d < 2\sigma$. If we compare the histograms of the ERO sample with a subsample where the χ^2-fitting produced well matching results with $d < 2\sigma$, we see some variations in each case (Fig. 6.10). The redshift distribution of the ERO population contains a peak around $z \sim 0.9$ with a steep rise in the left hand side and a slowly descending tail to higher redshifts. The amplitude of this peak is decreased by the exclusion of the objects with non-satisfactory template fitting, but it is still present in the histograms of the restricted samples with bluer color cuts. We conclude that the full ERO sample can be used to study the properties of the ERO populations, at least in their qualitative analysis.

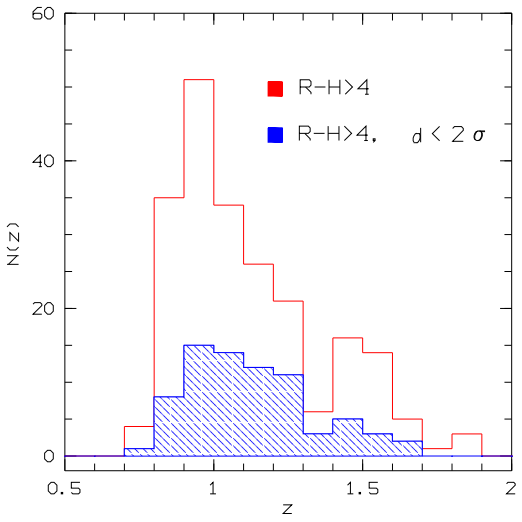

Figure 6.10: The observed redshift distribution of two EROs sample with different color cuts in the COMBO S11 field. The blue histograms show the total ERO sample selected by the corresponding criterion, while the red ones represent subsamples with matching spectral templates.

6.2.3 The Redshift Distribution of EROs

In Section 2.1.2 we discussed the redshift distribution of the total R- and H-band selected galaxy sample in the COMBO S11 field. Here, we concentrate on the ERO population in this sample. As already mentioned in the introduction, a large fraction of EROs are thought to be passively evolving galaxies at high redshift, thus the study of their redshift distribution helps to place constraints on the evolution of elliptical galaxies at $z \gtrsim 1$.

In this section, we discuss the observed redshift distribution, $N(z)$, of the ERO populations in the COMBO S11 field, defined by the selection criterion $R-H > 4$. The shape of $N(z)$ for our ERO sample has a strong peak around its median value z_m with a steep rise at lower redshifts and a slowly descending tail towards the higher ones, for each brightness limit (Fig. 6.11). The median redshifts were measured to be 1.02, 1.01 and 0.97 for the brightness limits $H < 21.4$, 20.5 and 20.0. Although, the number of the red galaxies detected in the COMBO-17+2 NIR survey is

lower at $z \sim 1$ than that measured in the LCIR survey, the semi-analytic model still underpredicts our observed ERO counts by a factor of two. The PLE models generally overpredict the number of EROs even in the case of the LCIR survey, no matter if E/S0 population is modelled by a burst of a simple star population (SSP) at high-redshifts or an exponential starburst with $\tau = 1$ Gyr (McCarthy et al. 2001). Nevertheless, by adjusting the e-folding time and z_f, it is possible to produce results in the PLE models which fit the observed ERO numbers (Sommerville et al. 2004).

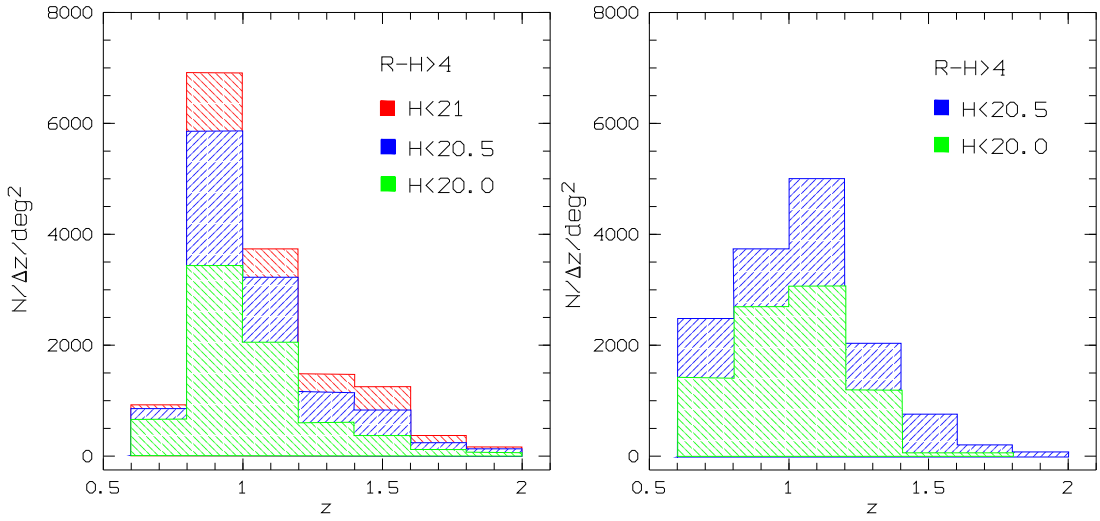

Figure 6.11: The observed redshift distribution of ERO samples in COMBO S11 field (left hand panel) and the LCIR survey (right hand panel) with the color cut $R - H < 4$ for different brightness limits in H band.

The shape of $N(z)$ for our ERO sample would also suggest that a color cut of $R-H > 4$ selects mainly early-type galaxies with advanced stellar population. Our ERO sample has a sharply peaked redshift distribution around z_m, while $N(z)$ for the spiral-like galaxies and irregular ones is broader as there is a lower level clustering among the dusty star-forming EROs. The weak clustering of high redshift blue galaxies does not support our EROs being major mergers building up an elliptical galaxy. In contrast, the clustering amplitudes we derive later will show that our EROs are much more positively correlated, indicating they are early-type galaxies at $z \sim 1$.

Similar redshift distributions were measured for ERO population in the H-band selected sample of the Las Campanas Infrared Survey as well (McCarthy et al. 2001, Firth et al. 2002). The median redshifts of the EROs with the color cuts $R - H > 4$,4.5 and $I - H > 3$,3.5 and the flux limits $H < 20$,20.5 are typically 1-1.2, where the redder samples, dominated by luminous spheroidals, have medians at the higher redshifts. The redshift range is relatively restricted, especially for the redder populations, also confirming the strong angular clustering observed for these objects.

The shape of the redshift distribution of galaxies indicates stronger or weaker clustering properties in a particular field but the cosmic variance in their abundance can only be characterized with their differential number counts and surface densities measured in different fields. In the COMBO S11 field 292 EROs, defined by the color cut $R - H > 4$ with the brightness limit $H < 20.0$, were found in an area of ~ 710 arcmin^2 of 3 OMEGA2000 pointings. It gives the

total surface density of $0.41^{+0.15}_{-0.11}$ arcmin^{-2} for EROs with the uncertainties corresponding to 1σ confidence limits.

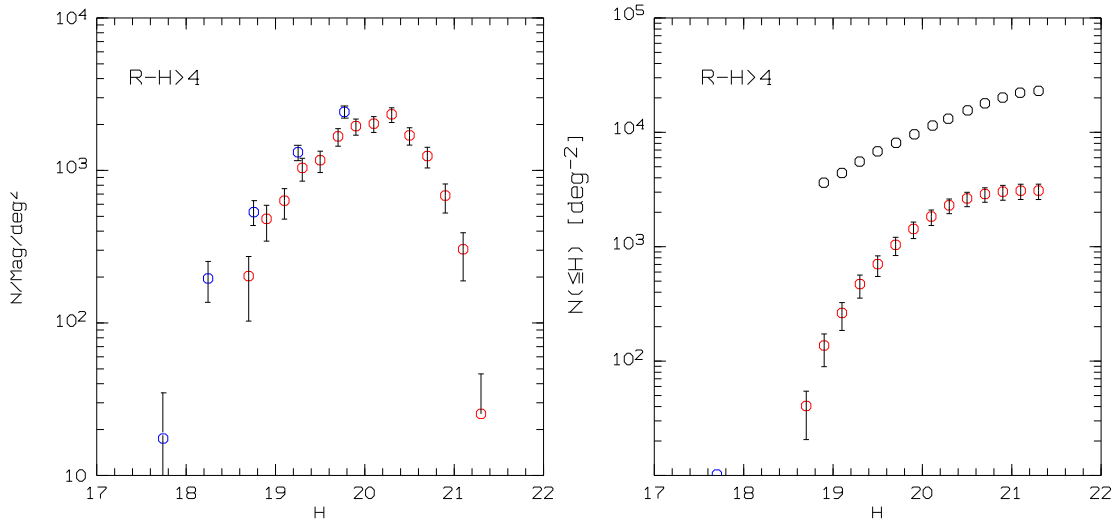

Figure 6.12: The differential number counts (left hand panel) and the cumulative surface density (right hand panel) for EROs as a function of H magnitude over 0.2 deg^2 of the COMBO S11 field. The red circles are the H counts from the COMBO S11 field for $R-H>4$ and the black squares represent the total galaxy sample. The blue circles are the H counts measured in the LCIR survey for $R-H>4$ (McCarthy et al. 2001). The error bars show the 95% confidence interval assuming Poisson statistics.

In Fig. 6.12, we present the H-band differential number counts and the cumulative surface brightness for the ERO sample of the COMBO-17+2 NIR and the LCIR surveys. The left hand panel contains the red galaxy counts measured in the COMBO S11 field and in the LCIR survey for $R-H<4$. Both the magnitudes and the slopes of the galaxy counts are almost the same for the COMBO and LCIR ERO sample. The red galaxies have steeply-rising number counts with the H magnitude in both surveys. The steeper bright end slopes are due to the shape of the bright-end luminosity function of the red population, and to the fact that most of the foreground galaxies ($z \lesssim 1$) have been excluded from the red samples. The consistent slopes between the two red subsamples suggest that the underlying luminosity function is very similar. The right hand panel in Figure 6.12, shows the cumulative surface density measurements of the galaxies with $R-H>4$ as a function of the H-band magnitude (red circles) for COMBO S11 field and the LCIR survey. The surface density of EROs were measured to be 0.5 arcmin^{-2} in the LCIR ERO population for $R-H>4$ and $H<20.0$ over an area of 744 arcmin^2 (Firth et al. 2002), in a good agreement with results of the COMBO-17+2 NIR survey.

In the K20 survey of a flux-limited sample with $K \leq 20$, Cimatti et al. (2003) obtained spectroscopic redshifts for a subsample of 47 EROs with $R-K>5$. The redshift distribution of their ERO population split into E/S0, spiral-like and irregular types by morphological classification is strongly peaked at about 1.3 (Fig. 6.13).

Moustakas et al. (2004) likewise constructed a large sample of EROs in the GOODS-South field using U'- trough K_s-band imaging with the selection criterion $R-K_s>5.0$, 5.6 and 6.0 for two magnitude limits $K<21$ and 22. Their full sample ($R-K_s>5.0$, $K_s<22$) consists

$H_{lower} - H_{upper}$	N [mag^{-1}deg^{-2}]	N($\leq H_{upper}$) [deg^{-2}]
18.6-18.8	203^{+100}_{-070}	40^{+019}_{-014}
18.8-19.0	482^{+137}_{-109}	136^{+048}_{-036}
19.0-19.2	634^{+154}_{-126}	264^{+078}_{-061}
19.2-19.4	1039^{+188}_{-161}	472^{+116}_{-093}
19.4-19.6	1166^{+198}_{-171}	705^{+156}_{-128}
19.6-19.8	1673^{+232}_{-205}	1039^{+202}_{-169}
19.8-20.0	1952^{+249}_{-222}	1430^{+252}_{-213}
20.0-20.2	2028^{+253}_{-226}	1835^{+303}_{-258}
20.2-20.4	2332^{+269}_{-243}	2302^{+356}_{-306}
20.4-20.6	1699^{+234}_{-207}	2641^{+403}_{-348}
20.6-20.8	1242^{+204}_{-177}	2890^{+444}_{-384}
20.8-21.0	6845^{+159}_{-131}	3027^{+476}_{-410}
21.0-21.2	3042^{+115}_{-086}	3088^{+499}_{-427}
21.2-21.4	2535^{+580}_{-021}	3093^{+510}_{-431}

Table 6.2: The differential number counts and the cumulative surface density for EROs as a function of H magnitude over 0.2 deg^2 of the COMBO S11 field. The quoted errors are Poisson with 95% confidence interval.

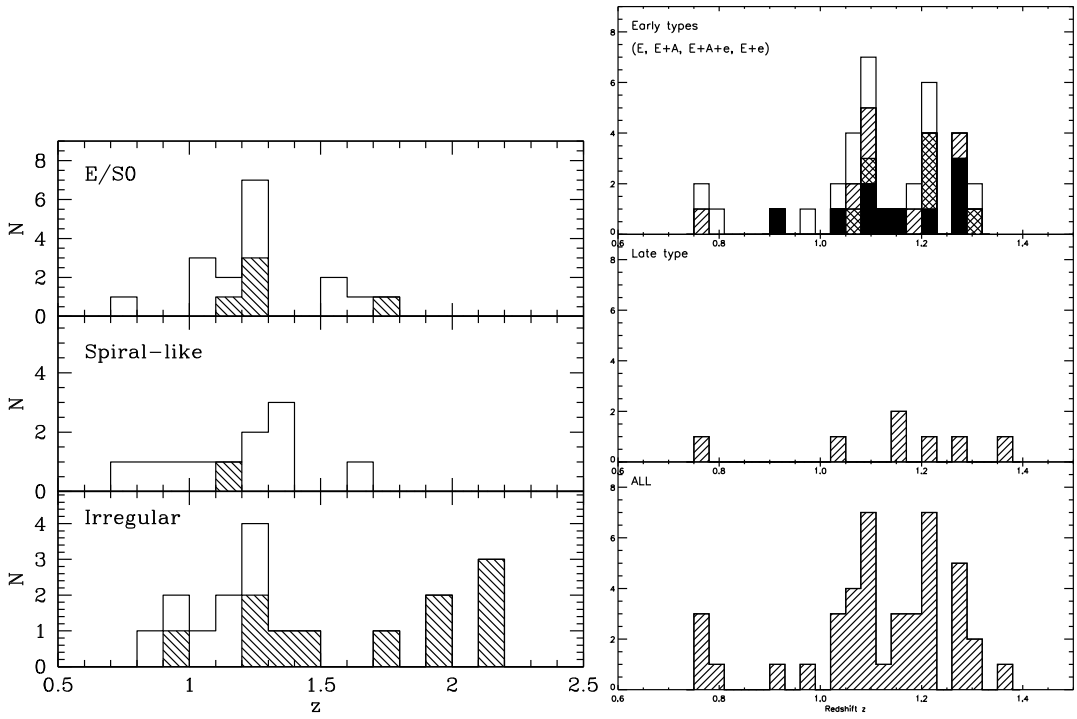

Figure 6.13: The observed redshift distribution of the ERO populations in the K20 Survey (left, In Cimatti et al, 2003), and the Las Campanas IR survey (right, Doherty et al. 2005.). In the shaded histograms of the K20 sample indicate the photometric redshifts. The ERO sample of the LCIR Survey is defined by $I - H > 3$, $H < 20.5$.

of 275 objects, where 66 have spectroscopic redshifts and the rest have photometric ones. The redshift distribution for their ERO populations has a fairly sharp edge at about 1 and a median value of $z_m \approx 1.2$, which is comparable to the value found in our sample.

The LCIR, the K20, and the GOODS surveys also found that this narrow redshift distribution of their ERO sample is due to the strong clustering properties of this galaxy type. Here, we derive the angular clustering signal for the ERO population detected in the COMBO S11 field as well.

The angular two-point correlation function $\omega(\theta)$ gives the excess probability over a random Poisson distribution of finding two galaxies in the solid angle elements $d\Omega_1$ and $d\Omega_2$ separated by an angle θ:

$$dP = N^2[1 + \omega(\theta)]d\Omega_1 d\Omega_2 \ , \tag{6.1}$$

where N is the mean number density of objects per steradian. For the estimation $\omega(\theta)$ of the ERO population detected in the COMBO S11 field, we used a standard procedure. In the first step, we generated a random sample within the same area covered by the observations (tiles B, C, and D) and the objects locating near the bright stars were removed from the random catalogue. Then, we counted the number of the data pairs for the data-data sample DD, the data-random sample DR, and the random-random sample RR in logarithmic distance intervals, $[\theta, \theta + d\theta]$. From these normalized counts we estimated the angular correlation function with the expression

$$\omega(\theta) = \frac{DD - 2DR + RR}{RR} \ , \tag{6.2}$$

which was proposed by Landy & Szalay (1993). At low redshifts $\omega(\theta)$ can be approximated by a power law with a bias

$$\omega(\theta) = A(\theta^{-\delta} - C) \ , \tag{6.3}$$

where A is the clustering amplitude and C is the integral constraint

$$C = \frac{1}{\Omega^2} \int \int \theta^{-\delta} d\Omega_1 d\Omega_2 \ . \tag{6.4}$$

Typically, $0.6 \leq \delta \leq 0.8$, depending to some extent on Hubble type. In the NIR galaxy surveys, like the K20 or the LCIR surveys, it is fixed to $\delta = 0.8$ for EROs and we also chose this value. The intergal constraint is ~ 0.15 for the area of 710 arcmin^2 observed in the COMBO S11 field. After fitting the $\omega(\theta)$ values over the angular range 3-300 arcsec, we derived the clustering amplitude for EROs at 1 arcmin of $\omega(\theta)$ and the 1σ error of A were derived from the formule $\sqrt{[1 + \omega(\theta)]/DD}$.

Fig. 6.14 shows that the angular two-point correlation functions of the COMBO S11 ERO sample are consistent with those derived in the LCIR survey for different H magnitude limits and without redshift selection. We obtained high clustering amplitudes for EROs as well. The values listed in Tab.6.3 demonstrate that as we move to fainter H magnitudes the A decreases - a fainter sample covers more objects with lower clustering signal than the brighter sample. Comparing our values with the clustering amplitudes $A = 0.33$ for $H < 20$ and 0.17 for $H < 20.5$ measured in the LCIR survey, we see this trend in both surveys but the difference of the clustering amplitudes for the COMBO S11 sample is more moderate.

We saw that several characteristics of the ERO population detected in the COMBO S11

H magnitude limit	N	z_{med}	A(1 arcmin)	A(1 arcmin) /LCIR/
$H < 20$	292	0.94	0.25 ± 0.1	0.33 ± 0.11
$H < 20.5$	498	0.95	0.18 ± 0.09	0.17 ± 0.09

Table 6.3: The number of galaxies N, median photometric redshift z_{med}, and the amplitude A of $\omega(\theta)$ at 1 arcmin for the ERO population detected in the COMBO-17+2 NIR and the LCIR surveys.

field, such as the redshift distribution, the differential number counts, the cumulative surface brightness, and the angular clustering are in good agreement with the results of the LCIR survey. This means the properties of the COMBO S11 ERO sample provide very similar constraints on the galaxy evolution models to those of the LCIR survey data. However, the LCIR survey finds higher clustering amplitude for the brighter ERO sample, thus their results lead to stronger constraints. The strong clustering of EROs measured in both surveys may be an evidence that the majority of them are indeed massive galaxies in a restricted redshift range. This supports either the early mergings of their progenitors or their passive evolution after forming at high redshift since the relative fraction of actively star-forming systems to the evolved ellipticals in the ERO population is different in these models. It is therefore important to investigate the nature of the EROs as well, which we will do in the next section.

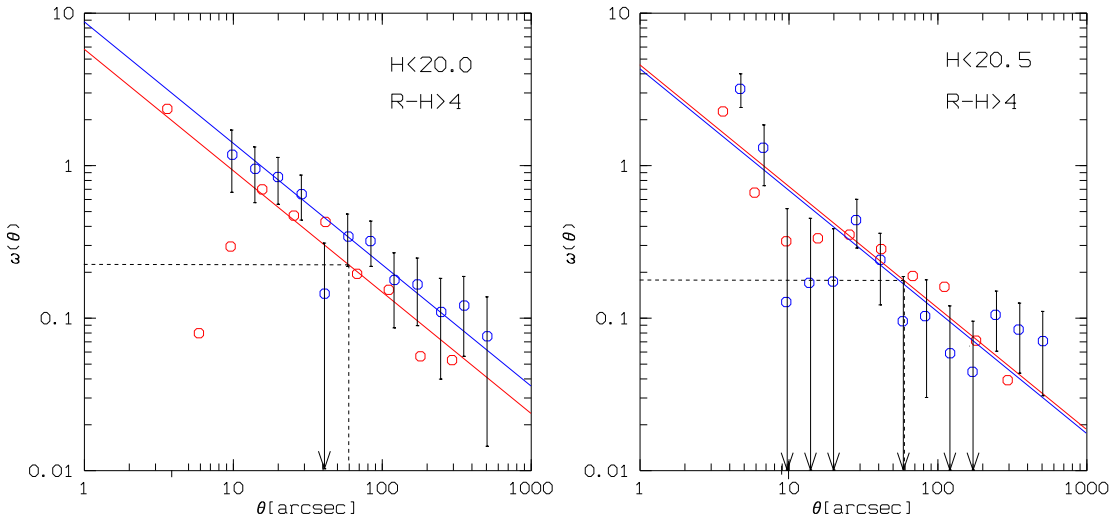

Figure 6.14: The angular two-point correlation function of EROs with $R-H>4$ for H limiting magnitudes of 20 and 20.5. The red circles denote the COMBO S11 sample and the blue ones are the ERO population detected in the LCIR survey (Firth et al., 2002). The solid lines are the power low fits on these data points with $\delta = 0.8$. The dashed lines indicate the value of $\omega(1$ arcmin). For $H < 20$ we ignored the two outlier values in the bins at smaller angular separations where there are too few data-data pairs to obtain a reliable measurement.

6.2.4 The Nature of EROs

Since the first reports on the detection of EROs, there has been a controversy over their nature. As mentioned in the introduction, they were first thought to belong to the classical primeval galaxy population at very high redshift. Since then several surveys have shown that the EROs consist of a heterogeneous galaxy population of old ellipticals and dusty starburst. The identification of some EROs as early-type galaxies is based on the fact that the broadband spectra of these galaxies can be fitted well for old stellar populations, such as is found in present-day elliptical galaxies. Assuming their colors are not affected by dust reddening, we can attribute the high $R-K$ color and K magnitude to intrinsically red SEDs of old, passively evolved elliptical galaxies at high redshifts, $1 < z < 2$. In this scenario, the redshifted strong 4000 Å break, falling between the R and H band, and the lack of any appreciable rest-frame UV light from a young population of stars are responsible for the extremely red colors. The alternative interpretation considers these objects as dust shrouded starburst galaxies or AGNs perhaps in a very active phase or during a merging event. In this case, the extremely red colors (and the relatively high K-band magnitudes) can be explained by the presence of the large amount of the interstellar dust, which hides the star-forming regions or AGNs and considerably reddens either the starburst population or the AGN itself, and therefore their observed SEDs. These objects would also lie at higher redshifts ($1 < z < 2$), shifting their rest-frame UV and optical-NIR bands into the optical and the K bands, respectively. In both cases, the EROs are most likely to lie in the redshift range $1 < z < 2$, since it is difficult to produce such red colors at lower redshifts and objects at higher redshifts than $z > 2$ would need to be extremely luminous.

The nature of various ERO samples was studied in great detail in some spectroscopic surveys which confirmed that both the two classes described above contribute to the ERO population but their relative fraction remains still unconstrained. The basic dichotomy between evolved early-type galaxies and dusty starbursts remains one of the central questions in the study of these objects and it is still not clear if they can be divided so simply. Because of their completely different evolutional histories, the determination of the relative fractions among the two classes of galaxies is indeed essential. If we knew this relative fraction we could give a correct interpretation of many statistical properties of EROs, such as space densities, luminosity functions and clustering strength. In fact, clarifying the contribution of the different classes to the total ERO population will also provide a crucial test for the models of structure formation and galaxy evolution, since it has contrasting implications of the mass assembly history of galaxies. The presence of a widespread population of high-redshift ellipticals among EROs would support the models based on the old merging scenario or monolithic dissipative collapse (Eggen, Lynden-Bell and Sandage 1962), in which the present day massive spheroidals formed at very early cosmological epochs ($z > 2-3$) through merging or only a relatively short episode of star burst followed by a pure and passive luminosity evolution (PLE) to nowadays. If the ERO population is dominated by dusty starburst galaxies at intermediate redshift, it would confirm the standard hierarchical merging scenario of galaxy formation and evolution in the CDM paradigm (White & Frenk 1991; Kauffmann, Charlot & White 1996), where the most massive present day ellipticals were assembled through a series of mergings of pre-existing less massive systems at later times ($z < 1$), even though the bulk of their starts may already be very old at the time of the last major merging.

Although the color degeneracy between these two very different galaxy populations makes the classification of EROs difficult, either spectroscopically or morphologically, there are several observational features which help to distinguish the two classes. Their spectra could show either the presence of emission lines, indicating on-going star formation activity or sharp spectral breaks owing to old stellar population. The submillimetre observations can also detect far-IR emission from the hot dust heated by the starburst regions, while the optical and near-IR images reveal the morphology, which is expected to be regular and centrally peaked for old ellipticals or irregular and disturbed for dusty starburst galaxies. However, EROs are normally very weak at optical wavelengths, therefore spectroscopy is not a viable method for classifying a large number of EROs. We can apply broad band colors not only for the ERO selection but also for the separation of old ellipticals from the dusty starburst population. In photometric methods measuring color properties, the different spectral shapes near 4000 Å are used as the primary discriminant. The spectra of early-type galaxies with ages of ~ 1 Gyr or more become flatter in the 4000-5000 Å range and have a steep drop shortward of 4000 Å. The galaxies with younger stellar population and sufficient reddening and redshift have steeper slopes longward of 4000 Å but may exhibit similar slopes to that of the ellipticals in the rest-frame UV regime.

The two-color approach developed by Pozetti & Manucci (2000) measures these differences in terms of colors. They separated the two classes of EROs on the basis that the two populations in the redshift ranges $1 \leq z \leq 2$ and $2 \leq z \leq 2.5$ fall in different regions in both $I-K$ vs. $J-K$ and $R-K$ vs. $J-K$ two-color diagrams for sources in the lower redshift range and in $H-K$ vs. $J-K$ plots in the higher redshift range. Pozetti and Manucci studied these relations for a variation of dust contents, star formation histories, formation redshifts, and metallicities and found that their result is viable in a wide range of them.

Pierini et al. (2003) extended the study of the color-color method for ERO classification by considering galaxies formed in short bursts as well as old and multiple-burst population in the $1 < z < 2$ interval. Besides the nominal dust-free evolved ellipticals and dusty starbursts, they also included dusty post-starburst galaxies in the analysis and studied the effects of various dust distributions within the model galaxies. However, it did not have a large impact on the overall results, as the validity of the two-color method originally proposed by Pozetti & Manucci is not strongly dependent on the the geometry of the dust and the degree of mixing between gas and stars. They could establish only that the separation of old, dust-free systems and dusty starburst systems is less distinct because of the presence of dusty post-starburst systems in their model.

Bergström & Wiklind (2004) carried out a comprehensive analysis on the separation of EROs based on their broad band color-color properties by studying the selectivities of all possible color-color combinations of the five broad band filters $RIJHK$ for ellipticals and dusty starbursts derived from PEGASE2 spectra with two IMFs and a range of metallicities and extinctions. They found that among the configurations of filter triplets, the ones with the center waveband as pivot band (i.e. the H band in the $R-H$ vs. $H-K$ configuration) perform best as discriminators. Bergström & Wiklind determined the separation line of the two ERO populations in the two-color diagrams for each each filter set by minimizing the misclassification. These separation criteria are valid for given redshift ranges, $0 < z < z_{max}$, where z_{max} is the redshift beyond which the color regions become entangled for a specific two-color diagram. The test of the different filter

Filter set	Separating line: color of ERO ellipticals at $z \leq z_{max}$	z_{max}
$\{RJH\}$	$R-J > 1.77\ (J-H)\ +1.10$	2.1
$\{RIJ\}$	$R-I > -0.38\ (I-J)\ +2.05$	1.6
$\{RIH\}$	$R-I > 0.25\ (I-H)\ +0.56$	1.2
$\{RIJH\}$	$R-J > 0.65\ (I-H)\ +1.20$	1.8

Table 6.4: The separation lines of the ERO classification given by Bergström & Wiklind (2004) for all the color configurations available in the COMBO-17+2 NIR survey. The last column contains the redshift limits beyond which the color regions become entangled, z_{max}.

configurations showed that the $R-H$ vs. $H-K$ colors provide a fundamental criterion for EROs and have a very small overlap between the different galaxy populations up to redshifts of 2.9 for $E(B-V) \leq 2$. Nonetheless, from the different NIR broad bands used in the test, the K band is not present in the COMBO-17+2 NIR imaging. Only the broad band H band filter is available and the medium band J_1(1190/130nm) filter can also be taken into account. We consider the difference between the colors containing the J_1 or the broad J (1250/380nm) bands negligible for the spectra of the COMBO galaxy sample. The table 6.4 shows the separation lines of the ERO classification into old ellipticals and dusty starburst given by Bergström & Wiklind for all the configurations excluding the broad band K filter and containing the H and J filters. We used these configurations to check the consistency between the criteria given by Bergström & Wiklind (2004) for ERO separation and the result of the multi-color classification of COMBO-17+2 NIR for EROs.

First we present the results of the two-color separation method applied for our ERO sample. In Table 6.4 we list the separation criteria adapted from Bergström & Wiklind. These criteria are represented with diagonal lines in the color-color diagrams in Fig. 6.15. The $R-I$ vs. $I-H$ color diagram contains only evolved EROs for $z < z_{max}$. This is a good agreement with the expectation that the filter pair $R-H$, being more sensitive to the 4000 Å break in the spectra of evolved galaxies than the smother spectral breaks in dusty star-forming systems, selects mainly early-type galaxies. Nevertheless, the other three color configurations give a slightly different view. In the $R-J_1$ vs. J_1-H diagrams only about 60 % of the population, with $z < z_{max}$, belongs to the class of ellipticals, while this number is about 80 and 88 % for the separation criteria applying the $R-I$ vs. $I-J_1$ and $R-J_1$ vs. $I-H$ color pairs, respectively. By checking the overlap between the objects classified as starburst galaxies in the three color-color diagrams, we find that all the objects detected as the star-forming systems in the $R-J_1$ vs. $I-H$ plot are also identified as dusty starbursts in the $R-I$ vs. $I-J_1$ diagram. In turn, all the star-forming galaxies in the $R-I$ vs. $I-J_1$ plot belong to the starbursts in the $R-J_1$ vs. J_1-H two-color plot as well. The SED vs. extinction plot of these objects in Fig. 6.16 demonstrates this selectivity of the ERO classification criteria. The criterion based on the $R-J_1$ vs. J_1-H colors selects the widest range of galaxies as elliptical from E/S0 to Sbc while $R-J_1$ vs. $I-H$ color pair probes a more bluer subset of this population, mainly Sb-Sbc galaxies. The $R-I$ vs. $I-J_1$ colors are sensitive to bluest subset of the previous subgroup and help to find manly Sbc

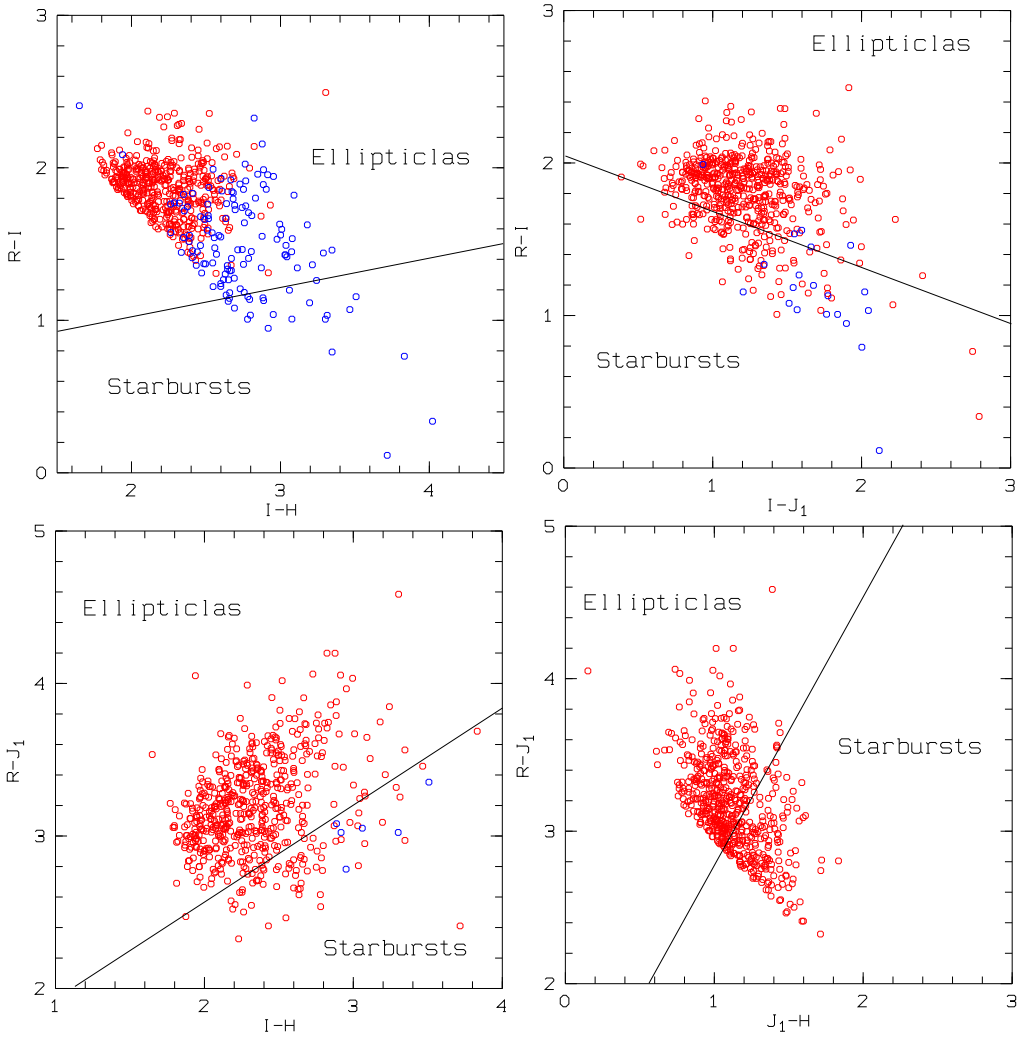

Figure 6.15: Two color plots of the ERO sample selected with the color cut $R - H > 4$ in the COMBO S11 field. The red circles denote the EROs with $z < z_{max}$ for the given two color configuration. The blue circles represent the EROs with $z > z_{max}$, for which the separation criteria become uncertain. The diagonal solid lines separating the EROs into ellipticals and dusty starbursts are from Bergström & Wiklind (2004).

galaxies.

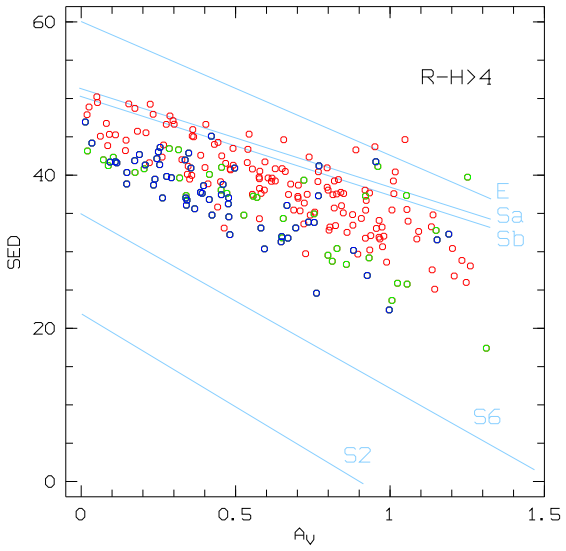

Figure 6.16: The SED vs. extinction diagram for the EROs in the COMBO S11 field, which are identified as starburst galaxies by the separation criteria proposed by Bergström & Wiklind (2004). The red circles denote the EROs determined as starburst with respect to their $R-J$ vs. $J-H$ color pair. The green circles represent the EROs classified as starburst in both the $R-J$ vs. $J-H$ and the $R-J$ vs. $I-H$ two-color plots. The blue circles are coding the EROs, which are considered starburst with respect to three criteria, the $R-J$ vs. $J-H$, $R-J$ vs. $I-H$, and $R-I$ vs. $I-J$ color pairs.

The limits of the two-color separation method for EROs proposed by Bergström & Wiklind are the consequence of their definition of the elliptical and dusty starburst galaxies used in the test. They modelled the elliptical galaxies as ones that, after an instantaneous burst of star formation, evolve passively without any interstellar gas or dust. They are considered ellipticals 100 Myr after the starburst, and are then let to evolve for a Hubble time. The starburst galaxies are modelled as galaxies with constant star-formation during 100 Myr. The spectral templates for galaxies applied in the COMBO-17+2 NIR multi-color classification were also derived from the PEGASE2 stellar synthesis model, but with an exponential decline in the star formation law ($\tau = 1$) instead of using a simple star population. By comparing the results of the two-color separation method and the multi-color classification, we see the definition of ellipticals applied by Bergström & Wiklind still covers the series of early-type galaxies and evolved spirals for EROs but the galaxies determined as dusty sartbursts by the ERO separation criteria are identified as E/S0-Sc galaxies in the COMBO-17+2 NIR multi-color classification.

Fig. 6.17 shows the SED vs. extinction diagram of the total ERO population found in the COMBO S11 field. It demonstrates that the galaxies are identified in the multi-color classification as E/S0 galaxies and mainly Sa- and Sb-type spirals with some Sbc galaxies, while the actively star-forming systems (S1-S6) in this ERO population are completely missing. Fig. 6.17 the SED vs. $R-H$ color plot of the R- and H-band selected galaxy sample for $z > 0.8$ shows the colors of dusty starburst galaxies (with $E(V-B) > 0.4$ or $A_V \gtrsim 1.11$) in the expected redshift range of EROs are not red enough to enter the ERO sample.

This result may be due to various factors. The first one is the selectivity of the $R-H$ filter

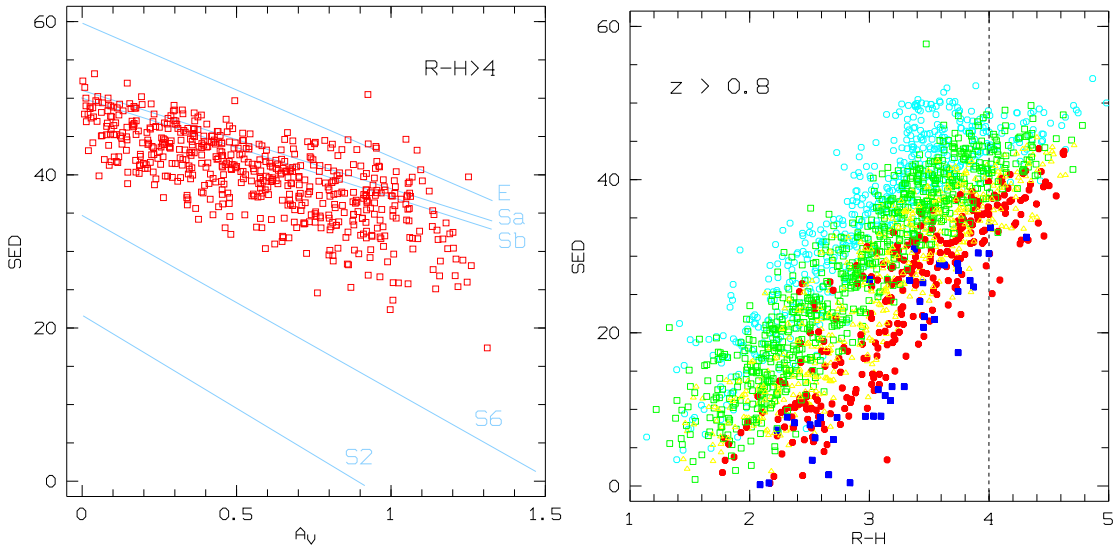

Figure 6.17: The left hand panel shows the SED vs. extinction diagram for the EROs selected with $R-H>4$ color cut in the COMBO S11 field. The red circles denote the ERO population and light blue lines represent the the spectral templates at $z=0$ used for the COMBO-17+2 NIR survey. The right hand panel shows the SED vs. $R-H$ color for the total R- and H-band selected galaxy sample for $z>0.8$ in the COMBO S11 field. The points are color-coded on the basis of their extinction: $E(B-V)<0.1$ (cyan open circles), $0.1<E(B-V)<0.2$ (green open squares), $0.2<E(B-V)<0.3$ (yellow filled triangles), $0.3<E(B-V)<0.4$ (red filled circles) and $0.4<E(B-V)<0.5$ (blue filled squares). The vertical dashed line separates the EROs from the bluer part of the galaxy sample.

pair. As already mentioned, the color cut $R-H>4$ is more sensitive to the spectral features of the advanced galaxies than those of the dusty starbursts dominated by younger stellar population. In the spectroscopic analysis of the LCIR Survey Doherty et al. (2005) find that most of their $I-H$ selected ERO sample contains a clear signature of old stellar population and only 16 % of the EROs appear to be dusty stary starburst systems. Since we used the $R-H$ color to select EROs in the COMBO S11 field, we would expect a similar result. This means the choice of this color could explain that low number of the actively star-forming systems in the COMBO S11 sample but not their total absence.

Another important factor causing this absence may be the usage of non-evolving spectral templates for the galaxies in the COMBO-17+2 NIR multi-color classification. The previous chapter discussed the improvements of the spectral template fitting for the COMBO-17+2 NIR data. We saw there that a large amount of objects classified as S1-S6-type galaxies by using only optical colors become Sb-Sbc-type or even more evolved spiral galaxies in the classification based on the NIR-supplemented data. We interpreted this result as the improvement in the detection of spectral contribution of the the old stellar population. However, the reduction in the number of the starburst galaxies might also be heightened by the imperfections of the template libraries. The non-evolving templates may characterize the spectral properties of the galaxies in the local Universe satisfactorily but there is no guarantee that they will fit the spectra of starburst galaxies at higher redshift as well. If the discrepancy between them is too strong it is likely to cause these to be misclassified. There is already a plan to replace the non-evolving spectral template library

with a template set derived for a wider redshift range, which can help to avoid any occurrent false fitting due to the imperfections of the synthetic spectra obtained for $z = 0$.

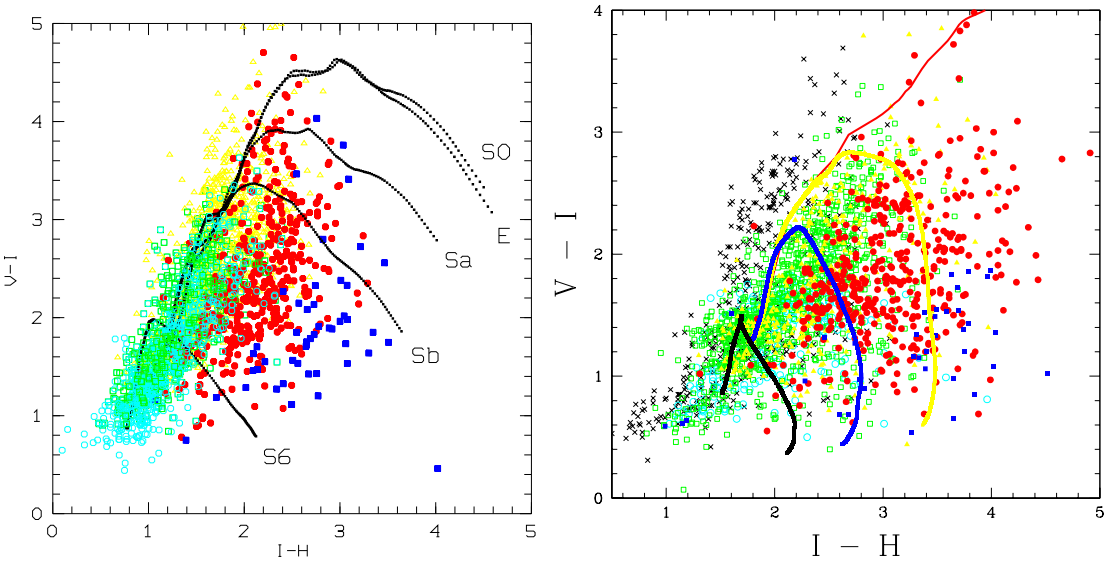

Figure 6.18: The $V - I$ vs. $I - H$ colors for objects with $19 < H < 20.5$ in the COMBO S11 field (left hand panel) and the CDF-S field in the LCIR Survey (right hand panel). The points are color-coded on the basis of their photometric redshift: stars (black crosses), $z < 0.25$ (cyan open circles), $0.25 < z < 0.75$ (green open squares), $0.75 < z < 1.0$ (yellow filled triangles), $1 < z < 1.5$ (red filled circles), and $1.5 < z < 2.0$ (blue filled squares). The model curves show the loci of evolving population models with various star formation laws: a single burst with $z_f = 30$ (red curve), exponential decline with $\tau = 1$ and 2 Gyr (yellow and blue curves), and continuous (black curve).

The lack of the dusty starburst population in our ERO sample may be attributed to a third factor as well, which is more closely related to the nature of the EROs. We have seen that the COMBO S11 ERO sample defined by $R - H > 4$ contains only evolved galaxies but these are mainly spirals and not ellipticals. Among the early forming and slowly evolving systems, there might be galaxies with periods of a modest star-formation or even massive starbursts due to merger events. As a result, these galaxies depart from the color tracks of the PLE models in the rest-frame UV and may in addition produce strong emissions lines in their spectra. If the strength of the starburst remains small, the NIR-band fluxes can still be dominated by the old stellar population. Since the merger-rate appears to increase with look back time (e.g. Calberg et al. 2000), these composite objects might be more numerous at high redshifts. The two-color $V - I$ vs. $I - H$ diagram of the COMBO-17+2 NIR and LCIR galaxy in Fig. 6.18 infers the high redshift red $I - H$ population has bluer rest-frame UV colors. The objects with blue $V - I$ and red $I - H$ colors are more likely to be at high redshifts than those lying closer to the track of the E/S0 templates plotted in the COMBO sample or to that of passively evolving model with single starburst of $z_f = 30$ plotted in the LCIR sample. The red galaxies with $I - H > 3$ in the LCIR survey sample and with $I - H \gtrsim 2$ in the COMBO sample span more than 3 mag in $V - I$. This wide range of optical colors covers that of the templates from early-type systems to spirals (E-Sb) in the redshift interval $0.8 < z < 1.5$. This means the ERO population is not

clearly divided into the two simple classes. Whereas the younger galaxies (Sa and Sb) can have the similar broadband colors to those of older systems (E/S0), some early-type systems can be identified erroneously as spirals in rest-frame UV emission line and continuum spectra. Hence the separation of the ERO population into PLE and actively star-forming models is blurred and may be artificial.

As some concluding remarks, we can claim that the H-band selected NIR surveys, using the $R-H$ color to define ERO samples, find a dominant population of old ellipticals and evolved spirals whereas they can only detect a small fraction of dusty starburst among the ERO population. The ERO population found in the COMBO S11 field does not contain any dust reddened star-forming systems at all but it may be due to the imperfections of the spectral templates used in the multi-color classification. In order to obtain a more reliable result for the relative fraction of these types in the ERO population, the spectral library with redshift evolution must be used in the multi-color classification. However, the COMBO-17+2 NIR survey also indicated that the debate on the dichotomy of the nature of ERO needs to be reinterpreted. Instead of two well defined morphological types of EROs, we have to consider a wide range of morphological types or types defined by internal colors (Bell et al. 2004), where the ellipticals and the dusty starburst galaxies represent only the two opposite endpoints of the broad scale. If the following surveys observing various ERO populations concentrate on the study of the relationship between color-color properties and the full scale of the expected ERO types, a more comprehensive picture can be drawn about the nature of these mysterious objects.

List of Figures

List of Tables

Acronyms

ADU	-	Analog-Digital Unit
APS	-	Active Pixel Sensor
CDM	-	Cold Dark Matter
CDS	-	Correlated Double Sampling
CITA	-	Capacitive TransImpendance Amplifier
ERO	-	Extremely Red Object
FPA	-	Focal Plane Array
NIR	-	Near Infra-Red
PLE	-	Passive Luminosity Evolution
PPS	-	Passive Pixel Sensor
SED	-	Spectral Energy Distribution
SFD	-	Source Follower Detector
SSP	-	Simple Star Population

Bibliography

[Bailer et al., 2000] C. A. Bailer-Jones, P. Bizenberger, and C. Storz, "Achieving a wide field infrared camera for the Calar Alto 3.5m telescope," in *Optical and IR Telescope Instrumentation and Detectors*, M. Iye and A. F. Moorwood, eds., *Proc. SPIE* **4008**, pp. 1305–1316, 2000.

[Baumeister et al., 2002] H. Baumeister, P. Bizenberger, C.A. Bailer-Jones, Z. Kovács, H.-J. Röser, and R.-R. Rohloff, "Cryogenic engineering for Omega 2000: Design and performance," in *Instrument Design and Performance for Optical/Infrared Ground-based Telescopes*, *Proc. SPIE* **4842**, pp. 343–354, 2002.

[Bell et al. 2003] E.F. Bell, D.H. McIntosh, N. Katz, and M.D. Weinberg: 2003. The Optical and Near-Infrared Properties of Galaxies. I. Luminosity and Stellar Mass Functions *Astrophysical Journal Suppl.* **149**, 289+

[Bell et al. 2004] E.F. Bell, C. Wolf, K. Meisenheimer, H.-W. Rix, A. Borch, S. Dye, M. Kleinheinrich, L. Wisotzki, and D.H. McIntosh: 2004. Nearly 5000 Distant Early-Type Galaxies in COMBO-17: A Red Sequence and Its Evolution since $z \sim 1$ *Astrophysical Journal* **608**, 752+

[Bergström and Wiklind] S. Bergström, and T. Wiklind: 2004. On the colour-colour properties of the Extremely Red Objects. *Astronomy and Astrophysics* **414**, 95B+

[Bruzual, 1983] A.G. Bruzual: 1983. Spectral evolution of galaxies. I - Early-type systems *Astrophysical Journal* **273**, 105+

[Carlberg et al., 2000] R.G. Carlberg, J.G: Cohen, D.R. Patton, R. Blandford, D.W. Hogg, H.K.C. Yee, S.L. Morris, H. Lin, P.B. Hall, M. Sawicki, 2000. Caltech Faint Galaxy Redshift Survey. XI. The Merger Rate to Redshift 1 from Kinematic Pairs *Astrophysical Journal* **521**, L1+

[Chen et al., 2003] H.-W. Chen, R.O. Marzke, O. Ronald, P.J. McCarthy, Patrick. P. Martini, R.G. Carlberg, S.E. Persson, A. Bunker, C.R. Bridge, and R.G. Abraham: 2003. The Las Campanas Infrared Survey. IV. The Photometric Redshift Survey and the Rest-frame R-band Galaxy Luminosity Function at $0.5 \leq z \leq 1.5$ *Astrophysical Journal* **586**, 745-764

[Cimatti et al., 1999] A. Cimatti, E. Daddi,S. di Serego Alighieri, L. Pozzetti, F. Mannucci, A. Renzini, E. Oliva, G. Zamorani, P. Andreani, and H.J.A. Röttgering: 1999. New clues on the nature of extremely red galaxies. *Astronomy and Astrophysics*, **352**, 45+.

[Cimatti et al., 2002] A. Cimatti, L. Pozzetti, M. Mignoli, E. Daddi, N. Menci, F. Poli, A. Fontana, A. Renzini, G. Zamorani, T. Broadhurst, S. Cristiani, S. D'Odorico, E. Giallongo and R. Gilmozzi: 2002, The K20 survey IV. The redshift distribution of galaxies: A test of galaxy formation models. *Astronomy and Astrophysics* **391**, L1-L5

[Conselice, Blackburne, and Papovich, 2005] C. J. Conselice, J. A. Blackburne, and C. Papovich: 2005. The luminosity, stellar mass, and number density evolution of field galaxies of known morphology from $z = 0.5 - 3$. *Astrophysical Journal* **620**, 564-583

[Cowie et al., 1996] L.L. Cowie, A. Songaila, E.M. Hu, and J.G. Cohen: 1996. New Insight on Galaxy Formation and Evolution From Keck Spectroscopy of the Hawaii Deep Fields *Astrophysical Journal* **112**, 839+

[Daddi et al. 2000] E. Daddi, A. Cimatti, L. Pozzetti, H. Hoekstra, H. J. A. Röttgering, A. Renzini, G. Zamorani, and F. Mannucci: 2000. Detection of Strong Clustering of Extremely Red Objects: Implications for the Density of $z > 1$ Ellipticals. *Astronomy and Astrophysics* **361**, 535+

[de Vaucouleurs et al., 1991] G. de Vaucouleurs, A. de Vaucouleurs, H.G. Corwin, Jr., R.J. Buta, G. Paturel, and P. Fouqué: 1991. Third Reference Catalogue of Bright Galaxies, New York: Springer

[Dickinson et al., 2003] M. Dickinson, C. Papovich, H.C. Ferguson, and T. Budavári: 2003. The Evolution of the Global Stellar Mass Density at $0 < z < 3$. *Astrophysical Journal* **587**, 25+

[Doherty] M. Doherty, A.J. Bunker, R.S. Ellis, and P.J. McCarthy: 2005. The Las Campanas Infra-red Survey. V. Keck Spectroscopy of a large sample of Extremely Red Objects. astro-ph/0505119

[Drory et al., 2001] N. Drory, R. Bender, J. Snigula, G. Feulner, U. Hopp, C. Maraston, G. J. Hill, and C. Mendes de Oliveira: 2001. The Munich Near-Infrared Cluster Survey (MUNICS) - Number density evolution of massive field galaxies to $z \sim 1.2$ as derived from the K-band selected survey. *Astrophysical Journal* **562**, L111-L114

[Eggen, Lynden-Bell and Sandage, 2001] O.J. Eggen, D. Lynden-Bell, and A.R. Sandage: 1962. Evidence from the motions of old stars that the galaxy collapsed. *Astrophysical Journal* **136**, 748+

[Elston, Rieke & Rieke, 1988, 1989] R., Elston, G.H. Rieke and M.J. Rieke: 1988. Deep 2 micron imaging of the sky: evidence for a new extragalactic population. *Astrophysical Journal*, **331**, L77-L80.

[Elston, Rieke & Rieke, 1989] R, Elston, G.H. Rieke and M.J. Rieke: 1989. Observations of deep 2 micron survey galaxies: primeval galaxy candidates. *Astrophysical Journal*, **341**, 80-88.

[Finger. 2002] G. Finger: "Test Report on HgCdTe Infrared Focal Plane Arrays", Garching, European Southern Observatory. 2002.

[Firth et al. 2002] A. E. Firth, R. S. Somerville, R. G. McMahon, O. Lahav, R. S. Ellis, C. N. Sabbey, P. J. McCarthy, H.-W. Chen, R. O. Marzke, J. Wilson, R. G. Abraham, M. G. Beckett, R. G. Carlberg, J. R. Lewis, C. D. Mackay, D. C. Murphy, A. E. Oemler, and S. E. Persson: 2002. Las Campanas IR Survey. II. Photometric redshifts, comparison with models and clustering evolution. *Monthly Notes R. Astron. Soc.* **332**, 617+

[Fioc & Rocca-Volmerange] M. Fioc, B. Rocca-Volmerange: 1997. PEGASE: a UV to NIR spectral evolution model of galaxies - Application to the calibration of bright galaxy counts. *Astronomy and Astrophysics* **326**, 950-962

[Giallongo et al. 2005] E. Giallongo, S. Salimbeni, N. Menci, G. Zamorani, A. Fontana, M. Dickinson, S. Cristiani, L. Pozzetti: 2005. The B-Band Luminosity Function of Red and Blue Galaxies up to $z = 3.5$. *Astrophysical Journal* **622**, 116-128

[Gear et al. 2000] Authors: W. K. Gear, S.J. Lilly, J.A. Stevens, D.L. Clements, T.M. Webb, S.A. Eales, and L. Dunne: 2000. High spatial resolution observations of CUDSS14A: a SCUBA-selected Ultraluminous galaxy at high redshift. *Monthly Notes R. Astron. Soc.* **316**, L51

[Gil de Paz & Madore] A. Gil de Paz, and B. F. Madore: 2002 On the Optimization of Broad-Band Photometry for Galaxy Evolution Studies. *Astronomical Journal* **123**, 1864+

[Haas, 2002] A. Haas, "Users Guide for the HAWAII-2 2048x2048 Pixel Focal Plane Array," Rockwell Scientific Company, LLC, 2002

[Hansen et al., 1982] G.L. Hansen, J.L. Schmidt, and T.N. Casselman, Energy gap versus alloy composition and temperature in $Hg_{1-x}Cd_xTe$, *J. Appl. Phys.* **53**(10) pp. 7099-7101, 1982.

[Hodapp et al., 1995] K. Hodapp, D. H. J.L. Hora, L. Cowie, M. Metzger, E. Irwin, T. Keller, K. Vural, L. Kozlowski, and W. Kleinnhans, "Astronomical characterization results of 1024x1024 HgCdTe HAWAII detector arrays," in *Infrared Detectors and Instrumentation for Astronomy*, A. M. Fowler, ed., *Proc. SPIE* **2475**, pp. 8–14, 1995.

[Hodapp, 2000] K. Hodapp, "Near-infrared detector arrays: Current state of the art," in *Optical and IR Telescope Instrumentation and Detectors*, M. Iye and A. F. Moorwood, eds., *Proc. SPIE* **4008**, pp. 1228–1239, 2000.

[Hu & Ridgaw, 1994] E.M. , Hu, and G.H. Ridgaw: 1994. The extremely red galaxies. *Astronomical Journal* **107**, 1030+.

[Kauffmann, Charlot and White] G. Kauffmann, S. Charlot, and S.D.M. White: 1996. Detection of strong evolution in the population of early-type galaxies. *Monthly Notes R. Astron. Soc.* **283**, L117+.

[Kozlowski et al., 1998] L.J. Kozlowski, K. Vural, S.A. Cabelli, A. Chen, D.E. Cooper, C. Cabelli, K. Hodapp, D. Hall, and W.E. Kleinhans, "HgCdTe 2048^2 FPA for Infrared Astronomy Development Status," in *Infrared Detectors and Instrumentation for Astronomy*, A.M. Fowler, ed., *Proc. SPIE* **3354**, pp. 8-21, 1998.

[Kovács et al., 2004] Z. Kovács, U. Mall, P. Bizenberger, H. Baumeister, H.-J. Röser Characterization, testing, and operation of Omega2000 wide-field infrared camera: in *Optical and Infrared Detectors for Astronomy*, J. D. Garnett, J. W. Beletic, Eds. *Proc. SPIE* **5499**, 432-441, 2004

[Kroupa et al. 1993] P. Kroupa, C. A. Tout, G. Gilmore: 1993. The distribution of low-mass stars in the Galactic disc. *Monthly Notes R. Astron. Soc.* **322**, 231+.

[Landy & Szalay, 1993] S.D. Landy & A.S. Szalay: 1993 Bias and variance of angular correlation functions. *Astrophysical Journal* **412**, 64+

[Lilly et al. 1995] S.J. Lilly, L. Tresse, F. Hammer, D. Crampton, and O. Le Fevre: 1995. The Canada-France Redshift Survey. VI. Evolution of the Galaxy Luminosity Function to z approximately 1. *Astrophysical Journal* **455**, 108L+

[Martini, 2001] P. Martini: 2001. A Deep Multicolor Survey. VII. Extremely Red Objects and Galaxy Formation. *Astronomical Journal* **121**, 2301+

[Marzke et al., 1998] R.O. Marzke, L.N. da Costa, P.S Pellegrini, C.N.A Willmer, and J.M. Geller: 1998. The Galaxy Luminosity Function at $z \leq 0.05$: Dependence on Morphology *Astrophysical Journal* **503**, 617+

[McCarthy et al., 2001] P. J. McCarthy, R. G. Carlberg, H.-W. Chen, R. O. Marzke, A. E. Firth, R. S. Ellis, S. E. Persson, R. G. McMahon, O. Lahav, J. Wilson, P. Martini, R. G. Abraham, C. N. Sabbey, A. Oemler, D. C. Murphy, R. S. Somerville, M. G. Beckett, J. R. Lewis, and C. D. MacKay: 2001. The Las Campanas IR Survey: Early Type Galaxy Progenitors Beyond $z = 1$. *Astrophysical Journal* **560**, 131+

[Moustakas et al., 2004] L.A. Moustakas , S. Casertano, C. Conselice, M.E. Dickinson, P. Eisenhardt, H.C. Ferguson , M. Giavalisco, N.A. Grogin, A.M. Koekemoer, R.A. Lucas, B. Mobasher, C. Papovich, A. Renzini, R.S. Somerville, and D. Stern: 2004. Morphologies and Spectral Energy Distributions of Extremely Red Galaxies in the GOODS-South Field. *Astrophysical Journal* **600**, L131-L134

[Miyazaki et al., 2002] M. Miyazaki, K. Shimasaku, T. Kodama, S. Okamura, H. Furusawa, M. Ouchi, F. Nakata, M. Doi, M. Hamabe, M. Kimura, Y. Komiyama, S. Miyazaki, C. Nagashima, T. Nagata, T. Nagayama, Y. Nakajima, H. Nakaya, A. J. Pickles, S. Sato, K. Sekiguchi, M. Sekiguchi, K. Sugitani, T. Takata, M. Tamura, M. Yagi, and N. Yasuda: 2002. Evolution of Elliptical Galaxies at $z \gtrsim 1$ Revealed from a Large, Multicolor Sample of Extremely Red Objects. *Publications of the Astronomical Society of Japan* **55**, 1079

[Pei, 1992] Y. C. Pei: 1992. Interstellar dust from the Milky Way to the Magellanic Clouds. *Astrophysical Journal* **395**, 130.

[Pierini et al. 2004] D. Pierini, C. Maraston, R. Bender, and A.N. Witt: 2004. Extremely red galaxies: dust attenuation and classification. *Monthly Notes R. Astron. Soc.* **347**, 1+

[Pozzetti & Mannucci, 2000] L. , Pozetti, and F. Mannucci: 2000. Extremely red galaxies: age and dust degeneracy solved? *Monthly Notes R. Astron. Soc.* **317**, L17-L21.

[Pozzetti et al., 2003] L. Pozzetti, A. Cimatti, G. Zamorani, E. Daddi, N. Menci, A. Fontana, A. Renzini, M. Mignoli, F. Poli, P.T. Saracco, S. Broadhurst, S. Cristiani, S. D'Odorico, E. Giallongo, and R. Gilmozzi: 2003. The K20 survey. V. The evolution of the near-IR Luminosity Function. *Astronomy and Astrophysics* **402**, 837+

[Roche et al., 2003] N. Roche, J. Dunlop, and O. Almaini: 2003. The Nature, Evolution, Clustering and X-ray Properties of Extremely Red Galaxies in the CDFS/GOODS field. *Monthly Notes R. Astron. Soc.* **346**, 803+

[Röser, 2004] H.-J. Röser, "OMEGA2000 User's Manual", Heidelberg, Max-Planck-Institut für Astronomie, 2004.

[Röser & Meisenheimer, 1991] H.-J. Röser & K. Meisenheimer: 1991. The synchrotron light from the jet of 3C 273. *Astronomy and Astrophysics* **252**, 485-474.

[Rudnick et al., 2003] G. Rudnick, H.-W. Rix, M. Franx, I. Labbé, M. Blanton, E. Daddi, N.M. Förster Schreiber, A. Moorwood, H. Röttgering, and I. Trujillo: 2003. The Rest-Frame Optical Luminosity Density, Color, and Stellar Mass Density of the Universe from $z = 0$ to $z = 3$. *Astrophysical Journal* **599**, 847+

[Saracco et al., 2001] P. Saracco, E. Giallongo, S. Cristiani, S. D'Odorico, A. Fontana, A. Iovino, F. Poli, and E. Vanzella: 2001. Deep near-IR observations of the Chandra Deep Field and of the HDF-South - Color and Number Counts. *Astronomy and Astrophysics* **375**, 1+

[Smail et al., 1999] I. Smail, R.J. Ivison, J.-P. Kneib, L.L. Cowie, A.W. Blain, A.J. Barger, F.N. Owen, and G.E. Morrison: 1999. The Discovery of ERO Counterparts to Faint Submm Galaxies. *Monthly Notes R. Astron. Soc.* **308**, 1061+

[Soifer et al. 1999] B.T. Soifer, K. Matthews, G. Neugebauer, L. Armus, J.G. Cohen, S.E. Persson, and I. Smail: 1999. Near-Infrared Observations of the Extremely Red Object CL 0939+4713B: An Old Galaxy at $z \sim 1.58$? *Astrophysical Journal* **118**, 2065+

[Spinrad et al. 1997] H, Spinrad, A. Dey,D. Stern, J. Dunlop, J. Peacock, R. Jimenez, and B.T. Windhorst: 1997. An old, red Galaxy at $z = 1.552$. *Astrophysical Journal* **484**, 581+..

[Thomson et al. 1999] D. Thomson, S.V.W. Beckwith, R. Fockenbrock, J. Fried, H. Hippelein, J.-S. Huang, B. von Kuhlmann, Ch. Leinert, K. Meisenheimer, S. Phleps, H.-J. Röser, E. Thommes, and Ch. Wolf 1999. The surface density of extremely red objects. *Astrophysical Journal* **523**, 100+.

[van den Bergh et al. 2001] S. van den Bergh, J. G. Cohen, C. Crabbe: Caltech Faint Galaxy Redshift Survey XV: Classification of Galaxies with $0.2 < z < 1.1$ in the Hubble Deep Field (North) and its Flanking Fields. *Astronomical Journal* **122**, 611

[White & Frenk, 1991] S.D.M. White, and C.S. Frenk: 1991. Galaxy formation through hierarchical clustering *Astrophysical Journal* **379**, 52+

[Wolf et al. 2001] C. Wolf, K. Meisenheimer, and H.-J. Röser: 2001. Object classification in astronomical multi-color surveys *Astronomy and Astrophysics* **365**, 660+

[Wolf et al. 2003] C. Wolf, K. Meisenheimer, H.-W. Rix, A. Borch, S. Dye, and M. Kleinheinrich: 2003. The COMBO-17 survey: Evolution of the galaxy luminosity function from 25 000 galaxies with $0.2 < z < 1.2$ *Astronomy and Astrophysics* **401**, 73+

[Wolf et al. 2005] C. Wolf, M. Gray, and K. Meisenheimer: 2005. The cluster Abell 901/902 seen with COMBO-17: Dusty star-forming galaxies in the red-sequence. astro-ph/0506150

[Yan et al., 2000] L. Yan, P.J. McCarthy, R.J. Weymann, M.A. Malkan , H.I. Teplitz, L.J. Storrie-Lombardi, M. Smith, and A. Dressler: 2000. Extremely Red Objects from the NICMOS/HST Parallel Imaging Survey. *Astronomical Journal* **120**, 575+

Acknowledgments

I would like to express my special gratitude to Prof. Klaus Meisenheimer for being my supervisor for the last two years of this study.

I also acknowledge the support of my former supervisor, Dr. Hermann-Josef Röser.

I am deeply indebted to Prof. Dietrich Lemke and the directors Prof. Thomas Henning and Prof. Hans-Walter Rix for given my the opportunity to work at MPIA.

I would like to thank Dr. Christian Wolf and Siegfried Falter for their invaluable help during my study in astronomy.

I am grateful to Peter Bizenberger, Ulrich Mall, Harald Baumeister, Clemens Storz, Florian Briegel and René Fassbender for their guidance and support related to the OMEGA2000 project.

Final thanks go to Dr. Fabiola Zelada González, Jeffrey Mark Burkhartsmeyer, and Ernest Krmpotic for their encouragement, language expertise, and helpful remarks.